

Effects Of Space Weather On Earth's Ionosphere And Nominal LEO Satellites' Aerodynamic Drag

Thesis submitted for the degree of
Doctor of Philosophy (Science)
in Physics (Theoretical)

by

Victor Uchenna Jonathan Nwankwo
Department of Physics
University of Calcutta

2016

To Dad and Mum (God's gift), with love

ABSTRACT

Solar and geomagnetic activity drives certain changes in magnetospheric condition and results in coupled effects that modify thermospheric and ionospheric parameters. Such parameters are mainly the atmospheric density distribution, electron content, ionospheric current system, ionisation rates, and the conductivity gradient and reference height of D-region ionosphere. These changes and associated effects vary with the timescale of solar activity cycle. The direct implication of the variability of atmospheric temperature (T) and density (ρ) on space probes in low Earth orbit (LEO) include increase in atmospheric drag leading to accelerated orbital decay with grave consequences for satellite operation in the near-Earth space. In the first part of this thesis, we perform a study of solar forcing (space weather) induced perturbations of thermospheric T and ρ at an altitude of 400-450 km and the consequential atmospheric drag on LEO satellites to understand both long and short-term atmospheric variability and the resultant increase of satellites' nominal aerodynamic drag. The goal of the study is to quantitatively estimate drag-induced orbital decay (on the satellites) at different phases of the solar cycle and during intervals of strong geomagnetic perturbations and storms condition. In modeling drag effect on the orbit of two hypothetical LEO satellites (SAT-BCI and SAT-BCII) with different ballistic coefficients initially at 450 km, we found that the mean annual decay rate of the satellites during the peak of 23rd solar maximum was almost twice that of 24th maximum phase. SAT-BCI decayed by 48 ± 2 km/year and 25 ± 7 km/year during solar maximum in 2000-2002 and 2012-2014 respectively, whereas SAT-BCII decayed by 62 ± 1 km/year and 31 ± 10 km/year respectively in those years. However, a LEO satellite initially at $h=450$ km could experience a decay rate of up to 41 ± 19 km per year during solar maximum and 11 ± 6 km per year during the solar minimum. These rates also depend on a satellite's ballistic coefficient and the solar activity. The thermospheric T and ρ range is about 915-1470 K and 1.15×10^{-12} - 14.70×10^{-12} kg/m³ during the maxima, and about 756-1212 K and 0.31×10^{-12} - 3.59×10^{-12} kg/m³ during the minimum phase. These defines the condition in near-Earth space environment through which the satellites traversed. Using a modified density model, we also found that dominant corotating interaction region-induced effect on the satellites orbit could result in additional decay rate of up to 3 km/year during the declining phase of solar activity or solar minimum. We showed that intervals of strong density perturbations and additional heating from geomagnetic storms can result in an additional 60% decay in each event. This impact could vary depending on the severity and duration of the event. We then implemented our new drag model on real LEO satellites and simulated known decay profile of the Challenging Mini-satellite Payload (CHAMP), the Gravity field and steady state Ocean Circulation Explorer (GOCE) and the International Space Station (ISS). We also

studied the effects of drag on an interplanetary mission spacecraft, the Mangalyaan Mars Orbiter (MMO). We found that the results of our simulations compared well with those of actual decay parameters. This provides a justifications for the theoretical consideration used in the model. In the second part of the thesis, we perform a study of geomagnetic storm-induced magnetosphere-ionosphere dynamics in mid-latitude (40° - 54°) D-region (60-90 km) using VLF radio signal. The aim of the study is to understand VLF signal characteristics that are related to storms driven ionospheric changes, for efficient probing of solar-induced changes in lower ionosphere. We analysed the trends in variation of ‘characterised’ metrics of signal amplitude under varying degree of geomagnetic storm conditions. We found that the trends in variation generally reflected the prevailing space weather conditions at various time scales. In particular, ‘dipping’ of VLF mid-day signal amplitude (MDP) occurs following geomagnetic perturbed or storm conditions in the time scale of 1-2 days. The MDP signals that showed no dipping scenario include some cases of propagation paths-matched and mismatched increase of the signal. While the mismatched increase of the signal may be related to distinct characteristics of each propagation path and X-ray flux-induced spike in amplitude, the matched increase appeared to be influenced by M-class flares concurrent with storm events, and delayed responses of the local ionosphere to storm effects. The mean signal before sunrise (MBSR) and mean signal after sunset (MASS) also exhibit storm-induced dipping, but they appear to be influenced by the individual event’s exact occurrence time, and the highly variable conditions of dusk-to-dawn ionosphere. The magnitude of induced dipping (or rise) appear to significantly depend on the intensity and duration of event(s) as well as the propagation path of the signal. Also, the post-storm day signal (following a main event, with lesser or significantly reduced geomagnetic activity) exhibited a tendency of recovery to pre-storm day level. The trends in variation of the sunrise terminator (SRT) and sunset terminator (SST) mostly favoured post-storm rise in signal amplitude levels but required further investigation because such variations could be propagation path dependent, and detailed modeling is required to understand these phenomena.

ACKNOWLEDGMENTS

On 25 September, 2011 I arrived the shores of India and the S.N. Bose National Centre for Basic Sciences, Kolkata to begin my doctoral research fellowship that was awarded me earlier that year. Subsequently, I resumed my research programme on 26 September under the TWAS-Bose Postgraduate Fellowship. Today, looking back to that historic day, it is fulfilling to say that ‘I am better equipped (intellectually), and richer in knowledge and experience with enhanced research capabilities to contribute to the development of science and technology at local and global levels’. This ‘journey’ was not without hurdles - great were the challenges but by the grace of the Almighty God, and the love and support of some individuals I came out stronger! I want to acknowledge and appreciate the persons, groups and organisations that supported me while this programme lasted. I thank the Third World Academy of Science (TWAS), International Centre for Theoretical Physics (ICTP), Trieste, Italy and my host, S.N. Bose National Centre for Basic Sciences, Kolkata, for the award of the S.N. Bose-TWAS Postgraduate Fellowship. I am indebted to my host supervisor, Prof. Sandip K. Chakrabarti. I thank him for his intellectual drilling through demonstration of profound knowledge and multidisciplinary research approach. Thank you for believing in and allowing me to explore my area of interest and for your unflinching support. It wouldn’t have been better with any other here! I thank the management and staff (academic & non-academic) of S.N.Bose Centre, including the supporting staff (e.g. security, canteen etc.). I thank the Astrophysics & Cosmology department and faculties, especially Dr. S. Mondal, Dr. R. Das and others. I thank my group members between 2011 and 2016, and all other colleagues in the Centre (irrespective of dept.) - it’s been nice working with/among you! I thank Prof. R. Weigel for his helpful suggestions, and my collaborators Dr. S. Sasmal, and colleagues at the Indian Centre for Space Physics. I thank colleagues who assisted me in areas of difficulties with FORTRAN programming such as Dr. T. Basak, Mr. B. Chakraborty, Mr. S. Ghosh, Dr.D. Roy, Dr.A.P. Jena and Mr. P. Tarafdar, who was also there as I adjusted to my work environment. I also thank colleagues who assisted me with some technicalities associated with preparation of this Thesis such as Mr. A. Ghosh, Mr. A. Roy, Mr. S. Bose, Mr. S. Dutta, Mr S.Kundu and Ms R. Rupali. I am grateful to S.N. Bose Centre, COSPAR and IUGG for the financial support to attend COSPAR 2012 (India), COSPAR 2014 (Russia) and IUGG 2015 (Czech Rep.) conferences respectively. I thank my elder brother, Mr. C.C. Nwankwo for being there, and my family (parents, brothers & sisters) for their love, support and prayers, as well as Mrs. F. Okonji (‘Mother of the Pilgrims’) & family, Prof. S. Dada, Prof. I. Jideani, Mr. I.I. Otegwu & family, Pst. R. Rabidas & family, Ms P. Chakraborty & family, Princess Deepa Das & family, and others.

PUBLICATIONS IN REFEREED JOURNALS

1. **Nwankwo V. U. J.**, Chakrabarti S. K. and Ogunmodimu O., 2016. Probing geomagnetic storm-driven magnetosphere-ionosphere dynamics in D-region via propagation characteristics of very low frequency radio signals. *J. Atmos. Solar-Terr. Phys.* 145, 154-169.
2. **Nwankwo, V. U. J.**, Chakrabarti S. K. and Weigel R. S., 2015. Effects of plasma drag on low Earth orbiting satellites due to solar forcing induced perturbations and heating. *Adv. Space. Res.* 56, 47-56.
3. **Nwankwo, V. U. J.** and Chakrabarti K. S., 2015. Analysis of planetary and solar-induced perturbations on trans-Martian trajectory of Mars missions before and after Mars orbit insertion. *Indian J. Phys.* 89, 1235-1245.
4. **Nwankwo, V. U. J.** and Chakrabarti K. S., 2014. Theoretical Modeling of Drag Force Impact on a Model International Space Station (ISS) during Variation of Solar Activity. *Trans. JSASS Aerosp. Technol. Jpn.* 12, 47-53
5. **Nwankwo, V. U. J.** and Chakrabarti S. K. (2016), Diagnostic study of geomagnetic storm-induced ionospheric changes in mid-latitude D-region using VLF signal propagation characteristics. *Ann. Geophys. angeo-2016-84* (submitted).

PUBLICATIONS IN CONFERENCE PROCEEDINGS

1. **Nwankwo V.U.J.** and S. K. Chakrabarti (2015), The analysis of long-term trends of drag effect on model LEO satellites due to upper atmospheric influence by solar/geomagnetic activity. **IUGG-0654**, 26th IUGG General Assembly 2015, Prague, Czech Republic.
2. **Nwankwo V.U.J.** and S. K. Chakrabarti (2014), A Probe of Magnetosphere-Ionosphere Coupling Using Very Low Frequency (VLF) Radio Signal from NWC (Australia) to Kolkata (India). **2014cosp-40E2317N**, 40th COSPAR Assembly 2014, Moscow, Russia.
3. **Nwankwo V.U.J.**, S. K. Chakrabarti and Sasmal S. (2014), Study of Magnetosphere-Ionosphere Coupling as Precursory Indicator of Earthquakes. **2014cosp-40E2320N** 40th COSPAR Assembly 2014, Moscow, Russia.
4. **Nwankwo Victor U. J.**, S. K. Chakrabarti (2014), Effects of Plasma Drag on Low Earth Orbiting Satellite (LEOS) due to Atmospheric Heating by Coronal Mass Ejections and other solar events. **2014cosp-40E2318N**, 40th COSPAR Assembly 2014, Moscow, Russia.
5. **Nwankwo V.U.J.** and Chakrabarti S. K. (2014), Effects of Space Weather Conditions on the Upper Atmosphere and LEO Artificial Satellites. 2014-A002-002, African Geophysical Society Conference, Abuja, 2014.
6. **Nwankwo V. U. J.**, Sudipta Sasmal and Chakrabarti K. S. (2014), A study of magnetosphere-ionosphere coupling as a precursory indicator of Earthquake. IEEE Proceedings of the General Assembly and Scientific Symposium (URSI GASS), 2014 XXXIth URSI, doi:10.1109/URSIGASS.2014.6929814.
7. **Nwankwo V.U.J.** and Chakrabarti S. K. (2012), Computation and Prediction of Plasma Drag on Earth-orbiting Satellites due to Space Environmental Perturbation by Coronal Mass Ejections (CMEs). **2012cosp-39.1384N** 39th COSPAR Assembly 2012, Mysore, India.
8. **Nwankwo V.U.J.**, Chakrabarti S. K. and Sasmal S. (2012), Daily Variation of Very Low Frequency (VLF) Signal Amplitude and Phase from North-West Cape (19.8kHz) to Kolkata. 39th COSPAR Assembly 2012, Mysore, India.

Contents

1	Introduction	1
1.1	Background and motivation of the study	3
1.2	Specific objectives of the study	6
1.3	Scientific contribution of the research reported in this thesis	7
1.4	Outline of the thesis	8
2	Solar activity and the geospace environment	9
2.1	The Sun at a glance	9
2.1.1	Solar atmosphere	9
2.1.2	Source of energy of the Sun	12
2.1.3	Solar activity and the Solar cycle	14
2.2	Solar energetic events	16
2.2.1	Solar wind and its properties	16
2.2.2	Solar flares, CMEs and prominences	21
2.3	Earth's magnetosphere and atmosphere	27
2.3.1	The magnetosphere	27
2.3.2	The Atmospheric profile of the Earth	29
2.3.3	The Ionosphere	32
2.4	Space weather: atmospheric responses to Solar energetic events	34
2.5	Atmospheric drag on LEO Satellites	36
3	Atmospheric Drag on Low Earth Orbit Satellites (LEOS)	37
3.1	Upper atmospheric density profile	40
3.2	Atmospheric drag force affecting LEO satellites	43
3.3	Orbital and ballistic parameters of Model LEO satellites and computation of drag force components	45
3.4	CIR-induced periodic changes on atmospheric density profile and LEO satellites orbit	46
3.5	Results and Discussion	47
3.5.1	Orbital decay at difference phases of the solar cycle	47
3.5.2	Orbital decay during short-term strong geomagnetic disturbances	53

4	Implementation of Drag model on Orbits of some satellites	58
4.1	Modeling orbital decay profile of CHAMP, GOCE and ISS satellites .	59
4.1.1	CHAMP Satellite	59
4.1.2	GOCE Satellite	60
4.1.3	ISS Satellite	63
4.2	Analysis of solar forcing-induced atmospheric drag Effect on Mangalyaan Mars Orbiter (MMO)	68
4.2.1	The mission plan of the Mangalyaan and its trans-Martian flight profile	71
4.2.2	Computational results	73
5	Geomagnetic storm induced magnetosphere-ionosphere dynamics using very low frequency (VLF) radio signal	77
5.1	VLF propagation in the Earth-ionosphere waveguide	78
5.1.1	Sudden Ionospheric Detection (SID) by VLF Radio Signal . .	81
5.1.2	Geomagnetic storms induced variations of the ionosphere and effects	82
5.2	Data and Analysis	83
5.3	Diagnostic study of geomagnetic storm-induced ionospheric changes in mid-latitude D-region	85
5.4	Results and Discussion	86
5.4.1	Analysis of VLF signal amplitude behaviour during geomagnetic storms in mid-latitude D-region	86
5.4.2	Further investigation of storm-induced changes of the ionosphere and VLF signal amplitude	105
5.4.3	Statistical analysis of signal variations during 15 storm cases .	114
6	Summary and Conclusion	121
6.1	Summary and conclusion	121
6.2	Future work	12
A		124

ABBREVIATIONS

CHAMP	Challenging Mini-satellite Payload
CIR	Corotating Interaction Region
CSA	Canadian Space Agency
ESA	European Space Agency
ESOI	Earth's Sphere of Influence
GIC	Geomagnetic Induced Current
GNSS	Global Navigation Satellite System
GOCE	Gravity field and steady state Ocean Circulation Explorer
GOES	Geostationary Operational Environmental Satellite
GPS	Global Positioning System
GRACE	Gravity Recovery and Climate Experiment
HILDCAA	High-intensity, Long-duration Continuous AE Activity
HSS	High Speed Stream
HST	Hubble Space Telescope
IPM	Interplanetary Mission
ISRO	Indian Space Research Organisation
ISS	International Space Station
JAXA	Japan Space Exploration Agency
LAM	Liquid Apogee Motor
LASCO	Large Angle Spectroscopic Coronagraph
LEO	Low Earth Orbit
LEOS	Low Earth Orbiting Satellite
SMC	Small Magnetic Cloud
MASS	Mean Signal Amplitude after Sunset
MBSR	Mean Signal Amplitude before Sunrise
MDP	Midday signal amplitude Peak
MMO	Mangalyaan Mars Orbiter
MOI	Mars Orbit Insertion
MSISE	Mass Spectrometry and Incoherent Scatter Extended
NASA	National Aeronautics and Space Administration
NGS	National Geographic Society
NOAA	National Oceanic and Atmospheric Administration
NRL	Naval Research Laboratory
SID	Sudden Ionospheric Disturbances
SMM	Solar Maximum Mission
SOHO	Solar and Heliospheric Observatory
SRT	Sunrise Terminator
SST	Sunset Terminator
STEREO	Solar Terrestrial Relations Observatory
TPS	The Planetary Society

List of Figures

1.1	The principal features of the solar wind plasma (or energetic events) interaction with the Earth's magnetic field (Adapted from Hunsucker and Hargreaves, 2003).	2
2.1	The sun at different wavelengths. (a) Visible light, (b) blue light (393 nm), (c) Ultraviolet light (30.4 nm), (d) Extreme ultraviolet 17.1 nm, (e) Extreme ultraviolet (19.5) and (f) Extreme ultraviolet (28.4): Courtesy NASA	10
2.2	Internal structure and the atmosphere of the Sun (web.utah.edu/astro/sun.html)	13
2.3	Cross section of the Sun showing energy transfer layers (from Prolss, 2004)	14
2.4	The sunspots showing the umbra and penumbra (Royal Swedish Academy of Sciences)	15
2.5	solar cycle variation of daily sunspot area averaged over individual solar rotation (D. Hathaway, NASA/MSFC)	17
2.6	View of solar wind structure in the ecliptic plane (from Prolss, 2004) . . .	20
2.7	Formation and propagation of corotating interaction region in the solar wind (from Prolss, 2004)	20
2.8	Solar flares (NASA)	22
2.9	Solar flare emission components and their probable locations (from Prolss, 2004)	22
2.10	(a) A CME erupted from the lower right of the Sun on 2 Dec. 2003 (Credits: ESA/NASA/SOHO) (b) a powerful CME occurred on 8 Jan. 2012. The broad front of the particle cloud had already expanded to about 120 degrees when this image was taken. Here the Sun itself has been enlarged about 50% and superimposed on the background image to cover the coronagraph's occulting disk. The occulting disk blocks out the Sun's bright light so that the fainter structures in the corona can be observed (images are from the STEREO spacecraft)	24

2.11	The Earth's magnetosphere. When solar wind encounters and interacts with the Earth's magnetic field, it compresses its sun-ward side to a distance of about $6-10R_E$, creating a supersonic shock wave known as the <i>Bow Shock</i> . Although its exact length is not know, the solar wind drags out the night-side of the inner magnetosphere to probably $1000R_E$, an extension that is known as the <i>Magnetotail</i> . The <i>Magnetopause</i> is the outer boundary of Earth's confined geomagnetic field. (Credit: Aaron Kaase/NASA/Goddard (Adapted))	28
2.12	Height profile of temperature, pressure, and mass density in the Earth's atmosphere (from Prolss, 2004)	30
2.13	The atmospheric composition (from Hunsucker and Hargreaves, 2003)	30
2.14	Vertical profile of the ionosphere (from Hunsucker and Hargreaves, 2003)	34
3.1	Atmospheric drag-induced decay on satellites in (left) circular and (right) elliptical orbit (right panel from Nwankwo and Chakrabarti, 2015)	38
3.2	The number of satellites lost in connection with the March 13-14, 1989 storm (http://ccar.colorado.edu/muri/).	38
3.3	Comparison between sunspot number (smoothed), CME, CIR, and interplanetary shock rates (Lindsay et al., 1994)	48
3.4	Time variations of model satellite's mean altitude, orbit decay rate, thermospheric temperature and density in 2000-2002 for (a) SAT-BCI and (b) SAT-BCII (from Nwankwo et al. 2015)	49
3.5	Time variations of model satellite's mean altitude, orbit decay rate, thermospheric temperature and density in 2004-2006 for (a) SAT-BCI and (b) SAT-BCII (from Nwankwo et al. 2015)	51
3.6	Time variations of model satellite's altitude, orbit decay rate, thermospheric temperature and density in 2012-2014 for (a) SAT-BCI and (b) SAT-BCII (from Nwankwo et al. 2015)	52
3.7	Ap and Dst index variations during 1st-31st July 2000 (from Nwankwo et al. 2015)	54
3.8	Time variations of model satellite's mean altitude, orbit decay rate, thermosphere temperature and density for SAT-BCI and SAT-BCII during 1st-31st July 2000 (from Nwankwo et al. 2015)	55
4.1	Hubble space telescope orbit-boost between 1993 and 2002 (Williams G., NASA).	59

4.2	(a) Artist impression of the Challenging Mini-satellite Payload (CHAMP) satellite (Credit: Astrium GmbH) (b) the Gravity field and steady state Ocean Circulation Explorer (GOCE) satellite (ESA) (c) The International space station (ISS) satellite [NASA] (d) Artist impression of the Mangalyaan Mars Orbiter (MMO) [ISRO]	61
4.3	Model decay profile of CHAMP satellite during 2003-2005 (from Nwankwo et al. 2015)	62
4.4	Model decay profile of (a) GOCE satellite during 2009-2013 (b) re-entry evolution of GOCE satellite during 21st October - 11 November 2013 (Nwankwo et al. 2015)	64
4.5	The time variation of model ISS altitude, orbit decay rate, thermospheric density and temperature during (a) 2000-2002 and (b) 2005-2007 (Nwankwo & Chakrabarti, 2014)	66
4.6	Time variation of model ISS altitude, orbit decay rate, thermospheric density and temperature during 2005 -2007 (Nwankwo & Chakrabarti, 2014)	67
4.7	Relative magnitudes of main sources of perturbation acting on spacecrafts (Adapted from Fortescue et al., 2003)	69
4.8	(a) Planned trans-Martian trajectory of Mangalyaan spacecraft (b) maneuvered orbits (heights) after consecutive velocity boost (from Nwankwo and Chakrabarti, 2015)	70
4.9	(a) Region of the orbit R_1 to R_3 where the drag effects have been considered, while the spacecraft is in Earth and Martian orbits (from Nwankwo and Chakrabarti, 2015)	73
4.10	Maneuvered orbits of Mangalyaan Mars orbiter (Blue line with triangles) with corresponding decay rate (red line with stars). Triangles correspond to number of days the MOM stayed before the orbit boost (from Nwankwo and Chakrabarti, 2015)	74
4.11	Mangalyaan (a) mean altitude, (b) orbit decay rate, (c) thermospheric temperature and (d) density during heliocentric trajectory (from Nwankwo and Chakrabarti, 2015)	75
4.12	Mangalyaan (a) mean periapsis height and (b) decay rate during first 100 days of Martian trajectory (from Nwankwo and Chakrabarti, 2015)	76
5.1	VLF radio signal propagation (and reflection) in the Earth-ionosphere waveguide (Image: Morris Cohen, Stanford University)	80

5.2	Diurnal VLF signal amplitude variations showing marked and analysed signal metrics. (a and c) DHO-A118 propagation path signal; (b and d): GQD-A118 propagation path signal and (e-f) to illustrate pseudo-terminators.	81
5.3	VLF signal propagation paths (PP) used in the study: the three transmitters are DHO, GQD and ICV, and the A118 receiver (adapted from A118 SID station Web page)	84
5.4	(a) Diurnal VLF amplitude for GQD-A118 PP; (b) VLF amplitude for ICV-A118 PP; (c) X-ray flux output; (d) solar wind speed (V_{sw}) and particle density (PD); (d) B_z magnetic field component; (e) H_T magnetic field; (f) Dst and (g) A_p variations during 14-19th February 2011 (from Nwankwo et al. 2016).	87
5.5	Daily Dst standard deviation, 4-hour mean signal amplitude before sunrise (MBSR), mid-day signal peak (MDP), 4-hour mean signal amplitude after sunset (MASS), sunrise terminator (SRT) and sunset terminator (SST) variations for (a) GQD-A118 and (b) ICV-A118 propagation path during 14-19th February 2011 (from Nwankwo et al. 2016).	89
5.6	(a) Diurnal VLF amplitude for GQD-A118 PP; (b) VLF amplitude for ICV-A118 PP; (c) X-ray flux output; (d) solar wind speed (V_{sw}) and particle density (PD); (d) B_z magnetic field component; (e) H_T magnetic field; (f) Dst and (g) A_p variations during 26th-31st May 2011 (Blue and red lines in the Figure indicate storm commencement and peak time respectively) (from Nwankwo et al. 2016)	91
5.7	Daily Dst standard deviation, two-hour mean signal amplitude before sunrise (MBSR), mid-day signal peak (MDP), two-hour mean signal amplitude after sunset (MASS), sunrise terminator (SRT) and sunset terminator (SST) variations for (a) GQD-A118 and (b) ICV-A118 propagation path during 26th-31st May 2011 (from Nwankwo et al. 2016).	92
5.8	(a) Diurnal VLF amplitude for GQD-A118 PP (b) Diurnal VLF amplitude for DHO-A118 PP (c) X-ray flux output (d) solar wind speed (V_{sw}) and particle density (PD) (d) B_z magnetic field component (e) H_T magnetic field (f) Dst and (g) A_p variations during 24th-29th September 2011 (Blue and red lines in the Figure indicate storm commencement and peak time respectively) (from Nwankwo et al. 2016).	94

5.9	Daily Dst standard deviation, 4-hour mean signal amplitude before sunrise (MBSR), mid-day signal peak (MDP), 4-hour mean signal amplitude after sunset (MASS), sunrise terminator (SRT) and sunset terminator (SST) variations for (a) GQD-A118 and (b) DHO-A118 propagation path during 24th-29th September 2011 (from Nwankwo et al. 2016).	96
5.10	(a) Diurnal VLF amplitude for GQD-A118 PP (b) Diurnal VLF amplitude for DHO-A118 PP (c) X-ray flux output (d) solar wind speed (d) B_z magnetic field component (e) H_T magnetic field (f) Dst and (g) A_p variations during 23rd-28th October 2011 (from Nwankwo et al. 2016).	97
5.11	Daily Dst standard deviation, 4-hour mean signal amplitude before sunrise (MBSR), mid-day signal peak (MDP), 4-hour mean signal amplitude after sunset (MASS), sunrise terminator (SRT) and sunset terminator (SST) variations for (a) GQD-A118 and (b) DHO-A118 propagation path during 23rd-28th October 2011 (from Nwankwo et al. 2016).	99
5.12	Deviation of Daily Dst Index and trend in variation of MDP, MBSR, MASS, SRT and SST signals one day before and after each of the 16 selected storm conditions for (a) GQD-A118 and (b) DHO-A118 propagation paths. A '0' indicate absence of data (from Nwankwo et al. 2016).	102
5.13	Daily Dst deviation (fluctuation) and trend in variation of 2-day mean MDP, MBSR, MASS, SRT and SST before, during and after an event for (a) GQD-A118 and (b) DHO-A118 propagation paths. A '0' indicate absence of data (from Nwankwo et al. 2016)	104
5.14	Illustration of propagation path-matched and mismatched increase of the midday day peak signal (MDP) for GQD-A118 and DHO-A118 propagation paths (from Nwankwo & Chakrabarti. 2016).	107
5.15	(a) Diurnal VLF amplitude for DHO-A118 and (b) GQD-A118 propagation paths (c) daily variation in X-ray flux output (d) solar wind speed (V_{sw}) (e) solar particle density (PD) (f) Disturbance storm time (Dst) (g) planetary A_p and (h) Auroral Electrojet (AE) indices during 16-30 September 2011 (from Nwankwo & Chakrabarti. 2016).	109
5.16	Daily Dst standard deviation, 4-hour mean signal amplitude before sunrise (MBSR), mid-day signal peak (MDP), 4-hour mean signal amplitude after sunset (MASS), sunrise terminator (SRT) and sunset terminator (SST) variations for (a) GQD-A118 and (b) DHO-A118 propagation path during 23rd-28th October 2011 (from Nwankwo & Chakrabarti. 2016).	110

5.17	(a) Diurnal VLF amplitude for DHO-A118 and (b) GQD-A118 propagation paths (c) daily variation in X-ray flux output (d) solar wind speed (V_{sw}) (e) solar particle density (PD) (f) Disturbance storm time (Dst) (g) planetary A_p and (h) Auroral Electrojet (AE) indices during 22 October to 5 November 2011 (from Nwankwo & Chakrabarti. 2016).	112
5.18	Daily deviations of Dst and AE , variations in the peak value of midday signal amplitude (MDP), 4-hour mean signal amplitude before local sunrise (MBSR), 4-hour mean signal amplitude after sunset (MASS), variation in sunrise terminator (SRT) and sunset terminator (SST) for (a) DHO-A118 and (b) GQD-A118 propagation paths during 22 October - 5 November 2011 (from Nwankwo & Chakrabarti. 2016).	113
5.19	Dst deviation (fluctuation), and variations in MDP, MBSR, MASS, SRT and SST signals 1-day before, during and after each of the 15 events for (a) DHO-A118 and (b) GQD-A118 propagation paths (from Nwankwo & Chakrabarti. 2016).	115
5.20	Diurnal VLF amplitude for (a) DHO-A118 and (b) GQD-A118 propagation paths, daily variation in (c) X-ray flux output (d) V_{sw} , (e) PD and (f) Dst indices for a day before and after each of the 15 storms (from Nwankwo & Chakrabarti. 2016).	117
5.21	Dst deviation and 2-day mean variations of MDP, MBSR, MASS, SRT and SST signals before, during and after each event for (a) GQD-A118 and (b) DHO-A118 propagation paths (from Nwankwo & Chakrabarti. 2016). . .	118

List of Tables

3.1	Orbital and ballistic parameters used in this study	46
3.2	Trends in time variation of mean altitude, orbit decay rate, thermosphere temperature and density for SAT-BCI and SAT-BCII at different phases of the solar cycle (from Nwankwo et al. 2015)	53
3.3	Trends in time variation of mean altitude, orbit decay rate, thermosphere temperature and density for SAT-BCI and SAT-BCII (initially at $h=450$ km) during interval of strong geomagnetic perturbations and/or storms in July 2000 (from Nwankwo et al. 2015)	56
4.1	The orbital parameters of CHAMP, GOCE, ISS and MMO satellites: values are assumed where they are not explicitly provided.	60
5.1	Trend of time variation of VLF amplitude, Dst and flare count during 15-18th February 2011 for GQD-A118 and ICV-A118 propagation path (from Nwankwo et al. 2016).	88
5.2	Trend of time variation of VLF amplitude, Dst standard deviation and flare count during 26-31st May 2011 for GQD-A118 and ICV-A118 propagation path (from Nwankwo et al. 2016).	93
5.3	Trend of time variation of VLF amplitude, Dst and flare count during 25th-28th September 2011 for GQD-A118 and DHO-A118 propagation path (from Nwankwo et al. 2016).	95
5.4	Trend of time variation of VLF amplitude, Dst and flare count during 23rd-28th October 2011 for GQD-A118 and DHO-A118 propagation path (from Nwankwo et al. 2016).	98
5.5	Summary of analysed geomagnetic storm conditions (from Nwankwo et al. 2016).	101
5.6	Summary of analysed 15 geomagnetic storm events (from Nwankwo & Chakrabarti. 2016).	106

5.7	Summary of trend in dipping of the signals' metrics during 15 geomagnetic storm case in (a) DHO-A118 and GQD-A118 propagation path (from Nwankwo & Chakrabarti. 2016).	114
5.8	Summary of trend in 2-day mean signals dipping following 15 geomagnetic storm case in (a) DHO-A118 and GQD-A118 propagation path (from Nwankwo & Chakrabarti 2016).	119

Chapter 1

Introduction

The body of knowledge resulting from several decades of research in space and planetary sciences have unequivocally confirmed that the sun is not only the main source of energy but also the dominant driver of magnetosphere-thermosphere-ionosphere dynamic processes in the geo-space environment. With core and surface temperature of about 1.56×10^7 and 5800 K respectively, the sun releases enormous amount of internally generated energy into the interplanetary space through energetic phenomena such as solar wind streams, solar flares, prominence eruption, coronal mass ejections (CMEs), etc. Like every other planets in the solar system, the Earth is a target of the emissions from solar energetic events, mainly energised particles (plasma) and electromagnetic (EM) radiations. When accelerated in the heliosphere (usually with supersonic speed), the complex interaction between solar emissions and the Earth's magnetosphere produces disturbances in the near-Earth space environment that often result to a number of interrelated phenomena, including geomagnetic storms and magnetospheric substorms, solar particle events, shock waves and corotating interactive region (CIR) in solar wind, and interplanetary magnetic field (IMF) variation (Lastovicka, 1989, 1995; Zurbuchen and Richardson, 2005; Gopalswamy, 2009). The principal features resulting from the interaction of Earth's magnetic field with the solar wind plasma is depicted in Figure 1. The sun also exhibits periodicity in its activity (e.g., 11-year activity cycle that includes a minimum and a maximum phase, and 27-day rotation period), which also influences the evolution, frequency, intensity and impact of solar energetic events and associated phenomena. The resultant dynamic, variable conditions in the near-Earth and space environment due to both periodic and aperiodic solar phenomena is referred to as space weather. Space weather condition can affect the performance and reliability of space- and ground-based technology (usually interdependent) including effects of accelerated orbital decay for low Earth orbit (LEO) satellites due to increase in atmospheric drag, degradation of satellite sensor and solar array, and precision of Global Positioning System (GPS) measurement, single event effects (SEEs) in satellites'

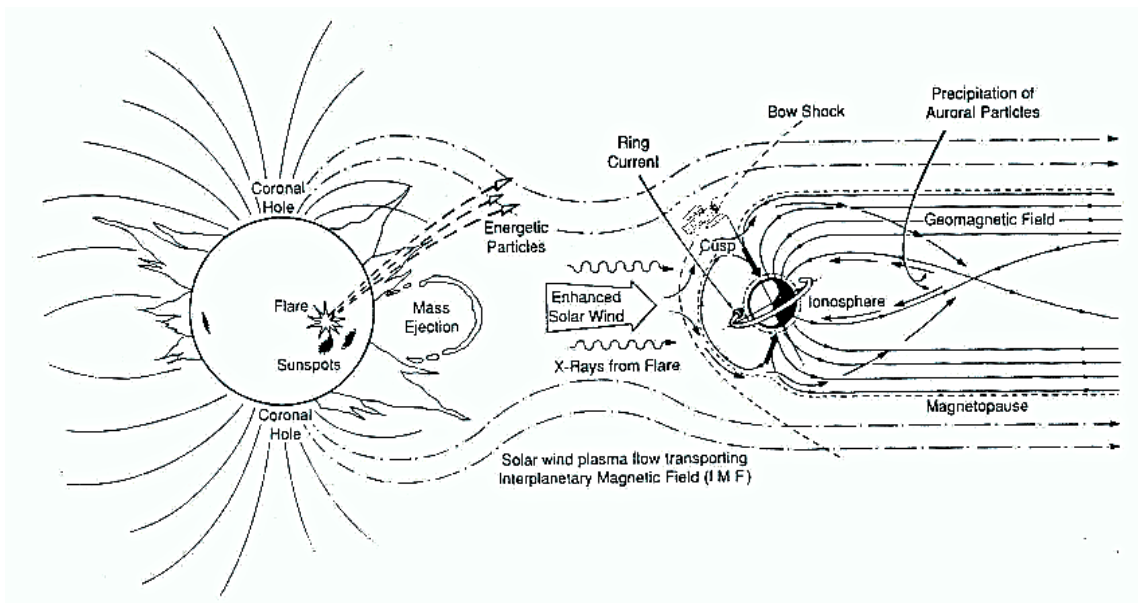


Figure 1.1: The principal features of the solar wind plasma (or energetic events) interaction with the Earth's magnetic field (Adapted from Hunsucker and Hargreaves, 2003).

electronic components, spacecraft charging, radiation threat to crew and astronauts of high-flying aircraft, and geomagnetic induced current (GIC) that can damage electric power grids and cause accelerated corrosion of oil and gas pipelines (Baker, 2000; Gopalswamy, 2009; Nwankwo, 2010; Jibiri et al., 2011). Even services that rely on these technology (e.g., communication, navigation, meteorology, defense, etc.) can be severely affected. Therefore, studies that enhance our understanding of sun-magnetosphere-ionosphere system are critical and of practical importance because space application systems are designed to operate in the ionospheric plasma environment, even as societal, economical and technological dependence on satellites (and space technology) is increasing with unmatched precedence.

The magnetosphere-ionosphere system plays a key role in conveying solar-induced geoeffective phenomena. Despite their large distances apart, solar and magnetospheric disturbances are usually conveyed to the ionosphere arena via the magnetic field of the Earth, making the regions (magnetosphere and ionosphere) physically coupled into one global system. The magnetosphere is the cavity formed by Earth's magnetic field when the solar wind interact with and is deflected by the magnetic field. The ionosphere is the ionised component of Earth's atmosphere (60-800 km), mainly created by solar extreme ultraviolet (EUV) and X-ray, and impact of charged particles. There is a coupling effect in the magnetosphere-ionosphere system (driven

by solar forcing mechanisms), which also modifies ionospheric parameters such as atmospheric density distribution, total electron content (TEC), ionospheric current system, ionisation rates, and conductivity gradient and reference height of the D-region (Wait, 1959; Wait and Spies, 1964; Mitra, 1974; Buonsanto, 1999; Burke, 2000; Simoes et al., 2012). Other sources of ionospheric variability include planetary, thermosphere and troposphere tides, and stratospheric warming (Pancheva et al., 2008; Forbes et al., 2009; Obeheide et al., 2009; Zhang et al., 2010a; Hagan and Forbes, 2002; Leonard et al., 2012; Goncharenko et al., 2012; Chen et al., 2013; Polyakov et al., 2014). This thesis focuses on the effects of solar forcing (space weather) on two specific space regions viz. the upper ionosphere (thermosphere) and the lower ionosphere (mainly the D region), and LEO satellites' nominal aerodynamic drag.

1.1 Background and motivation of the study

In low Earth orbit (also corresponding to the upper ionosphere), atmospheric drag is the strongest force perturbing the orbit and motion of satellites. Nominal atmospheric drag on LEO satellite is usually enhanced by solar forcing induced variation in thermospheric temperature and density profile. Accelerated drag scenario can cause difficulty in identification, tracking, maneuvering of satellites, and premature re-entry. It can also induce uncertainties in predicting re-entry of satellites and other natural space debris (Klinkrad, 1999; Mark et al., 2005; Doornbos and Klinkrad, 2006; Xu et al., 2011; Walterscheid, 1989). Solar forcing induced variations of the atmospheric density and the consequent satellites' orbital decay have been studied by several authors (e.g., Walterscheid, 1989; Klinkrad, 1999; Doornbos and Klinkrad, 2006; Kim et al., 2006; Pardini et al., 2009; Hausleitner et al., 2007; Xu et al., 2011; Chen et al., 2012; Leonard et al., 2012; Lei et al., 2013). Walterscheid (1989) studied the effects of solar cycle on the upper atmosphere and its implications on satellite drag, and estimated the lifetime of satellites in LEO (at 500 km) to be about 30 years under solar cycle minimum conditions and only 3 years under the solar maximum conditions. Chen et al. (2012) studied the effects of CIR- and CME-induced geomagnetic storm condition on thermospheric densities and spacecraft orbits. They reported that CME-induced storms can cause large thermosphere density variations and consequent orbital decay rates than CIR-induced storms during its main phase. However, the mean thermospheric density changes and orbital decay during the entire period of CIR storms could be comparable or larger than those of CME-induced storms in each case (Chen et al., 2012). This is because perturbations from CIR-induced storms persist longer (up to a week or more) than those induced by CMEs (about 1 day) (Tsurutani et al., 2011; Verkhoglyadova et al., 2013). Sim-

ilarly, Lei et al. (2013) investigated the impacts of solar forcing on thermospheric densities and spacecraft orbits from CHAMP and GRACE satellites' data for CME- and CIR-induced geomagnetic storms during September 15-27 and November 19-22 2003. Their findings were consistent with those of Chen et al. (2012). Although quite insightful, these studies (e.g., Chen et al., 2012; Lei et al., 2013) mainly relied on satellite drag data i.e., in-situ mass spectrometer, accelerometer and temperature measurement aboard particular satellites (e.g., CHAMP and GRACE), and focused on short-term drag effect during particular storm events. Studies relating to long-term impact of space weather condition on LEO satellites have, therefore, not been fully explored. Whereas Walterscheid (1989) provided a fair estimate of the lifetime of satellites in LEO with respect to the solar cycle, the calculations were based on approximated phase (maximum and minimum) values of solar and geomagnetic index (e.g., solar radio flux ($F_{10.7}$) and planetary A (A_p) index). In today's space era with efficient satellite-based data (achieved for several decades) and well-developed atmospheric models with increasing sophistication, modeling (and/or studying) the long-term evolution of space weather-induced effect on low Earth orbiting satellites (LEOSs), based on day-to-day solar and geomagnetic data will be instructive and resourceful. Such models or simulations could supplement existing scientific theory and experimentation, and provide resources for forecast, situational awareness and impact mitigation. Also, accurate prediction of satellite's lifetime and re-entry is vital for satellite operation in near-Earth space environment (Kwak et al., 2011; Chen et al., 2012) and largely depend on a good knowledge of atmospheric density profile. Many atmospheric models have been developed (and more are being developed) over the years with good approximation (e.g., Jacchia-71, CIRA-72, DTM-77, Jacchia-77, MSIS-77, GOST-84, MSIS-83, CIRA-86, MSIS-86, TD-88, MSISe-90, DTM-94, DTM-2000, NRLMSISE-00, JB2006, JB2008). While the improvements in atmospheric density model have been unprecedented, concerns about the accuracy of the models remain, due to the difficulties associated with modeling the individual effects of various solar forcing mechanisms, which causes fluctuations in neutral and ionized density. Therefore, efforts towards further improvement have continued. Against these backdrops, the first part of this thesis is well motivated. It focuses on developing new drag model that incorporate a widely used empirical model of the atmosphere to simulate and quantitatively estimate LEOSs decay rate at different phases of the solar cycle as a function of day-to-day solar and geomagnetic parameters. The work also include implicit modification to the atmosphere density model used in this work, to better include the effect of an under-represented solar forcing mechanism (the CIR) for improved drag calculation/estimation.

The lower ionosphere also responds to prompt changes in solar energetic events, due to solar flare associated bursts in EUV, X-ray and relativistic particles (Mitra,

1974; Bounsanto, 1999; Alfonsi et al., 2008), delayed changes, related to geomagnetic storm conditions with time scale from several hours to 1-3 days (Lastovicka, 1996; Bounsanto, 1999; Kutiev, 2013), as well as periodic changes with time scales of several days to months, and those of several solar cycles (Alfonsi, 2008; Kutiev, 2013). The ionosphere also exhibits diurnal and seasonal (e.g. summer/winter) variations (Miller and Brace, 1969; Zhang et al., 1999). Solar-induced ionospheric phenomena in the upper atmosphere are well studied with the help of satellites in orbit, but probing related phenomena in the lower ionosphere is quite challenging, because the region is not wholly accessible to satellites. Many studies explored one or combination of observational and experimental tools or techniques to investigate the coupling effects of the magnetosphere and ionosphere in lower ionosphere, including ground-based Global Navigation Satellite system (GNSS) receivers, vertical and oblique sounding, Riometers, incoherent scatter radars (e.g., EISCAT), coherent scatter radars (e.g., Goose Bay radar, SuperDARN), very low frequency (VLF) radio waves, ground-based magnetometers, etc. (e.g., Greenwald et al., 1995, 1996; Honary et al., 1995; Lastovicka, 1996; Wild et al., 2003; Danilov and Lastovicka, 2001; Goldstein et al., 2005; Ruohoniemi and Greenwald, 2005). The VLF radio waves (in the 3-30 kHz) is proving to be useful and efficient in studying space weather induced changes in lower ionosphere (e.g. Araki, 1974; Kikuchi and Evans, 1983; Kleimenov et al., 2004; Peter et al., 2006; Clilverd et al., 2010; Kumar and Kumar, 2014), as well as changes from other atmospheric and lithospheric sources (e.g., Hayakawa et al., 1996; Molchanov et al., 1998; Clilverd and Rodger., 1999; Soloviev et al., 2004; Chakrabarti et al., 2005, 2010). The signal is sensitive to changes in the electrical conductivity of the lower ionosphere (Prolss, 2004; Alfonsi et al., 2008). This characteristic makes it an ideal tool for probing solar-induced variable conditions in the ionosphere, especially the D region. Hence, it has been widely used by many researchers to study changes in the atmosphere. Many of the studies are related to flare/X-ray flux induced changes in the ionosphere. There is a characteristic increase in diurnal VLF signal amplitude, as well as phase enhancement during solar events such as solar flares and gamma ray bursts (GRBs). The signal can also be significantly affected by geomagnetic disturbances and storms induced ionosphere perturbations (Kikuchi and Evans, 1983). While the response of the signal's amplitude and phase (especially during daytime) are well correlated with X-ray flux induced sudden ionospheric disturbances (and well studied), geomagnetic storm-induced disturbances are often not immediately detectable on the signal's signature.

Besides, the response of VLF signal to geomagnetically induced ionospheric disturbances significantly depend on the propagation characteristics of signal propagation path, and the signal mode interference significantly depends on ionospheric

conditions at the time, propagation paths and energetic electron precipitation level on the ionosphere due to the magnetic storm, which also depends on geomagnetic latitude. Kikuchi and Evans (1983) reported the occurrence of VLF phase anomaly associated with sub-storm of 13 November 1979 in trans-auroral propagation path. Peter et al. (2006) also reported significant depression of VLF signal amplitude magnitude in mid-latitude during storms of 7 April 2000 and 31 October 2003 that was later observed in lower latitudes. However, the statistical significance of the observed effect and/or responses need to be verified because the studies considered few particular storms, mostly of super-storm category ($Dst > -250$). Inclusion of several storm cases with varying degree of disturbance index over an extended period of time is vital to understanding geomagnetic footprint in the D-region. Also, the signatures of VLF dawn, daytime and dusk signal have distinct characteristic, and controlled by the local ionospheric conditions (mainly the solar related) at the time. An analysis that maximises the characteristics of the signal regiments could be elucidating, but have not been fully explored in previous studies. Therefore, in the second part of this thesis, we perform a diagnostic study of geomagnetic disturbances or storm-induced ionospheric changes in mid-latitude D region using the VLF signal characteristics. In a new and more efficient approach we characterise the diurnal signature of the signal's amplitude into a reasonable metrics, and analyse the trends in variation of the signal metrics during geomagnetic storm conditions (including pre-storm and post-storm conditions) to understand signal behaviour that are attributable to geomagnetic storms-induced variations in the region of the ionosphere.

1.2 Specific objectives of the study

In particular, we study (1) solar forcing induced variations of thermospheric temperature and density (at an altitude of 400-450 km) and the consequential accelerated orbital decay (due to increase in atmospheric drag) on satellites in the region and (2) perform a diagnostic study of geomagnetic storm-induced ionospheric changes in mid-latitude D-region (60-90 km) using VLF radio signal. The specific objectives of the study are:

1. To understand solar forcing induced variability of thermospheric density and temperature profile and their implications on LEO satellites' normal aerodynamic drag for quantitative estimation (by simulations) of atmospheric drag-induced satellites' orbital decay at different phases of the solar cycle and during interval of strong geomagnetic perturbations using appropriate atmospheric density and drag models.

2. To understand VLF signal propagation characteristics or behaviour that are related to geomagnetic storms-driven magnetosphere-ionosphere dynamics in mid-latitude D-region ionosphere (besides the well known X-ray flux induced amplitude increase and phase enhancement of the signal) for efficient probing of solar-induced changes in lower ionosphere.

1.3 Scientific contribution of the research reported in this thesis

1. We developed a new drag model that incorporated NRLMSISE-00 empirical atmosphere model, as a function of appropriate solar parameters, to simulate the orbital decay profile of two hypothetical LEO satellites (due to atmospheric drag) at different phases of the solar cycle and during interval of strong geomagnetic disturbances or storm conditions.
2. We identified a solar forcing mechanism (the corotating interactive region, hereafter CIR), whose effects are usually under-represented in atmospheric or drag model, and include an implicit modification that fairly accounted for CIR-induced effect on thermospheric density and drag in the utilised models.
3. We implemented our new drag model on real satellites orbit, such as the Challenging Mini-satellite Payload (CHAMP), the Gravity field and steady state Ocean Circulation Explorer (GOCE), the International Space Station (ISS) and an interplanetary space mission, the Mangalyaan Mars Orbiter (MMO). We then compare the outcomes with the utilised methods.
4. In a new and more efficient approach, we characterised the amplitude of the diurnal signature of VLF radio signal into certain metrics, namely, mid-day amplitude peak (MDP), mean signal amplitude before sunrise (MBSR), mean amplitude after sunset (MASS), sunrise termination (SRT) and sunset terminator (SST), and perform a diagnostic study of solar-induced ionospheric changes in the lower ionosphere. The parameterised metrics enabled more accomplished and profound analysis of the signal's response to geomagnetic induced variations on the D-region ionosphere, thereby enhancing our understanding of how aspects of the diurnal signal responds to such changes.

1.4 Outline of the thesis

The thesis consists of six Chapters and presented as follows: First we introduced the subject in the present Chapter. Then we discuss types of Solar activity and the geospace environment based on existing literature. We then present the first part of the work on effects of Space weather-induced increase in atmospheric drag on low Earth orbiting satellites, and summarise the drag model implementation on real satellites orbits. We present the second part of our work on the study of geomagnetic storm induced changes on the D-region ionosphere in mid-latitude using the VLF radio signal. We then we summarize our findings.

In Chapter one, the background, specific objectives, motivation and scientific contribution of the thesis are presented in detail. In Chapter two, relevant literature in the area of study are reviewed in detail including the Sun, solar atmospheres, energy source of the Sun, solar activity and activity cycle, solar energetic events such as the solar wind, solar flares, coronal mass ejections (CMEs), prominence eruptions, Earth's magnetosphere and atmosphere, the ionosphere, and the atmospheric responses to solar energetic events leading to space weather condition.

Chapters three and four describe the work done in the first part of the thesis. In Chapter three we present the work on space weather induced increase in atmospheric drag on LEO satellites including the description of the upper atmospheric density model used in this work, and the analysis of atmospheric drag force, model of CIR-induced effects on atmospheric drag and satellites orbit. The presented results in the Chapter include satellites orbital decay profile at different phases of the solar cycle and during interval of strong geomagnetic disturbances or storms. In Chapter four, we present the results of the implemented drag model on real satellite orbit such as CHAMP, GOCE, the ISS and MMO.

In Chapter five, we present the second part of the thesis on probing geomagnetic storm induced dynamic changes of the ionosphere via magnetosphere-ionosphere coupling. Here, detailed description of the following are presented: the propagation characteristic of VLF radio signal in Earth-ionosphere waveguide, VLF signal detection mechanism of sudden ionospheric disturbances, and the results relating analysis of trends in variation of signal amplitude under varying degree of geomagnetic disturbances and storm conditions, and statistical analysis of the signal during for extended period of time with several storm cases.

Finally, in Chapter six, we present the summary and conclusion of the work.

Chapter 2

Solar activity and the geospace environment

2.1 The Sun at a glance

The Sun is a typical main-sequence star of spectral class $G2$ with mass M_{\odot} of 1.989×10^{30} kg ($3.33 \times 10^5 M_E$), mean density of 1427 kg/cm³ ($0.255\rho_E$), and equatorial radius and circumference of 6.957×10^5 and 4.379×10^6 km, respectively ($109.2M_E$). The sun radiates energy at a constant rate of 3.90×10^{26} J/s. This distinct and steady energy (mainly emitted in form of visible and infra-red radiation) from the sun's photosphere, when integrated over certain wavelength band, gives the solar luminosity (L_{\odot}) in that band. Figure 2.1 shows the image of the sun taken at different wavelengths. The sun exhibits a differential rotation. Different parts of the sun rotate at different angular speeds e.g., points on the solar equator have a sidereal period of about 25 days and points further north or south at latitude of 30° to 60° have periods of around 26-30 days. The period is more than 35-36 days at the poles (also see, Green and Jones, 2004). The sun is mainly composed of hydrogen (about 74%), helium (25%) and various metals that make up less than 0.1% of its mass. Nuclear fusion is the main process by which the sun generate energy in its core. This generated energy flows out of the core to solar surface by processes of radiation, conduction and convection while passing through the respective layers - photosphere, chromosphere and corona.

2.1.1 Solar atmosphere

Although the solar surface appears to have abrupt and clear edge when visually observed, an actual surface does not exist. The sun's observable surface is a thin, semi-transparent shell of hot gaseous ball; optically thin region from which originating photons travel freely through space (Carroll and Ostlie, 1996; Green and Jones, 2004). Solar atmosphere (that makes up the photographic image) emanates

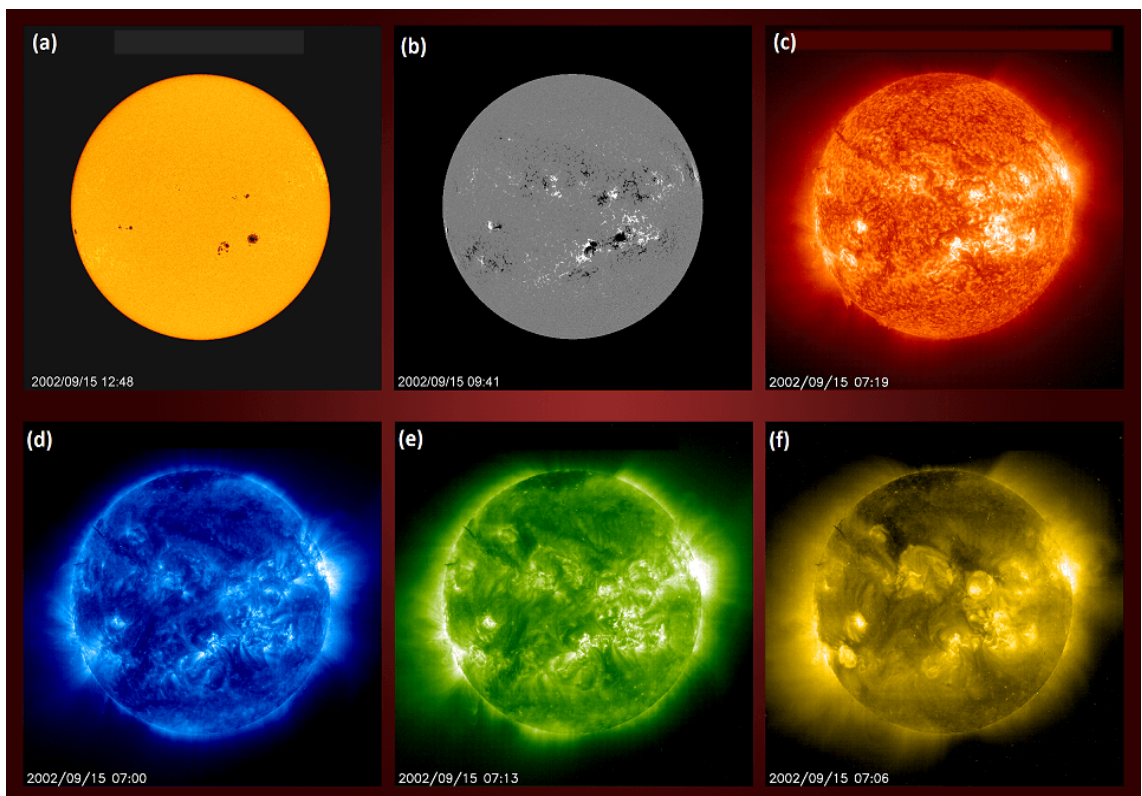


Figure 2.1: The sun at different wavelengths. (a) Visible light, (b) blue light (393 nm), (c) Ultraviolet light (30.4 nm), (d) Extreme ultraviolet 17.1 nm, (e) Extreme ultraviolet (19.5) and (f) Extreme ultraviolet (28.4): Courtesy NASA

from a range of depths - the photosphere (about 500 km thick), chromosphere (2000 km thick) and corona, which extends several solar radii out into space. The internal structures of the Sun and its atmosphere is shown in Figure 2.2. The solar atmosphere is directly observable using space probes and/or telescopes, but information on the solar interior is largely theoretical and based on solar models, because telescopic probing of the sun is limited to its atmospheres, and satellites cannot withstand the extreme temperature of the sun's inner parts. The photosphere, chromosphere and corona are briefly described below.

The Photosphere

The photosphere is the innermost layer of the solar atmosphere. This layer is about 500 km deep, and its temperature varies between 4500 K and 6500 K. However, its mean temperature is ~ 5800 K. The study of the magnified view of localised photospheric regions showed an arrangement of bright cell-like granules covering the photosphere that is now understood or referred to as solar granulation. Each granule is about 1000 km across and last for about 5-10 minutes. The granules are known to be the top of rising columns of hot materials (traveling upwards at about 1 km/s), and radiating its thermal energy away. The hot materials are subsequently cooled in the dark portion between granules and sinks down into the solar interior. Radiation is the dominant mechanism for energy transport in the photosphere.

The Chromosphere

The chromosphere is the portion of the solar atmosphere that lies immediately above the photosphere, extending upward for nearly 2000 km. The chromosphere was initially identified by studying eclipse, which has continued to play a key role in its scientific probe (Green and Jones, 2004). Investigation have shown that gas density in this region drops by a factor of about 10^4 and that temperature increases with increasing altitude, from about 4400 K to about 25,000 K. Restricted observations (using filters) of the wavelengths of emission lines produced in the chromosphere (the hydrogen Balmer lines (H_α) in particular) makes it possible to see quite interesting and appreciable structure in this region of solar atmosphere, including supergranulation that becomes clearly seen on scales of 30,000 km, and showing the progressive effects of the masked convection zone. Studies (Doppler) have shown presence of convective velocities on the order of 0.4 km/s, with gases rising at the centres of the supergranules and sinking at their edges. The presence of vertical filaments (the spicules) have also been observed, which extends upwards from the chromosphere for about 10,000 km. Up to 30,000 spicules have been estimated to exist at any given

moment (with each granule having a lifetime of about 15 minutes). Mass motions are present in spicules, with materials moving outward at about 20 km/s (Carroll and Ostlie, 1996). Temperature rises rapidly above the chromosphere, exceeding 10^6 K before the temperature gradient becomes evenly distributed.

The Corona

The corona is the Sun's outer atmosphere, which extends out into the space for several solar radii. This region is transparent to most electromagnetic radiation because of its very low density. The photographs taken during eclipses and/or from measurements using a coronagraph are used in gauging coronal extent. Such photographs show that the structures of the corona changes with time and solar activity (e.g., sunspot number); the corona is more active with streamers spreading in all directions (looking almost circular) during high solar activity, but less active and elongated at the Sun's equator during solar minimum activity. The spectrum of the corona shows spectral lines (from ions) that indicates plasma temperatures of $2-3 \times 10^6$ degrees that emits X-rays which can also be observed from rockets and satellites. Another important feature observable in X-ray images of the corona is a *coronal hole*. Coronal holes occur mainly in regions of 'open' magnetic field lines - they are regions where the solar magnetic field opens outwards to interplanetary space. Here, solar corona is darker, cooler, and has lower-density plasma than average because of lower energy and gas levels. The dark areas around the Sun in Fig. 2.1f are examples of coronal holes. The size and shape of the hole changes with time (and seems to fragment) and then merged together again. Coronal holes are thought to be the main source of the solar wind (especially the high speed solar wind). For further readings, see, Carroll and Ostlie (1996, 2007), Green and Jones (2004), Prolss, 2004, Meyer-Vernet (2007).

2.1.2 Source of energy of the Sun

The Sun generates energy in its core (a hot dense plasma) through nuclear fusion. In this process, nuclei of relatively low mass (mainly hydrogen) are fused together to form nuclei of relatively greater mass (mainly helium). Consequently, this energy flows from the photosphere by radiation through the radiative layer, by convection (in the chromosphere) through the convective layer, and then by radiation (in the corona) (see, Figs. 2.2 and 2.3). The energy-release process in the Sun is quite complicated. We describe the more dominant one, i.e., the ppI (proton-proton) chain process, assumed to be the Sun's predominant radiant energy source. The nuclei involved in the chain (ppI) are the hydrogen nuclides ^1_1H and ^2_1H (deuterium) and

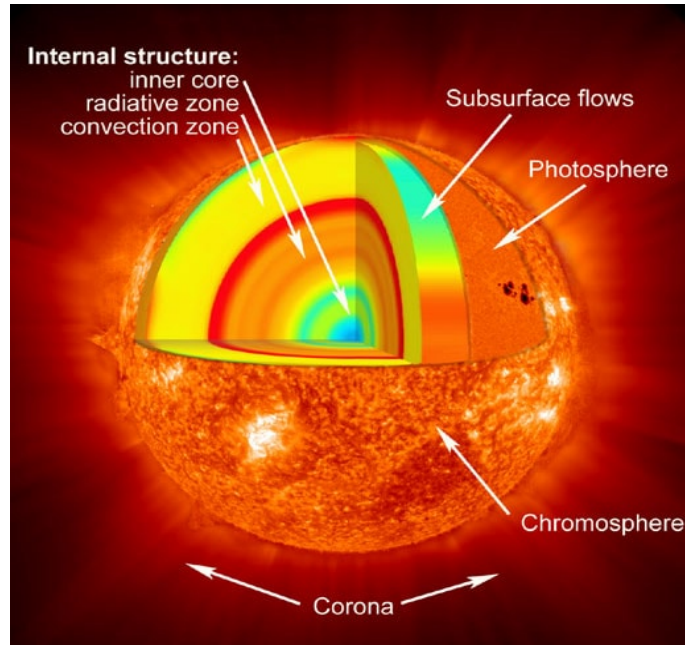


Figure 2.2: Internal structure and the atmosphere of the Sun (web.utah.edu/astro/sun.html)

the helium nuclides ${}^3_2\text{H}$ and ${}^4_2\text{H}$. Other components that involved include γ -rays, Positrons (e^+) and Neutrinos (ν). The steps involved in the ppI chain processes are shown in the equations to follow. In the process, four protons are consumed and a helium nucleus (with 2 protons and 2 neutrons) is produced along with two positrons, two neutrinos and two γ -rays. The overall effect of the chain is as follows (Prolss, 2004):



The first two reactions occur twice and create the input products for the third reaction. Each ppI chain reaction is associated with annihilation of two positrons,

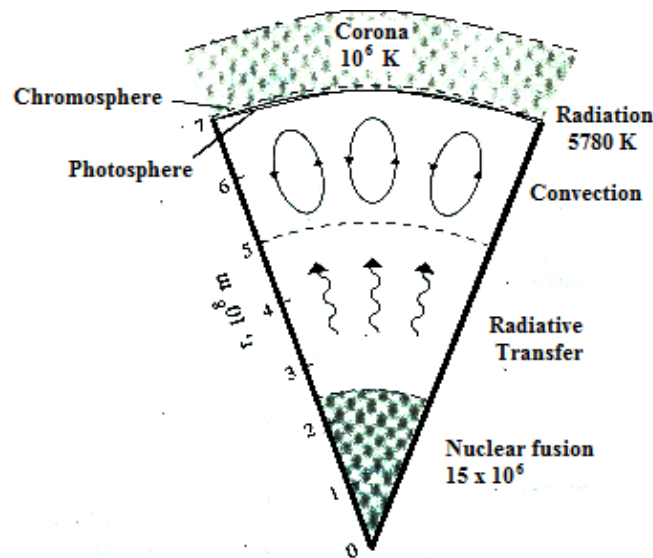


Figure 2.3: Cross section of the Sun showing energy transfer layers (from Prolss, 2004)

and the release of more γ -rays, that are subsequently the source of most of the Sun's electromagnetic radiation. Energy in the form of kinetic energy (of the nuclei or particles that are formed) is also released in the process. The kinetic energy of a particle is redistributed to other particle in random movement in the plasma, and ultimately the energy is converted into the thermal energy of the plasma.

2.1.3 Solar activity and the Solar cycle

Solar activity describes all forms of output from the sun including light, solar wind, and energetic events and particles, which vary with time and position on the Sun. The sunspot, a transient phenomenon seen as dark patches against photospheric bright background on the Sun, is viewed as the main indicator of solar activity. Individual sunspots are large, relatively cool regions of the photosphere with temperature of 3700-4500 K (against the surrounding photospheric temperature of about 6000 K), having lifetime of few weeks (usually not more than a month). A typical sunspot is shown in Fig. 2.4. The darkest portion of the sunspot is called the umbra, surrounded by the penumbra, a filament-like structure. Sunspots are associated with intense magnetic fields. Magnetic field strengths of several thousand gauss have been measured in the centre of umbral region, with field strength decreasing across penumbra region (Carroll and Ostlie, 1996). The strength and polarity of magnetic fields can be measured by observing the Zeeman effect. Hence,

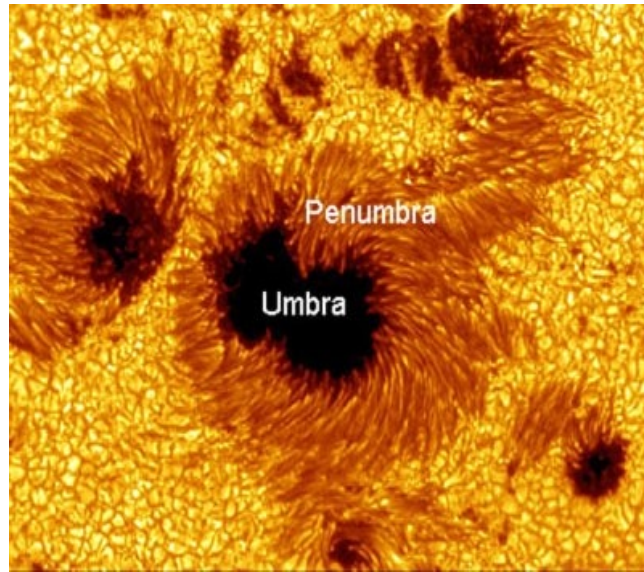


Figure 2.4: The sunspots showing the umbra and penumbra (Royal Swedish Academy of Sciences)

measurements of polarisation showed that the direction of umbra magnetic field is vertical, and assuming horizontal across the penumbra. Sunspots are usually located in groups (with tendency to occur in pairs), in which a dominant sunspot leads one or more sunspots in the direction of rotation. Also, measured magnetic fields show that the two members of a sunspot pair have opposite polarities. Observations made over the past two centuries have shown that the number of sunspots vary periodically, moving from minimum count to maximum in approximately every 11 years. This characteristic is known as the *solar cycle* or solar activity cycle. Essentially, there are more numbers of sunspots during the solar maximum phase than there are during solar minimum. The average latitude of sunspot formation also exhibit this periodicity with 11-year timescale. Figure 2.5 shows the solar cycle variation in the number of sunspots (lower panel) and the average latitude of sunspot formation (upper panel), also known as the butterfly diagram. A sunspot relative number (also known as Wolf number) which considers the sunspot size and its relation to other spots or an active region can be used to account for the statistical appearance of sunspots, and given as (Kallenrode, 2001; Prolss, 2004)

$$R = k(10g + f), \quad (2-4)$$

where g is the number groups of the spots, f is the number of single spot, and k is

a normalisation factor to standardise the observations.

During an 11-year cycle, a lead sunspot will normally have the same polarity in one hemisphere (e.g., a north pole in the geographic northern hemisphere). On the other hand, a lead sunspot in another hemisphere will have the opposite polarity (e.g., a south pole in the southern hemisphere), while trailing sunspots have opposite polarity. The polarities of the lead sunspots reverses during the next solar cycle - the sunspot with a magnetic south polarity will lead the northern hemisphere and one with a magnetic north leading the southern hemisphere. There is also a global polarity reversal following this local polarity reversal in which the Sun's overall dipole field changes, such that the magnetic north pole of the Sun switches from the geomagnetic north pole to the geographic south pole. Due to this polarity reversal (which always occurs during solar/sunspot minimum) the Sun is said to have a 22-year cycle (from magnetic field polarity view point). Some other phenomena are also associated with sunspot activity (e.g. plages), and participate in the solar activity circle. However, sunspots are more easily observable than others. Generally, the regions of heightened magnetic field on the photosphere are normally probable locations of various solar energetic events. Such regions are called *active regions*. For further readings, see, Carroll and Ostlie (1996, 2007), Green and Jones (2004).

2.2 Solar energetic events

2.2.1 Solar wind and its properties

Solar wind is the continuous outflow of streams of energized charged particles from the Sun, primarily protons and electrons with small mixture of α particles (He^{2+}). The velocity of the solar wind ranges between 170 km/s and more than 3000 km/s, with mean speed of about 400-500 km/s. Fast and/or high-speed solar wind streams ($V_{sw} > 600$ km/s) and their slow-speed streams counterpart ($V_{sw} < 400$ km/s) have been identified, emanating from different coronal origin. The slow solar wind originates from coronal streamers, an active region associated with closed magnetic fields structures and high densities. The high-speed (with low density) solar wind originates from the coronal holes, a region located over open magnetic fields lines such as the polar caps (Alurkar, 1997; Kallenrode, 2001; Prolss, 2004; Meyer-Vernet, 2007; Golub and Pasachoff, 1997, 2010; Crammer, 2009). The solar wind is supersonic and takes about 3-4 days to reach the Earth. The density, temperature and velocity of the solar wind vary, but the particle flux is relatively constant and may fluctuate by less than a factor or two about its mean. The various components of the solar wind have different temperature. This systematic variations in the temperature are found to be coupled to the velocity of the solar wind (Prolss,

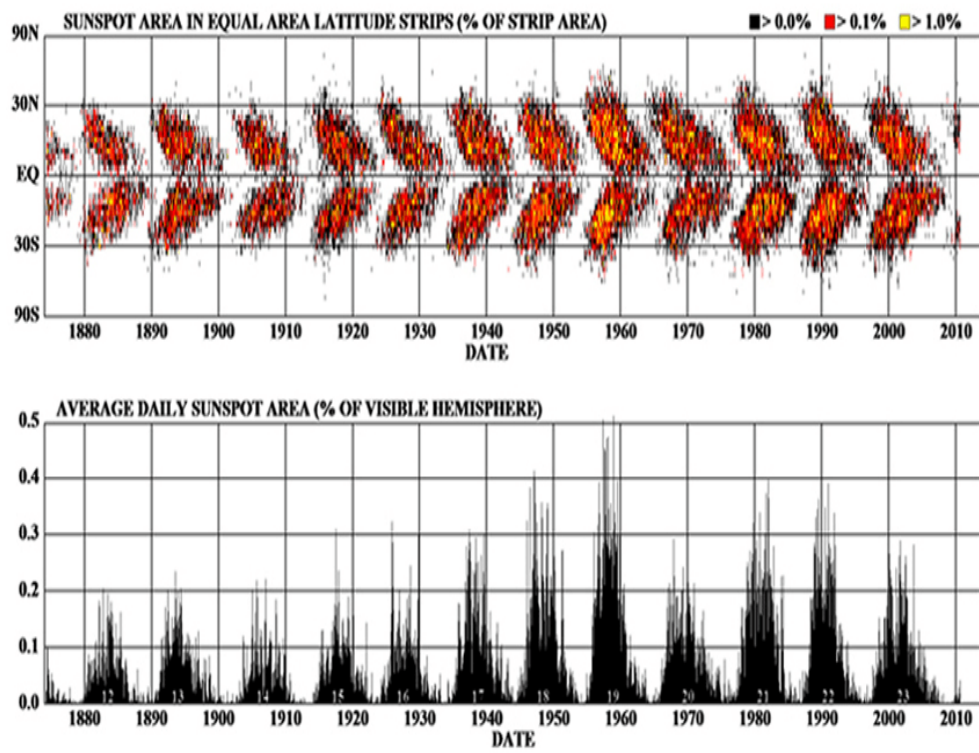


Figure 2.5: solar cycle variation of daily sunspot area averaged over individual solar rotation (D. Hathaway, NASA/MSFC)

2004). The typical temperature of the slow-speed solar wind is about 0.3×10^5 K though the mean temperature of the high-speed solar wind is about 2.3×10^5 K. The Sun constantly loses mass through the solar wind with an average energy per proton that is about a tenth of the gravitational binding energy near the solar surface. However, due to the efficient thermal conductivity, the temperature stays high out to large distances, and near $10R_\odot$ the thermal energy exceeds the binding energy. Therefore, the outer corona evaporates, and matter from below moves up to replace the lost mass (Parker, 1997; Schijver and Zwaan, 2000). The Sun's mass loss rate can be estimated from the following equation if the particle flux is known (Prolss, 2004).

$$\frac{dM_s}{dt} = n_p u m_H 4\pi(1AU)^2 > 10^9 kg/s, \quad (2-5)$$

Thus, the Sun loses more than a million tons of mass each second through the solar wind. The energy density of the solar wind is determined by the flow motion. Hence, the energy flux of the solar wind (to a good approximation) is given by,

$$\phi_{sw}^E(1AU) \simeq n_p u (m_H u^2 / 2) \simeq 0.5 mW/m^2, \quad (2-6)$$

To estimate the total energy loss to the Sun from the solar wind, the work performed by the motion of the particle against the solar gravitational attraction must be accounted for. The potential energy is given by,

$$E_{pot} \simeq \int_{R_s}^{\infty} m_H g s dr = G m_H M_s / R_s, \quad (2-7)$$

The flux associated with this potential energy is,

$$\phi_{pot}^E \simeq n_p u E_{pot} \simeq 0.9 mW/m^2, \quad (2-8)$$

Therefore, the total energy expense of the Sun to the solar wind is given by the equation below:

$$(\phi_{sw}^E + \phi_{pot}^E) 4\pi(1AU)^2 \simeq 4 \times 10^{20} W. \quad (2-9)$$

Mechanisms of solar wind flow

We will describe the large-scale structure of the solar wind using the jetlines that form Archimedean spirals with various curvature, determined by the local wind velocity (see, Fig. 2.6). The flow within a given sector is prevented from penetrating into adjacent sector by the interplanetary magnetic fields, which is rooted in and borne by the solar wind. Contact discontinuities form at the sector boundaries that separate and tend to isolate the individual sectors, and the jetlines at the boundaries also flexes and adjust to the different adjacent flow profiles, leading to formation of rarefaction and compression regions (see Kallenrode, 2001; Prolss, 2004). In this propagation mode the trailing high-speed solar wind ‘sweeps through’ the slow solar wind along their common sector boundary, and the fast solar wind is decelerated by the trailing slow wind with the two flows parallel to, and increasingly perpendicular to the sector boundary within their unperturbed regions. As the wind propagates to large distance away from the Sun (outside the Earth’s orbit), the curvature of the jetlines becomes huge that the normal component of the relative velocity between the respective solar wind flows, such that the boundary reaches ‘supermagnetosonic’ range. In relation to the sector boundary, the leading flow (in front) is due to the low speed solar wind and the flow behind is from the high-speed solar wind, with relative velocities in the supermagnetosonic values. This flow scenario could result in formation of two shocks (one on each side of the sector boundary), recognised as ‘forward’ and ‘reverse’ shock (Kallenrode, 2001; Prolss, 2004).

Corotating interaction region (CIR)

Because the source regions (coronal holes and streamers) of the two different solar wind streams (high- and low-speed) rotate with the Sun, the stream-stream interaction region leading to compression of the solar wind plasma on the forward propagating edge of the high-speed, as well as compressed magnetic field, and the shocks, all propagate in association with the solar rotation (forming an interface between low and high speed solar plasma). This compressed region of high density is known as a *corotating interaction region* (CIR) and shown in Fig. 2.7. The CIR can cause geomagnetic storms when the region interacts with the Earth’s magnetosphere (Prolss, 2004; Borovsky and Denton, 2006; Tsurutani et al., 2006; Burns et al., 2012), especially when the embedded magnetic field has negative B_z (Prolss, 2004). CIR and associated particles and effects are frequently observed at intervals of solar rotation (27 days) and dominates the solar minimum phase of the solar cycle. The solar wind speed is also known to vary with geographical latitude. At high latitudes, the solar wind flows with a very high velocity (about 750-800 km) and relatively low density (about 3 protons/electrons per cm^3), but with slower and denser solar wind

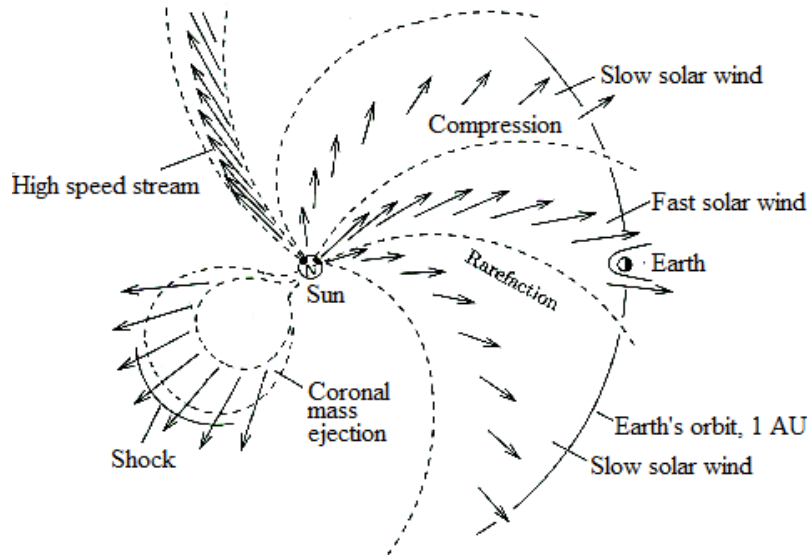


Figure 2.6: View of solar wind structure in the ecliptic plane (from Prolls, 2004)

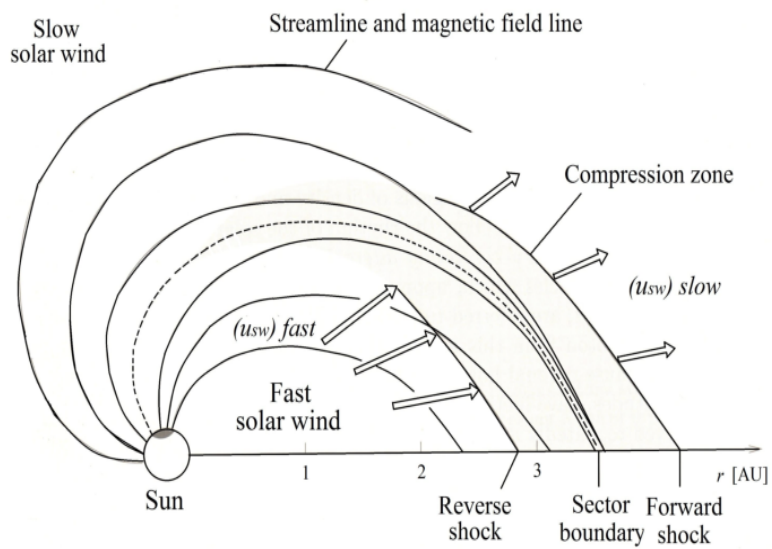


Figure 2.7: Formation and propagation of corotating interaction region in the solar wind (from Prolls, 2004)

at low latitudes (Kallenrode, 2001; Prolss, 2004).

2.2.2 Solar flares, CMEs and prominences

Solar flares

Solar flares are strong, momentary release of great amount of magnetic energy from the Sun with the potential of heating up materials to many millions of degrees or Kelvin (more than 10^7 K). The duration of solar flare is usually ≤ 1 hr, and localised (about $\leq 0.1R_{\odot}$), with energy release up to 10^{25} J (Kallenrode, 2001; Green and Jones, 2003; Prolss, 2004). The eruption flare from the Sun is shown in Fig. 2.8. EM radiation and energetic particles are released during solar flare from regions that often lie between sunspot pairs (or, within sunspot group), and sometimes in active regions where sunspots are not present. Hence the frequency of solar flares also exhibit solar cycle variation (Green and Jones, 2003; Prolss, 2004). Solar flares are easily observed in the light of the H_{α} and $CaII$ lines, but also in γ -ray and radio parts of the spectrum (Schrijver and Zwaan, 2000; Kallenrode, 2001; Green and Jones, 2003; Prolss, 2004). Whereas EM radiation is emitted over a range of wavelengths, the dominant emission is the X-ray and EUV (Golub and Pasachoff, 1997, 2010; Schrijver and Zwaan, 2000; Kallenrode, 2001; Green and Jones, 2003; Prolss, 2004). X-ray levels are routinely monitored by satellites such as the Geostationary Operational Environmental Satellite (GOES) (also see Manckol and Veireck, 2016).

One of the probable mechanisms that accounts for flare radiation from the Sun is shown in Fig. 2.9, described in Prolss (2004) as a loop-like magnetic flux tube from the Sun that extends out into the corona. The energy released by reconnection process results to strong acceleration of charged particles at the tip of the flux tube. The particles are then injected into the chromosphere during which the electrons emit synchrotron radiation at radio wavelengths along the trajectory. This is thought to be responsible for the spontaneous rise in intensity usually observed as a spike in X-ray flux signature. When the electrons strike the denser gases of the chromosphere, they become decelerated by collision and consequently produce emission by bremsstrahlung in the EUV and ‘hard’ X-ray range (in particular) leading to rapid increase in the short wavelength emission. Hard X-rays are photons with energies between a few 10 keV and a few 100 keV and wavelength below 0.2-0.1 nm. Also, the precipitating protons with energies of several 10 MeV can simultaneously trigger nuclear emission in the γ range, and/or release neutrons and positrons at higher energies. Strong ionisation and heating of the ‘local’ gases occur due to the thermalisation of the incident energetic particles in the chromosphere. The intensity

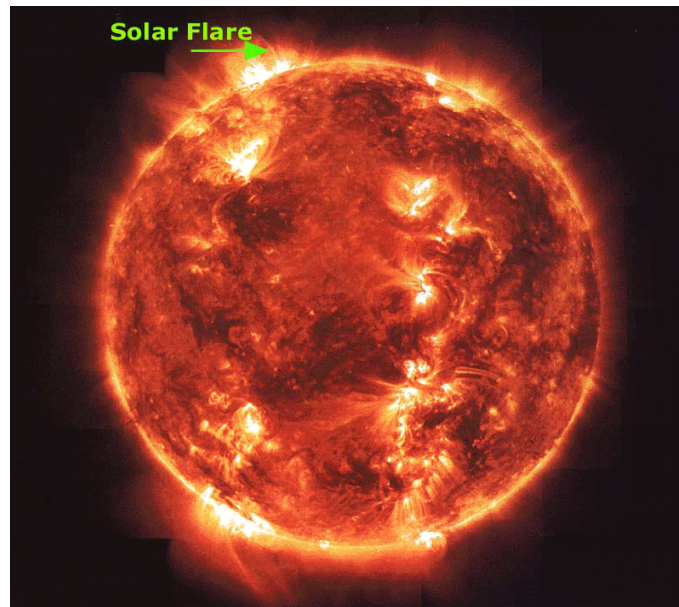


Figure 2.8: Solar flares (NASA)

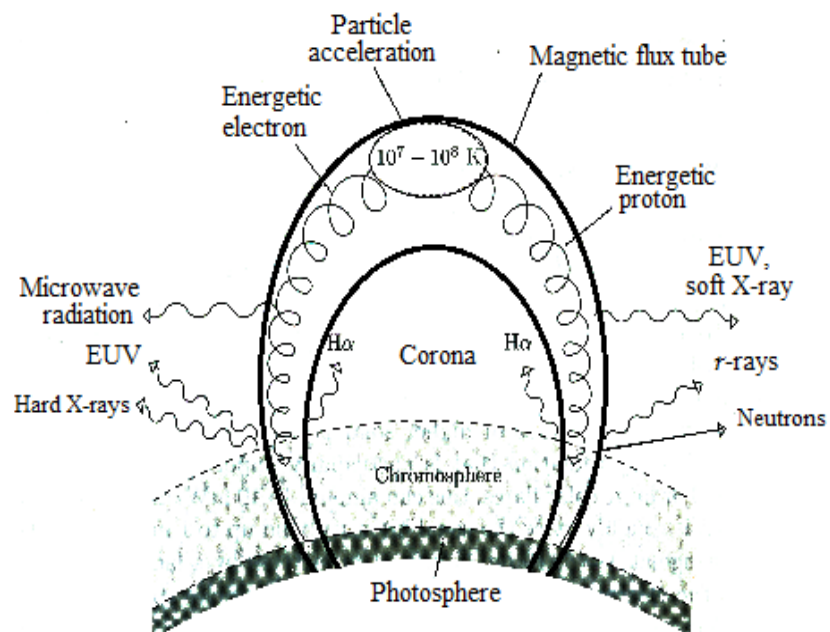


Figure 2.9: Solar flare emission components and their probable locations (from Prolss, 2004)

of this heating leads to the evaporation of the chromosphere as plasma into the coronal extension of the flux tube. In the mean time, the hot plasma of the tip region (simultaneously created by the acceleration of the particles) heats the adjacent base regions such that the whole flux tube is ultimately filled with ionised hot gas at a very high temperature (10-100 million K). This scenario (thermal bremsstrahlung of the plasma) is thought to be responsible for increase of the EUV and soft X-ray radiation (with wavelength between 0.1 and 10 nm) accompanying the spontaneous phase of flare emission. The H_α radiation may be attributed to the direct excitation of chromospheric hydrogen from the thermalisation of the incident energetic particles, as well as to the emission stimulated from the recombination of ionised hydrogen. During this process the hot plasma in the coronal magnetic flux tube (with energy of several KeV) maintains a continuous contact with the chromosphere. The energy released by/during solar flares accelerate particles (in the direction of denser solar atmosphere (downwards) as well as into the interplanetary space along the magnetic field lines that have been opened by the reconnection processes) (Prolss, 2004; Gopalswamy, 2009; Golub and Pasachoff, 2010). The accelerated particle beams (often in pulsating manner) excite the background plasma of the corona leading to oscillations (Langmuir) at the local plasma frequency that is usually recorded in form of Type III radio emission at the Earth (Schrijver and Zwaan, 2000; Kallenrode, 2001; Prolss, 2004).

A solar flare is ranked based on its X-ray output, and classified according to the order of magnitude of the peak burst intensity (I), measured at the Earth in 0.1 to 0.8 nm band; B = $I < 10^{-6}W/m^2$, C = $10^{-6}I < 10^{-5}W/m^2$, M = $10^{-5}I < 10^{-4}W/m^2$, X = $10^{-4}IW/m^2$ (also see Golub and Pasachoff, 2010 and references therein; Nwankwo et al. 2016). A and B categories are very small flares, added below C to recognise that such flares occur very often during any phase of the solar cycle. C flares are stronger and more frequent (especially during solar maximum) but have fewer noticeable consequences on Earth compared to M and X. The M category is medium in size while X flares are extreme. Relating to their geoefficiency, the M-class can cause brief radio blackouts (especially in the Earth's polar regions), and the X-class can trigger global radio blackouts and long-lasting radiation storms (Also see NOAA1).

Coronal mass ejections

One other important source of geoeffective solar wind is the coronal mass ejections (CMEs). A CME is a large-scale, high-mass, eruptions of plasma from the Sun, which propagates into the interplanetary space. The phenomena originate from active and/or filament regions of closed magnetic field, with eruptive promi-

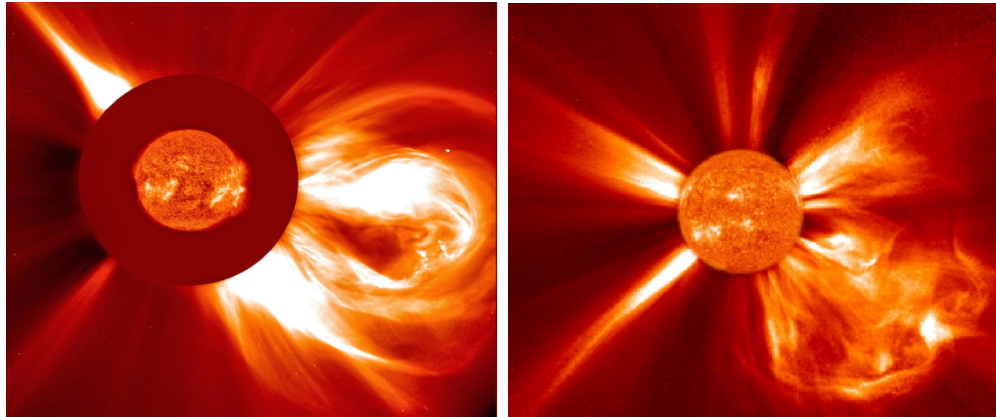


Figure 2.10: (a) A CME erupted from the lower right of the Sun on 2 Dec. 2003 (Credits: ESA/NASA/SOHO) (b) a powerful CME occurred on 8 Jan. 2012. The broad front of the particle cloud had already expanded to about 120 degrees when this image was taken. Here the Sun itself has been enlarged about 50% and superimposed on the background image to cover the coronagraph's occulting disk. The occulting disk blocks out the Sun's bright light so that the fainter structures in the corona can be observed (images are from the STEREO spacecraft)

nence forming the inner core of many CMEs (House et al., 1981; Gopalswamy, 2004, 2006; Gopalswamy et al., 2009). CMEs are powered by strong or large-scale concentration and reorganisation of the coronal magnetic field (Kahler, 1992; Gosling, 1994; Golub and Pasachoff, 2010). It is believed that CMEs contribute up to 10% to the whole solar wind mass loss by estimation of their mass and frequency of occurrence (Stix, 2002; Golub and Pasachoff, 1997, 2010; Schrijver, 2000). The rate of CME is solar cycle dependent. The daily CME rate (averaged over Carrington Rotation period of about 27.3 days) increases from one every other day during solar minimum to more than six per day during solar maximum (Gopalswamy et al., 2009). The mean mass ejected during a CME could be up to 10^{13} kg, kinetic energy of about 10^{25} J, and mean velocity ~ 400 -500 km/s (also, see Hundhausen et al., 1972; Golub and Pasachoff, 1997, 2010; Kallenrode, 2001; Prolss, 2004). The annual average width (angular span) range of CMEs is about 47° to 61° (Yashiro et al., 2004; Gopalswamy, 2006), for CMEs with width $\leq 120^\circ$. Halo CMEs ($\geq 120^\circ$) are excluded from this estimate because their true width is unknown. Halos are those that appear to surround the occulting disk of the coronagraph, and can originate from the frontside or on the backside of the Sun (Gopalswamy et al., 2009). Satellite images of CMEs are shown in Fig. 2.10(a-b).

However, values of these parameters have been modified over the years because CME properties have been largely studied with observational data from various

satellites since the advent of the Seventh Orbiting Solar Observatory (OSO-7) satellite in 1971. The OSO-7 recorded about 27 CMEs between September 1971 and July 1974 for about 19.5 months before the end of its mission (also see Tousey, 1973); the Skylab recorded about 110 CMEs between 1973 and 1974 for 227 days (also see MacQueen et al., 1974); the Solarwind coronagraph on board P78-1 recorded about 1607 between 1979 and 1985; the Solar Maximum Mission (SMM) recorded about 1206 during 1980 and 1984-1989 (also see MacQueen et al., 1980) and the Large Angle and Spectrometric Coronagraph (LASCO) on board Solar and Heliospheric Observatory (SOHO) recorded about 8000 CMEs between 1996 and 2003 (see Brueckner et al., 1995; Gopalswamy, 2004). These details were first compiled by Hundhausen (1997) and updated by Gopalswamy (2004). However, only after the advent of the SOHO/LASCO mission that uninterrupted and uniform CME data became available (Gopalswamy et al., 2009). The properties of CMEs are mainly characterised by observational and statistical studies using data from various space probes. As more data became available statistical values fluctuated (slightly) e.g. their mean speed have been given as 470 km/s, 460 km/s, 350 km/s and 482 km/s in statistical studies with data from Skylab, Solwind, SMM and LASCO/SOHO respectively (e.g. Gopalswamy, 2004). About 4 years later (in 2007), the CME mean speed calculated from SOHO data was updated to 435 km/s as data increased from about 8000 to 1441 points (e.g. Mittal and Narain, 2009). So do CME ejected mass, rate, width, kinetic energy, acceleration and central angle position also fluctuate (also, see Gopalswamy et al., 2009 and references therein). However, the CMEs speed ranges from a few km/s to more than ~ 3000 km/s (up to 3387 km/s) (Yashiro et al., 2004; Gopalswamy, 2009), and also show a solar cycle variation. The mean speed during solar minimum is less than 300 km/s, and nearly 600 km/s during solar maximum. Also, depending on its speed, CMEs take about less than a day to a maximum of six days to reach Earth (Gopalswamy et al., 2009). CMEs have positive acceleration at the onset but eventually suffers a retarding ‘drag’ force. This drag force is given by the following equation (Cargill et al., 1996; Gopalswamy, 2004; Mittal and Narain, 2009).

$$F_d = C_d A \rho - V_{cme} - V_{sw} - (V_{cme} - V_{sw}). \quad (2-10)$$

where, C_d is the drag coefficient, A is the surface area of the CME, ρ is the plasma density, V_{cme} is the CME speed and V_{sw} is the solar wind speed. The solar wind speed is negligible close to the Sun.

The CME height-time profiles reflected a combination of various propelling and retarding forces viz. the accelerating, constant-speed and decelerating profile. While

the accelerating profile indicated that the propelling force is active in pushing the CME outward, the constant-speed and decelerating profile suggested that the retarding forces either balance or exceed the propelling force (Gopalswamy, 2004).

Geoefficiency of CMEs

CMEs propagate into the solar wind and drive shocks, which in turn accelerates solar energetic particles (Gosling, 1993; Reames, 1999; Gopalswamy, 2009), and also deflect the galactic cosmic rays (GCRs) entering the heliosphere from outside (Gopalswamy, 2009 and references therein). CME propagation in the interplanetary space has important consequences. When the eruption is directed towards the Earth, its impact and interaction with the Earth's magnetosphere causes geomagnetic storms and other associated phenomena, especially when the embedded magnetic field has southward components (Prolss, 2004; Gopalswamy, 2006). Geomagnetic storms can cause a large-scales disturbances and adverse consequences in the geospace environment. The size, speed, direction and density of a CME, and the strength of embedded magnetic field generally determine the intensity and impact of a geomagnetic storm. The evolution and propagation features (special population) of CMEs that produces geoefficiency, and their distinct effects are presented in detail in Gopalswamy (2006, 2009). CMEs are associated with a number of phenomena including solar flares and prominence eruptions (Munro et al., 1979; MacQueen, 1985; Low, 1994, Golub and Pasachoff, 1997, 2010; Gopalswamy, 2004). Prominences and solar flares will be discussed below. Other CMEs associated phenomena include H-alpha flare ribbons, moreton waves, dimming, arcade formation, X-ray and EUV ejecta, EUV wave transients, metric radio bursts, magnetic clouds, interplanetary radio bursts (Gopalswamy, 2004). These phenomena are essentially observed as motion, wave and electromagnetic radiation.

Prominence eruption

Prominences are often observed as bright arches against a dark background (seen beyond the solar limb) with temperature of about 10^4 K harboured in surrounding hot corona of temperature 10^6 K. When projected on the solar disk, they appear like a filament nearly vertical on solar surface, reaching a height of 0.03-0.07 R_{\odot} (Alurkar, 1996). Filaments are long, winding dark feature caused by huge clouds of relatively cool gas held above the chromosphere by magnetic forces (Green and Jones, 2003; Golub and Pasachoff, 2010). Prominences are formed in the regions of sunspots and are thought to be visible when the hotter coronal material condenses in the presence of magnetic fields. In prominence eruption, dense clouds of materials suspended above the Sun's surface by the magnetic fields are spontaneously released

over the course of a few minutes to some hours. Flare-induced shock can potentially cause prominence activation, and loop prominences are sometimes observed several hours after a major flare, and often associated with solar protons (Alurkar, 1996 and references therein).

2.3 Earth's magnetosphere and atmosphere

2.3.1 The magnetosphere

The bulk of atmospheric responses to the induced forcing by solar energetic events are mainly triggered by the interaction between emitted EM radiations and energetic particles with the Earth's magnetosphere. The Earth's magnetosphere has been described in Chapter 1, but also pictured as the surrounding region of the Earth in which its magnetic fields dominate the behaviour of electrically charged particles (mainly protons, electron and ions) (Lang, 2011). Usually, hot, high-speed, and magnetised solar wind (with embedded energetic particles and magnetic field) collide and interacts with the Earth's magnetic field at a distance of about $6-10R_E$ on the dayside (facing the Sun), pushing the fields in and compressing its outer magnetic boundary. This scenario forms a shock wave, recognised as the bow shock. The bow shock is formed because the solar wind flow is supersonic, in a motion that has been compared to the flow of air around a supersonic aircraft (Lang, 2011). The size, shape and behaviour of the magnetosphere are essentially controlled by the varying properties of the solar wind plasma and the attached magnetic fields (McPherron et al., 2008; Lang, 2011). The Earth's magnetosphere is shown in Fig. 2.11.

After the formation of the bow shock, the solar wind encounters and flows around the boundary between the solar wind and the magnetosphere called the *magnetopause*, and the magnetic field embedded in the solar wind merges with that of the Earth, stretching out into a long *magnetotail* on the nightside of the Earth. The magnetic field approximately points towards the Earth in the northern half of the tail and away in the southern part. At the centre of the tail (where the opposite magnetic orientations lie next to each other) the magnetic field strength drops to zero value so that currents can flow (Lang, 2011). However, the energetic charged particles can penetrate the magnetosphere and become trapped within the magnetosphere. These regions of trapped energetic particles lie approximately at distances 1.5 and 4.5 Earth radii, and known as the *Van Allen radiation belts*, named after James A Van Allen (1914-2006) who discovered the region in 1958 (Hunsucker and Hargreaves, 2003; Lang, 2011). The inner belt consists mainly of proton with energies exceeding 100 MeV, and the outer belt consisting mainly electrons with range

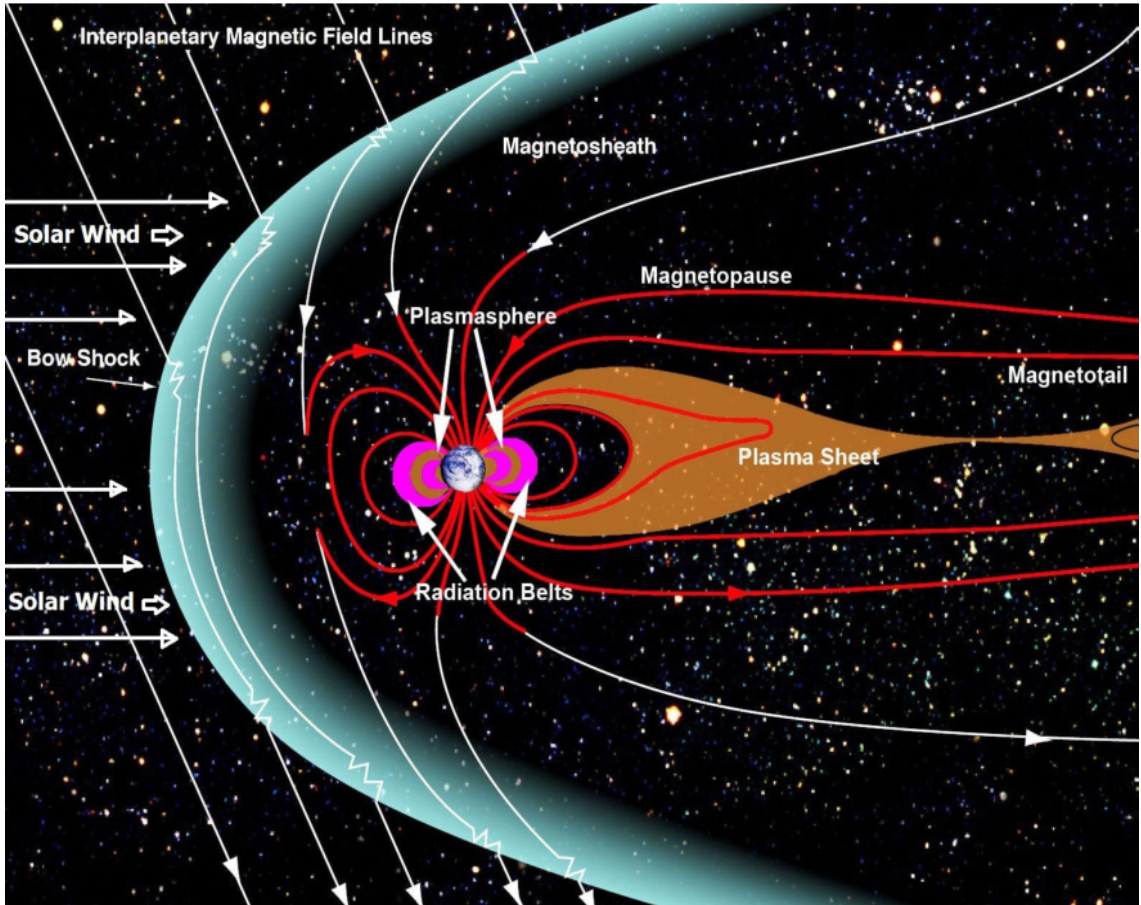


Figure 2.11: The Earth's magnetosphere. When solar wind encounters and interacts with the Earth's magnetic field, it compresses its sun-ward side to a distance of about $6-10R_E$, creating a supersonic shock wave known as the *Bow Shock*. Although its exact length is not known, the solar wind drags out the night-side of the inner magnetosphere to probably $1000R_E$, an extension that is known as the *Magnetotail*. The *Magnetopause* is the outer boundary of Earth's confined geomagnetic field. (Credit: Aaron Kaase/NASA/Goddard (Adapted))

of energies 0.1-10 MeV. The trapped particles exhibit three types of motions: (i) they gyrate around a line of geomagnetic field, (ii) bounce back and forth along the line of force between mirror points, and (iii) gradually drift longitudinally around the Earth (Hunsucker and Hargreaves, 2003). The solar magnetic field can open up the Earth's magnetic field when two fields (embedded magnetic field in solar wind streams and the solar magnetic field) points in opposite directions where they intercept. This scenario connects the two fields in the process known as *magnetic reconnection*. The process can create a channel in Earth's magnetic field through which particles can flow (and/or exchanged)(Cowley et al. 2003; Lang, 2011).

2.3.2 The Atmospheric profile of the Earth

The atmosphere can be conveniently described by its pressure, density, temperature and composition. However, it is mainly based on its variation in temperature with height (Hunsucker and Hargreaves, 2003; Prolss, 2004). Different regions of the atmosphere are recognised as 'spheres' and the boundaries between them as 'pauses'. The factors that play significant role in atmospheric temperature variations include direct absorption of solar radiation, heating of the lowest air layers by the Earth's surface, and re-absorption of atmospheric infrared radiation primarily reflected from atmospheric water vapour (Prolss, 2004). The typical height profile of temperature, pressure, and mass density in the Earth's atmosphere is shown in Fig. 2.12.

The *troposphere* is the lowest region of the atmosphere (extending up to about 10 km). Here the temperature falls off with increasing height at the rate of 10 K per km. The upper boundary of the troposphere is the tropopause at the height of 10-12 km. Above this region is the *stratosphere* (reaching up to about 50 km) and its upper boundary (the stratopause), the temperature rise again in this region due to absorption of solar UV radiation (usually at wavelength above 242 nm) by the trace gas ozone. The region above the the stratosphere is the *mesosphere*. Temperature decreases again in this region, reaching a minimum at the boundary (the mesopause) at 80-85 km. Here, the mean temperature in the region is about 160-180 K, but under extreme conditions lower temperatures (less than 120 K) have also been measured (also see Hunsucker and Hargreaves, 2003; Prolss, 2004). In the thermosphere (above the mesosphere and mesopause) the temperature increases drastically, principally due to the heating (and absorption) by solar EUV radiation. At heights above 200 km atmospheric temperature approaches somewhat constant value known as thermospheric temperature and typically about 1000 K. Atmospheric pressure and mass density are significantly determined by atmospheric temperature. The atmosphere is also composed of various major species (oxygen and nitrogen)

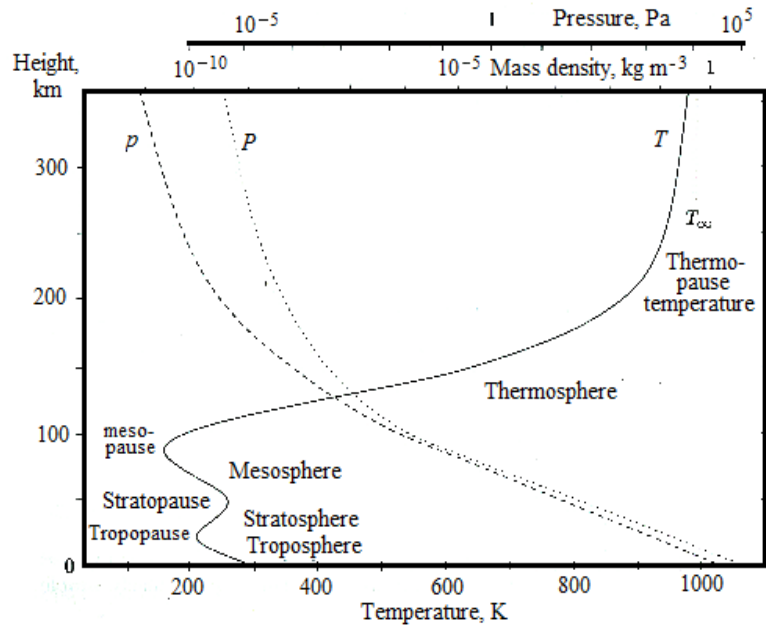


Figure 2.12: Height profile of temperature, pressure, and mass density in the Earth's atmosphere (from Prolss, 2004)

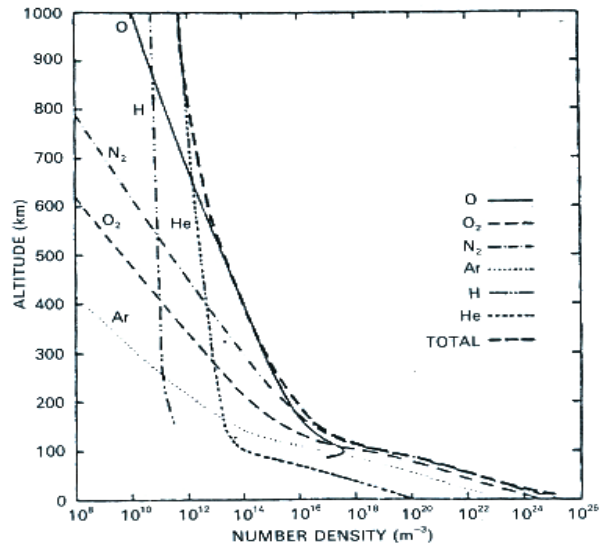


Figure 2.13: The atmospheric composition (from Hunsucker and Hargreaves, 2003)

and minor species (water, carbon dioxide, oxides of nitrogen, ozone and alkaline metals). The atmospheric compositions for a typical temperature profile is shown in Fig. 2.13.

Hydrostatic equilibrium in the atmosphere

Atmospheric temperature, pressure, density, and composition are dependent, and determine much of the behaviour of the atmosphere. These properties can be related by the universal laws, and can be written in the form (Hunsucker and Hargreaves, 2003):

$$P = nKT, \quad (2-11)$$

n is the number of molecules per unit volume or number density. Atmospheric pressure and density decreases with increasing altitude. This height variation is described by the hydrostatic equation (or barometric equation). The pressure variation with height is given by,

$$P = P_0 \exp\left(-\frac{h}{H}\right), \quad (2-12)$$

where, P is the pressure at height h , P_0 is the pressure where $h=0$, and H is the scale height given by,

$$H = \frac{KT}{mg}. \quad (2-13)$$

Here, K is the Boltzmann's constant, T is the absolute temperature, m is the mass of single particle of the atmospheric gas, and g is the acceleration due to gravity. If T and m are constant, H is the vertical distance over which n fall by a factor of e , and defines the thickness of an atmosphere. If the gas is hotter or lighter, then H is greater, which implies that the atmosphere is thicker.

Using the Eqn. 2-11, the hydrostatic equation may be written in the form,

$$\frac{P}{P_0} = \exp\left(-\frac{(h - h_0)}{H}\right) = e^{-z}, \quad (2-14)$$

where, $P=p_0$ at the height $h=h_0$, and z is the reduced height defined by,

$$z = \frac{(h - h_0)}{H}. \quad (2-15)$$

The hydrostatic equation can also be written in terms of the density (ρ) and the number density n . The equation is the same in terms of P , ρ , and n if T , g , and m are constant over one scale height, since $n/n_0 = \rho/\rho_0 = P/P_0$. More detail about the hydrostatic equation can be found in Hunsucker and Hargreaves (2003).

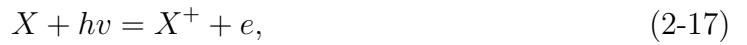
2.3.3 The Ionosphere

The ionosphere is the ionised component of the upper atmosphere. It is composed of three distinct space regions viz. the D (60 km to 90 km), E (100 km to 160 km), and the F (from 160 km up to 400 km). The F region often splits into two layers, namely, F1 and F2. The vertical profiles of the ionosphere are shown in Fig. 2.14. The existence of the ionospheric layers are primarily due to ionisation (of atmospheric gases such as N_2 , O_2 and O) by UV radiation and X-ray wavelength (Kelley, 1989; Hunsucker and Hargreaves, 2003; Prolss, 2004; McRae and Thomson, 2004; Raulin et al., 2006; Heikkila, 2011) and isotropic cosmic rays. Another important process in the ionosphere is recombination, which occurs when free electrons are captured by positive ions, and react with other gaseous species to produce other ions. Hence, the net concentration of free electrons (electron density) depends on the relative speed of the production and loss processes (Hunsucker and Hargreaves, 2003). Therefore, ionisation and recombination controls the overall electron density at any instant. The high rate of ionisation in the day time makes the D region ionosphere highly active (with mean daytime electron density of $10^8 - 10^{10}$ per m). However, its density falls significantly at night largely due to rapid recombination at the altitude. The E region (with mean daytime electron density of several times 10^{11} per m^3) also exhibits the same dynamics as the D region but ionisation state persists longer in the region due to low rate of recombination. Hence, the reflection of signals appear to occur at the bottom of the nighttime E region (Han and Cummer, 2010a and references therein). The F region with electron density of 10^{11} - 10^{12} per m^3 , is present both day and night; air density and recombination rate is very low in the region, such that ionisation persists in the nighttime (also, see, Mimno, 1937; Poole, 1999; Prolss, 2004). The dynamics of ionospheric species in different regions have been described in detail (e.g. see, Hunsucker and Hargreaves, 2003; Prolss, 2004). The terms rate of change of electron density is expressed by the continuity equation (Hunsucker and Hargreaves, 2003):

$$\frac{\partial N}{\partial t} = q - L - \text{div}(N\mathbf{v}), \quad (2-16)$$

where, q is the production rate (per unit volume), L is the rate of loss by recombination, and $\text{div}(N\mathbf{v})$ expresses the loss of electrons by movement, \mathbf{v} is their mean drift velocity.

Considering a representative ionisation and recombination reaction and neglecting movements,



from the law of mass action, at equilibrium,

$$[X][hv] = \text{constant} \times [X^+][e], \quad (2-18)$$

where the square brackets indicate concentrations. Therefore, since $[e] = [X^+]$ for electrical neutrality,

$$[e]^2 = \text{constant} \times [X][hv][X^+]. \quad (2-19)$$

The intensity of ionising radiation changes with the Sun's elevation during the day, causing the electron density to respond to the variation of dominant $[hv]$, but the source of the radiation (e.g. the Sun) is absent at night so that the electron density falls dramatically. The electron density changes with altitude, as well as the intensity of ionising radiation (which increases). However, the concentration of ionisable gas $[X]$ decreases with height (Hunsucker and Hargreaves, 2003).

In general, the parameters of ionospheric layers are prone to strong fluctuations by phenomena of various sources such as solar and geomagnetic activity, planetary and tidal waves, thermospheric tides and stratospheric warming (Pancheva et al., 2008; Leonard et al., 2012; Chen et al., 2013; Goncharenko et al., 2012; Polyakova et al., 2014), and the ranges of typical daily values have been given as (Prolss, 2004);
 Maximum ionisation density (n_m) $\simeq 1\text{-}30 \times 10^{11}/\text{m}^3$
 Height of the maximum (h_m) $\simeq 220\text{-}400$ km
 Layer thickness $\simeq 100\text{-}400$ km, and
 Column density (N_e) $\simeq 1\text{-}10 \times 10^{17}/\text{m}^2$

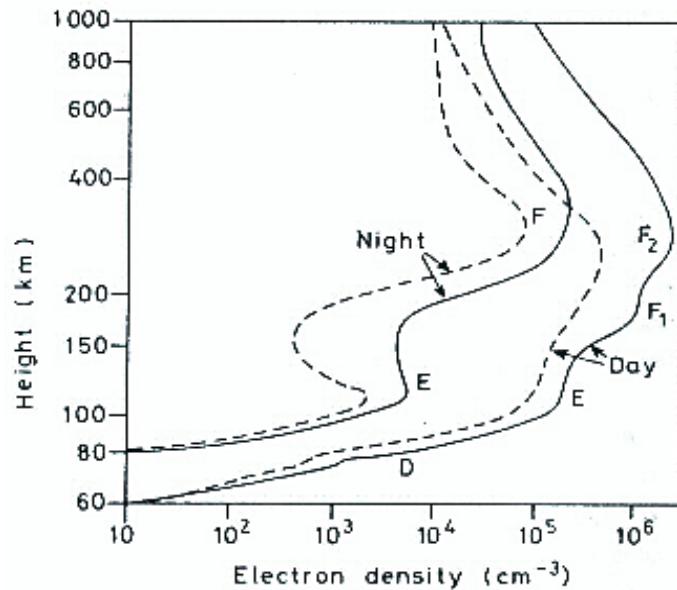


Figure 2.14: Vertical profile of the ionosphere (from Hunsucker and Hargreaves, 2003)

However, effects at different heights, locations or latitudes vary in development, depending on time and intensity (of driving force). Ionospheric signature variations also reflect different mechanisms and aspects of solar and other induced phenomena (Nwankwo et al. 2016).

2.4 Space weather: atmospheric responses to Solar energetic events

The variability of the solar wind (especially those of the ubiquitous solar wind and CMEs) and associated high-energy charged particle flux (including those accelerated by solar flare events) form an important channel of solar activity influence on the Earth's atmosphere. Associated phenomena (or effects) in the near Earth and interplanetary atmosphere include the variability of the IMF, Earth crossings of the IMF sector boundary (heliospheric current sheet), shock waves and interaction regions in the solar wind, modulation of galactic cosmic ray fluxes (including ground level events and forrush decreases), solar particle events, relativistic electron precipitation events (including highly relativistic electrons), geomagnetic storms, magnetospheric substorms, etc. (also see, Lastovicka, 1989, 1996). These phenomena are often interrelated and their effects on the atmosphere (and heliosphere) sometimes

overlap each other. Geomagnetic storms are the leading driver of large-scale coupled magnetosphere-ionosphere dynamics in the geospace environment. They are mainly products of strong variations in solar wind conditions via energy transfer. The initiation of geomagnetic storms is largely favoured by conditions of sustained periods of high speed solar wind, and a southward IMF (Lastovicka, 1989; Baker, 2000; Borovsky and Denton, 2006; Kozyra et al., 2006; McPherron et al., 2008; Tsurutani et al., 1995, 2006, 2011). The impact of Earth-directed CMEs and CIRs, with their embedded magnetic fields on the magnetosphere has direct consequence of producing geomagnetic storms and associated phenomena (Gosling and Pizzo, 1999; Borovsky and Denton, 2006; Lang, 2011; Tsurutani et al., 2006, 2011; Burns et al., 2012; Verkhoglyadova et al., 2013). CME-induced geomagnetic storms are often large, more geo-effective and frequent during solar maxima, while CIR-induced storms are usually less intense and dominates the solar minima. However, more energy is transferred (or, deposited) in the magnetosphere during CIR-induced storms over a characteristic longer duration (a week or more) in comparison to CME-induced storm scenario (lasting about 1 day) (Tsurutani et al., 2011; Verkhoglyadova et al., 2013). The disturbances induced by solar flares on the Earth's atmosphere are less severe than their geomagnetic storms counterpart, and mainly consist of additional (or enhanced) ionisation produced by EUV radiation, X-ray emission and/or sometimes the energetic particles. The abrupt increase in atmospheric ionisation rate, often referred to as *sudden ionospheric disturbance* (SID), leads to sudden (and significant) change in the reflection conditions for radio waves that are usually observed as abrupt shifts in the received frequency, amplitude and phase (Prolss, 2004). The increase in electron density, especially in the D region that are produced by hard X-ray causes short-term attenuation of radio waves. Such conditions (SID) also increase the conductivity of the ionosphere and consequently trigger sudden intensification of ionospheric electric currents together with their associated magnetic field disturbances (Prolss, 2004).

Strong geomagnetic storms can also produce significant voltages and currents in near-earth regions and in extended conductors (e.g., high voltage transmission cables and oil pipelines). These geomagnetic induced currents (GIC) can trip safety relays, interrupt electric circuits, shift operational range of voltage transformers into saturation and melt down of transformer windings, and cause accelerated corrosion of oil and gas pipelines (Jansen et al., 2000; Lang, 2003; Prolss, 2004; Hejda and Sochnicek, 2005; Odenwald, 2015). In the thermosphere, geomagnetic storms lead to enhanced (additional) atmospheric heating and subsequent density enhancements. This scenario increases atmospheric drag on LEO satellites, and consequently accelerated orbit decay that causes their premature re-entry (Walterscheid, 1989; Klinkrad, 1996; Lang, 2003; Prolss, 2004; Mark et al., 2005; Doornbos and

Klinkrad, 2006; Xu et al., 2011). Also, solar energetic particles emitted during solar events (e.g., solar flares and CMEs) and/or those accelerated by flares or geomagnetic storms can degrade, disrupt or destroy satellites system; particles can penetrate and interfere with satellite instruments or sensitive components causing single event effects (SEEs), producing erroneous commands and destroying microelectronics (Lang, 2003, 2011; Prolss, 2004; Nwankwo, 2010; Jibiri et al., 2011). In the ionosphere, geomagnetic storm conditions lower the maximum reflections frequency of ionospheric radio communication leading to loss of transmitted radio signal. When passing through storm-induced dispersive ionosphere GPS signals of navigation satellites are also affected; transmitted signals are delayed thereby causing error in GPS (Prolss, 2004). Also, strong flares (such as M- and X-class) cause ionospheric ‘radio blackouts’, a condition of absence of communication capability on high frequency radio bands in 5-35 MHz spectral range, and also significantly degrade low frequency radio communication. Radio blackouts also affect radio transmission for weather, and airline traffic and information, posing a challenge to commercial airline industries (Lang, 2003, 2011). This thesis mainly focus on two aspects of space weather induced effects, namely, enhanced atmospheric heating and accelerated atmospheric drag (orbital decay) on LEO satellites, and radio signal (VLF) variations for probing solar-induced ionospheric changes.

2.5 Atmospheric drag on LEO Satellites

The optimum performance and survival of successfully launched satellites depend on their ability to withstand both gravitational (e.g., solar/lunar gravitational attractions and Earth’s oblateness (J_2) and its triaxiality) and non-gravitational perturbing forces (e.g., atmospheric drag, solar radiation pressure and environment, outgassing and tidal effects). Atmospheric drag is the strongest force affecting low Earth orbiting satellites (LEOs) at altitudes < 800 km. It describes the force exerted on a spacecraft (or, any object) moving through the atmosphere (or, fluid medium), with orientation in the direction of relative flow. Such force acts in opposition to the direction of motion with tendency of slowing the motion of the spacecraft or object. The effects of atmospheric drag on LEO satellites can be profound depending on the severity of solar activity and the satellite’s orbital parameters. In general, drag force constantly takes energy away from the orbit, and gradually decreases the semimajor axis and period, but increases the velocity components of the satellite as it spirals inward (Wertz and Larson, 1999; Chobotov, 2002), and usually enhanced by increase in solar activity. Detail analysis of atmospheric drag effects on LEO satellites are presented in Chapter 3.

Chapter 3

Atmospheric Drag on Low Earth Orbit Satellites (LEOS)

Atmospheric drag is the main force affecting the trajectory or motion of satellites in low Earth orbit. A satellite in circular orbit moving under the influence of atmospheric drag force can gradually decay from its orbit and eventually re-enter or spiral into atmosphere if not boosted occasionally by thrusters. Those in elliptic orbits (with large eccentricity) experience significant drag at the perigee, which can also significantly lower the apogee, causing the orbit to become more and more circular (see Fig. 3.1b), until the entire orbit is at the perigee altitude before re-entry (Chobotov, 2002). Scenarios of atmospheric drag-induced decay on satellites in circular and elliptical orbit are depicted in Fig. 3.1. Atmospheric drag on satellites also causes premature re-entry, difficulty in maneuvering, identifying, tracking, and prediction of lifetime and actual re-entry of satellites and other space objects (as mentioned in Chapter 1). It has been estimated that thousands of space objects (under tracking/monitoring) were lost during ‘the great’ geomagnetic storm of 13-14 March 1989 (Knipp, 2014). The number of satellites lost in connection with the storm is shown in Fig. 3.2.

Atmospheric drag-induced accelerated orbit decay on low Earth orbiting satellites (LEOSs) is mainly due to solar forcing induced variations in thermospheric density profile. The density of the thermosphere and the vertical extent of the upper atmosphere varies on time scales of solar flare events (few minutes to an hour), geomagnetic storms (several hours to 1-3 days) and the solar cycle (Alfonsi, 2008; Buonsanto, 1999; Kutiev et al., 2013). The upper atmosphere is significantly heated and consequently expands during solar and geomagnetic activity, leading to an increase in density, and consequential increase in nominal LEOSs aerodynamic drag. It is known that solar EUV and thermospheric temperature could increase by a factor of two (or more), and thermospheric density by a factor of up to ten from solar minimum to solar maximum (Emmert and Picone, 2010; Walterscheid,

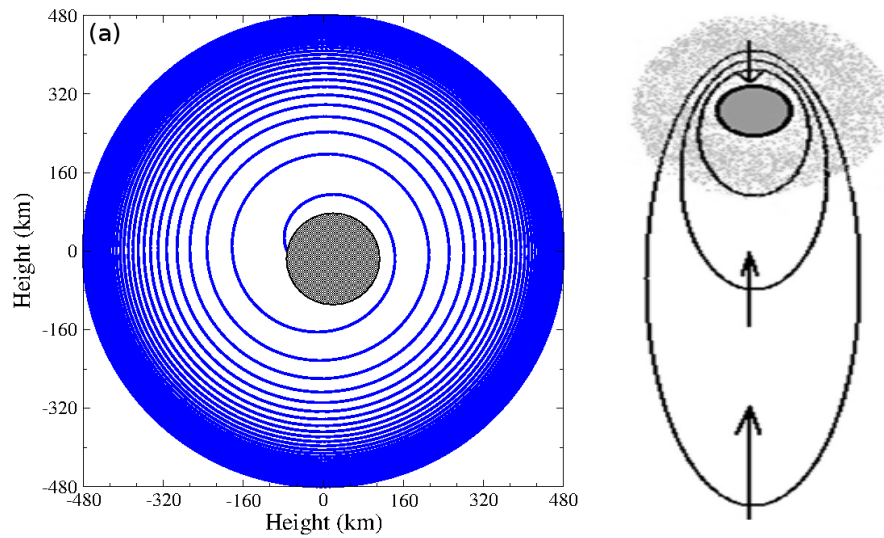


Figure 3.1: Atmospheric drag-induced decay on satellites in (left) circular and (right) elliptical orbit (right panel from Nwankwo and Chakrabarti, 2015)

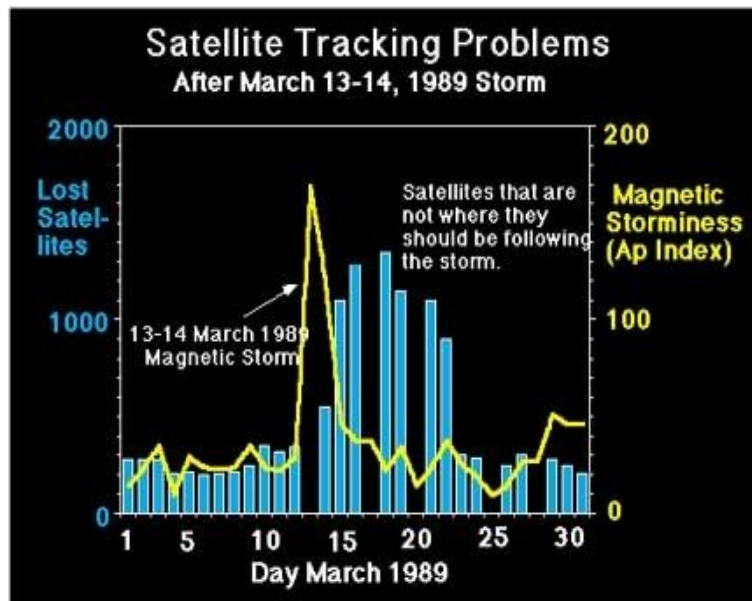


Figure 3.2: The number of satellites lost in connection with the March 13-14, 1989 storm (<http://ccar.colorado.edu/muri/>).

1989). The heating of the upper atmosphere is largely due to solar EUV radiation (but also due to geomagnetic current enhancement during interval of enhanced geomagnetic activity). However, geomagnetic field induced Joule heating becomes important and dominates the intervals of strong geomagnetic perturbations and can increase by up to 134% when the K_p index increases from 1 to 6 (also see, Rhoden et al., 2000; Kim et al., 2006; Chen et al., 2012; Kutiev et al., 2013). Several authors have studied or investigated the response of the atmosphere and/or satellites orbit to solar forcing (or activity) induced variations using one or combination of several methods such as simulations, satellite drag data, on-orbit mass spectrometers, accelerometers, sounding rockets and ground-based incoherent scatter radars (e.g., Walterscheid, 1989; Klinkrad, 1999; Sutton et al., 2005; Lei et al., 2008; Kwak et al., 2011; Xu et al., 2011; Burns et al., 2012; Chen et al., 2012; Deng et al., 2012; Liu et al., 2012; Solomon et al., 2012; Kutiev et al., 2013; Lei et al., 2013). Solar energetic events that causes space weather conditions have been reviewed in Chapter 2 (e.g., high-speed solar wind streams, CMEs, prominence eruptions, solar flares), as well as their effects on near-Earth space environment, and ground- and space-based systems (including satellite systems). CIRs (and solar wind high-speed streams (HSS)) are the dominant drivers of magnetic storms and/or atmospheric perturbations during the declining or minimum phase of the solar cycle and contributes to thermospheric density and satellite orbital variations during this phase of the cycle (Burns et al., 2012; Chen et al., 2012). Much of atmospheric perturbations and consequent drag-induced accelerated LEOs orbital decay during solar maximum are driven by CMEs-induced magnetic storms and EUV (including M and X-class flare events). Other sources of atmospheric density and orbit perturbations include thermal tides propagating upwards from the lower atmosphere (Forbes et al., 2009; Hagan and Forbes, 2002; Zhang et al., 2010a; Obeheide et al., 2009; Leonard et al., 2012). Studies that investigated the effects of space weather on satellite drag or orbit include those of Walterscheid (1989), Doornbos and Klinkrad (2006), Kim et al. (2006), Xu et al. (2011), Burns et al. (2012), Chen et al. (2012), Leonard et al. (2012), Liu et al. (2012), Solomon et al. (2012), Lei et al. (2013) and others. The insightful contributions of some of the mentioned studies to this study area have been outlined in Chapter 1. The study in this Thesis will enhance the understanding of how satellite orbits are affected during short- and long-term variations in solar and geomagnetic activities using a realistic atmospheric density and drag model.

3.1 Upper atmospheric density profile

The rate of satellites orbital decay largely depends on the atmospheric density. Therefore, an accurate prediction of a satellite's lifetime, re-entry or drag depends on

a thorough knowledge of atmospheric density profile, which is an important space environmental parameter for satellite operation in the near-Earth space (Doornbos and Klinkrad, 2006; Kwak et al., 2011; Chen et al., 2012). Most satellites are launched and operated in the upper atmosphere (the thermosphere). The thermosphere is known to exhibit large solar cycle changes in temperature, density, composition and winds due to variations in the solar cycle, especially in the amount of absorbed solar radiation, and magnetospheric and ionospheric processes. The total mass density of a mixture of gases is given by (Walterscheid, 1989),

$$\rho = \frac{P}{(R/m)T}, \quad (3-1)$$

where, ρ is the total mass density, P is the atmospheric pressure, m is the mean molecular weight and R is the universal gas constant, T is the air temperature.

and

$$m = \frac{\sum n_i m_i}{\sum n_i}, \quad (3-2)$$

where, n_i is the number density of i th constituent and m_i is the molecular weight of i th constituent. Since atmosphere is near in hydrostatic balance (see, Section 2.3.2 in Chapter 2), one obtains the well-known hydrosometric relation:

$$P = P(z_0) \exp\left(-\int_{z_0}^z \frac{dz'}{H}\right), \quad (3-3)$$

where

$$H = \frac{R^*T}{mg}, \quad (3-4)$$

The quantity z_0 is chosen to be low enough such that solar cycle variations are small. Using eqn 3-3 in eqn 3-1, we obtain,

$$\rho(z) = \frac{P(z_0)}{gH} \exp\left(-\int_{z_0}^z \frac{dz'}{H(z')}\right). \quad (3-5)$$

The density at z is thus a function of the local and integrated values of temperature and composition. An increase in H results in an increase in pressure because lesser mass is encountered in going from the reference altitude z_0 to a height z . The smaller the amount of mass encountered in going from z_0 to z , the less weight per unit area that must be reduced from the pressure at reference height z_0 in order to obtain the pressure at z . Descriptively, pressure surfaces expand upward, and therefore a particular pressure is recorded at a greater height.

Although atmospheric density profile is not precisely known at any given instant (Chobotov, 2002), many atmospheric models have been developed (and more are being developed) over the years with good approximation. The first version of upper atmospheric model was developed and released in the early 1960s (Storz et al., 2005; Kwak et al., 2011). Examples of earlier models include Jacchai-71, CIRA-72, and GOST-84, Jacchia-77, DTM-77, MSIS-77, MSIS-83, MSIS-86 and TD-88 and MSIS-90. Many of the recent models are based on modification or upgrade of previous models (e.g., Picone et al., 2002; Bruinsma et al., 2003; Bowman et al., 2006; Emmert et al., 2010; Liu et al., 2013 and others). Such modifications and/or upgrade are aimed at improving the accuracy of atmospheric density, and hence the engineering drag models. Pardini et al. (2006) studied orbital decay of 11 satellites in the 150-1500 km altitude, to check the performances of JR-71 and MSISE-90 density models. They highlighted the strength and weakness of each of the models at different heights, and concluded that none of the two models used in their study accurately produced air density at all reference altitudes, and given environmental conditions (i.e., one performed better than another at any given reference height). Picone et al. (2002) upgraded MSISE-90 thermosphere model to NRLMSISE-00 empirical thermospheric model. They achieved an improvement over MSISE-90 and Jacchia-70 by incorporating the advantages of one over the other. Bruinsma et al. (2000) upgraded DTM-94 empirical atmospheric model to DTM-2000 and reproduced total density with an average bias of 1-5% depending on the altitude and solar activity. Bowman et al. (2008) developed Jacchai-Bowman 2008 (JB2008) empirical atmospheric density model, which is actually an improved version of Jacchai-Bowman 2006 (JB2006). They pointed out a significant reduction in error associated with atmospheric density profile models when (and compared the outcome with models such as JB2006, Jacchai 1970 and NRLMSISE 2000). Storz et al. (2005) used Dynamic Calibration Atmosphere (DCA) algorithm in their High Accuracy Satellite Drag Model (HASDM) initiative, to solve for the thermospheric neutral density near real-time from observed drag effects on a set of low-perigee calibration satellites. They pointed out major innovations for improvement in determination and prediction of satellite drag. However, despite the unprecedented improvement in modeling atmospheric density, the accuracy of the models remains a concern, because the

individual effects of various solar forcing mechanism, which causes fluctuation in neutral and ionized density are very difficult to estimate or model (also, see Kutiev et al., 2013; Storz et al., 2005; Nwankwo et al. 2015 and references therein). Therefore, in order to improve on our calculations, we identify solar forcing mechanisms (such as the CIR), whose effects are usually under-represented in drag and atmospheric models, and included an implicit modification that considerably accounted for CIR-induced effect on thermospheric density in the utilised atmospheric density model, and hence the drag model (see section 3.4).

NRLMSISE-00 empirical model of the atmosphere

In this work, the densities of the atmosphere under given space weather condition are obtained from the NRLMSISE-00 empirical atmospheric model. The model is a global model of Earth's atmosphere from the ground to the exobase. The exobase is at approximately 500 km, and defined as the altitude for which the mean free path of atmospheric constituents is equal to the density scale height (Shizgal and Arkos, 1996). The region above the exobase is referred to as the exosphere. The NRLMSISE-00 atmospheric model is based on earlier models (e.g., MSIS-83,86 and 90), but updated with actual satellite drag data. MSISE-class model formulation is composed of parametric analytic approximations to physical theory for vertical structure of atmosphere as a function of time, location, solar activity (via solar flux index, $F_{10.7}$) and geomagnetic activity (via planetary geomagnetic A_p index) (Hedin, 1987; Picone, 2002). The model gives output of the altitude profiles of temperature, number densities of Helium, Oxygen (and its molecule), Nitrogen (and its molecule), Argon, and Hydrogen, in equilibrium at the temperature, total mass density, and number density of a high-altitude 'anomalous oxygen' component of total mass density that is not in thermal equilibrium at temperature $T(z)$. $F_{10.7}$, A_p and the moving average of $F_{10.7}$ over three solar rotations (81 days) were used as input in the model. $F_{10.7}$ indirectly estimates upper atmospheric heating from solar energetic particles and EUV. Planetary A_p (or K_p) index estimates the additional Joule heating associated with geomagnetic activity (Pardini et al., 2004; Kennewell, 1999; NOAA3). The moving average of $F_{10.7}$ flux over three or four solar rotations, denoted by $\bar{F}_{10.7}$ represents a slowly varying component of solar radiation (Doornbos, 2012). The model has been used to aid prediction of satellite orbital decay due to atmospheric drag. It has also been used by astronomers to calculate mass of air between telescopes and laser beams in order to the assess impact of laser guide stars on non-lasing telescopes. Some authors have utilised the model in their studies e.g. Policastri and Simons (2003), Doornbos (2012) and Klenzing et al. (2013).

3.2 Atmospheric drag force affecting LEO satellites

The general equation of motion for a satellite moving under the attraction of a point mass planet with perturbations effect (e.g., gravitational or non-gravitation forces) is given by the equation (Chobotov, 2002),

$$\frac{d^2\mathbf{r}}{dt^2} = -\frac{GM\mathbf{r}}{r^3} + a_p, \quad (3-6)$$

where, \mathbf{r} is the position vector of the satellite, G is the gravitational constant, M_e is the mass of the Earth, a_p is the resultant vector of all perturbing accelerations.

As stated earlier, atmospheric drag is the main force perturbing the motion (and orbit) of satellites in LEO (hence, $a_p \simeq a_d$). The drag force on a satellite acts in the opposition to its velocity vector and constantly removes energy from the orbit. The orbit of the satellite gradually decays due to this energy expense, leading to further drag increase. The equation of drag force (or acceleration) is given by (King-Hele, 1987; Wertz and Larson, 1999; Chobotov, 2002; Xu et al., 2011),

$$F_d = -\frac{a_d}{m_s} = -\frac{1}{2}\rho A_s C_d V_s^2, \quad (3-7)$$

where, V_s is the velocity of the satellite with respect to the atmosphere, A_s is the satellite effective (projected) area, ρ is atmospheric density, m_s is the mass of the satellite and C_d is the dimensionless drag coefficient of the satellite.

Neglecting the effect of Earth's gravitational perturbations on the satellite's orbit (King-Hele, 1987), the change in the radius of the satellite in near circular orbit per revolution is given by (Wertz and Larson, 1999; Chobotov, 2002; Xu et al., 2011).

$$\Delta r = -2\pi\left(\frac{AC_d}{m}\right)\rho r^2, \quad (3-8)$$

where, r is the initial radius of the satellite's orbit (with respect to Earth's centre).

The centripetal acceleration experienced by a satellite in a circular orbit is equal to gravitational acceleration and is given by (Xu et al., 2011)

$$F_r = -\frac{mv^2}{r} = -\frac{GMm}{r^2}, \quad (3-9)$$

Therefore, the speed of the satellite is given as:

$$v = \sqrt{\frac{GM}{r}}. \quad (3-10)$$

The period of the satellite orbit per revolution is,

$$\Delta t = \frac{2\pi r}{v} = \frac{2\pi r^{\frac{3}{2}}}{(GM)^{\frac{1}{2}}}. \quad (3-11)$$

The differential equation for the mean radius per revolution (mrpr) is given by,

$$\frac{dr}{dt}(mrpr) = -\rho \frac{C_d A}{m} \sqrt{GM r}. \quad (3-12)$$

The above equation describes the changes in the mean radius of the satellite orbit per revolution (Wertz and Larson, 1999; Chobotov, 2002; Xu et al., 2011; Chen et al., 2012). In this work, we formulated and solved a set of coupled differential equations to obtain instantaneous positions and velocities of the satellites, under the influence of varying space weather conditions (and atmospheric drag force). We used a spherical polar co-ordinate system (r, θ, ϕ) with origin at the center of the Earth, and assumed that the satellite always remains in the same plane (i.e., $\theta = \text{constant}$), while changing its position (with time) through the azimuthal parameters $(\phi, \dot{\phi})$. The orbital decay due to atmospheric drag on the satellite is computed from the following equations,

$$\dot{v}_r = -\dot{\phi} r^2 (A_s C_d / m_s), \quad (3-13)$$

$$\dot{r} = v_r, \quad (3-14)$$

$$\ddot{\phi} = -\frac{1}{2} r \rho \dot{\phi}^2 \frac{A_s C_d}{m_s}, \quad (3-15)$$

$$\dot{\phi} = v_\phi / r, \quad (3-16)$$

where, v_r and v_ϕ are the respective radial and tangential velocity components, r is the instantaneous radius of the orbit. The result of the calculation using the above set of equations are comparable to those obtained from the differential equation for changes in mean radius per revolution ($dr/dt = -\rho(A_s C_d / m_s) \sqrt{GM r}$).

3.3 Orbital and ballistic parameters of Model LEO satellites and computation of drag force components

In this work, we develop a new drag model that incorporate NRLMSISE-00 empirical atmosphere model (as a function of appropriate solar parameters) to simulate the decay profile of two hypothetical LEO satellites at different phases of the solar cycle and during intervals of strong geomagnetic disturbance or storms. We considered two satellites viz. SAT-BCI and SAT-BCII with different ballistic coefficients initially injected at an altitude of 450 km. The specific orbital and ballistic (and drag) parameters used in this study are given in Table 3.1. The ballistic coefficient (B) of a satellite is the parameter that is used to quantify the ability of the body to overcome air resistance (or atmospheric drag) in flight, and described by the equation (Chobotov, 2002),

$$B = \frac{C_d A_s}{m_s}. \quad (3-17)$$

Besides atmospheric density, the satellite's orbital parameters such as height and ballistic coefficients (A_s , C_s , m_s) are also important consideration for the determination of the extent of atmospheric drag on LEOSs. Spacecrafts with smaller values of ballistic coefficient (or, massive) experience less drag, and likely to stay longer in the orbit than those with large value (Chobotov, 2002). The B of a satellite can be affected by its orientation and may vary by a factor of up to 10 (Wertz and Larson, 1999; Trinh, 2013). The value of C_d (ratio of the drag on a body moving through air to the product of the velocity and the surface area of the body ($drag/VA$)) depends on the shape of the spacecraft, its altitude (with respect to the velocity vector) and the type of motion (e.g. spinning, tumbling or stable) (Chobotov, 2002). The C_d of 2.2 is generally used for convex satellites of compact shape whose ratio of maximum-to-minimum diameter is less than 1.5, and without large external structures like solar paddles (Cook, 1965, 1966; Moe et al., 1995), while 3.0-3.5 is used for long cylindrical satellites depending on their length-to-diameter ratio and the air temperature (Moe et al., 1995 and references therein). C_d is also important for accurate determination of atmospheric density (Moe et al., 1995). Studies have shown that assumption of C_d values (e.g., 2.2) introduces a bias into thermospheric density model, because C_d is affected by the complex interaction of reflection, molecular content, altitude etc., such that it varies with altitude (Bowman and Moe, 2005). However, such variation is typically small because the satellite materials usually remain almost constant (Vallado and Finkleman, 2008). For further reading on drag coefficient also see Moe et al. (1995), Anselmo et al. (2010), Pardini et al. (2010), Koppenwallner (2011), Mehta et al. (2013).

Table 3.1: Orbital and ballistic parameters used in this study

Name	Initial Altitude (km)	Mass (kg)	Projected area (M^2)	Drag coefficient
Sat-BCI	450	250	0.25	2.2
Sat-BCII	450	522	0.72	2.2

Atmospheric drag force on the satellites due to long-term solar and geomagnetic activity were computed for 2 solar maxima and a solar minima viz. during 2000-2002 (being typical solar peak of the 23rd solar maximum), 2004-2006 (assumed typical solar ‘quiet’ period of last solar minimum), and 2012-2014 (assumed the peak of the 24th solar maximum). We obtain an estimate of the mean annual decay rate of the satellites during the solar minimum and maximum phases. We then simulate satellites decay scenarios during intervals of strong geomagnetic disturbances and storms in three regimes (with and without control on the solar parameters), aimed at providing insight into how the drag model works.

3.4 CIR-induced periodic changes on atmospheric density profile and LEO satellites orbit

The atmospheric density variations arising from CIR-induced perturbations is known to dominate the solar minimum or declining phase of the solar cycle, and therefore significantly influence the extent of satellites orbit decay at this phase. While the model indirectly include CIR effects on the thermosphere via the geomagnetic activity index, and the varying component of solar rotation (introduced through the $F_{10.7}$, geomagnetic A_p index and $\bar{F}_{10.7}$), its associated effects may have been underestimated since the phenomena is somewhat periodic and not well represented in the model. Lindsay et al. (1994) reported the occurrences of up to two CIRs per solar rotation before solar maximum. The comparison of the solar minimum index of sunspot number, rate of CME, CIR stream interaction, and interplanetary shock rate with those of the solar maximum is presented in Figure 3.3, showing the dominance of the solar wind stream-stream interaction (CIRs) during solar minimum. To better represent this periodic CIR-induced effect, we introduce a term ρ_γ that would account for the enhanced thermospheric density during CIRs, particularly at solar minimum phase. An implicitly modified density ρ that includes ρ_γ is used to model the effect:

$$\rho = \rho_{bcir} + \rho_\gamma, \quad (3-18)$$

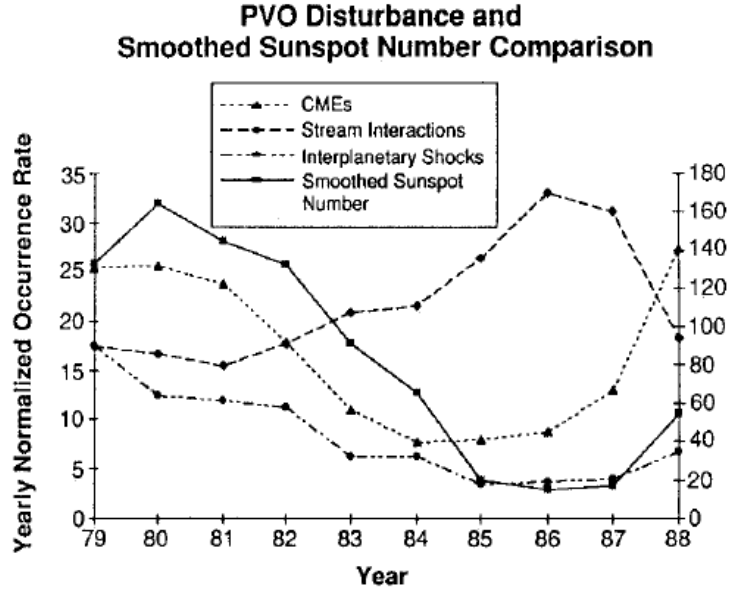


Figure 3.3: Comparison between sunspot number (smoothed), CME, CIR, and interplanetary shock rates (Lindsay et al., 1994)

where, ρ_{bcir} is the thermospheric density before the formation of CIR in solar wind, and ρ_γ is the thermospheric density increase due to CIR-induced effect (after the formation of CIR), modeled as,

$$\rho_\gamma = (\rho - \rho_{bcir})\alpha \exp\left(-\frac{(\gamma t - 1)^2}{2}\right)m$$

where, α is the amplitude of density oscillation (ρ increases by a factor of up to 2), γ is the frequency of oscillation ($2\pi/T$), T is the period of oscillation (13.5 days in this study).

3.5 Results and Discussion

3.5.1 Orbital decay at difference phases of the solar cycle

We calculate (and/or simulate) the orbital decay profile of Sat-BCI and Sat-BCII at different phases of a cycle for two maxima (2000-2002 and 2012-2014) and a minimum (2004-2006). We present the typical range of values or trend in variations

of the mean altitude, decay rate, thermosphere temperature and density for each satellite, and estimate the mean annual decay rates of the satellites in a given phase.

Solar maximum decay trend

Figure 3.4 shows the time variations of satellite's mean altitude, orbit decay rate, thermosphere temperature and density for (a) SAT-BCI and (b) SAT-BCII initially during 2000-2002. The orbital decay of SAT-BCI during 2000, 2001 and 2002 is about 46.13 km, 49.10 km and 47.38 km respectively (see, Fig. 3.4a), corresponding to a mean decay of 48 ± 2 km per year. The mean orbit decay rate is 47-327 m/day. SAT-BCII decayed by 61.14 km, 62.23 km and 61.19 km, respectively during the same period (see, Fig. 3.4b), and corresponds to a mean decay of about 62 ± 1 km per year. The orbit decay rate varied between 55 and 391 m/day. The Thermosphere temperature variations during the respective years are 1075-1416 K, 1021-1469 K and 1004-1470 K. Density variations are 2.27×10^{-12} - 7.96×10^{-12} kg/m³, 2.06×10^{-12} - 14.70×10^{-12} kg/m³ and 1.15×10^{-12} - 8.23×10^{-12} kg/m³ respectively (Nwankwo et al. 2015). The extreme values of the computed parameters occurred between July 2001 and early 2002 with up to 30 km decay in 175 days, and associated with the period of high solar activity.

Solar minimum decay trend

The time variation of the satellite's mean altitude, orbit decay rate, thermosphere temperature and density for (a) SAT-BCI and (b) SAT-BCII in 2004-2006 is shown in Figure 3.5. The decay values of SAT-BCI in 2004, 2005 and 2005 is about 13.55 km, 9.03 km and 6.15 km respectively (see, Fig. 3.5a), with an average decay of 10 ± 4 km per year. The mean orbital decay rate is 9-92 m/day. SAT-BCII decayed by 18.77 km, 12.51 km and 8.17 km the the respective years, corresponding to decay of about 13 ± 6 km per year (see, Fig. 3b). The range of variation in orbital decay rate is 10-133 m/day, and the respective variations in thermosphere temperature are 834-1212 K, 790-1129 K and 756-975 K. The ranges of density variations are 0.73×10^{-12} - 3.59×10^{-12} kg/m³, 0.50×10^{-12} - 1.83×10^{-12} kg/m³ and 0.31×10^{-12} - 1.18×10^{-12} kg/m³ respectively. In general, the mean values of computed parameters dropped consecutively in 2004-2006 as solar minimum phase approached. However, we observed a significant spike in the rate of decay, temperature and density around days 195-210, 225-238 and 314-318 following geomagnetic storm conditions. The simulation of CIR-induced effect on the satellites produced respective decays of 16.5 km, 11 km and 7.5 km for SAT-BCI and 24.3 km, 15.8 km and 10.7 km for SAT-BCII (in 2004-2006). These values corresponds to additional annual 2 – 4 km decay (with

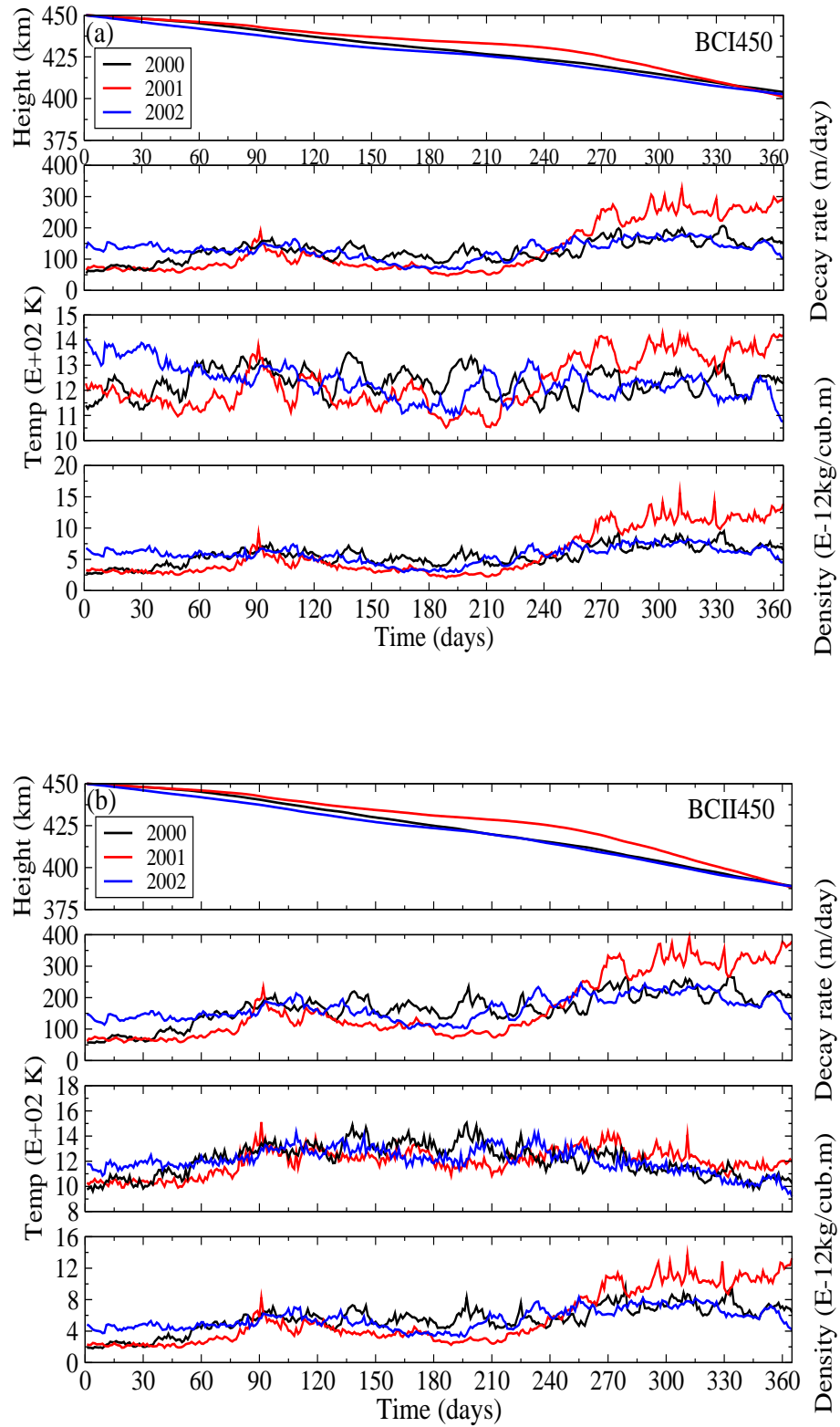


Figure 3.4: Time variations of model satellite's mean altitude, orbit decay rate, thermospheric temperature and density in 2000-2002 for (a) SAT-BCI and (b) SAT-BCII (from Nwankwo et al. 2015)

respect to the values obtained with unmodified model) due to effect from ‘assumed’ periodic occurrence of two CIRs per solar rotation during solar minimum phase.

Emerging solar maximum decay trend

Figure 3.6 shows the time variations of model satellite’s mean altitude, orbit decay rate, thermosphere temperature and density for (a) SAT-BCI and (b) SAT-BCII in 2012-2014. This work was initiated well before the end of 2014. Therefore, this computation of decay profile during this phase is based on $2\frac{1}{2}$ -year archival data (January 2000 - June 2014) and 6 months predicted solar radio flux (July-December 2014) and assumed geomagnetic A_p index ($F_{10.7}$ and A_p data (from NOAA4, NOAA5 in reference list). SAT-BCI respectively decayed by 19.88 km, 21.17 km and 32.44 km in 2012, 2013 and 2014 (see Fig. 3.6a), corresponding to a mean decay of 25 ± 7 km per year with mean orbit decay rate of 30-125 m/day. SAT-BCII (Fig. 3.6b) decayed by 24.77 km, 25.90 km and 41.65 km respectively, corresponding to decay of about 31 ± 10 km per year. The Mean orbital decay rate varied between 27 and 219 m/day. Thermosphere temperature variations during the respective year are 889-1180 K, 879-1203 K and 959-1254 K. The density variations are 1.48×10^{-12} - 3.03×10^{-12} kg/m³, 1.38×10^{-12} - 3.77×10^{-12} kg/m³ and 1.62×10^{-12} - 5.51×10^{-12} kg/m³ respectively. The observed trend in the mean values of computed parameters showed a consecutive increase from 2012 to 2014. The general consensus is that the 24th peak would occur in 2013/2014. Clearly, the annual mean decay rate of both satellites in the current solar peak is considerably less than the last peak (2000-2002).

SAT-BCI (0.001) and SAT-BCII (0.00138) has a area-to-mass ratio difference of 3.8×10^{-4} . This difference produced decay rate increase of about 13.98 km, 3.57 km and 6.24 km per year in the 3 respective solar phase regimes (for SAT-BCII). The summary of the trend in variations of computed parameters for SAT-BCI and SAT-BCII is presented in Table 3.2.

3.5.2 Orbital decay during short-term strong geomagnetic disturbances

In July 2000, data showed that solar and geomagnetic activity was very high, with up to $F_{10.7}=253$ (on 20th July) and $A_p=152$ (on 15th July). Such activity include record occurrence of a halo CME on 14 July 2000, with speed up to 1674 km/s and associated X class solar flares (X5), followed by solar energetic particle event on 15th July (SOHO; NOAA6). Fig. 3.7 shows the geomagnetic A_p and disturbance storm time (Dst) index for July 2000. The Dst is a measure of geomagnetic activity used to estimate the extent of geomagnetic storms, based on the measure of

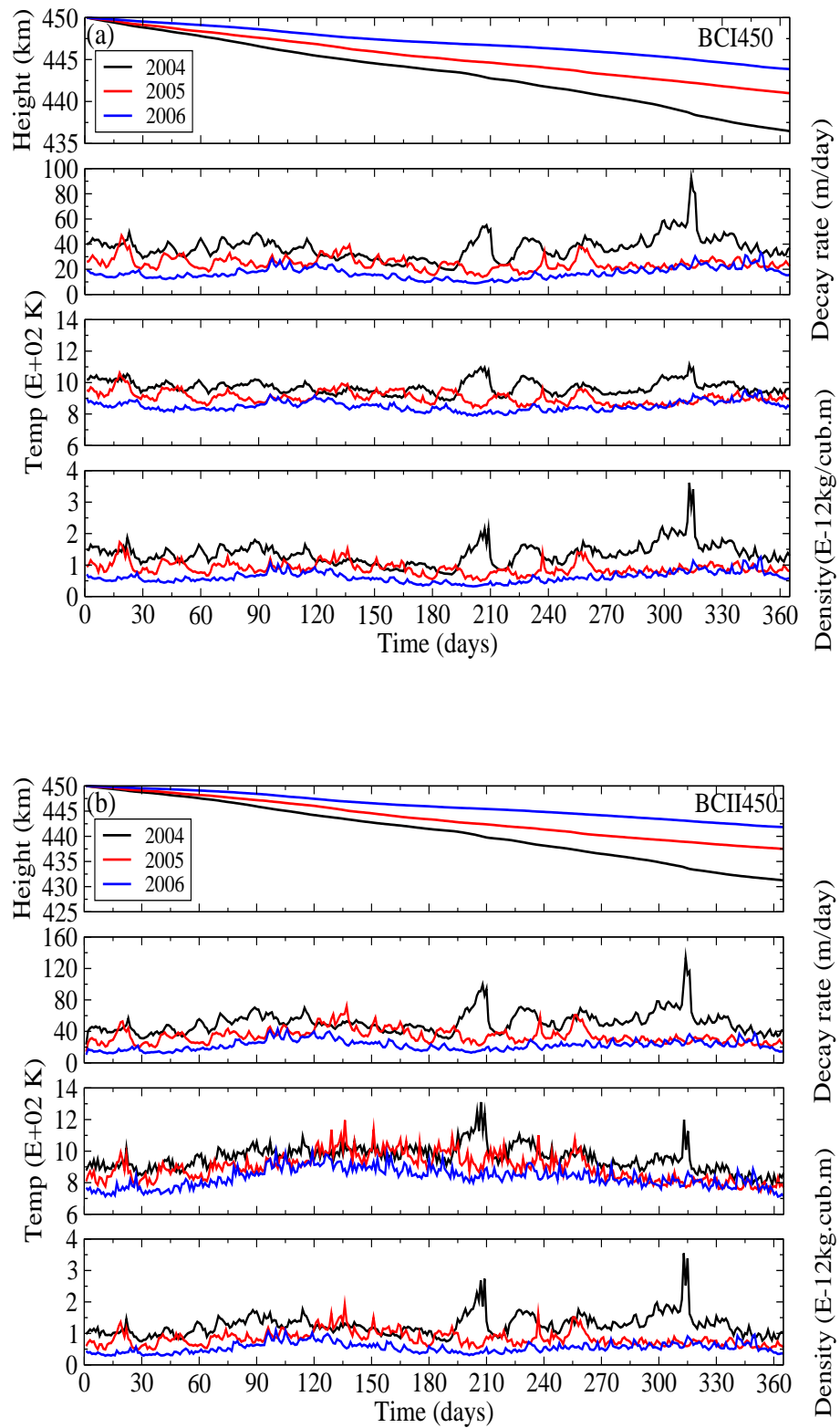


Figure 3.5: Time variations of model satellite's mean altitude, orbit decay rate, thermospheric temperature and density in 2004-2006 for (a) SAT-BCI and (b) SAT-BCII (from Nwankwo et al. 2015)

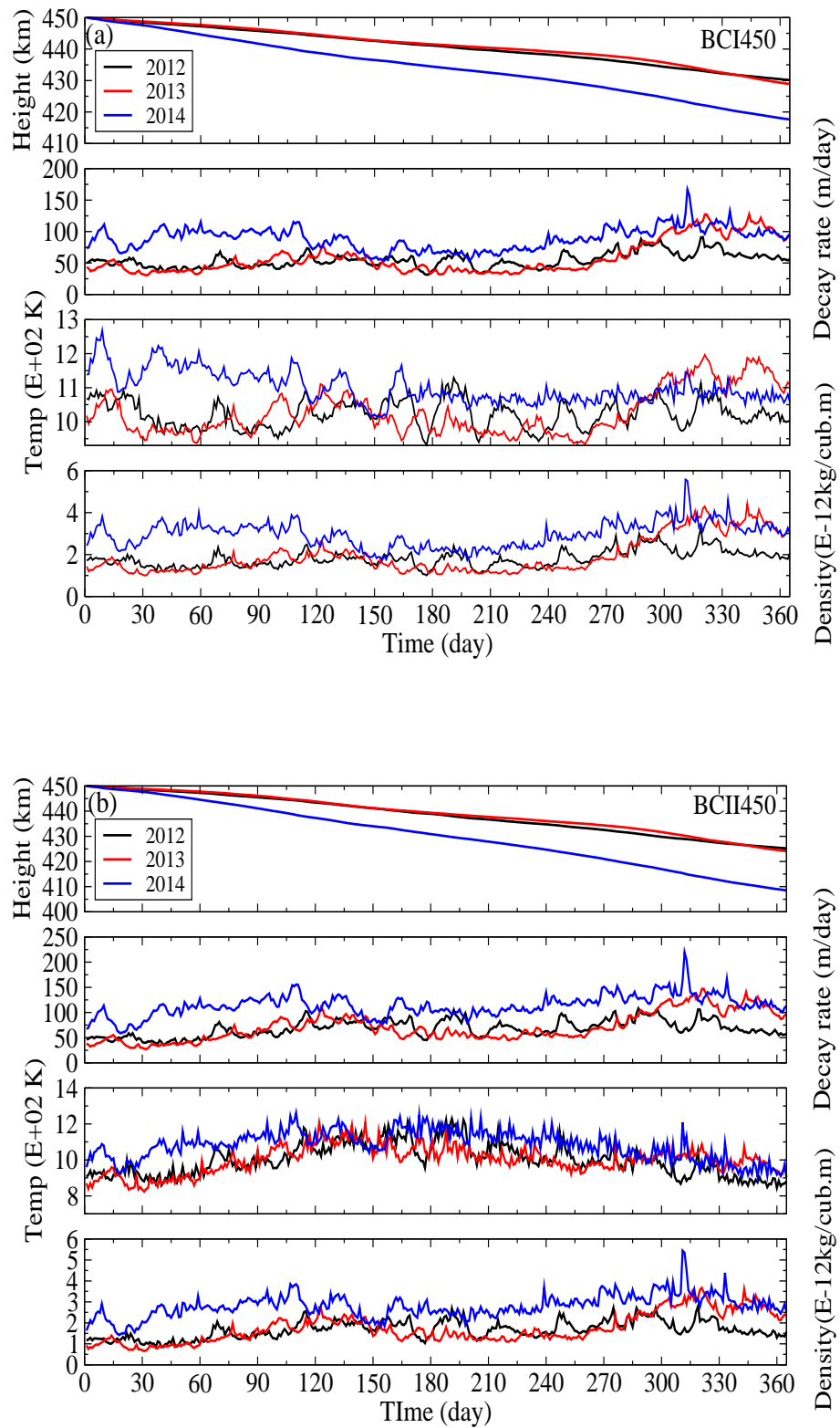


Figure 3.6: Time variations of model satellite's altitude, orbit decay rate, thermospheric temperature and density in 2012-2014 for (a) SAT-BCI and (b) SAT-BCII (from Nwankwo et al. 2015)

Table 3.2: Trends in time variation of mean altitude, orbit decay rate, thermosphere temperature and density for SAT-BCI and SAT-BCII at different phases of the solar cycle (from Nwankwo et al. 2015)

Year	Decay (km)		Decay rate (m/day)				Temperature (K)		Density($10^{-12}\text{kg}/\text{m}^3$)	
	BCI	BCII	Low BCI	Low BCII	High BCI	High BCII	Mean Low BCI/BCII	Mean High BCI/BCII	Mean Low BCI/BCII	Mean High BCI/BCII
2000	46.13	61.14	55.00	57.51	205.86	265.28	1075.12	1416.03	2.27	7.96
2001	49.10	62.23	47.25	57.89	327.10	391.31	1021.24	1469.05	2.06	14.70
2002	47.38	61.19	67.68	102.65	182.21	245.62	1004.13	1417.17	3.15	8.23
Mean	47.54	61.52								
2004	13.55	18.77	19.57	23.19	92.85	133.69	834.44	1212.36	0.73	3.59
2005	9.03	12.51	13.91	14.20	46.9	72.33	790.33	1129.29	0.50	1.83
2006	6.15	8.17	9.03	10.33	33.36	43.06	756.22	975.34	0.31	1.18
Mean	9.58	13.15								
2012	19.88	24.77	31.42	35.06	91.15	105.68	889.24	1180.41	1.48	3.03
2013	21.17	25.90	30.51	27.22	127.69	146.87	879.34	1203.29	1.38	3.77
2014	32.44	41.56	53.69	58.94	157.68	219.50	959.18	1254.10	1.62	5.51
Mean	24.50	30.74								

value of the horizontal component of the Earth's magnetic fields. It is known that the strength of the surface magnetic field at low latitudes varies inversely with the energy content of the ring current, which significantly increases during geomagnetic storms (Hamilton et al., 1988). There was clearly a strong geomagnetic storm conditions and perturbations (e.g. on 15th and 20th), associated with the solar energetic events, which suddenly increased the number of high speed solar wind particles (accelerated by CMEs and solar flares) (Doornbos, 2012), as well as increase in solar flux ($F_{10.7}$) connected with 27-day rotation of the solar active region (Woods et al., 2004; Doornbos, 2012).

Here, we study this period of strong EUV enhancement and intervals of strong geomagnetic disturbances on the upper atmosphere, and simulate their effect on thermospheric temperature, density and satellite orbit. We compute the drag scenarios in three regimes, viz. with i) actual daily $F_{10.7}$ and A_p index associated with the event ($F_{10.7}, A_p$), ii) mean $F_{10.7}$ and A_p index during the observed period ($\overline{F_{10.7}}, A_p$), and iii) keeping $F_{10.7}$ constant (mean value) while A_p (actual) varied accordingly ($\overline{F_{10.7}}, A_p$), in consistency with the intervals of the perturbation (Nwankwo et al. 2015). In Fig. 3.8(a-b) we show the time variations of model satellite's mean altitude, orbit decay rate, thermospheric temperature and density for SAT-BCI and SAT-BCII during 1st-31st July 2000.

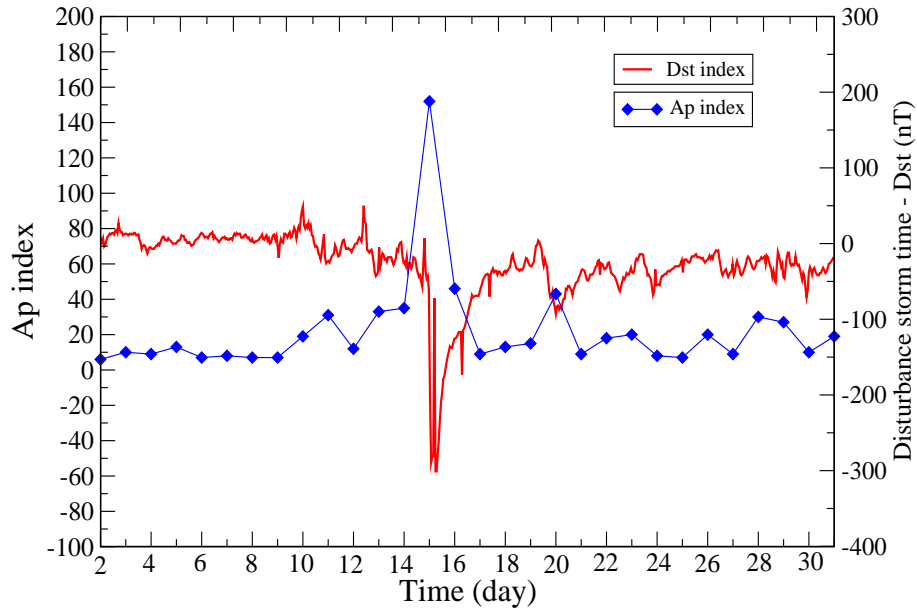


Figure 3.7: Ap and Dst index variations during 1st-31st July 2000 (from Nwankwo et al. 2015)

We found that the total decay is about 2.57 km for SAT-BCI and 3.67 km for SAT-BCII. The range of thermospheric temperature variation is 1183-1407 K, and that of density is 2.87×10^{-12} - 5.61×10^{-12} kg/m³. The orbital decay rate for SAT-BCI increased from 63 m/day (1st July) to a peak of 113 m/day on the day of the geomagnetic event (15th July). The rate of decay for SAT-BCII increased from 91 m/day to 170 m/day. With $F_{10.7}$ constant (mean value) while A_p (actual) varied (third regime (red plot)), the decay rate for SAT-BCI increased from a mean value (dotted black line) of 82 m/day to about 111 m/day, and 118 m/day to 166 m/day for SAT-BCII. This produced additional decay of 29 and 48 m/day (respectively) due to intervals of geomagnetic disturbances and/or storm-induced thermospheric density perturbations and heating (Nwankwo et al. 2015). The summary of variations in mean altitude, orbit decay rate, thermospheric temperature and density for SAT-BCI and SAT-BCII during July 2000 is shown in Table 3.3.

In this model we simulated the orbital decay scenarios of two LEO satellites having different ballistic coefficients. In particular we investigated the effect of the solar cycle (and intervals of strong geomagnetic activity) on the orbit of the satellites. The direct consequence of solar and geomagnetic events on the atmosphere, which drives such effects is mainly thermospheric perturbations and heating. We showed

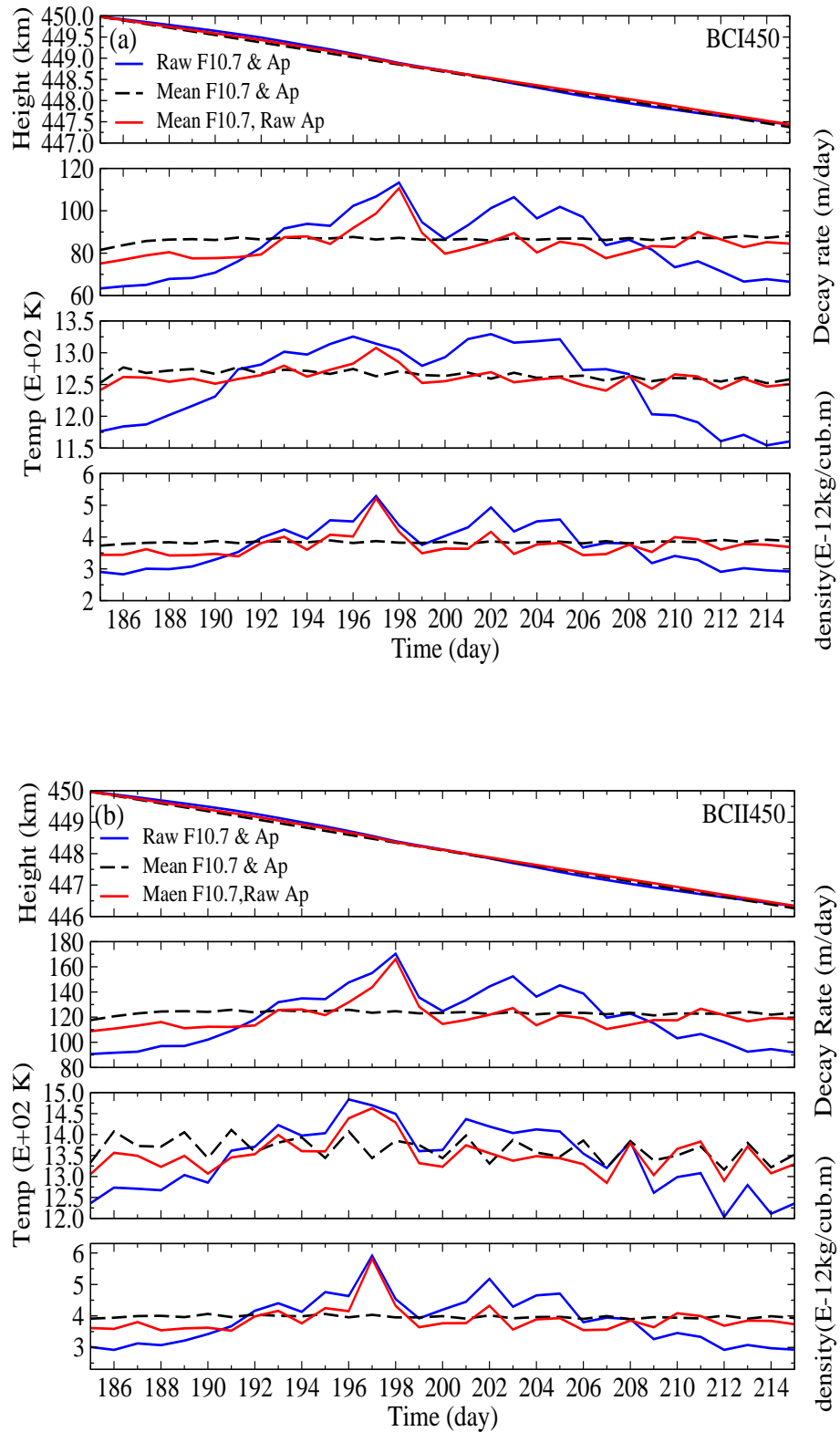


Figure 3.8: Time variations of model satellite's mean altitude, orbit decay rate, thermosphere temperature and density for SAT-BCI and SAT-BCII during 1st-31st July 2000 (from Nwankwo et al. 2015)

Table 3.3: Trends in time variation of mean altitude, orbit decay rate, thermosphere temperature and density for SAT-BCI and SAT-BCII (initially at $h=450$ km) during interval of strong geomagnetic perturbations and/or storms in July 2000 (from Nwankwo et al. 2015)

	Decay (km)		Decay rate (m/day)				Temperature (K)		Density($10^{-12}\text{kg}/\text{m}^3$)	
	BCI	BCII	Low BCI	Low BCII	High BCI	High BCII	Mean	Mean	Mean	Mean
							Low	High	Low	High
							BCI/BCII	BCI/BCII	BCI/BCII	BCI/BCII
$F_{10.7}, A_p$	2.57	3.67	63.36	90.68	113.30	170.39	1183.32	1407.20	2.87	5.61
$\overline{F_{10.7}}, \overline{A_p}$	2.63	3.74	81.53	117.64	88.25	124.77	1284.41	1344.14	3.82	3.99
$\overline{F_{10.7}}, A_p$	2.56	3.66	75.11	108.84	110.65	166.15	1265.09	1386.40	3.50	5.52

the dependence of orbital decay rate on the severity of both solar cycle and phase, and the extent of geomagnetic disturbances on the atmosphere. The mean annual decay rate around the peak of the 23rd solar maximum (2000-2002) was almost twice that of the 24th solar maximum (2012-2014). The mean annual decay rate for SAT-BCI and SAT-BCII is respectively 48 ± 2 and 62 ± 1 during 200-2002, and 25 ± 7 and 31 ± 10 during 2012-2014. However, depending on ballistic coefficient and nature of a solar cycle phase, a typical LEO satellite initially at $h=450$ km could experience a decay rate of up to 41 ± 19 km per year (~ 3 km/month) during solar maximum and 11 ± 6 km per year (~ 1 km/month) during the solar minimum. During solar minimum phase, dominant CIR-induced effects could result to additional decay rate of up to 3 km/year. We also showed that intervals of strong density perturbations, and additional heating due to geomagnetic activity and/or storms can result in an additional 60% decay in each event. This impact could vary depending on the severity and duration of the event (Nwankwo et al. 2015). In the next Chapter, we implement our new drag model on the orbits of real satellites, such as the Challenging Mini-satellite Payload (CHAMP), the Gravity field and steady state Ocean Circulation Explorer (GOCE), the International Space Station (ISS), and on an interplanetary mission spacecraft - the Mangalyaan Mars Orbiter (MMO).

Chapter 4

Implementation of Drag model on Orbits of some satellites

Since the successful launch of the first satellite into space in the 1950s (and many others that followed till date), there has been quite a number of cases of satellites' re-entry due to atmospheric drag effects including Skylab (launch 14 May 1973, re-entered 11 July 1979), Russian RORSATs, Kosmos-954 (launched 18 September 1977, re-entered 24 January 1978) and Kosmos-1402 (launched 30 August 1982, re-entered 7 February 1983), Space Station compound Salyut-7/Kosmos-1686 (launched 27 September 1985, re-entered 7 February 1991), the Chinese FSW-1-5 capsule (launched 8 October 1993, re-entered 12 March 1996) (also see Klinkrad, 1996), and the Gravity field and steady-state Ocean Circulation Explorer, GOCE (launched 17 March 2009, re-entered 11 November 2013) (Nwankwo & Chakrabarti, 2014; Nwankwo et al. 2015 and references therein). To minimise drag impact and/or increase the lifetime of a spacecraft in orbit, satellite operators perform a routine orbit maintenance (or control) in order to boost a satellite's orbit, using any of on-board propulsion, the Orbiter, an orbit-transfer vehicle or tug (Wertz and Larson, 1999). It has been estimated that LEO satellites boost their orbits (or maneuvered) about four times per year during solar minimum to maintain their orbits, but every 2-3 weeks during solar maximum (NASA2). The National Aeronautics and Space Administration (NASA) adopted a three-year on-orbit maintenance to boost the orbit of Hubble Space Telescope (HST). The orbit-boost scenarios of HST between 1993 and 2002 is shown in Fig. 4.1 (also see, Nwankwo & Chakrabarti, 2014). In this Chapter we implement our drag model on some real satellites orbit and compared the outcomes with the already utilized methods.

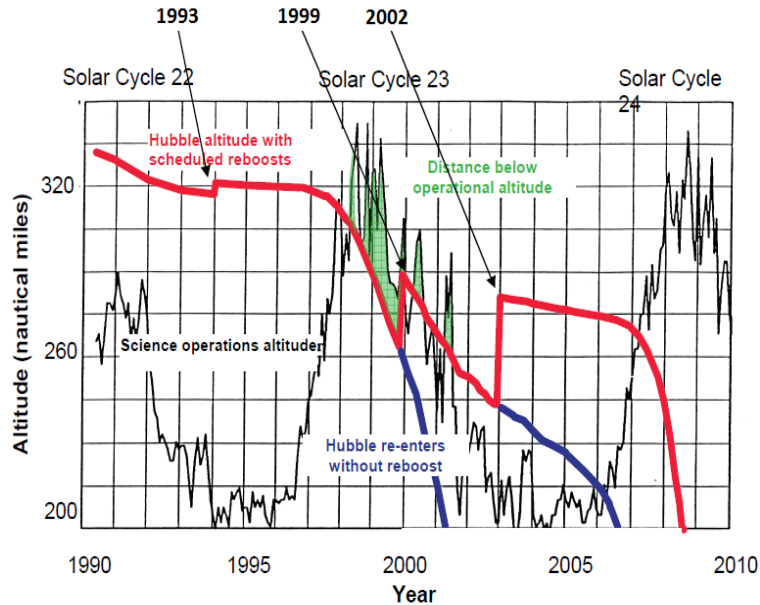


Figure 4.1: Hubble space telescope orbit-boost between 1993 and 2002 (Williams G., NASA).

4.1 Modeling orbital decay profile of CHAMP, GOCE and ISS satellites

In this Chapter, we implement (and/or apply) our new drag model on the orbits of some real satellites. In particular, we simulate the decay profile of the Challenging Mini-satellite Payload (CHAMP) during 2003-2005, the Gravity field and steady state Ocean Circulation Explorer (GOCE) during 2009-2013 and the the International Space Station (ISS) during solar maxima (2000-2002, 2012-2014) and minimum (2005-2007) regimes. We also simulate the decay profile of the Mangalyaan Mars orbiter during its geocentric, heliocentric and areocentric trajectories. We then compared the outcomes with the already utilized methods. The ballistic parameters of the satellites are provided in Table 4.1.

4.1.1 CHAMP Satellite

CHAMP is a German satellite mission managed by GeoForschungsZentrum Potsdam (GFZ). The main science objectives of the mission include i) highly precise measurement of global long-wavelength features of the static Earth gravity field and the temporal variations of this field, ii) global estimates of the main and crustal

magnetic field of the Earth and space/time variability of these field components, and iii) atmospheric and ionospheric GPS signal refraction data which can be converted into temperatures, water vapour and electron content (see Reigber et al., 2002; Hausleitner et al., 2007). CHAMP was launched on 15 July 2000 at initial injected height of about 454 km. The satellite re-entered Earth atmosphere on 19 September 2010. The artist impression of CHAMP satellite image is shown Fig 4.2a.

Xu et al. (2011) studied the effects resulting from periodic variations of thermospheric density on CHAMP (~ 450 km) and GRACE (~ 500 km) satellites orbits, and reported that the orbit of the satellites decayed by 70 km and 20 km respectively between 2003 and 2005 due to thermospheric drag. Here, we simulate CHAMP's decay profile during 2003-2005 using the satellite's orbital parameters indicated in Table 4.1 (also see Hausleitner et al., 2007; Koppenwallner, 2011). CHAMP's model decay profile during the period is shown in Fig. 4.3. The simulated decay profile produced orbital decay of about 70.98 km during 2003-2005 in orbit. However, there is about ~ 1 km difference when compared with satellite's actual decay profile for the period; the satellite decayed by about 70 km (Nwankwo et al. 2015).

Table 4.1: The orbital parameters of CHAMP, GOCE, ISS and MMO satellites: values are assumed where they are not explicitly provided.

Name	Initial Altitude (km)	Mass (kg)	Projected area (M^2)	Drag coefficient
CHAMP	450	522	0.72	2.20
GOCE	270 \pm 2	1,100	1.10	3.65
ISS	405	419,455	130	2.20

4.1.2 GOCE Satellite

The GOCE ESA's satellite was launched into near-circular orbit with mean altitude 300-250 km in March 2009. The specific mission objectives of the satellite include i) to determine gravity-field anomalies with an accuracy of 1 mGal (where $1\text{mGal} = 10^{-5} \text{ms}^{-2}$), ii) to determine the geoid with an accuracy of 1-2 cm, iii) to achieve the above at a spatial resolution better than 100 km (see, Johannessen et al., 2003; ESA1, 2013; ESA2, 2013). Its mission ended in October 2013 but re-entered the atmosphere (from an approximate height of 224 km) on 11 November 2013. GOCE satellite is shown ion Fig. 4.2b. The GOCE (initially at an altitude of 250-300 km) re-entered the the atmosphere from an approximate height of 224 km. In Fig. 4.4a we show the simulated decay profile of the satellite between launch date (17 March 2009) and just before re-entry (21 October 2013), and during the

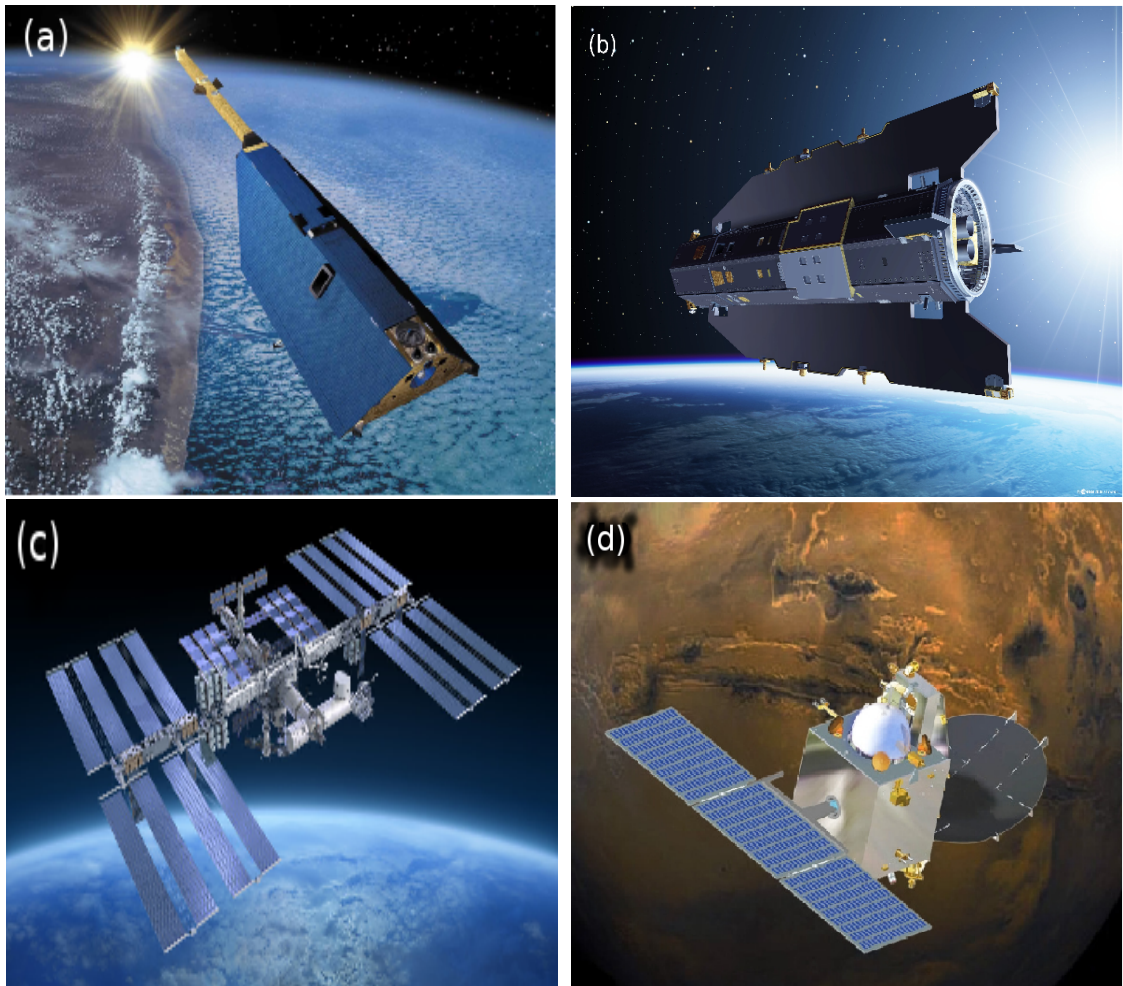


Figure 4.2: (a) Artist impression of the Challenging Mini-satellite Payload (CHAMP) satellite (Credit: Astrium GmbH) (b) the Gravity field and steady state Ocean Circulation Explorer (GOCE) satellite (ESA) (c) The International space station (ISS) satellite [NASA] (d) Artist impression of the Mangalyaan Mars Orbiter (MMO) [ISRO]

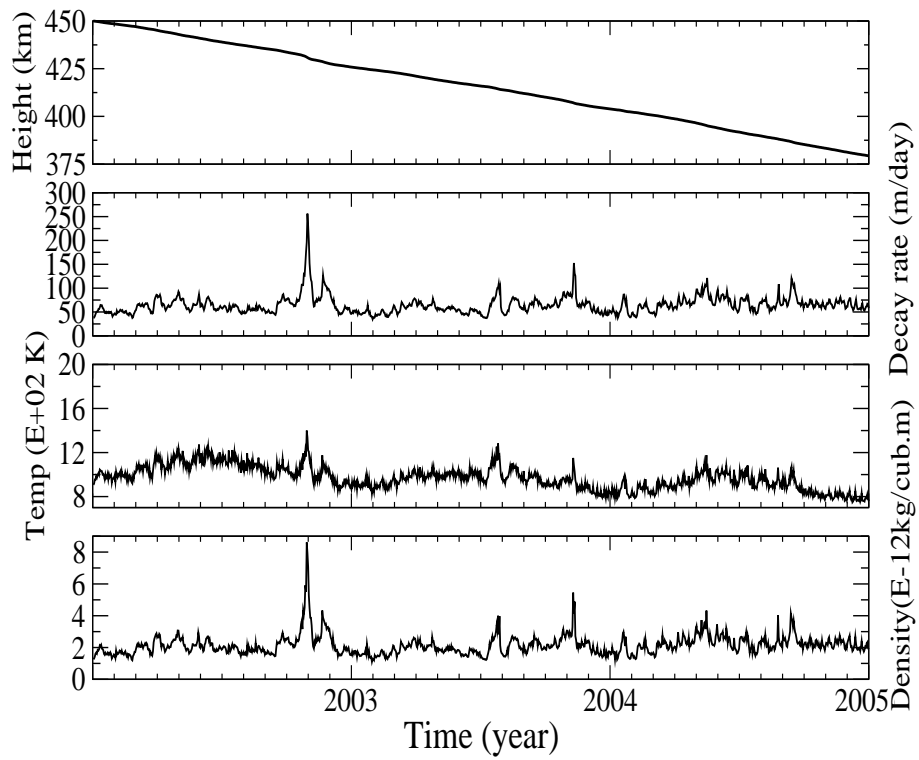


Figure 4.3: Model decay profile of CHAMP satellite during 2003-2005 (from Nwankwo et al. 2015)

re-entry phase (21st October - 11 November 2013) as a function of the actual solar and geomagnetic index.

One of the peculiar features of GOCE spacecraft is the aerodynamic design that minimises air drag and torque and eliminates mechanical disturbances, due to the need for low flight and stability. An electric ion thruster placed at behind the satellite constantly generate small forces that rectify any drag in flight. Therefore, we ‘conditioned’ minimal drag force effected of only 5% when modeling the trajectory profile. The drag force consistent with similar satellites of same ballistic coefficient in the injected height was restored (in the simulation) when the spacecraft ran out of fuel on 21st October, 2013. The simulated mean height just before GOCE re-entry on October 2013 is about 224.0487 km, and shown in Fig. 4.4a. The time variations of the satellites’ orbit decay rate, thermosphere temperature and density are also consistent with reported values (see Koppenwallner, 2011). In Fig. 4.4b we show the modeled result of the evolution of GOCE re-entry between 21st October and 11th November 2013. The simulated re-entry profile of GOCE (blue curve) is compared with the actual (approximate) re-entry evolution (red curve). The model re-entry occurred about 5 hours (10/11/2013, 20:00 CET) before the actual (reported) re-entry time (11/11/2013, 01:00 CET) (Nwankwo et al. 2015).

4.1.3 ISS Satellite

The first ISS module (Zarya) was launched in November 1998. Construction and assembly of other modules in space continued until its completion in 2011/2012. The spacecraft is pictured as an orbiting laboratory and construction site that synthesizes the scientific expertise of about 16 nations (NGS, 2013; NASA 2013). The space station is operated and maintained by five space agencies viz. the Canadian Space Agency (CSA), the European Space Agency (ESA), the Japan Space Exploration Agency (JAXA), the National Aeronautics and Space Administration (NASA) and the Russian Federal Space Agency (ROSCOSMOS). These space agencies are drawn from 16 countries - Belgium, Brazil, Canada, Denmark, France, Germany, Italy, Japan, Netherlands, Norway, Spain, Sweden, Switzerland, Russia, United Kingdom and United States (Boeing, 2012). The ISS satellite is shown in Fig 4.2c. The orbital decay profile of the ‘model ISS’ was simulated for the periods during (i) 2000-2002 (ii) 2005-2007, and (iii) 2012-2014. The main goal is to study how the orbit of a massive spacecraft could be affected by changing solar and geomagnetic activity. In determining the satellite’s exposed area A_s (in the direction of travel), we considered three sections of the ISS the pressurized section, the solar array section and other connecting sections (or arms). The spacecraft uses eight solar array wings. When fully extended, they are about 35 m by 12 m each (Stockman et al., 2009; NASA,

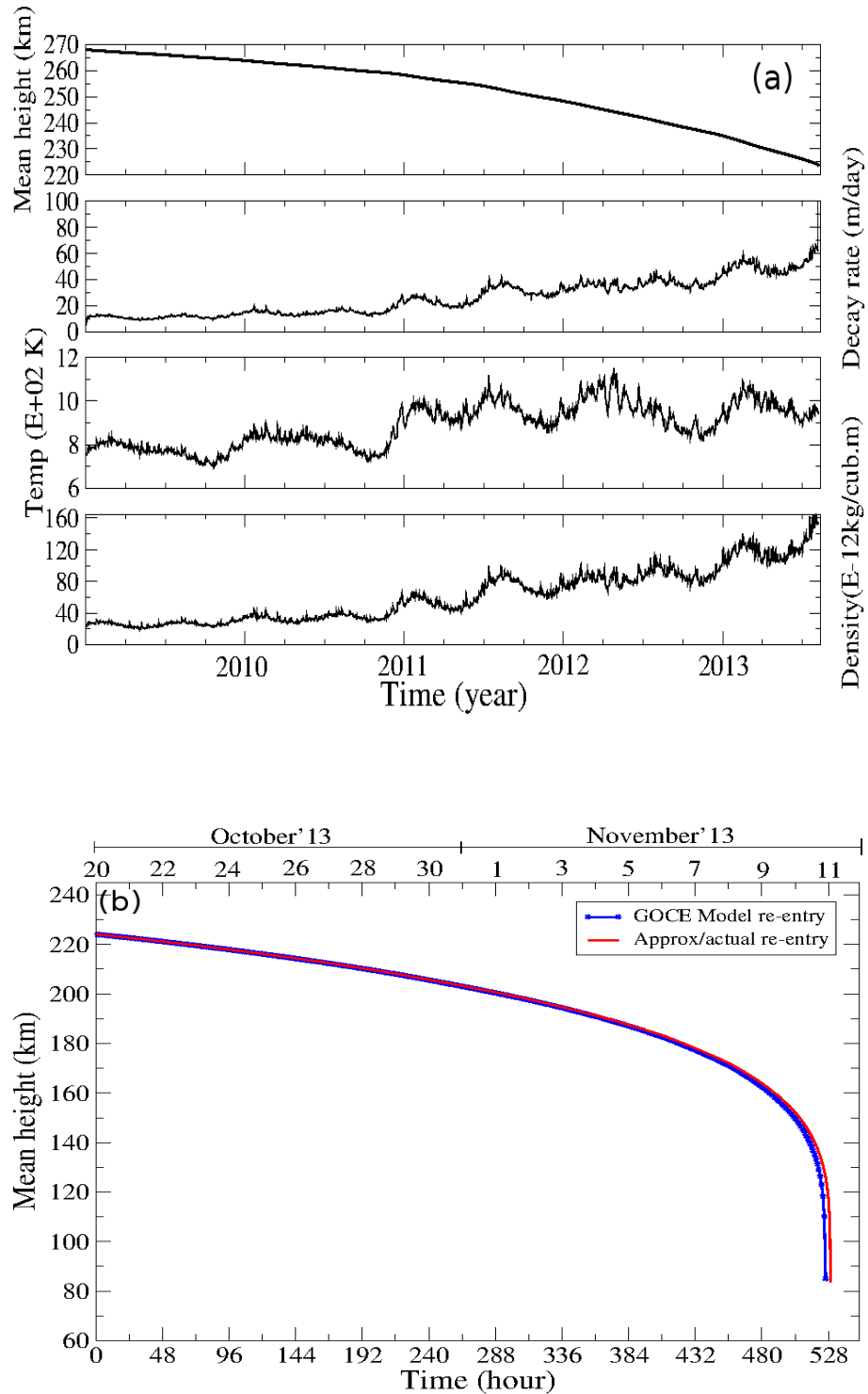


Figure 4.4: Model decay profile of (a) GOCE satellite during 2009-2013 (b) re-entry evolution of GOCE satellite during 21st October - 11 November 2013 (Nwankwo et al. 2015)

2013a). The wings are adjusted to maintain an optimum depth of battery discharge, and minimized frontal area projected to the ram direction, thereby reducing drag, and also saving propellant (Stockman et al., 2009). Therefore, we assumed a minimal effective projected area of 130 m^2 (pressurized section = 20 m^2 ; solar array section = 100 m^2 and other connecting sections, including the robotic arms = 15 m^2). The drag coefficient C_d used in this computation have been assumed. It is important to note that the mass, size or shape of the ‘real’ ISS may have varied during the time for which computations were done due to continuous assembly, upgrade and/or on-orbit maintenance. However, we ignore such variations at this stage (also see Nwankwo and Chakrabart, 2014). In Fig. 4.5a [Top] we show the time variation of the model ISS altitude, orbital decay rate, thermospheric density and temperature during 2000-2002.

The simulation produced a decay of about 39.93 km, 40.56 km and 40.06 km in 2000, 2001 and 2002, respectively. The mean decay per year is about 40 km per year. The typical time variation of orbit decay rate, atmospheric density and temperature were 50-230 m/day, 4×10^{-12} - $25 \times 10^{-12} \text{ kg/m}^3$ and 1000-1500 K respectively, with the extreme values occurring in 2001. Figure 4.5b [bottom] shows trajectory of the satellite and the space environmental condition (indicated by the thermospheric temperature and density) through which it traversed during 2005-2007. The satellite experienced orbital decay of about 17.31 km, 11.72 km and 9.23 km per year in 2005, 2006 and 2007 respectively. Mean decay during this period is about 13 ± 5 km per year. The time variation of orbit decay rate, atmospheric density and temperature were 15-90 m/day, 0.8×10^{-12} - $4.0 \times 10^{-12} \text{ kg/m}^3$ and 700-1150 K respectively (also see Nwankwo and Chakrabarti, 2014). Figure 4.6 shows time variation of the satellite’s altitude, decay rate, thermospheric density and temperature during 2012-2014.

Modeled results show annual decay of about 19.16 km, 28.12 km and 28.28 km in 2012, 2013 and 2014 respectively. The mean decay per year is about 25 ± 5 km. We assumed that this value excludes contribution from any possible major solar event during March 2013 to December 2014, since the data is predicted values. We therefore estimated that the occurrence of all major events during the time will cause the satellite an additional 5.5 km per year, bringing the mean decay per year to about 31 ± 5 km. This computation was based on more than 18 months predicted solar flux index data (March 2013-December 2014), and an assumed geomagnetic conditions of the year preceding last solar maximum. The time variation of orbit decay rate, atmospheric density and temperature were 25-150 m/day, 10×10^{-12} - $4.0 \times 10^{-12} \text{ kg/m}^3$ and 700-1150 K respectively. In summary our simulation showed that the ISS satellite decayed by up to 35 ± 6 km per year during solar maximum and 13 ± 5 km per year during solar minimum. These values correspond to respective

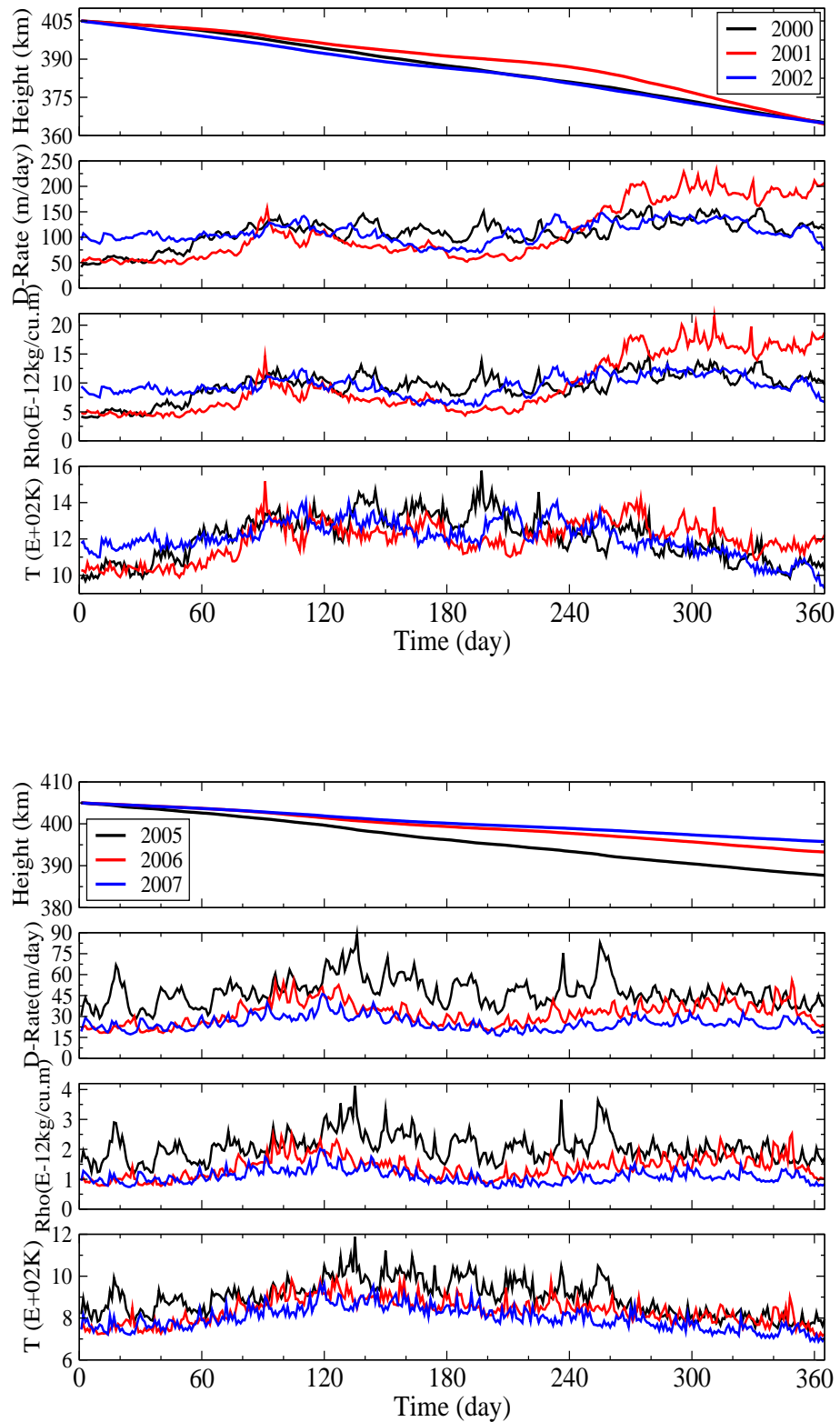


Figure 4.5: The time variation of model ISS altitude, orbit decay rate, thermospheric density and temperature during (a) 2000-2002 and (b) 2005-2007 (Nwankwo & Chakrabarti, 2014)

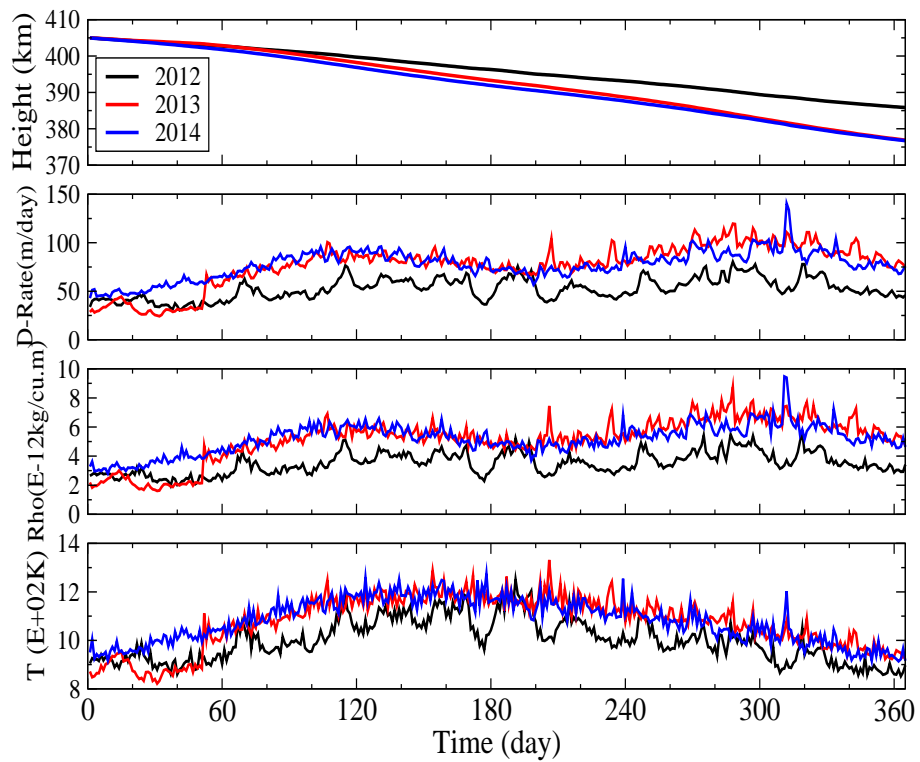


Figure 4.6: Time variation of model ISS altitude, orbit decay rate, thermospheric density and temperature during 2005 -2007 (Nwankwo & Chakrabarti, 2014)

mean decay rate of about 2.95 km/month and 1.0 km/month (also see Nwankwo and Chakrabarti, 2014).

4.2 Analysis of solar forcing-induced atmospheric drag Effect on Mangalyaan Mars Orbiter (MMO)

Interplanetary missions are also susceptible to gravitational and non-gravitational perturbing forces at every trajectory phase (if the man-made rockets and thrusters work as expected during launch). These forces are mainly related to planetary and solar-forcing perturbations during the mission's geocentric, heliocentric and Martian trajectories. There have been several attempts in the past towards the launch of interplanetary missions (IPMs) or spacecrafts, but only a few of them are successful; more than half of the attempted missions to explore the 'red planet' (Mars) were unsuccessful (Space.com, 2014). However, the failures obviously led to instructive and resourceful lessons that has translated to having more success in subsequent attempts (see Ezell and Ezell, 2009; TPS, 2013). Whereas IPMs launch attempts started in the 1960s, majority of the successful ones were launched within the last two decades. Planetary and solar-induced perturbations are among the probable reasons for the high failure rate, especially during phases of transit and arrival to their destination. High precision and accuracy in calculations are particularly crucial for success because small parametric fluctuations from perturbing forces can introduce errors that are detrimental to successful launch. In addition, under- and/or over-performance of thrusters, miscalculations in firing directions and Liquid Apogee Motor (LAM) alignments, failure of launch vehicles, communication/radio failures and type or mode of entry are all potential causes of IPMs failure (Patton et al., 2010; Fortescue et al., 2003; TPS, 2013; Space.com, 2014). The present Thesis work points to some sources of fluctuations that may arise in IPM launch and operation (mainly planetary and solar forcing-induced perturbations). The relative magnitude of solar and lunar perturbations acting on spacecrafts is shown in Fig. 4.7. A review of some planetary and solar driven perturbations on IPMs, especially for Mars missions (before and after orbit insertion) can be found in Nwankwo and Chakrabarti (2015). On 5 November 2013, the Indian Space Research Organisation (ISRO) in her first attempt launched the Mangalyaan spacecraft, an interplanetary mission to Mars. The Mangalyaan spacecraft orbited the Earth between 5 November and 1 December 2013, basically building up the required velocity (ΔV) to escape the Earth's sphere of influence (ESOI). Leaving ESOI on 1 December 2013 it traveled for about 300 days to Mars, and was successfully inserted in the orbit around Mars on 24 September 2014 (also see Nwankwo & Chakrabarti, 2015). The artist impression of the Mangalyaan Mars Orbiter (MMO) is shown in Fig. 4.2c. In this work

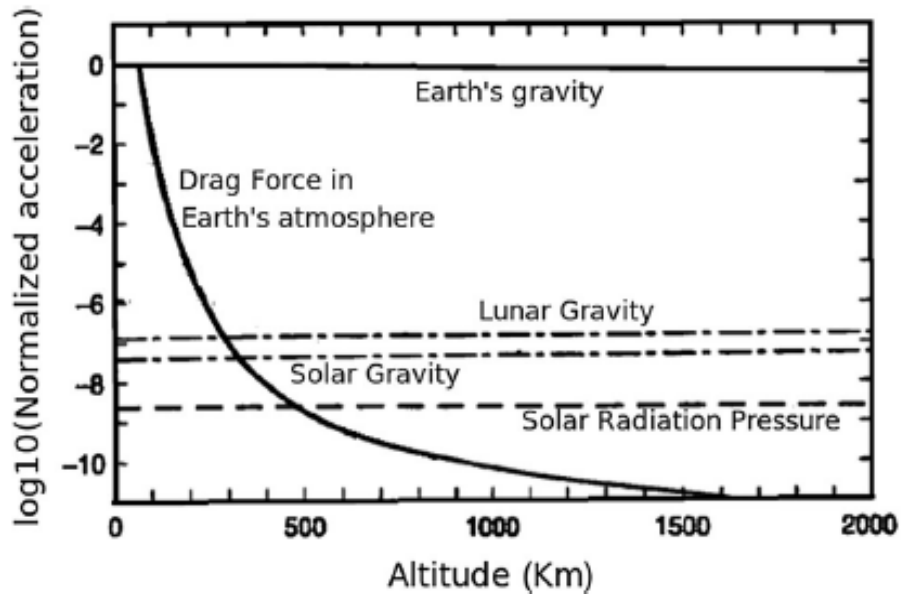


Figure 4.7: Relative magnitudes of main sources of perturbation acting on spacecrafts (Adapted from Fortescue et al., 2003)

we simulate and analyse the significance of atmospheric drag force on the spacecraft during its geocentric (in Earth's orbit), heliocentric (in the Sun's orbit) and Martian orbit or areocentric trajectory.

Whether an orbiter or a lander, the IPM spacecrafts begin their missions after successful orbit insertion and/or landing, mainly to explore a particular planet (e.g., Mars). For Mars lander missions (e.g., Curiosity Rover), entry, descent and subsequent landing are stages that must be undergone by the spacecraft, and quite challenging phases too. Braun and Manning (2006) in their study pointed out some system challenges associated with Mars exploration entry, descent, and landing, emanating from three sources: (i) an atmosphere which is thick enough to create substantial heating, but not low enough to reduce terminal descent velocity, (ii) a surface environment of complex rocks, craters, dusts and terrain patterns and (iii) the cost of replicating a Mars-relevant environment for space flight qualification of new entry, descent and landing technologies. In this case study, we are interested in the orbit-shrinking due to repeated passage of Mangalyaan around the perigee, during interplanetary phase trajectory and at the periapsis (in Mars orbit). In particular, using the equations that described variation in the mean radius of the satellite per revolution we computed the orbital decay of the Mangalyaan during the perigee passage for 28 days in Earth's orbit, 300 days heliocentric trajectory

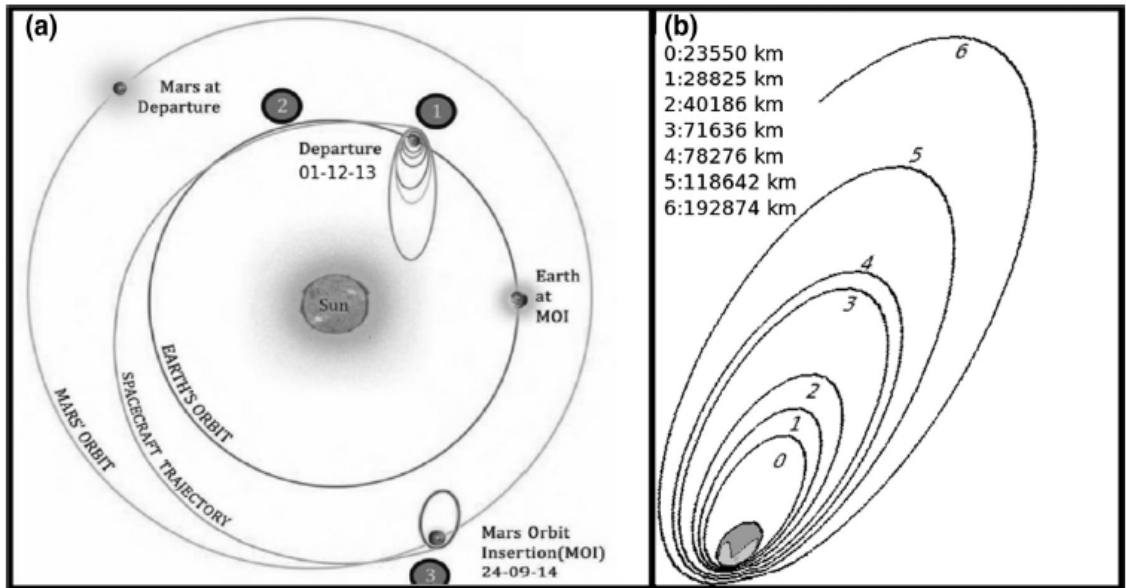


Figure 4.8: (a) Planned trans-Martian trajectory of Mangalyaan spacecraft (b) maneuvered orbits (heights) after consecutive velocity boost (from Nwankwo and Chakrabarti, 2015)

(with respect to the sun) and 100 days of periapsis passage in Martian orbit. The known effect of drag around the apogee (in Earth orbit) is somewhat insignificant in heliocentric orbit due to the large distance of the spacecraft from the sun and the Earth. In Martian orbit or atmosphere, drag effect is important but much less compared to that experienced in Earth orbit (which also depends on the type of orbit), especially on a long-term trajectory profile. The Mangalyaan would experience significant drag around the periapsis over time in its areocentric orbit (see Nwankwo & Chakrabarti, 2015).

4.2.1 The mission plan of the Mangalyaan and its trans-Martian flight profile

The Mangalyaan was delivered to an initial elliptical orbit of 248.4 km (perigee, r_p) by 23,500 km (apogee, r_a) and inclination of about 19.2° . The spacecraft requires three phases of mission-plan (MP) to reach Mars such as (i) the geocentric phase, (ii) the heliocentric phase and (iii) the Mars-centric (areocentric) phases. The Mangalyaan Mars Orbiter (MMO) will fire its liquid apogee motor (LAM) six times at a given interval when passing perigee to gradually increase the apogee of the orbit

and consequently moves through the phases up until departure and arrival in Mars. The planned trajectory of the spacecraft is shown in Fig. 4.8a. When in the geocentric phase, the MMO (with six engine burns) gradually maneuver into a ‘depart’ hyperbolic trajectory and eventually escape the Earth’s sphere of influence (ESI) with orbital velocity boost. Away from ESI, the perturbing force on the orbiter is due to the sun. Its apogee was raised to about 192,874 km from the initial 23,500 km between November 5, 2013 and November 16, 2013 after five consecutive raising maneuvers. In the computation which follows, we have assumed a corresponding perigee rises to approximately 500 km from an initial value of about 248.4 km (a total incremental height of 250 km) during velocity boost (ΔV). The maneuvered apogee heights after each velocity boost are shown in Fig. 4.8b. This work started shortly after the launch of the spacecraft with continuous update until MOI (also see Nwankwo and Chakrabarti 2015). The Mangalyaan departed Earth’s orbit and tangentially encountered Mars orbit (see, Fig. 4.8a). At the areocentric orbital phase the spacecraft reached the Mars sphere of influence (MSOI) in a hyperbolic trajectory on September 24, 2014. At the closest approach to Mars, it was captured into the planned orbit around Mars by imparting ΔV retro maneuver (ISRO, 2013). The planned orbital parameters of Mangalyaan in Martian orbit is shown in Fig. 3 of Nwankwo and Chakrabarti (2015).

Parametric requirements for trajectory analysis

We estimate the effective projected area (A_s) of the spacecraft from the satellite’s mainframe elements and/or specifications. We consider three essential parts of the spacecraft viz. the solar panels, the Yaw and Pitch deck assembly and the top and bottom deck assembly. We assumed each of the deck assemblies to be square-shaped of approximately 3.34 m². The solar panel wings of most satellites are usually designed to constantly adjust to maintain an optimum amount of battery charging and minimize frontal area projected to the ram direction. This mechanism also minimises atmospheric drag and saves propellant (Stockman et al., 2009). We, therefore assumed the projected surface area to be about 5.04 m². This value may fluctuate in flight because directional changes of the solar panel, which are usually offset with respect to the sun direction (Munir et al., 2012). The spacecraft has a mass of 1337 kg and orbiting the Earth at an initial injected elliptical orbit of radius 250 km perigee by 23,500 km (also see ISRO, 2013).

Heliocentric phase trajectory

We assumed a Hohmann-transfer heliocentric trajectory from Earth to Mars (Chobotov, 2002). In heliocentric motion, the formulation of the equations of the

changes in mean radius of the satellite (including the perigee and apogee velocity) is with respect to the sun. The required perihelion velocity v_p and apoapsis velocity v_a at transfer orbit are given by the Eqs. (2) and (3) in Nwankwo and Chakrabarti, 2015.

Earth and Martian atmospheric density profile

The atmospheric density model (NRLMSISE-00) used in this work was mainly developed for the Earth's atmosphere. Martian features are similar to those of the Earth in many ways, but their atmospheric composition and condition are not the same. For instance, the percentage composition of carbon dioxide and nitrogen in Martian atmosphere is about 93 % and 2.7% respectively, while that of Earth is less than 1% and 78%. In this analysis, without strict consideration for individual constituents of Martian atmosphere, we assume that the total mass density of Mars atmosphere is only one percent (1%) of Earth's atmosphere. Again, we assume the geometry of the ellipse orbit as shown in Fig. 4.9, for the analysis and computation of drag around and during satellite perigee passage in Earth and Martian orbits. We neglect drag effect around and during apogee passage and compute density (and drag) at an average distance R_m ,

$$R_m = (R_1^2 + R_2^2 + R_3^2)^{\frac{1}{2}}. \quad (4-1)$$

Thus, the effect of drag is assumed to be significant only during the interval of the satellite's passage from R_1 to R_3 .

4.2.2 Computational results

The maneuvered orbits of the Mangalyaan and the corresponding computed decay rate are shown in Fig. 4.10. Orbit maneuver was essentially done to boost or raise the orbit of the spacecraft while building up the velocity to escape ESOI. Thus, at respective maneuvered orbits of 248, 252, 257, 304, 348, 380, 420 and 500 km the spacecraft experienced respective orbital decay rates of about 47.34, 47.14, 51.01, 34.12, 22.67, 18.62, 12.42 and 6.87 m/day during the time/days spent in each orbit. The triangles at specified heights indicate the number of days the spacecraft stayed in corresponding orbit before velocity boost or orbit-rising. Wherever perigee height for each orbit boost/rise (maneuvered) is not explicitly provided, reasonable values were assumed. The rate at which the spacecraft decayed decreased with increased altitude (subsequent to orbit-rising). This is expected since density and drag force decrease with increase in altitude (from the earth) depending on the extent of solar

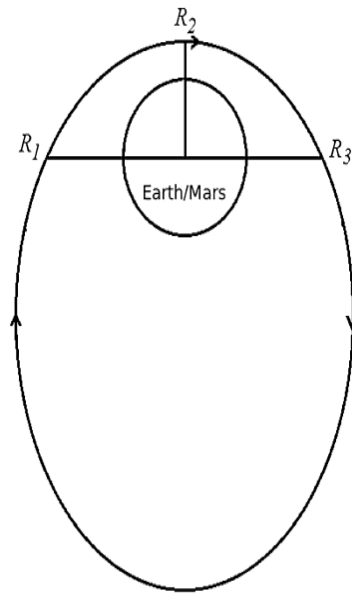


Figure 4.9: (a) Region of the orbit R_1 to R_3 where the drag effects have been considered, while the spacecraft is in Earth and Martian orbits (from Nwankwo and Chakrabarti, 2015)

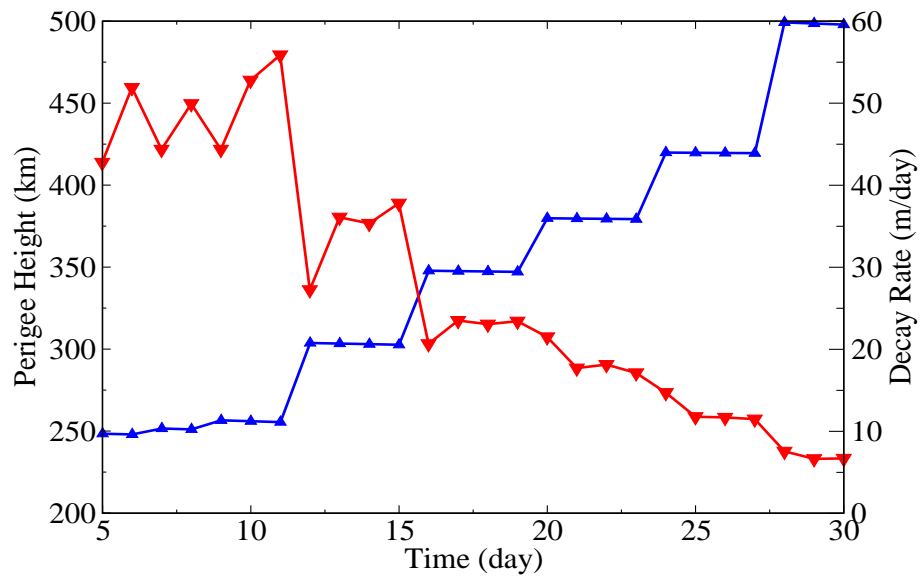


Figure 4.10: Maneuvered orbits of Mangalyaan Mars orbiter (Blue line with triangles) with corresponding decay rate (red line with stars). Triangles correspond to number of days the MOM stayed before the orbit boost (from Nwankwo and Chakrabarti, 2015)

and geomagnetic activity. Although the drag force decrease at the altitude (after orbit-rising), we have observed that severe space weather condition, especially during high geomagnetic activity, increased the drag force on the system. Orbit decay rate increased significantly on the ninth and eleventh days (after launch), due to high solar and geomagnetic activity. Upper atmospheric heating and associated density fluctuations are largely due to solar EUV. However, geomagnetic field-induced heating is important during short interval of geomagnetic disturbances and storms. We found that when perigee height increased by a total sum of about 250 km, the spacecraft decayed by a about 720 m within about 28 days in the Earth's orbit during geocentric trajectory.

Figure 4.11 shows computed mean altitude of Mangalyaan, rate of its orbit decay, thermospheric density and thermospheric temperature during the satellite's 300-day heliocentric trajectory. We assumed an elliptical orbit with mean radius (altitude) of 149, 502, 370 km during Earth-Mars (heliocentric) transfer. Typically, thermospheric temperature varied between 1050 K and 1350 K and density varied between 2.0×10^{-19} kg/m³ and 3.5×10^{-19} kg/m³. The total orbital decay is about 157.6 m. These calculated values are based on the indices of solar and geomagnetic activities in the intervening period (as inputs). Atmospheric drag and subsequent decay which may be experienced by Mangalyaan during heliocentric trajectory is small compared to geocentric trajectory scenario (up to a factor of four). Although quite nominal, but the implication of the seemingly small amount of decay is that the planned orbital parameters (such as the periapsis and apoapsis) during Mars orbit insertion may be influenced. This unforeseen change must be corrected before Mars arrival Phase. On the other hand, if the expected orbital parameters and hence the retro-velocity requirement are not critical (stringent requirement), fluctuation of this magnitude (157.6 m) may not influence the craft's orbit insertion in Mars.

The Martian atmosphere causes a drag only on a small part of the planned $365 \times 80,000$ km elliptical orbit. Since the density in Mars atmosphere is only about 1% of that of the Earth (We assume this for computational purpose also), drag effect is expected to be very minimal. However, this becomes important over a long period of time; for a very small decay of the apoapsis, the periapsis would decay by a large amount and thus, the orbit will gradually be circularized. Under such scenario the orbit decays faster and would 'theoretically' crash into Martian atmosphere. Figure 4.12 shows the (a) mean periapsis height and (b) decay rate of the Mangalyaan during 100 days trajectory. Our simulation produced a total decay of about 700.8 m with a decay rate of up to 9 m/day in areocentric orbit, based on the actual observed indices of solar and geomagnetic activity between September 24, 2014 and December 31, 2014 (after MOI), and assumed atmospheric density profile of Mars (based on Mars-Earth atmosphere and temperature ratio).

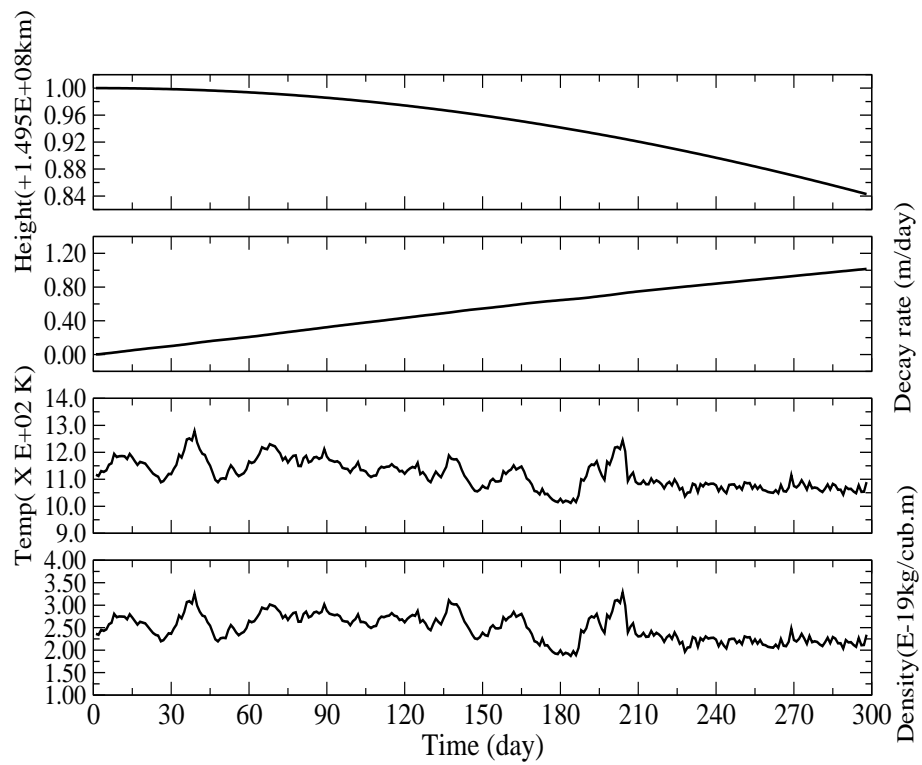


Figure 4.11: Mangalyaan (a) mean altitude, (b) orbit decay rate, (c) thermospheric temperature and (d) density during heliocentric trajectory (from Nwankwo and Chakrabarti, 2015)

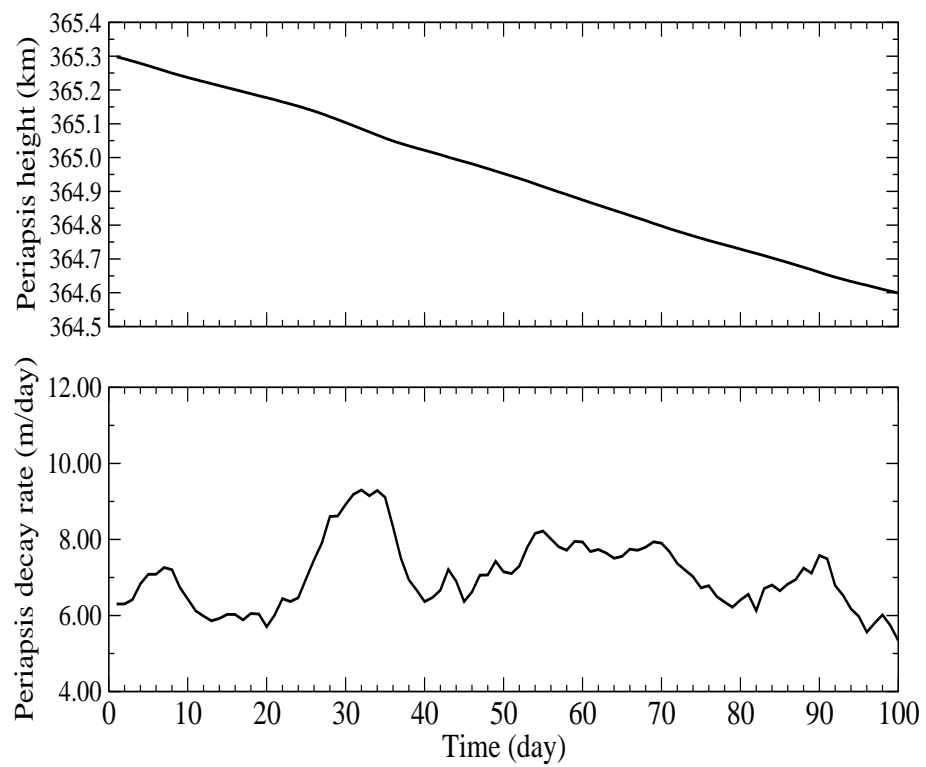


Figure 4.12: Mangalyaan (a) mean periapsis height and (b) decay rate during first 100 days of Martian trajectory (from Nwankwo and Chakrabarti, 2015)

Chapter 5

Geomagnetic storm induced magnetosphere-ionosphere dynamics using very low frequency (VLF) radio signal

Solar and geomagnetic activity and associated phenomena drive changes in magnetosphere conditions. The coupling effects of such conditions modify both thermospheric and ionospheric signatures (e.g., atmospheric density, electron content, ionospheric current system, ionisation rates, conductivity gradient and reference height of the D-region). Geomagnetic storms are the leading driver of large-scale coupled magnetosphere-ionosphere dynamics in the geospace environment. The response of the ionosphere to changes in solar and geomagnetic conditions involve the exchange of particles and electromagnetic energy, which is usually absorbed, reprocessed and deposited in the ionosphere by the magnetosphere (Burke, 2000; Streltsov and Lotko, 2004; Goldstein et al., 2006; Russell et al., 2010; Russell and Wright, 2012 Leonard et al., 2012; Kutiev et al., 2013). Magnetic reconnection is the dominant coupling process between the interplanetary magnetic field (IMF), usually embedded in solar wind, and terrestrial magnetic fields (Cowley et al. 2003). The effects of solar and other ionospheric change drivers (e.g., thermal tides, tropospheric warming etc.) at different heights, locations or latitudes of the ionosphere vary in development depending on time and intensity (Nwankwo et al. 2016). The resulting ionospheric variations also reflect different mechanisms and aspects of the the driving forces (see, detailed review of the ionosphere in Chapter 2). The parameters of most electromagnetic waves (e.g. velocity, direction and amplitude) are distinctly affected when propagating through the ionosphere. This propagation characteristic makes Radio waves one of the ideal tools for ionospheric study (Prolss, 2004). Other tools used for study or probing of solar forcing induced ionospheric variations have been mentioned in Chapter 1.

5.1 VLF propagation in the Earth-ionosphere waveguide

The amplitude and phase of very low frequency (VLF) radio waves in the 3-30 kHz are sensitive to changes in electrical conductivity of the lower ionosphere (Alfonsi et al., 2008), making it effective in probing solar induced variable conditions in the D region. The field strength of VLF radio signal can be calculated and/or predicted from the Ray theory or the waveguide mode theory. Detailed formulation of the theory can be found in Wait (1962, 1998). Some work have also been done in this regards (e.g., Chakrabarti et al., 2010 and others). For simplicity we provide a general background of radio wave propagation in ionospheric medium, because understanding the ionospheric medium is key to efficient radio propagation and communication (Hunsucker and Hargreaves, 2003). The ionospheric plasma medium through which the signal is propagated is composed of variety of atomic and molecular ions (see Section 2.3 of Chapter 2) that are interacting in a complex way by photochemical reactions. The main process can be described by the continuity and energy equations, and the equations of motion for individual charged particles, with consideration that the total number of ions is equal to the number of electrons in the plasma medium (Davies, 1990). The fundamental continuity equation for the electron is given by (Hunsucker and Hargreaves, 2003; Jakowski, 2015)

$$\frac{\partial n_e}{\partial t} = Q - L - \nabla(n_e v), \quad (5-1)$$

where, n_e is the electron density, t is the time, Q is the rate of electron production, L is the rate of electron loss, and v is the mean velocity of the electron. The composition and density of the neutral gas severely affect the production and loss term in the continuity equation, and forces of penetrating thermospheric winds and electric fields from the magnetosphere mainly determine the transport term.

The vertical electron density distribution can be described by the Chapman's theory. When a horizontal stratified layer of one-component isothermal gas is considered, which is ionised by a monochromatic beam of solar radiation at an incidence angle χ and assuming equilibrium conditions, the height dependence of the electron density is given by the Chapman's layer function (Chapman, 1931; Hunsucker and Hargreaves, 2003; Jakowski, 2015):

$$n_e = N_o \exp\left(\frac{1}{2}[1 - z - \sec(\chi)\exp(-z)]\right), \quad (5-2)$$

with

$$z = \frac{h - h_o}{H}. \quad (5-3)$$

Here, N_o is the peak density, h_o is the peak height and H is the pressure scale height of the neutral gas.

The production, loss and motion of ionospheric plasma, as well as strong coupling with the thermosphere and magnetosphere are driven by different processes, leading to a typical vertical structure of the ionospheric electron density (also, see, Section 2.3.1-2.3.2 of Chapter 2). Specific processes dominate different layers of the atmosphere (e.g. D, E, F1 and F2). For instance, the E layer is thought to be the region of the ionosphere where electric currents maximise (Jakowski, 2015). The total vertical electron density structure can be described by different Chapman layer function representing different layers (Hunsucker and Hargreaves, 2003; Jakowski, 2015). Electromagnetic waves interact with charged particle when traveling through the ionospheric plasma. The degree of such interaction is described by the refractive index of the medium, which have been derived by Appleton, Lassen and Hartree (also see Budden, 1985; Rawer, 1993). From Maxwell's equations, the refractive index n for a cold, homogeneous and collisionless plasma is given by the equation (Jakowski, 2015),

$$n^2 = 1 - \frac{f_p^2}{f^2}, \quad (5-4)$$

where the plasma frequency f_p is given by,

$$f_p^2 = \frac{n_e e^2}{4\pi^2 m_e \epsilon_o}, \quad (5-5)$$

where, e is the electron charge, m_e is the electron mass, and ϵ_o is the dielectric constant vacuum. If the frequency of a propagating radio wave is equal to the plasma frequency, the refractive index is equal to zero, implying that the wave is reflected (this is typical of VLF radio waves). In principle, the frequency of a vertically directed radio wave can be increased step-by-step such that reflection takes place at a growing heights where the wave reaches the plasma frequency. On the other hand, if the frequency of a vertically transmitted radio wave exceeds the plasma frequency, the radio wave can travel through the ionosphere (Jakowski, 2015). Radio waves propagation (and reflection) in the ionosphere is illustrated in fig 5.1.

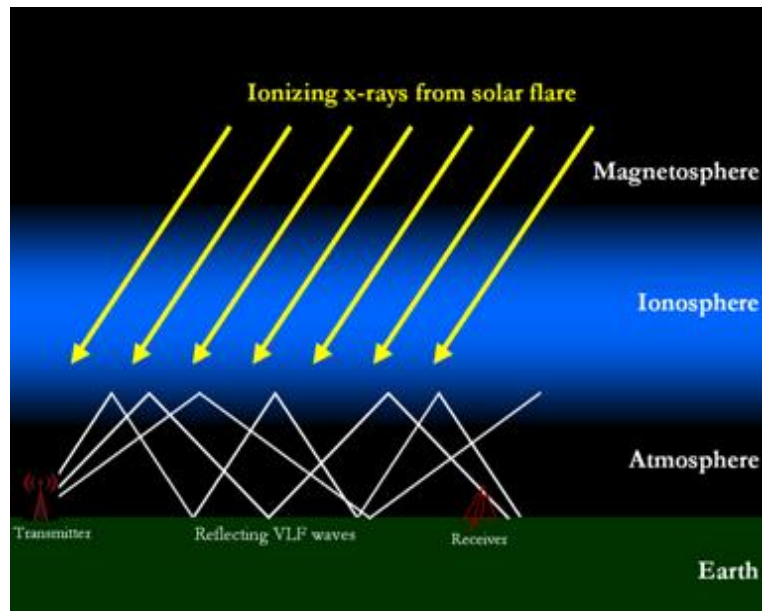


Figure 5.1: VLF radio signal propagation (and reflection) in the Earth-ionosphere waveguide (Image: Morris Cohen, Stanford University)

Since the ionosphere is constantly changing, the art of propagation prediction is usually to determine the best radio frequency for a given path for the current state of the ionosphere conditions (Hunsucker and Hargreaves, 2003). Transmitted VLF radio signals (from transmitters) are reflected alternately between the D region and the Earth's surface due to high conductivity (Mimno, 1937; Poole, 1999; Hunsucker and Hargreaves, 2003), and thus guiding and enabling the signal to propagate globally through the Earth-Ionosphere waveguide (EIWG). Such transmitted signal is then received at various receivers across the world. The propagation of VLF radio signal in the Earth-ionosphere waveguide is illustrated in fig 5.1. Typical VLF signals received at various stations are shown in figure 5.2(a-f). Variations in daytime VLF signal amplitude and phase appear to be well correlated with solar X-ray output (with almost prompt responses). Therefore, many researchers have used the tool/data to study solar-induced sudden ionospheric disturbances (SID) and other changes in the atmosphere (e.g., Araki, 1974; Hayakawa et al., 1996; Kleimenova et al., 2004; McRae and Thomson, 2004; Thomas et al., 2004; Grubor et al., 2005; Peter et al., 2006; Sasmal et al., 2009; Chakrabarti et al., 2010; Clilverd et al., 2010; Basak et al., 2011; Pal et al., 2012; Palit et al., 2013; Ray et al, 2013; Raulin et al., 2013; Nwankwo et al, 2014). Other methods used for related ionospheric studies have been mentioned in Chapter 1. Some of the methods that have been identified and often

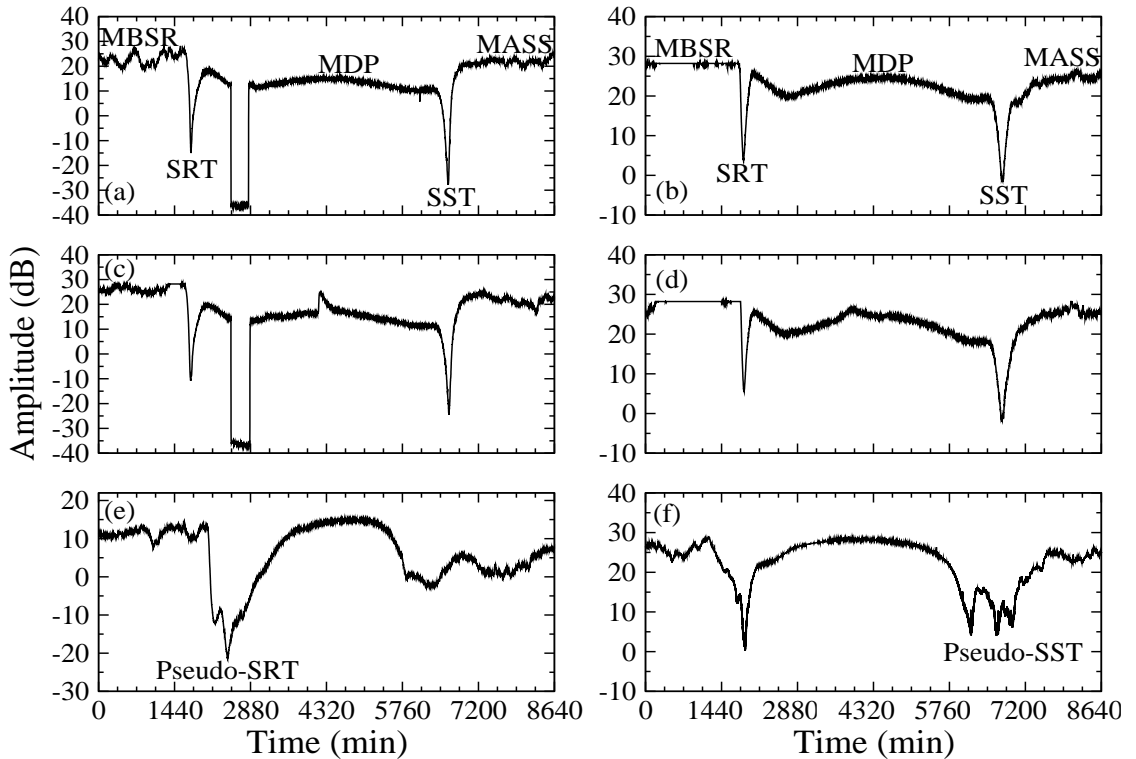


Figure 5.2: Diurnal VLF signal amplitude variations showing marked and analysed signal metrics. (a and c) DHO-A118 propagation path signal; (b and d): GQD-A118 propagation path signal and (e-f) to illustrate pseudo-terminators.

utilised in probing ionospheric variability using VLF signal include anomalous sunrise terminator (SRT) and sunset terminator (SST) time shifts, D-layer preparation time (DLPT) and D-layer disappearance time (DLDT), and anomalous nighttime and day-length signal fluctuation etc. (e.g., see above references).

5.1.1 Sudden Ionospheric Detection (SID) by VLF Radio Signal

The D region of the ionosphere (roughly 60-90 km) is maintained by the Lyman- α radiation at a wavelength of about 121.5 nm by ionisation of neutral nitric oxide (NO). Hard X-ray output ($\lambda < 1nm$) can also ionise N_2 and O_2 , especially during high solar activity. It is known that galactic cosmic rays are also involved in the ionisation of the lowest part of the lower ionosphere, including the troposphere (also, see Lastovika, 1996). Following a solar flare event, enormous amount of energy is

released in the form of energetic UV radiation (mainly X-ray flux enhancement) that can penetrate the D region and increase the ionisation rate. The electron density of the ionosphere is enhanced by the ionisation processes, leading to the enhancement of the ‘thickness’ of the D region, thereby decreasing the reflection height (h) of the EIWG (see fig 5.1). Such modification of the lower and upper boundary condition of the waveguide can lead to a change in the received signal (Wait and Spies, 1964; Mitra, 1974; Jakowski, 2015). Thus the modification is normally detected as a sudden change in the amplitude and phase of a VLF signal (see fig 5.2c-f). The dusk-to-dawn signal of VLF radio waves exhibit high variability due to significant fall in density of the D region. Also, VLF signals are generally sensitive to phenomena other than those originating from the Sun, but the daytime signal is primarily controlled by the Sun (Nwankwo et al. 2016).

5.1.2 Geomagnetic storms induced variations of the ionosphere and effects

Geomagnetic disturbances and storms produces significant global disturbances in the ionosphere. The effect of geomagnetic storms can also extend (coupled) to the middle atmosphere and the troposphere (Lastovika, 1996; Danilov and Lastovika 2001). In the ionosphere, the effects of geomagnetic storms mainly manifest through Joule heating, and energetic particles precipitation (especially below the dynamo region, ~ 95 -100 km). The particles lose their energy by impact and X-ray production by bremsstrahlung (Lastovika, 1996), causing significant enhancement of electron density (Chenette et al., 1993; Stoker 1993; Lastovika, 1996), modulation of galactic cosmic ray flux, global electric circuit and atmospheric electricity (that are influenced by local changes in conductivity and ionosphere/magnetosphere electric fields and currents) (Danilov and Lastovika, 2001). These scenarios cause significant increase in radio wave absorption and subsequent disappearance of radio signals in MF/HF values (Lastovika, 1996). It is known that VLF radio signals are significantly affected by geomagnetic disturbances (or storms) through dynamic coupling processes of the magnetosphere and ionosphere (also see, Kikuchi and Evans, 1983). While the daytime VLF signal amplitude and phase are well correlated with X-ray flux induced sudden ionospheric disturbances (e.g. during solar flares and gamma ray bursts) and well studied, geomagnetic storm-induced disturbances are often not immediately detectable. Nevertheless, a few researchers have used it to study such effects with insightful findings. Monitoring the trends in variation of VLF diurnal signal is proving to be useful in studying (and understanding) of space weather effects in the lower ionosphere (e.g. Araki, 1974; Kikuchi and Evans, 1983; Kleimenov et al., 2004; Peter et al., 2006; Clilverd et al., 2010; Kumar and Kumar, 2014; Tatsuta et al.,

2015, Nwankwo et al., 2016), as well as ionospheric changes from other atmospheric and lithospheric sources. The response of VLF signal to geomagnetically induced ionospheric disturbances, however, depends on the propagation characteristics of signal propagation path. The insightful findings and/or contribution of some of the investigations to this area of study have been discussed in Chapter 1, including those of Kikuchi and Evans (1983), Peter et al. (2006), Chakrabarti et al. (2010), Kumar and Kumar (2014) and Tatsuta et al. (2015).

In addition to the well correlated VLF signal amplitude variation and phase enhancement consistent with X-ray flux induced sudden ionospheric disturbances (SID), the present Thesis work seeks to understand how the effects of geomagnetic activity/storms are communicated to D region of the ionosphere (particularly in Mid-latitude) through monitoring of trends in variation or behaviour of VLF signal amplitude. In the first part of the present work, we characterize the dawn, day and dusk signal amplitude of VLF radio into reasonable metrics and analyse their trends in variation during 16 geomagnetic storms condition (also see, Nwankwo et al. 2016). In the second part, we will build on the analysis of the first part to perform a more detailed analysis in order to substantiate and/or further investigate the findings (of the previous work) using 20 storm cases (also see Nwankwo and Chakrabarti, 2016). Whereas this work is similar in some aspects to the work of the above mentioned authors, it also included several cases of storms with the goal of bringing in statistical significance in the study. Such approach, as well as the characterisation of the signal amplitude into metrics (for efficient and accomplished analysis) were not considered in previous work. This goal-oriented analysis led to an insightful finding that opened a new front for further investigation. We then made an attempt to further investigate such findings in the second aspect of the study (Nwankwo and Chakrabarti, 2016), while building on the analysis in the first path (Nwankwo et al. 2016).

5.2 Data and Analysis

In this work we analysed the amplitude metrics of diurnal VLF radio signal from 3 propagation paths, monitored at A118 SID receiving station in Southern France (<http://sidstation.loudet.org/data-en.xhtml>), in conjunction with solar and geomagnetic data including GOES solar X-ray flux, average z-components (B_z) and total magnetic field (H_T) (<http://satdat.ngdc.noaa.gov/sem/goes/data/>), geomagnetic A_p (from NOAA/SWPC database) and disturbance storm time (Dst) index (from World Data Centre for Geomagnetism (WDCG)), solar wind speed (V_{sw}) and particle density (PD) (<ftp://sohftp.nascom.nasa.gov/sdb/goes/ace/>). In figure 5.3, we show the 3 propagation paths, which include GQD-A118, ICV-A118, and



Figure 5.3: VLF signal propagation paths (PP) used in the study: the three transmitters are DHO, GQD and ICV, and the A118 receiver (adapted from A118 SID station Web page)

DHO-A118; GQD (22.1 kHz GQD, lat N54.73° long W002.88°), ICV (20.27 kHz, lat N40.92° long E009.73°), DHO (23.4 kHz, lat N53.08° long W007.61°).

The variable solar wind is studied because its velocity, density, strength and direction, the and strength and direction of its embedded interplanetary magnetic field modulate the structure of the surrounding magnetic field of the Earth and controls the processes of mass, momentum and energy transfer from the solar wind to the Earth's magnetosphere-ionosphere system (Lastovika, 1989; Singer et al., 1996). The component of the B_z indicates and contribute to energy transfer from the solar wind sector to the magnetosphere (Prolss, 2004). The H_T parameter can be used to deduce the solar wind influence on the magnetosphere because substorms enhances and intensify current systems in the magnetosphere-ionosphere system, which can also be detected via H_T component. The A_p (or, K_p) planetary indices is used as an indicator of geomagnetic activity (indirectly). The disturbance storm time index (Dst) is used as a measure of the severity of magnetic storms. The

energy content of the ring current increases during geomagnetic storms, and varies in inverse proportion with the strength of the surface magnetic field (Hamilton et al., 1988). The study of the solar wind, and solar and geomagnetic parameters are important to understanding the dynamic coupling between the magnetosphere and ionosphere, and associated effects. However, this present work is mainly focused on the behaviour of diurnal VLF signal in relation to changes in the ionosphere due to geomagnetic storms or perturbations.

First, we analyse 4 six-day periods of varying geomagnetic disturbances or storms viz. during 14th-19th February 2011 (recognised as moderately disturbed), 26th-31st May 2011 (recognised as a moderate storm), and 24th-29th September and 23rd-28th October 2011 (recognised as relatively intense storm conditions). We then analyse 2- to 4-hour mean VLF signal amplitude before sunrise and after sunset (hereafter respectively denoted as MBSR and MASS), and mid-day signal amplitude peak (MDP). We also identified typical values of the signal at sunrise and sunset, recognised as sunrise and sunset terminators (hereafter, denoted as SRT and SST). The diurnal VLF radio signal of some propagation paths indicating aspects of the characterised signal metrics (i.e., MBSR, MDP, MASS, SRT and SST) are shown in Fig. 5.2 (a-f); fig 5.2 (a and c) are for DHO-A118 propagation path, fig 5.2(b and d) for GQD-A118 propagation path. Figure 5.2(e and f) are shown for the purpose of illustration of complex nature of the terminators and descriptions of these will be made below.

5.3 Diagnostic study of geomagnetic storm-induced ionospheric changes in mid-latitude D-region

We analyse the characterised signal metrics (amplitude) of VLF radio signals in conjunction with geomagnetic indices, to describe magnetosphere-ionosphere coupling in mid-latitude D region. The analysis include daily solar flare count (for flares $\geq C$) to highlight the extent of flare activity and X-ray flux output during each period. We also calculated the standard deviation of daily Dst as a measure of the extent of and/or fluctuations in geomagnetic activity. The main goal of the analysis is to investigate the trend in variations of these signal metric under varying solar and geomagnetic induced space environmental conditions, for identification of the footprints of geomagnetic storms in D-region. Data were analysed for two signal propagation paths (PP) in each case. To start with, we perform a detailed study of four particular cases, and then investigate the statistical significance of our results with more cases.

5.4 Results and Discussion

5.4.1 Analysis of VLF signal amplitude behaviour during geomagnetic storms in mid-latitude D-region

In Figure 5.4(a-h) we show the diurnal VLF amplitude for GQD-A118 and ICV-A118 propagation paths, X-ray flux output, solar wind speed (V_{sw}), particle density (PD), B_z magnetic field component, H_T magnetic field, daily Dst standard deviation and A_p variation during 14th-19th February 2011. Up to 79 flares (C=69, M=9, X=1) and $Dst > -50$ were recorded during the period (also see, Table 5.1). We observe high flare events on 14th, 16th and 18th (see, Fig. 5.4c) and significant geomagnetic activity on the 14th and 18th February (see, Fig. 5.4e-g), as well as high variability of V_{sw} (from 06:00 pm, 14th - 12:00 noon, 15th and during most part of 18th February). This condition is associated significant magnetospheric impact (via B_z , H_T and A_p) (see, Fig. 5.4d-f). The prevailing Dst highlight the extent and/or severity of induced magnetospheric perturbations during late 14th and part of 18th (see, Fig. 5.4g). The signal (amplitude) of the two propagation paths appear to respond in a manner consistent with high flare events during the period. Because flare-induced influence (or, spikes) on daytime signal are distinct and appear to overshadow those of geomagnetic activity origin, we study the trend in the signal metrics variation (e.g. MBSR, MDP, MASS, SST and SRT) for distinct signal behaviour related to storm-induced variations (Nwankwo et al. 2016).

In Figure 5.5 we show the daily Dst standard deviation, 4-hour mean signal amplitude before local sunrise (MBSR), mid-day signal peak (MDP), 4-hour mean signal amplitude after sunset (MASS), variation in sunrise terminator (SRT) and in sunset terminator (SST) for (a) GQD-A118 and (b) ICV-A118 propagation paths during 14-19th February 2011. A summary of relative trend in variations of the parameters over the period is provided in Table 5.1. The reference disturbances are those of 14th (day 1) and the 18th (day 5), presumed to be caused by the increase in V_{sw} and PD (see, Fig. 5.4d). For proper analysis we consider the trend of pre-event day signal changes in order to determine that of the event(s) day, and also consider the post-event(s) day for extended effect, because of the varying timescale of ionospheric response to different aspects of solar forcing and mechanisms. We note the increase in MBSR and SRT, but ‘dipping’ of MDP, MASS and SST on 15th (day 2) (see, Fig. 5.5a). The influence of the induced perturbations is therefore expected to extend into a considerable part of 15th (day 2) because of the onset of the perturbations on the 14th (day 1). We observe that almost all the signal metrics increased on the 16th (day 3), with geomagnetic condition being relatively ‘quiet’ on the day. On the other hand, there was a significant and extended geomagnetic

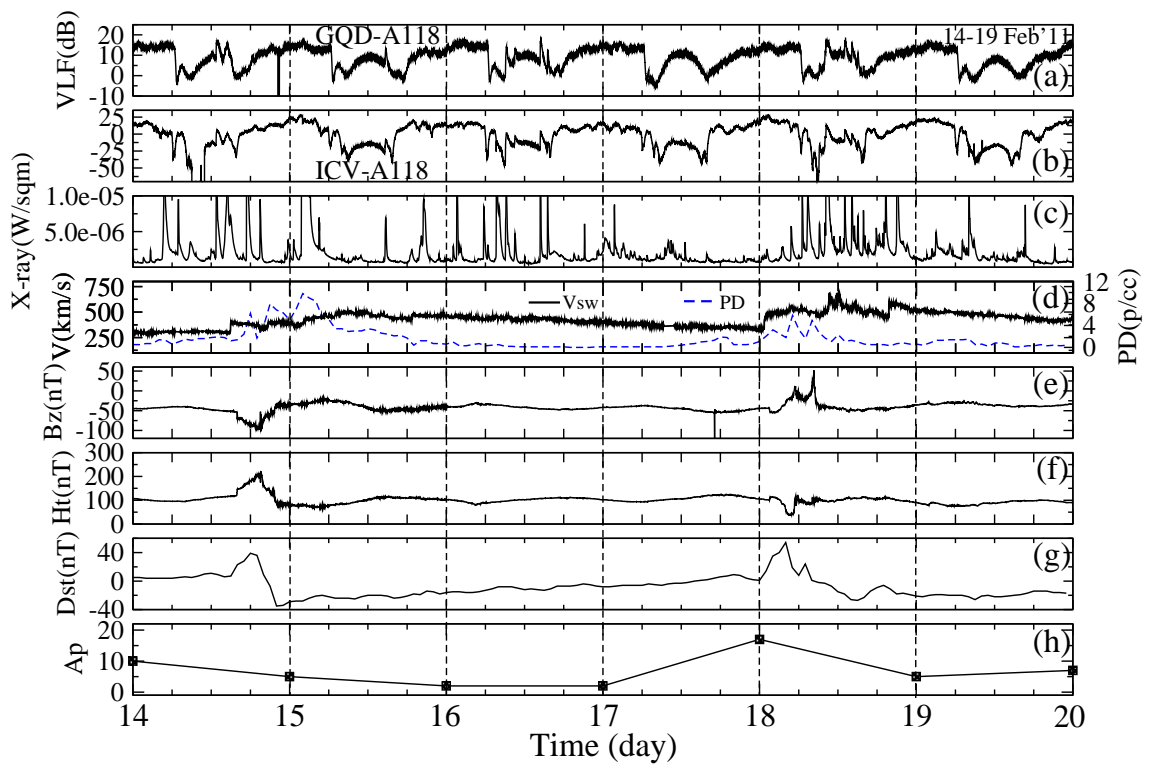


Figure 5.4: (a) Diurnal VLF amplitude for GQD-A118 PP; (b) VLF amplitude for ICV-A118 PP; (c) X-ray flux output; (d) solar wind speed (V_{sw}) and particle density (PD); (d) B_z magnetic field component; (e) H_T magnetic field; (f) Dst and (g) A_p variations during 14-19th February 2011 (from Nwankwo et al. 2016).

disturbed condition on 18th (day 5). On this day only the SST increased (during which a decline in the initial induced perturbation was expected), while all other metrics (MBSR, MDP, MASS and SRT) ‘dipped’ in GQD-A118 propagation path (Fig. 5.5a). This trend is replicated in ICV-A118 propagation path around 15th (day 2) but quite inconsistent on 18th (see, Fig 5.5b). However, the increase in MDP on 18th (in ICV-A118 signal) appear to be related to flare-induced signal amplitude variation on the signal as well as high fluctuation of signal amplitude in the propagation path (see, Fig 5.4b).

Table 5.1: Trend of time variation of VLF amplitude, Dst and flare count during 15-18th February 2011 for GQD-A118 and ICV-A118 propagation path (from Nwankwo et al. 2016).

GQD-A118 propagation path								
Date	Mean Signal peak (dB)			Signal dip (dB)		Dst (nT)	Flare count	
	MBSR	MDP	MASS	SRT	SST	σ_{Dst}	$\geq C$	C M X
14/2/11	14.08±0.78	9.77	12.57±2.18	-4.13	1.96	±16.19	12	11 1 0
15/2/11	14.20±1.15	8.80	11.22±0.72	-2.85	-2.13	±3.67	8	7 0 1
16/2/11	14.85±1.07	9.55	12.93±0.95	-2.69	0.47	±3.71	15	12 3 0
17/2/11	13.89±1.14	10.10	11.40±0.82	-2.83	-2.26	±5.27	12	12 0 0
18/2/11	13.21±0.90	9.64	11.25±1.09	-3.27	0.28	±21.29	20	15 5 0
19/2/11	13.99±1.10	8.14	11.81±2.23	-2.10	0.22	±2.90	12	12 0 0
ICV-A118 propagation path								
14/2/11	12.95±3.82	-12.89	13.46±3.40	-38.82	-33.99	±16.19	12	11 1 0
15/2/11	21.11±3.11	-16.05	12.05±4.17	-17.30	-40.80	±3.67	8	7 0 1
16/2/11	13.60±2.38	-14.56	10.56±3.49	-34.52	-32.80	±3.71	15	12 3 0
17/2/11	9.83±3.81	-14.04	10.24±2.57	-24.08	-40.50	±5.27	12	12 0 0
18/2/11	20.56±3.24	-13.11	11.39±3.95	-27.65	-41.75	±21.29	20	15 5 0
19/2/11	19.81±1.25	-16.28	14.26±3.88	-30.42	-35.67	±2.90	12	12 0 0

In Figure 5.6 we show the variations in VLF signal amplitude for GQD-A118 and ICV-A118 propagation paths, X-ray flux, V_{sw} , PD , B_z , H_T , daily Dst standard deviation and A_p variations during 26th-31st May 2011. The blue and red lines in the Figure indicate the storm commencement and peak time, respectively. About 43 flare events (C=41, M=2, X=0), and a moderate storm ($Dst < -50$ (up to -91) are associated with the period. The storm event on the 28th resulted in significant disturbances on 28 and 29 May (Fig. 5.6 c-h), and appear to be driven by sudden, significant rise in V_{sw} and PD , probably due to CMEs. Up to 3 CMEs with speed exceeding 1000 km/s were recorded between 27th and 29th (SOHO) suggesting that the solar wind is of CME origin. Solar wind density is known to influence

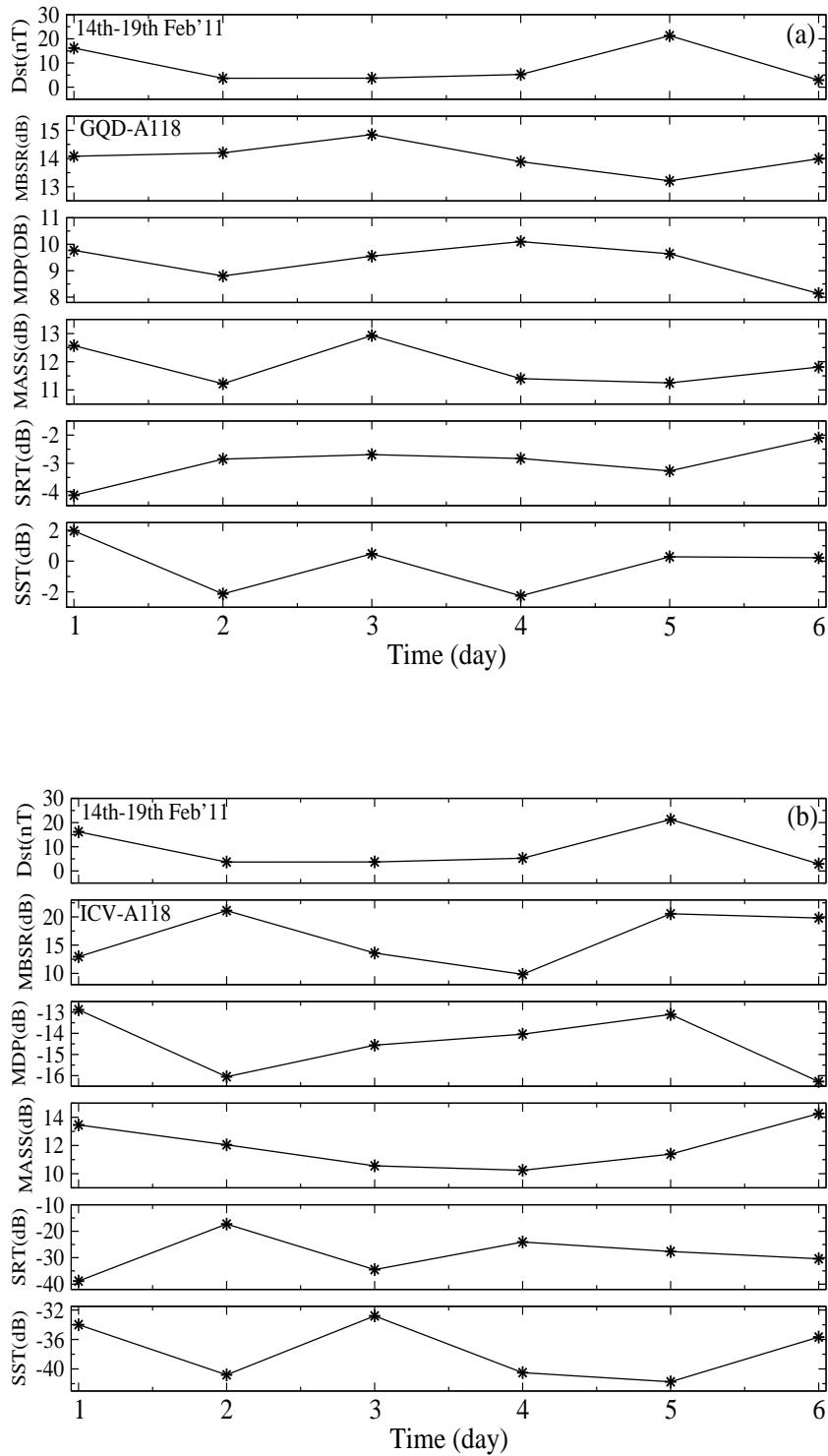


Figure 5.5: Daily Dst standard deviation, 4-hour mean signal amplitude before sunrise (MBSR), mid-day signal peak (MDP), 4-hour mean signal amplitude after sunset (MASS), sunrise terminator (SRT) and sunset terminator (SST) variations for (a) GQD-A118 and (b) ICV-A118 propagation path during 14-19th February 2011 (from Nwankwo et al. 2016).

the capability of a given value of the solar wind electric field (SWEF) to create a *Dst* disturbance (also see, Weigel, 2010). A CME influence is suggested because solar flares and prominence eruptions do also occur in association with the event. However, because of the specific scope and goal of this analysis we do not strictly attribute the solar wind and magnetosphere conditions of this period to CMEs as detailed analysis will be required. With relative high flare activity around 28th-29th May, the increase in daytime signal amplitude consistent with the signal's response to X-ray output tend to be diminished (in both propagation paths) under geomagnetic storm condition when compared with 14th-19th February scenario (see, Fig. 5.6 a-b). This situation is also replicated in the other three storm conditions investigated alongside (Nwankwo et al. 2016).

Figure 5.7 shows daily *Dst* standard deviation, MBSR, MDP, MASS, SRT and SST variations for (a) GQD-A118 and (b) ICV-A118 propagation paths during 26th-31st May 2011. A summary of the variation of each signal metric over the period is provided in Table 5.2. Here the reference storm case is that of 28 May (day 3). We observed an increase in MBSR, MDP and MASS, but a dipping of SRT and SST in GQD-A118 propagation path (Fig. 5.7a). However, dipping of the MBSR and MDP occurred on the day following the storm day (on 29th (day 2) with moderate but significantly disturbed). The MASS signal increased slightly while MBSR, MDP, SRT and SST dipped with high *Dst* in ICV-A118 propagation path (Fig. 5.7b). We note the spike in MDP is probably due to the influence of flare event in GQD-A118 propagation path on 28th; dipping need to be large or significant to overshadow flare-induced influence on the signal. Also, effects of geomagnetic activity or storm are expected on any portion of the signal (e.g., MBSR, MDP, MASS, SRT, SST) only after the event. We speculate that the increase (in MDP signal) could also be related to the characteristics of ICV-A118 propagation path, because mode interference significantly depends on ionospheric conditions at the time, propagation paths and energetic electron precipitation level on the ionosphere due to the magnetic storm, which depends on geomagnetic latitude.

In Figure 5.8 we show the variations in the diurnal amplitude of VLF signal for GQD-A118 and DHO-A118 propagation paths, X-ray flux, V_{sw} , PD , B_z , H_T , daily *Dst* standard deviation and A_p variations during 24th-29th September 2011. This period is associated with relatively high flare events (up to 51; C=33, M=17, X=1) and intense storm conditions with $Dst \leq -100$. A notable feature of the period is the recurrent storm of late 26th (red line) following the storm condition that commenced before noon (broken red line) (Fig. 5.8(e-g)). Less intense storms also occurred on 28th and 29th. The storms were driven by high variable solar wind (and PD spike) as could be clearly observed in Fig. 5.8d. The Dipping (or depression) of the daytime (and MDP) signal of DHO-A118 propagation path on 26th is clearly visible in Fig.

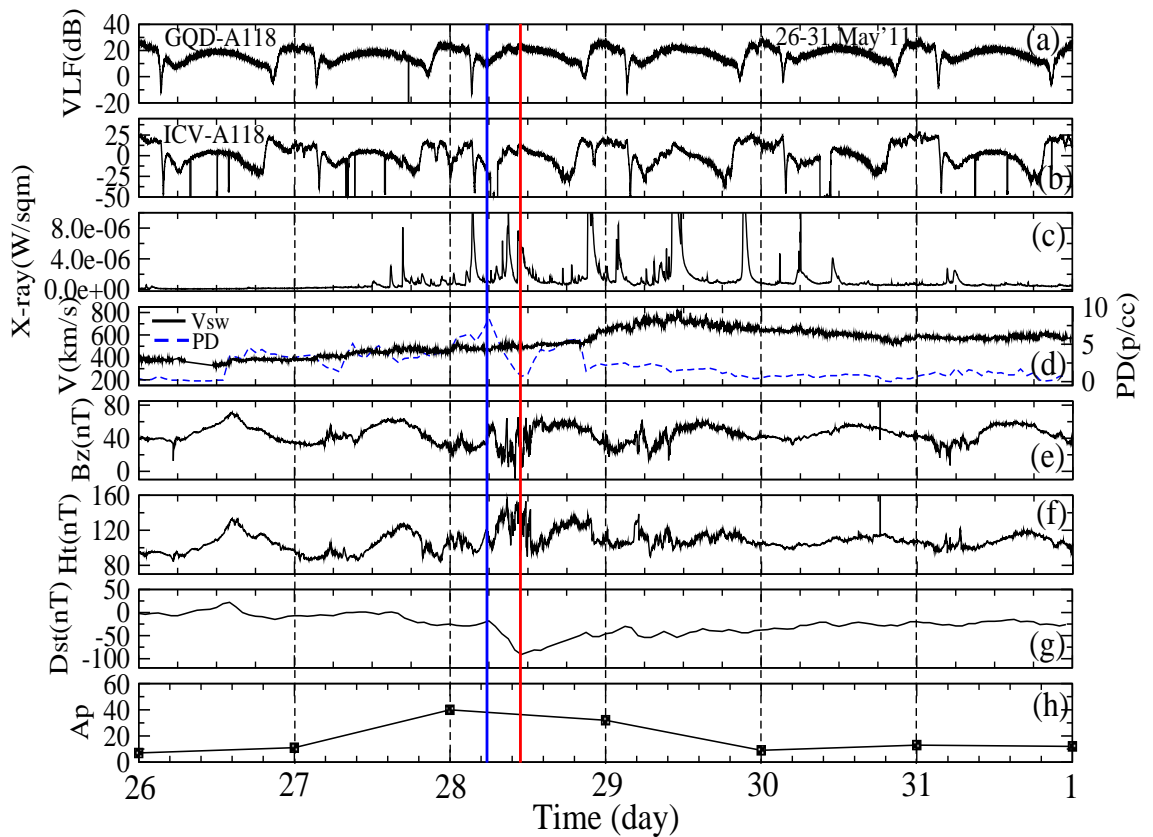


Figure 5.6: (a) Diurnal VLF amplitude for GQD-A118 PP; (b) VLF amplitude for ICV-A118 PP; (c) X-ray flux output; (d) solar wind speed (V_{sw}) and particle density (PD); (e) B_z magnetic field component; (f) H_T magnetic field; (g) Dst and (h) A_p variations during 26th-31st May 2011 (Blue and red lines in the Figure indicate storm commencement and peak time respectively) (from Nwankwo et al. 2016)

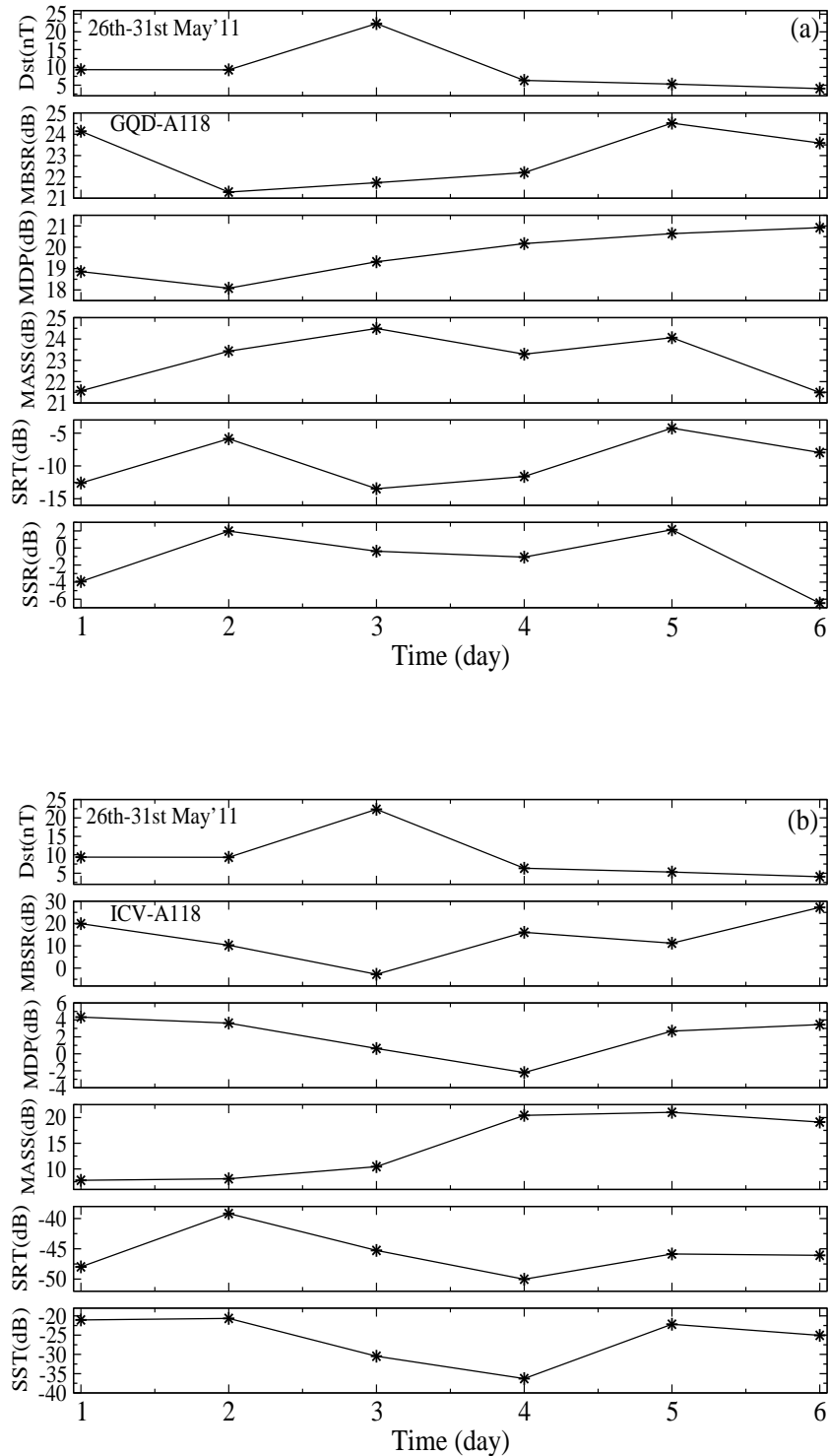


Figure 5.7: Daily Dst standard deviation, two-hour mean signal amplitude before sunrise (MBSR), mid-day signal peak (MDP), two-hour mean signal amplitude after sunset (MASS), sunrise terminator (SRT) and sunset terminator (SST) variations for (a) GQD-A118 and (b) ICV-A118 propagation path during 26th-31st May 2011 (from Nwankwo et al. 2016).

Table 5.2: Trend of time variation of VLF amplitude, Dst standard deviation and flare count during 26-31st May 2011 for GQD-A118 and ICV-A118 propagation path (from Nwankwo et al. 2016).

GQD-A118 propagation path								
Date	Mean Signal peak (dB)			Signal dip (dB)		Dst (nT)	Flare count	
	BSR	Mid-day	ASS	SRT	SST		σ_{Dst}	$\geq C$
26/5/11	24.14±1.24	18.86	21.57±1.01	-12.59	-3.93	±9.37	0	0 0 0
27/5/11	21.29±1.05	18.08	23.43±0.65	-5.86	1.98	±9.31	5	5 0 0
28/5/11	21.73±1.00	19.32	24.49±1.22	-13.47	-0.38	±22.33	19	18 1 0
29/5/11	22.20±1.42	20.17	23.29±1.63	-11.60	-1.07	±6.35	13	12 1 0
30/5/11	24.52±1.74	20.64	24.06±1.07	-4.24	2.14	±5.31	4	4 0 0
31/5/11	23.59±2.14	20.92	19.11±4.10	-7.75	-6.46	±4.04	2	2 0 0
ICV-A118 propagation path								
26/5/11	19.92±4.32	4.33	7.79±2.62	-47.18	-21.05	±9.37	0	0 0 0
27/5/11	10.26±4.32	3.62	8.08±8.74	-39.18	-20.66	±9.31	5	5 0 0
28/5/11	-2.74±8.39	0.63	10.44±9.05	-45.27	-30.47	±22.33	19	18 1 0
29/5/11	16.07±2.28	-2.21	20.42±3.17	-50.02	-36.28	±6.35	13	12 1 0
30/5/11	11.19±2.94	2.68	21.02±3.28	-45.85	-22.17	±5.31	4	4 0 0
31/5/11	22.21±3.83	3.45	19.11±4.10	-46.08	-25.07	±4.04	2	2 0 0

5.8b, and the post storm day signal (with lesser geomagnetic disturbance index) on 27th exhibited a tendency of recovery to pre-storm level. The trend of variations of other signal metrics (MBSR, MDP, MASS, SRT and SST) have also shown similar tendency (also see, Nwankwo et al. 2016).

Figure 5.9 shows daily Dst standard deviation, MBSR, MDP, MASS, SRT and SST variations for (a) GQD-A118 and (b) DHO-A118 propagation paths during 24th-29th September 2011. The summary of the variations of each signal metric over the period is provided in Table 5.3. Dipping of MDP, SRT and SST occurred on 26th (day 3), while MBSR and MASS increased in GQD-A118 propagation path (Fig. 5.9a). We note that the peak of the storms-induced perturbations, which commenced later on 26th are expected into greater part of 27th. As could be seen in Fig. 5.8g, the Dst recovery during 27th is associated with momentary perturbations, followed by the commencement of recurrent storm at 06:00 pm on the day. The dipping of MBSR, MDP, MASS and SST persisted until 27th (day 4; see Fig 5.9a) after which the MBSR, MDP and MASS increased following a decrease in Dst index on the 28th. Storm conditions were also recorded on the 28th and 29th, but the associated perturbations are not comparable to those of 26th-27th. In DHO-A118 propagation path, we observe dipping of the MDP, MASS and SST on the 26th (day

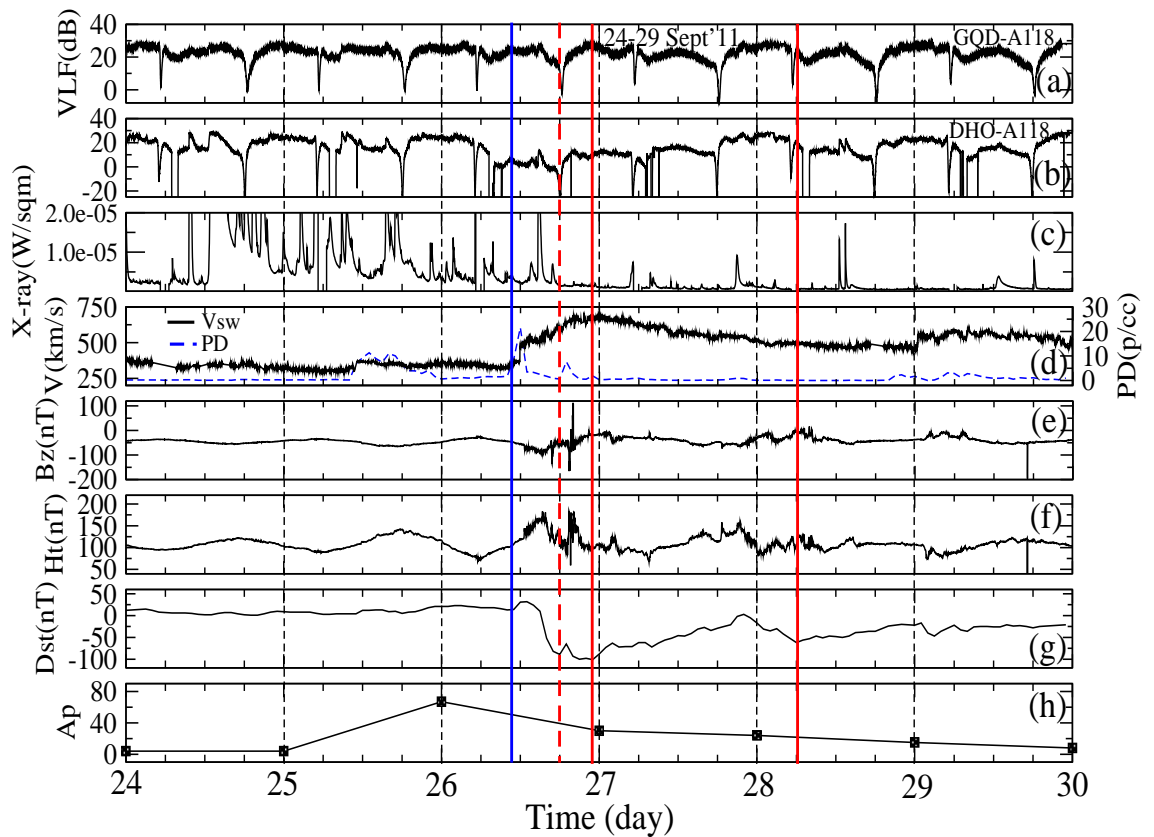


Figure 5.8: (a) Diurnal VLF amplitude for GQD-A118 PP (b) Diurnal VLF amplitude for DHO-A118 PP (c) X-ray flux output (d) solar wind speed (V_{sw}) and particle density (PD) (d) B_z magnetic field component (e) H_T magnetic field (f) Dst and (g) A_p variations during 24th-29th September 2011 (Blue and red lines in the Figure indicate storm commencement and peak time respectively) (from Nwankwo et al. 2016).

3) and 28th (day 4; see Fig 5.9b). The MBSR and SRT relatively increased on the days (3 and 4).

Table 5.3: Trend of time variation of VLF amplitude, Dst and flare count during 25th-28th September 2011 for GQD-A118 and DHO-A118 propagation path (from Nwankwo et al. 2016).

GQD-A118 propagation path								
Date	Mean Signal peak (dB)			Signal dip (dB)		Dst (nT)	Flare count	
	BSR	Mid-day	ASS	SRT	SST		σ_{Dst}	$\geq C$
24/9/11	26.42±1.02	23.10	25.38±2.10	1.30	-1.28	±4.08	13	4 8 1
25/9/11	24.94±1.16	23.30	24.98±0.96	-0.59	-0.40	±4.56	10	4 6 0
26/9/11	25.52±1.14	22.61	25.62±1.59	-0.75	-2.11	±50.73	11	9 2 0
27/9/11	22.91±1.35	22.15	24.87±1.63	-3.26	-7.25	±24.54	8	8 0 0
28/9/11	27.31±0.77	22.51	25.13±1.38	3.28	-7.57	±12.37	4	3 1 0
29/9/11	26.56±1.29	21.69	26.10±2.32	-3.85	-2.61	±6.73	3	3 0 0
DHO-A118 propagation path								
24/9/11	23.26±2.04	14.55	23.32±1.00	-12.96	-34.41	±4.08	13	4 8 1
25/9/11	23.33±1.29	14.57	24.60±0.99	-26.86	-26.34	±4.56	10	4 6 0
26/9/11	23.81±1.05	0.45	9.90±1.48	-26.79	-35.80	±50.73	11	9 2 0
27/9/11	11.38±1.05	14.00	23.68±1.90	-30.47	-25.82	±24.54	8	8 0 0
28/9/11	25.90±1.74	12.66	20.98±2.09	-9.85	-28.62	±12.37	4	3 1 0
29/9/11	22.49±2.04	15.43	25.87±3.31	-21.78	-36.25	±6.73	3	3 0 0

In Figure 5.10 we show the variations in diurnal amplitude of VLF signal for GQD-A118 and DHO-A118 propagation paths, X-ray flux, V_{sw} , PD , B_z , H_T , daily Dst standard deviation and A_p variations during 23rd-28th October 2011. This period is associated with only 11 C class flare events, and intense storm condition ($Dst < -132$). The storm commenced around sunset on 24th and peaked in the early hours of 25th, presumably driven by high speed solar wind (HSS) and PD of 24th October (Fig. 5.10(d-h)). The signal data for GQD-A118 propagation path during 12:00 noon, 25th - 06:00 pm, 26th October (Fig. 5.10a) are not available. Only the DHO-A118 propagation path (at A118 SID receiving station) recorded data during this time interval. 6 other propagation paths in the series have no data (e.g. GBZ-A118, ICV-A118, NAA-A118, TBB-A118). This time interval probably corresponds to the peak period of induced ionosphere perturbations. Therefore, further probing of the possible cause of such scenario (with respect to the prevailing geomagnetic condition) may be instructive, but outside the scope of this work. The dipping of DHO-A118 propagation path daytime and MDP signal on 25th, being the most disturbed day is clearly observed (Fig. 5.10b), with the post storm day signal also

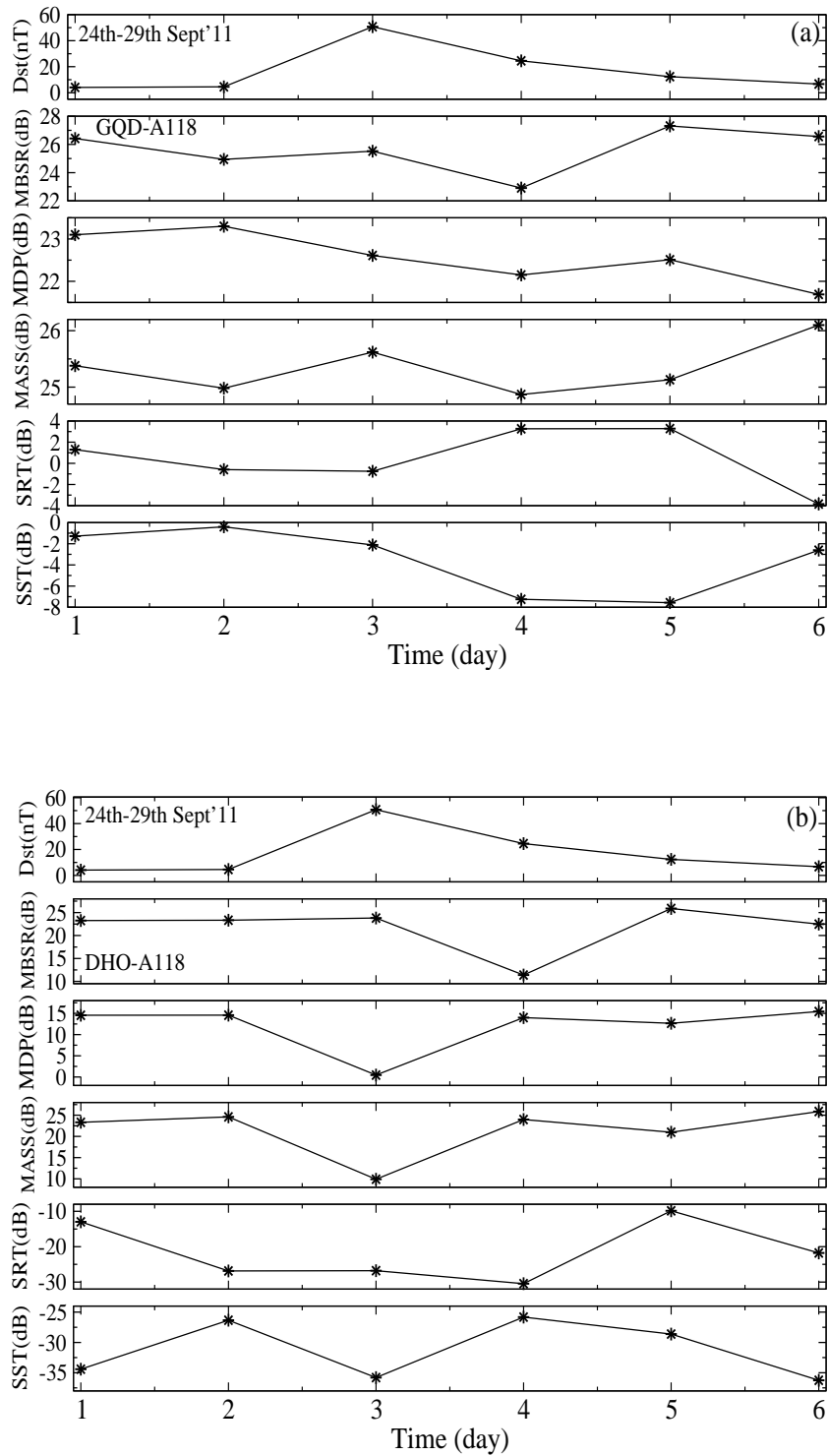


Figure 5.9: Daily Dst standard deviation, 4-hour mean signal amplitude before sunrise (MBSR), mid-day signal peak (MDP), 4-hour mean signal amplitude after sunset (MASS), sunrise terminator (SRT) and sunset terminator (SST) variations for (a) GQD-A118 and (b) DHO-A118 propagation path during 24th-29th September 2011 (from Nwankwo et al. 2016).

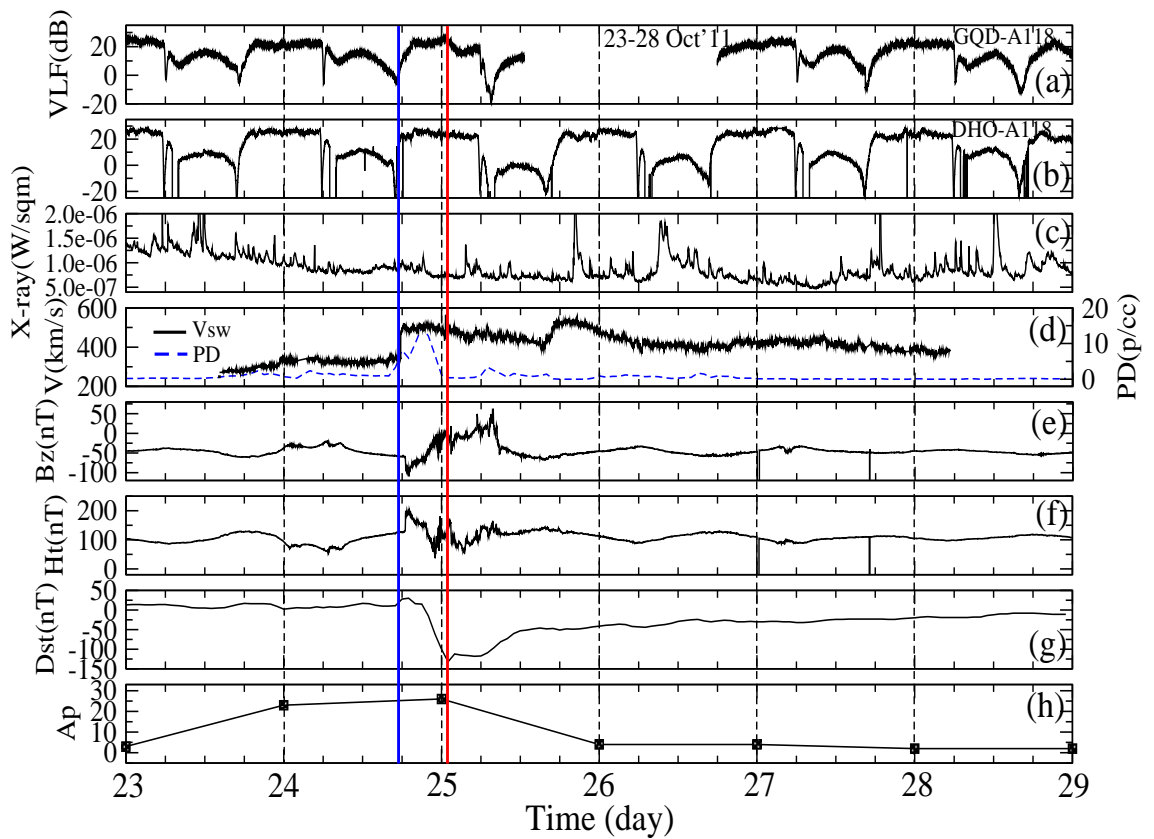


Figure 5.10: (a) Diurnal VLF amplitude for GQD-A118 PP (b) Diurnal VLF amplitude for DHO-A118 PP (c) X-ray flux output (d) solar wind speed (d) B_z magnetic field component (e) H_T magnetic field (f) Dst and (g) A_p variations during 23rd-28th October 2011 (from Nwankwo et al. 2016).

showing the signal's recovery to pre-storm level.

In Figure 5.11 shows daily Dst standard deviation, MBSR, MDP, MASS, SRT and SST variations for (a) GQD-A118 and (b) DHO-A118 propagation paths during 23rd-28th October 2011. The summary of variations of each metric of the signal over the period is provided in Table 5.4. The data of GQD-A118 propagation path during 25th-26th is not sufficient for the present analysis (Fig. 5.11a). The DHO-A118 propagation path signal showed dipping of the MBSR, MDP and MASS on 25th (day 3), corresponding to the storm's peak day, but an increase in SRT and SST (Fig 5.11a). The prevailing space weather conditions (with peak) of 25th (day 3) commenced at around 06:00 pm on 24th (day 2). Dipping of the MDP and MASS also commenced on 24th (day 2). There is a post-storm day increase of MBSR, MDP

and MASS with significant Dst low on 26th, a scenario that is characteristic of most post-storm day signals. Therefore, we view such scenario as post-storm day signal recovery tendency.

Table 5.4: Trend of time variation of VLF amplitude, Dst and flare count during 23rd-28th October 2011 for GQD-A118 and DHO-A118 propagation path (from Nwankwo et al. 2016).

GQD-A118 propagation path								
Date	Mean Signal peak (dB)			Signal dip (dB)		Dst (nT)	Flare count	
	BSR	Mid-day	ASS	SRT	SST		σ_{Dst}	$\geq C$
23/10/11	24.35±0.88	16.59	21.83±0.87	-3.31	-4.27	±4.08	3	3 0 0
24/10/11	21.63±1.02	15.28	22.66±0.93	-6.35	-4.89	±16.35	0	0 0 0
25/10/11	19.70±3.77	-	-	2.16	-	±30.76	1	0 0 0
26/10/11	17.14±2.59	-	-	-	-	±6.25	1	1 0 0
27/10/11	22.32±1.43	17.45	21.74±1.33	-4.92	-9.69	±3.53	1	1 0 0
28/10/11	21.83±0.86	19.35	19.47±2.52	-4.97	-11.98	±4.48	5	5 0 0
DHO-A118 propagation path								
23/10/11	26.18±1.05	10.45	25.51±0.82	-32.81	-37.10	±4.08	3	3 0 0
24/10/11	25.53±0.92	10.23	24.80±1.33	-26.64	-30.84	±16.35	0	0 0 0
25/10/11	22.75±0.99	-2.12	22.16±1.68	-19.19	-21.17	±30.76	1	1 0 0
26/10/11	25.51±1.22	5.23	24.17±1.18	-34.30	-15.40	±6.25	1	1 0 0
27/10/11	26.49±1.72	8.16	22.53±4.45	-25.25	-23.23	±3.53	1	1 0 0
28/10/11	23.96±1.68	11.02	20.42±1.32	-29.63	-37.10	±4.48	5	5 0 0

We now present a summary of the cases analysed above. We identify the most disturbed day in each of the four periods and analyse the signal metrics variation on the day viz. event 1 (E_1) on 18th February, 2011; event 2 (E_2) on 28th May, 2011; event 3 (E_3) on 26-27 September, 2011; and event 4 (E_4) on 25th October 2011. We allow two days interval for the analysis of the events during 26th-27th September because of the recurrent storms. In summary, 2 of 3 events (E_{1-3}) showed dipping of MDP in GQD-A118 propagation path (VLF data during E_4 is not available). 3 of the 4 events (E_{1-4}) showed dipping of MDP in ICV/DHO-A118 propagation paths. We note that solar flare occurred around mid-day in the days when MDP showed no dipping, and speculate possible flare-induced increase of signal metric on the MDP and/or due to other atmospheric phenomena. 2 of 4 events (E_{1-4}) showed dipping of MBSR in GQD-A118 propagation path, and dipping in all the four events in ICV/DHO-A118 propagation paths. 2 of 3 events (E_{1-3}) showed dipping of MASS in GQD-A118 propagation path (VLF data during E_4 is not available), and 2 of the 4 events in ICV/DHO-A118 propagation path. 3 of 4 events showed dipping of

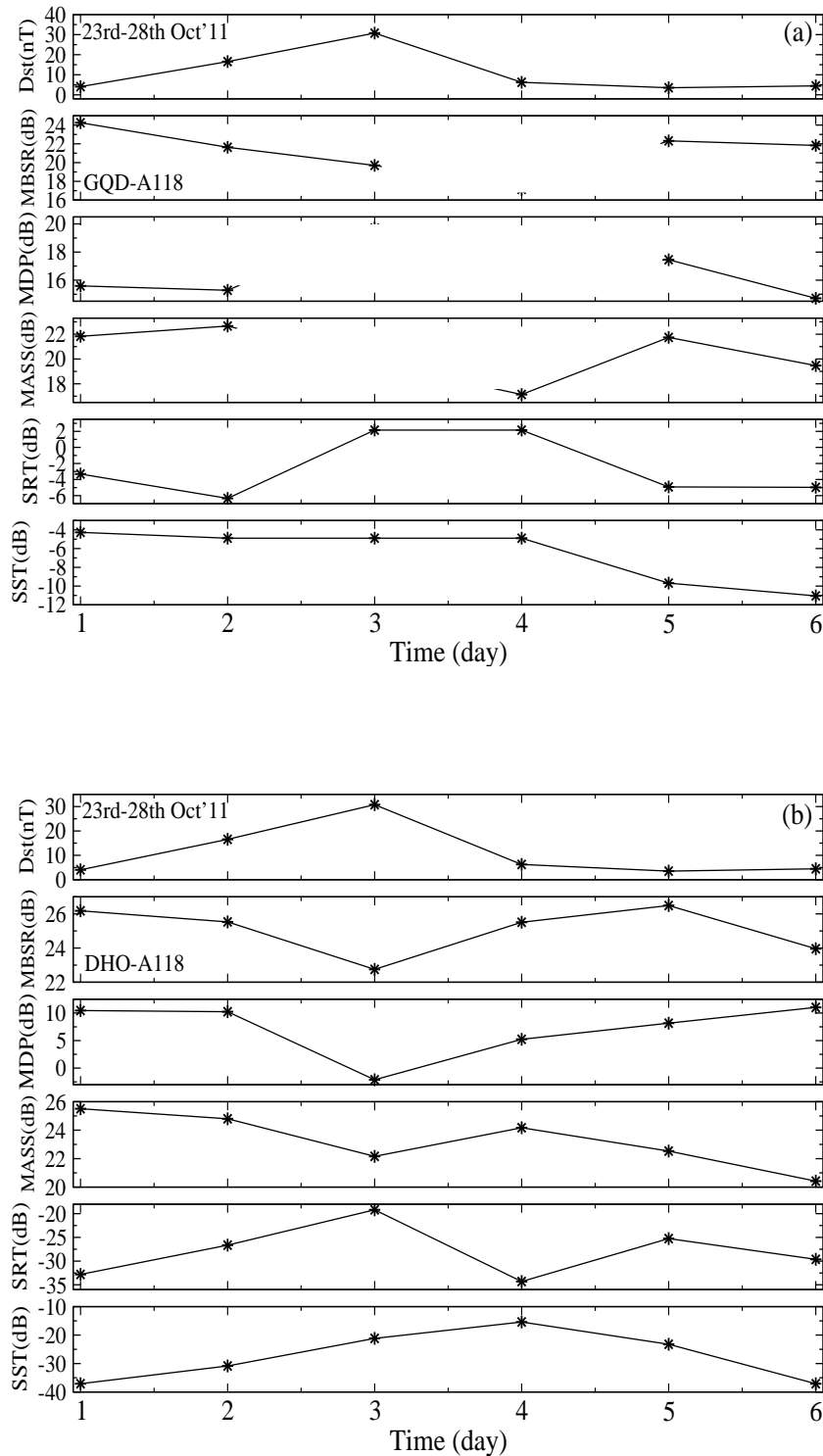


Figure 5.11: Daily Dst standard deviation, 4-hour mean signal amplitude before sunrise (MBSR), mid-day signal peak (MDP), 4-hour mean signal amplitude after sunset (MASS), sunrise terminator (SRT) and sunset terminator (SST) variations for (a) GQD-A118 and (b) DHO-A118 propagation path during 23rd-28th October 2011 (from Nwankwo et al. 2016).

SRT in GQD-A118 propagation path, and 2 of 4 in ICV/DHO-A118 propagation paths. 2 of 4 events showed dipping of SST in GQD-A118 propagation path, and 3 of 4 in ICV/DHO-A118 propagation paths. We have also observed that within the local day time interval, the events occurred well before or after 4 of 5 MBSR and MASS, and five of six SRT and SST that showed no dipping (or, maintained amplitude) in accordance with the events. Among other possible inferences, this observed trend suggest that geomagnetic effects are expected on aspects of the signal (e.g., MBSR, MDP, MASS, SRT, SST) only after the event(s). If the event occurs well before the component, the induced ionospheric perturbations is expected to have significantly reduced at the time interval. Among the 3 propagation paths, the signal of DHO-A118 appears to be more sensitive to geomagnetic induced magnetosphere-ionospheric dynamics. Since the number of the cases analysed so far are few, drawing a firm conclusion would be difficult at this stage. We, therefore, include more cases in the next analysis (see Table 5.5), and combine different signal aspects on a single graph (Nwankwo et al. 2016).

Table 5.5: Summary of analysed geomagnetic storm conditions (from Nwankwo et al. 2016).

No.	Date	Max Dst (nT)	σ_{Dst}	Flare count($\geq C$)
				C M X
1	05022011	-51	± 8.99	0 0 0
2	01032011	-81	± 36.28	7 0 0
3	06042011	-65	± 24.31	3 0 0
4	12042011	-51	± 22.11	3 0 0
5	26092011	-101	± 50.73	9 2 0
6	25102011	-132	± 30.76	1 0 0
7	22012012	-67	± 37.00	4 0 0
8	15022012	-58	± 9.63	0 0 0
9	19022012	-54	± 12.8	1 0 0
10	07032012	-74	± 25.41	1 0 0
11	15032012	-74	± 20.75	1 0 0
12	28032012	-55	± 12.09	1 0 0
13	05042012	-54	± 13.82	3 0 0
14	23042012	-95	± 32.23	3 0 0
15	12062012	-51	± 12.47	13 0 0
16	16062012	95	± 20.24	4 0 0
17*	17062012	80	± 46.75	7 0 0

Statistical analysis of signal amplitude variations during 16 storm cases

A statistical significance of the observed trend is important. Therefore, we analyse and study the trends in variation of combined signal aspects for 16 storm cases during February 2011 - June 2012 for GQD-A118 and DHO-A118 propagation paths. The detail of the storm events are provided in Table 5.5. The analysis we take (a) signal metrics (MBSR, MDP, MASS, SRT and SST) 1-day before an event (BE), during an event (DE) and after an event (AE), and (b) a 2-day mean signal metric BE, DE and AE. We selected an event based on availability and quality of signal data on the day, and relatively quiet BE and AE, particularly for the 2-day mean analysis. While the BE and AE data were carefully chosen to be consistent with relative geomagnetic quiet condition, a few choices on significantly perturbed days could not be avoided because of the extended intervals geomagnetic active condition and recurrent storms (in some cases). Such scenario can cause high variability of VLF radio signal. Other than solar induced fluctuations, the ionosphere and VLF radio signal also response to effects originating from a number of other sources (see Chapter two). Some of the effects are interconnected and sometimes interferes, leading to high variability of signal strength. Therefore, we do not expect a 'perfect' consistency in trend across all the cases. In Figure 5.12 shows deviations in Dst index and trend in variation of MDP, MBSR, MASS, SRT and SST signals one-day before and after (consecutive) each of the 16 selected storm conditions for (a) GQD-A118 and (b) DHO-A118 propagation paths. Detail of the data is provided in Appendix I.

In For GQD-A118 propagation path (left panel), 10 of 14 MDP, 10 of 15 MBSR, 7 of 14 MASS, 9 of 14 SRT and 7 of 14 SST have shown a dipping of the signals, corresponding to respective 71.4%, 66.7%, 50%, 64.3% and 50.0% of the combined cases. In DHO-A118 propagation path (right panel) 13 of 16 MDP, 9 of 16 MBSR, 8 of 16 MASS, 5 of 14 SRT and 7 of 16 SST showed dipping of the signals, corresponding to respective 81.3%, 56.3%, 50%, 35.7% and 43.8% of the combined cases. We note that dipping of any of DE and AE signal metric in cases 15 and 16 is taken as a response to the event because storm condition or the event commenced during late DE and peaked in AE. Recurrent storms also occurred on the day after case 16. In this analysis, we found that most of MDP signal in both propagation paths showed a notable evidence of dipping. However, a few number of propagation path-mismatched incidences of MDP signal rise (or, increase) on some events day have been also observed (e.g., events 8, 11 and 16 in GQD and 4 and 13 in DHO). This increase may be related to flare induced signal amplitude spike on the signal or phenomena arising from sources other than storm events. We also observed a matched-increase of the diurnal signal level (including MDP, MBSR and MASS) on DE 7 (22 Jan 2012) in both propagation paths. Further study of the available data

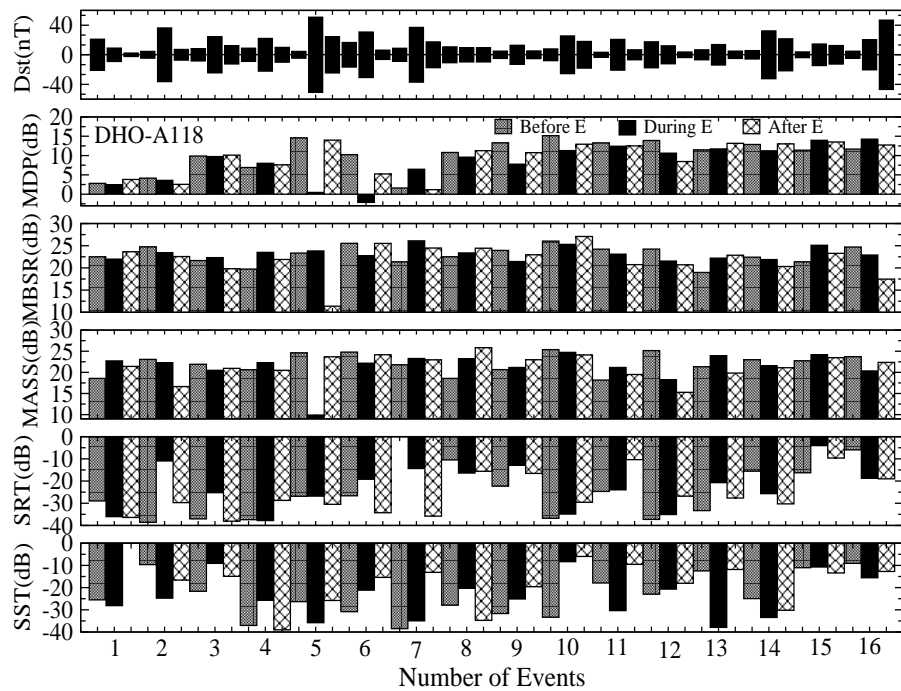
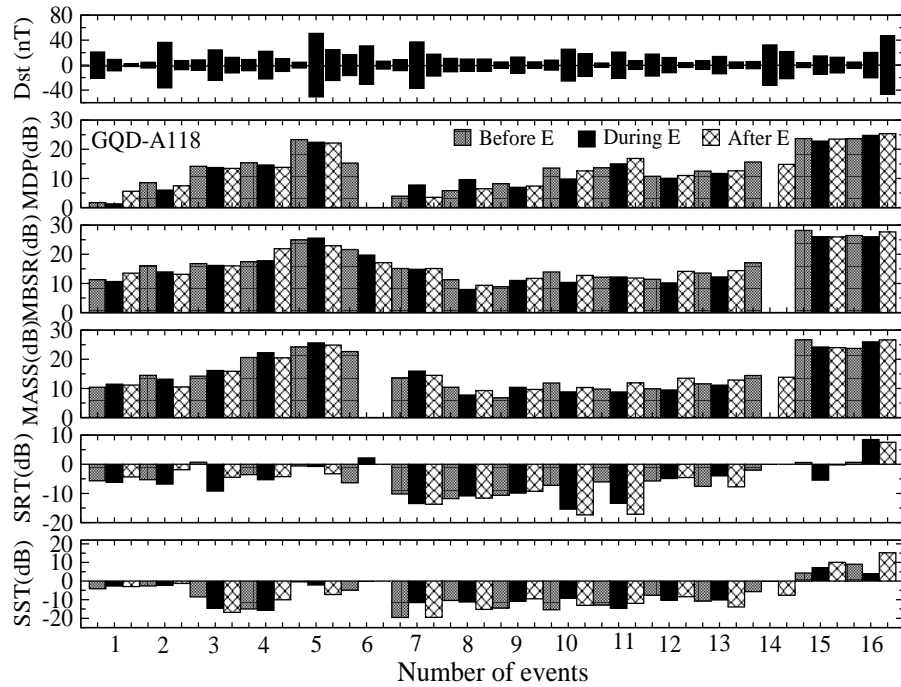


Figure 5.12: Deviation of Daily Dst Index and trend in variation of MDP, MBSR, MASS, SRT and SST signals one day before and after each of the 16 selected storm conditions for (a) GQD-A118 and (b) DHO-A118 propagation paths. A '0' indicate absence of data (from Nwankwo et al. 2016).

showed occurrence of storm associated M-class flare with corresponding peaks, suggesting an enhancement of not only the instantaneous but also background X-ray flux output. In Figure 5.13 shows *Dst* deviation and trend in variation of 2-day mean MDP, MBSR, MASS, SRT and SST signals before, during and after each event for (a) GQD-A118 and (b) DHO-A118 propagation paths. The detail of the data is provided in Appendix II. We used a different criterion for data selection; the analysis presented in Fig. 5.13 is a follow-up on the one presented in Fig. 5.12, and expected to complement and provide useful clue for the conclusion of the results. While BE, DE and AE represent data of three consecutive days with reference to the event's day (DE) in the former analysis (Fig 5.12), each acronym (BE, DE or AE) represent a 2-day mean (VLF) with respect to DE (but not necessarily in succession to DE). Apart from the quality and availability of data, another important criterion for data selection is a relatively quiet geomagnetic condition on BE and AE day with respect to DE (Nwankwo et al. 2016).

In GQD-A118 propagation path (left panel), 10 of 14 MDP, 9 of 15 MBSR, 7 of 14 MASS, 11 of 16 SRT and 5 of 14 SST showed dipping of the signals, corresponding to respective 71.4%, 60.0%, 50.0%, 68.8% and 35.7% of the combined cases. In DHO-A118 propagation path (right panel), 11 of 16 MDP, 11 of 16 MBSR, 10 of 16 MASS, 6 of 14 SRT and 7 of 16 SST showed dipping of the signals, corresponding to respective 68.8%, 68.8%, 62%, 42.9% and 43.8% of the combined cases. The MDP signal showed a high probability of a dipping scenario following significant geomagnetic disturbance or storm condition, as well as the MBSR and MASS signals. However, the MBSR and MASS appear to be significantly influenced by event's occurrence time and the highly variable conditions of dusk-to-dawn ionosphere. Fewer cases have shown a rise or increase of the components instead (e.g., MDP, MBSR, MASS) following a significant geomagnetic event. In contrast to the trend in other signal metrics, the SRT and SST signals have shown significant post-storm dipping in GQD-A118 propagation path but mostly increase in DHO-A118 propagation path. Therefore, a clear trend in variation of SRT and SST during geomagnetic disturbance or storm conditions seems inconclusive in the this work. One requires to carry out detailed simulations to pinpoint effects solely due to this type of disturbances (Nwankwo et al. 2016).

We now highlight the constraints associated with this analysis that may have also influenced the trends in the signals variation (with respect to storms). In addition to flare and X-ray flux induced amplitude variation, the daytime signal of VLF radio waves are usually quite stable. This factor may have contributed to the consistency in the trends related to variations of the MDP (about 73% cases of dipping). For the MBSR and MASS, the high fluctuation of dusk-to-dawn signal (see, Fig. 5.2(a-f)) remain a major setback to analysis relating to the signals (the

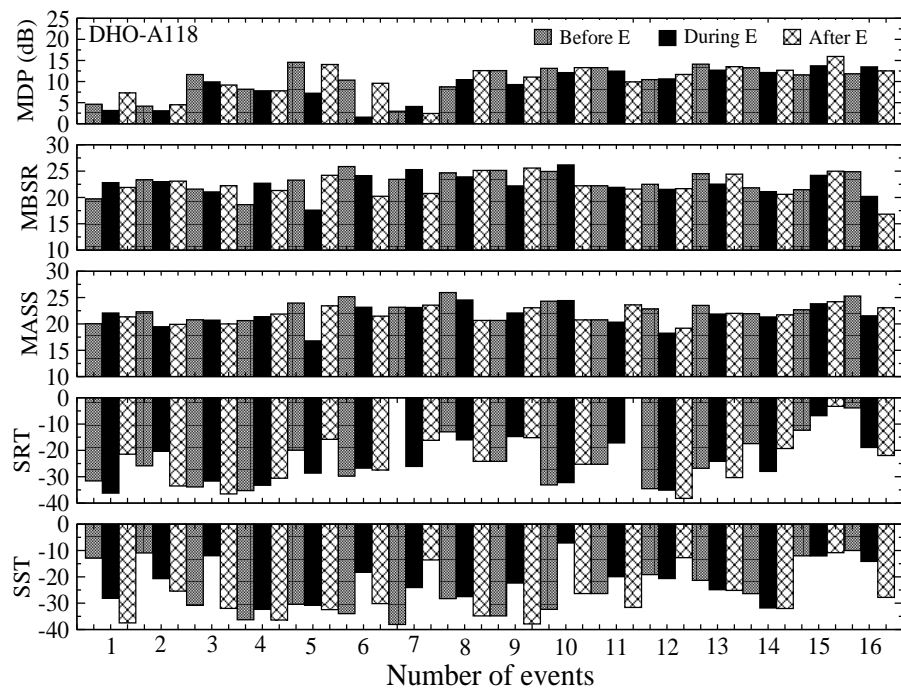
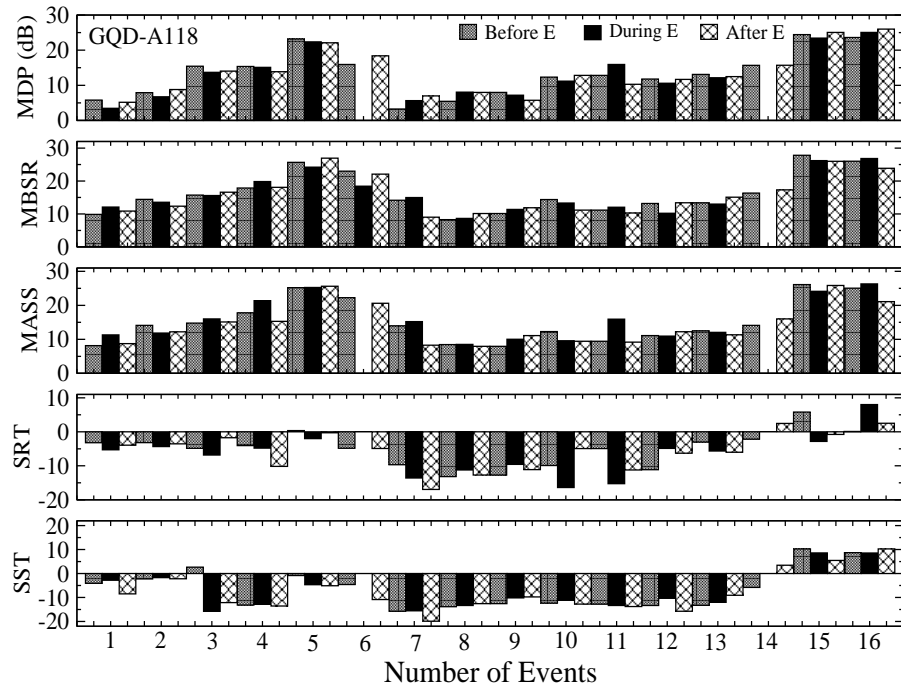


Figure 5.13: Daily Dst deviation (fluctuation) and trend in variation of 2-day mean MDP, MBSR, MASS, SRT and SST before, during and after an event for (a) GQD-A118 and (b) DHO-A118 propagation paths. A '0' indicate absence of data (from Nwankwo et al. 2016)

combined analysis showed 63% and 53% cases of dipping, respectively). Also, the occurrence of double or multiple-mode sunrise and/or sunset terminators (pseudo-SRT and SST) exhibited by the diurnal VLF signal (see, Fig. 5.2e-f) also affect the analysis of the signals (the combined analysis showed 52% and 43% dipping of the SRT and SST, respectively). It is important to decide the particular terminator tips to measure (in case of a pseudo-terminator) - this is challenging too!

5.4.2 Further investigation of storm-induced changes of the ionosphere and VLF signal amplitude

In section 5.4.1 we reported significant cases of dipping of VLF mid-day signal amplitude (MDP), mean signal amplitude before sunrise (MBSR) and mean signal amplitude before sunset (MASS) in mid-latitude D-region ionosphere, associated with geomagnetic storms during February 2011 to June 2012. While majority of the MDP signals (considering all the propagation paths (PP) used) showed a noteworthy evidence of dipping (following a storm condition), a few PP-mismatched incidences of MDP signal rise on some events day were also observed. A notable propagation path-matched increase of the diurnal signal level was also observed. These scenarios are illustrated in Fig. 5.14. In principle, the signal level or strength of VLF radio wave can also increase following a geomagnetic storm, but depending on the storm characteristics, associated phenomena or signal's propagation path. In the present study we perform a more detailed analysis to substantiate the initial findings, and further investigate the observed cases of increase of VLF amplitude (against dipping scenario) following geomagnetic storm conditions. The data and method of analysis are the same as in Section 5.3). However, in the present analysis we increase the data points of the MBSR and MASS by 30 minutes, and restrict the MDP interval to period of around 12.00 noon to 12.30 pm. We analyse the VLF signal amplitude data of DHO-A118 and GQD-A118 propagation paths (see Figure 5.3), in conjunction with solar and geomagnetic data (mentioned and described in section 5.4 of Chapter 5). To start with, we perform analysis for two 15-day periods that include geomagnetic storms of varying disturbance index. These periods are: 16th-31st September and 22 October-5 November 2011. This is followed by a statistical analysis of up to 15 more storm cases during September 2011 to October 2012. The 15 storm cases are presented in Table 5.6. In all, about 20 storm cases were analysed, which excluded some cases that were previously analysed in Chapter 5 (also see Nwankwo et al., 2016), but also included new cases.

Figure 5.15 shows diurnal VLF amplitude for (a) DHO-A118 and (b) GQD-A118 propagation paths, daily variation in (c) X-ray flux output (d) solar wind speed (V_{sw}) (e) solar particle density (PD) (f) Disturbance storm time (Dst) (g) planetary

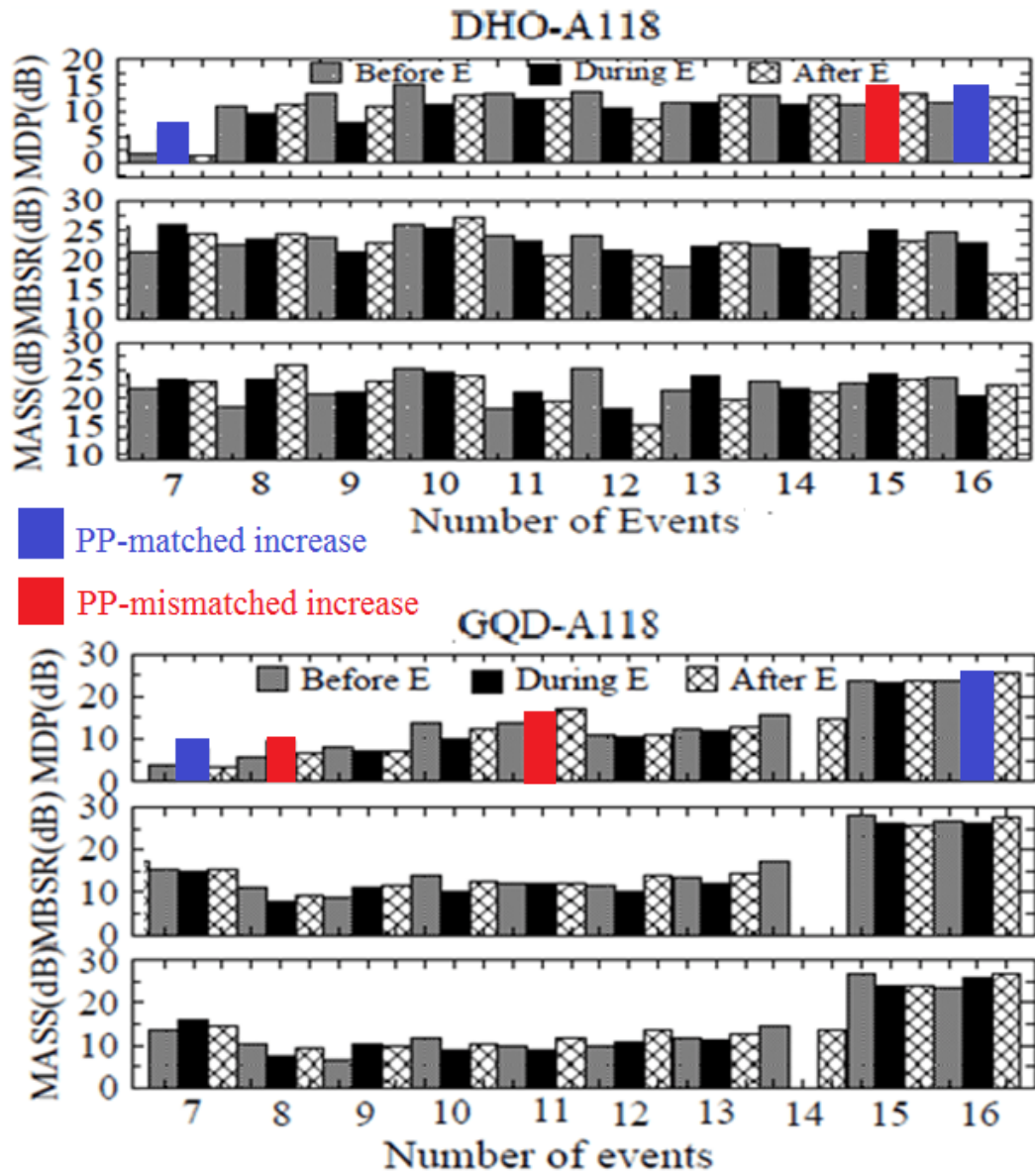


Figure 5.14: Illustration of propagation path-matched and mismatched increase of the midday day peak signal (MDP) for GQD-A118 and DHO-A118 propagation paths (from Nwankwo & Chakrabarti. 2016).

Table 5.6: Summary of analysed 15 geomagnetic storm events (from Nwankwo & Chakrabarti. 2016).

No.	Date	Max Dst (nT)	σ_{Dst}	Flare count(C M X)
1	26092011	-101	± 50.73	9 2 0
2	25102011	-132	± 30.76	1 0 0
3	22012012	-67	± 37.00	4 0 0
4	15022012	-58	± 9.63	0 0 0
5	19022012	-54	± 12.8	1 0 0
6	07032012	-74	± 25.41	1 0 0
7	15032012	-74	± 20.75	1 0 0
8	28032012	-55	± 12.09	1 0 0
9	05042012	-54	± 13.82	3 0 0
10	23042012	-95	± 32.23	3 0 0
11	12062012	-51	± 12.47	13 0 0
12	16062012	95	± 20.24	4 0 0
13	15072012	-126	± 47.88	8 0 0
14	02092012	-54	± 13.86	5 0 0
15	09102012	-105	± 25.64	10 1 0

geomagnetic A_p and (h) Auroral Electrojet (AE) indices during 16-30 September 2011. Four storm conditions were recorded during the period; moderate storm on 17th ($Dst=-60$) and consecutive storms on 26th ($Dst=-101$), 27th ($Dst=-88$) and 28th ($Dst=-62$), presumably driven by the significant increase in V_{sw} and PD on 17th and 26th (Fig. 5.15(a-f)). However, the main reference storms are those of 17th and 26th. The variation of the AE (especially between 26th and 29th) appear to be consistent with high-intensity, long-duration continuous AE activity events (HILDCAAs). Hence, ‘fresh energy was being injected’ in the magnetosphere in the process (Tsurutani et al., 2011). We observed a notable drop in DHO-A118 VLF signal level on 26th around midday following the relatively intense storm condition with Dst up to -101 (Fig. 5.15a). This scenario (signal strength decrease) have been associated with storm-induced variations in energetic electron precipitation flux (Kikuchi and Evans, 1983; Peter et al., 2006). During a geomagnetic storm, the current system in the ionosphere, and the energetic particles that precipitate into the ionosphere deposit energy in the form of heat that can influence the density and distribution of density in the atmosphere (NOAA7). Monitoring the trends in variations of the signal metrics (e.g., MBSR, MDP, MASS, SST and SRT) makes it easier to identify the influence of the storms on the D-region. Therefore, we further investigate variations in the signals metrics for possible distinction of storm induced signatures in the ionosphere.

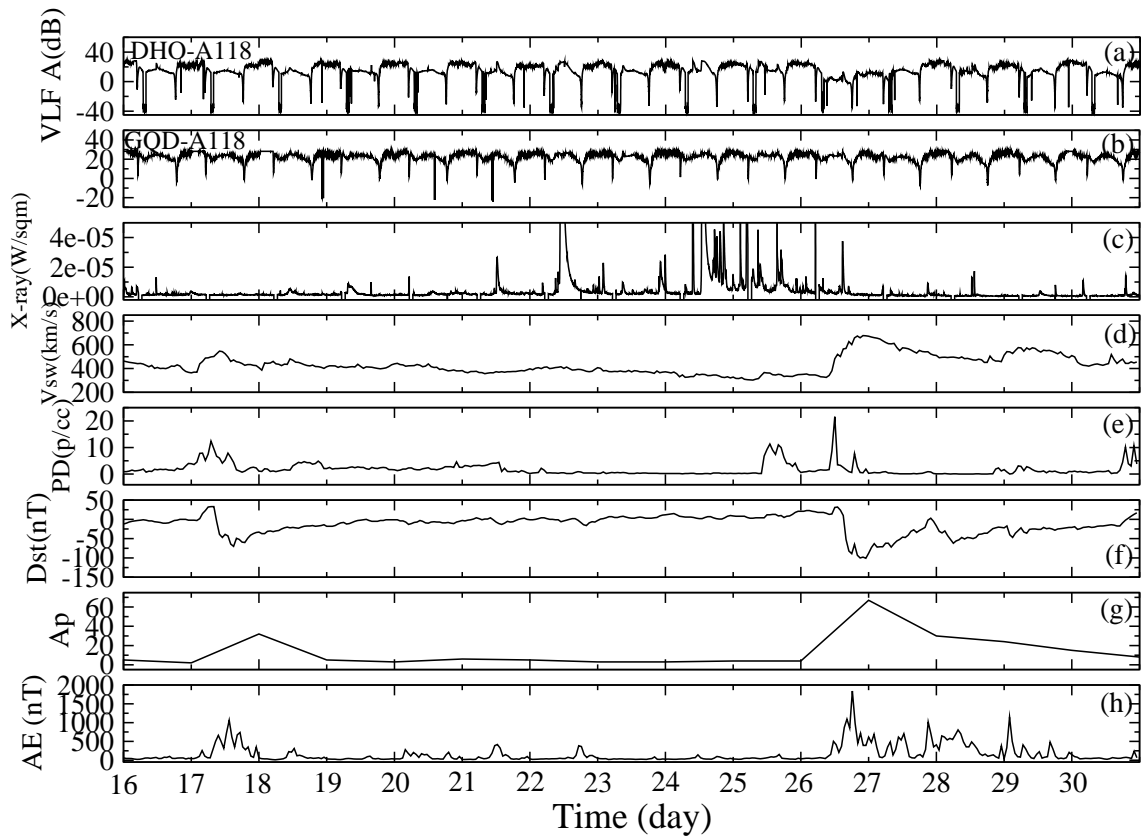


Figure 5.15: (a) Diurnal VLF amplitude for DHO-A118 and (b) GQD-A118 propagation paths (c) daily variation in X-ray flux output (d) solar wind speed (V_{sw}) (e) solar particle density (PD) (f) Disturbance storm time (Dst) (g) planetary A_p and (h) Auroral Electrojet (AE) indices during 16-30 September 2011 (from Nwankwo & Chakrabarti. 2016).

Figure 5.16 shows daily fluctuation of Dst and AE , and variations in the VLF midday signal amplitude peak (MDP), 4-hour mean signal amplitude before local sunrise (MBSR), 4-hour mean signal amplitude after sunset (MASS), sunrise terminator (SRT) and sunset terminator (SST) for (a) DHO-A118 and (b) GQD-A118 propagation paths during 16-30 September 2011. Values of the parameters over the period is presented in Appendix 1. In GQD-A118 propagation path (Fig. 5.16a), we observed a dipping of the MDP on 17th (extending to 20th), as well as dipping of the MASS on 17th, but an increase of the MBSR, SRT and SST. Following the recurrent storms of 26th-28th, we observed dipping of the MDP on 26th (extending to 29th). The slight increase of the signal (MDP) on 28th appear to be due to the significant flare activity (3 C-class and 1 M-class), suggesting the increase of both instantaneous and background X-ray flux output that usually results in prompt rise in signal amplitude. High flare activity often overshadow signal's response to geomagnetic storms when significant flare and storm events are concurrent. There is also a significant dipping of all signal metrics on 27th. We note dipping of the MBSR on the days following the main (reference) storms on 18th and 27th. Since the events occurred after dawn (around midday), the post-storm ionospheric effects are expected well into the day following the storm. The trend (post-storm day signal dip), therefore, suggest that the signals dipped in response to post-storm ionospheric effects on the days following the events. However, such response also depend on the characteristics of the signals propagation path. In DHO-A118 propagation path, dipping of the MDP, MBSR, SRT and SST have been observed on the 17th, and those of MDP, MASS and SST on 26th. The MASS and SRT maintained the pre-storm day values of 16th and 25th, respectively. While the MBSR increased slightly on 26th (main storm day), there is a significant dipping of the signal following recurrent storm of 27th.

Figure 5.17 shows diurnal VLF amplitude for (a) DHO-A118 and (b) GQD-A118 propagation paths, daily variation in (c) X-ray flux output (d) V_{sw} (e) PD (f) Dst (g) A_p and (h) AE indices during 22 October - 5 November 2011. This period is associated with three storms; a severe storm with main phase on 25th October ($Dst=-132$) and consecutive storms on 1st ($Dst=-71$) and 2nd November ($Dst=-57$), presumably induced by the highly variable V_{sw} and PD (Fig. 5.17(d-e)). It has been shown that the capability of a given value of the solar wind electric field (SWEF) to create a Dst disturbance or geo-efficiency is enhanced by high solar wind density (Weigel, 2010). Variation of the AE between 30th Oct. and 3rd Nov. also appear to be consistent with HILDCAAs (Fig. 5.17h). The DHO-A118 VLF signal level on 25th around midday also showed a visible reduction following the intense storm condition with Dst up to -132 (Fig. 5.17a). VLF signal data for GQD-A118 propagation path are not available during 12:00 noon, 25th - 06:00 pm, 26th October

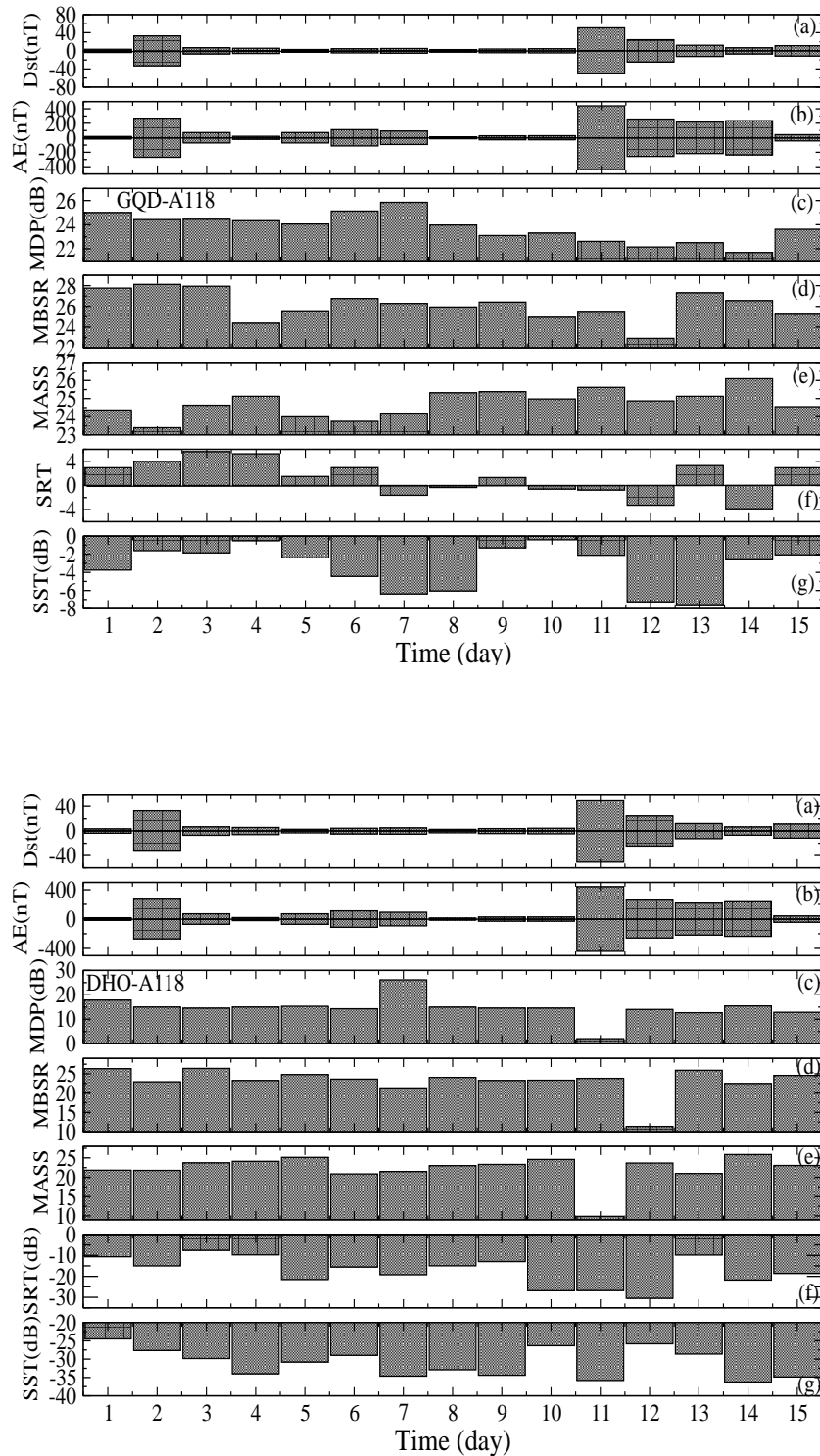


Figure 5.16: Daily Dst standard deviation, 4-hour mean signal amplitude before sunrise (MBSR), mid-day signal peak (MDP), 4-hour mean signal amplitude after sunset (MASS), sunrise terminator (SRT) and sunset terminator (SST) variations for (a) GQD-A118 and (b) DHO-A118 propagation path during 23rd-28th October 2011 (from Nwankwo & Chakrabarti. 2016).

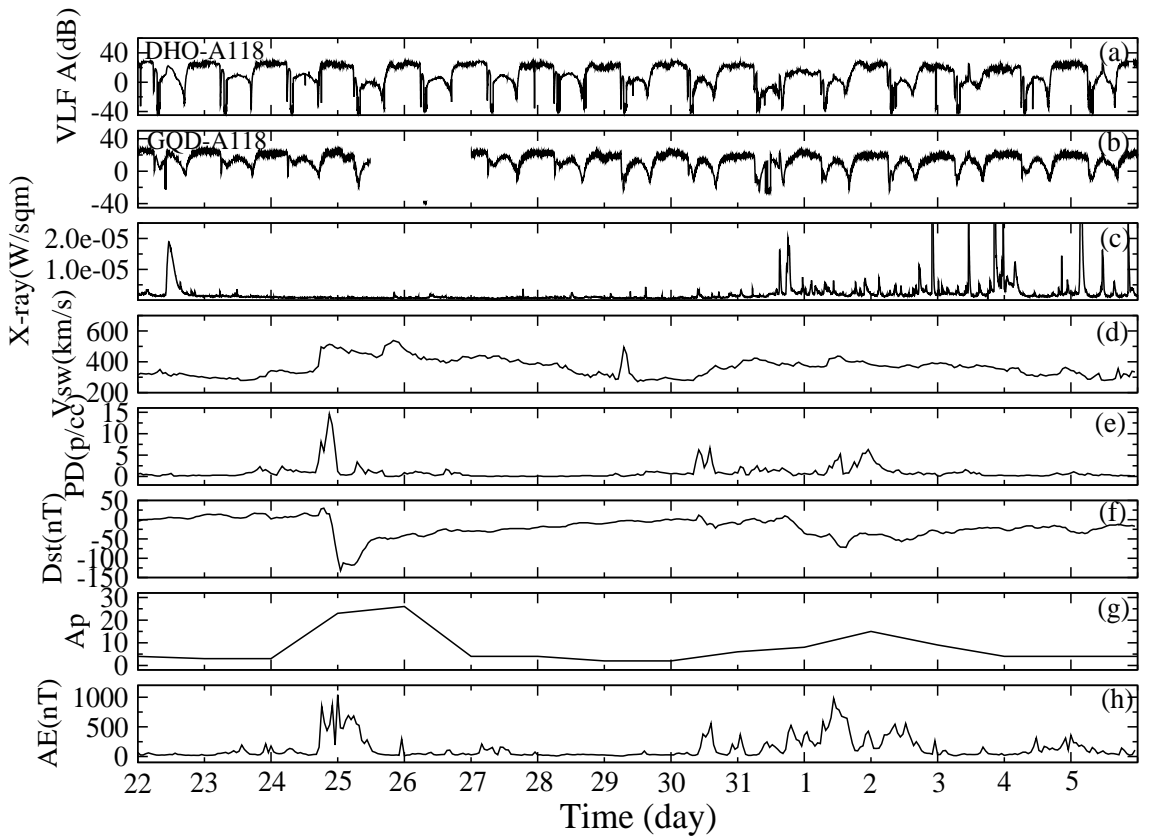


Figure 5.17: (a) Diurnal VLF amplitude for DHO-A118 and (b) GQD-A118 propagation paths (c) daily variation in X-ray flux output (d) solar wind speed (V_{sw}) (e) solar particle density (PD) (f) Disturbance storm time (Dst) (g) planetary A_p and (h) Auroral Electrojet (AE) indices during 22 October to 5 November 2011 (from Nwankwo & Chakrabarti, 2016).

(Fig. 5.17b).

Figure 5.18 shows daily deviations of Dst and AE , and variations in the MDP, MBSR, MASS, SRT and SST for (a) DHO-A118 and (b) GQD-A118 propagation paths during 22 October - 5 November 2011. Values of the parameters over the period are presented in Appendix 4. Although data for GQD-A118 propagation path during 25th and 26th is inadequate for the present analysis, we did observe a dipping of the MBSR on the main storm day, 25th Oct. Dipping of the MDP, MASS and SST have been observed on 1st Nov., and those of MBSR, MASS, and SRT on 2nd Nov., following the consecutive storms. In DHO-A118 propagation path, we observed dipping of the MDP, MBSR, MASS, and SRT on 25th Oct., dipping of

the MDP, MBSR, MASS, and SST on 1st Nov., and dipping of the MBSR and SRT on 2nd Nov. Similar to the first case (Figs. 5.17 and 5.18), we note the high flare events on 2nd Nov (up to 7 C-class and 1 M-class), that may have caused a spike in the MDP on the day in both GQD-A118 and DHO-A118 propagation paths. Although dipping of the MDP signal (following storm events) has shown a considerable consistency across the cases presented so far, the MBSR and MASS (in particular) appear to be influenced by storms occurrence time; pre-sunrise event appears to have more influence on the MBSR (dawn signal), while pre-sunset event appears to have more influence on the MASS (dusk signal). Also, the high variability or fluctuation of dusk-to-dawn ionosphere (and signal) does influence variations in MBSR and MASS, and hence their analysis (also see Nwankwo et al., 2016). However, presenting a consistency across a substantial number of cases is vital to better conclusion of this work. Against this backdrop, we statistically analyse up to 15 more storm cases between September 2011 and October 2012 in order to check the statistical significance of the observations. The 15 storm cases are presented in Table 5.7.

5.4.3 Statistical analysis of signal variations during 15 storm cases

In Figure 5.19, we show the deviation or fluctuation of the Dst and trend in variation of the MDP, MBSR, MASS, SRT and SST signals during successive one-day before and after each of the 15 selected storm cases for (a) GQD-A118 and (b) DHO-A118 propagation paths. Values of the signal metrics are provided in Appendix 3. We recognised 3 consecutive days as day before an event (BE), during event (DE) and after event (AE). A '0' indicate absence of data. In GQD-A118 propagation path (left panel), about 8 of 12 MDP, 10 of 13 MBSR, 7 of 12 MASS, 3 of 12 SRT and 5 of 12 SST showed dipping of the signals, and 12 of 15 MDP, 9 of 15 MBSR, 10 of 15 MASS, 5 of 15 SRT and 7 of 15 SST showed dipping of the signals in DHO-A118 propagation path (right panel). These values respectively corresponds to 73.5%, 68.5%, 62.5%, 29.0% and 44.5% of the combined cases. The signal levels, along with the percentage dip of the signals are presented in Table 5.8. The MDP signals (in both the propagation paths) have generally shown remarkable evidence of dipping following geomagnetic storm conditions. However, we did also observe few scenarios of propagation path-mismatched increase (of MDP) on some events day (e.g., events 4 and 7 in GQD-A118 and 9 in DHO-A118), as well as propagation path-matched increase of the signal in both propagation paths (e.g., events 3 and 12). This have been illustrated in figure 5.14. The probable reason for the former scenario is suggestive of the distinct propagation characteristics of each propagation path and X-ray flux induced spike in amplitude. Further investigation

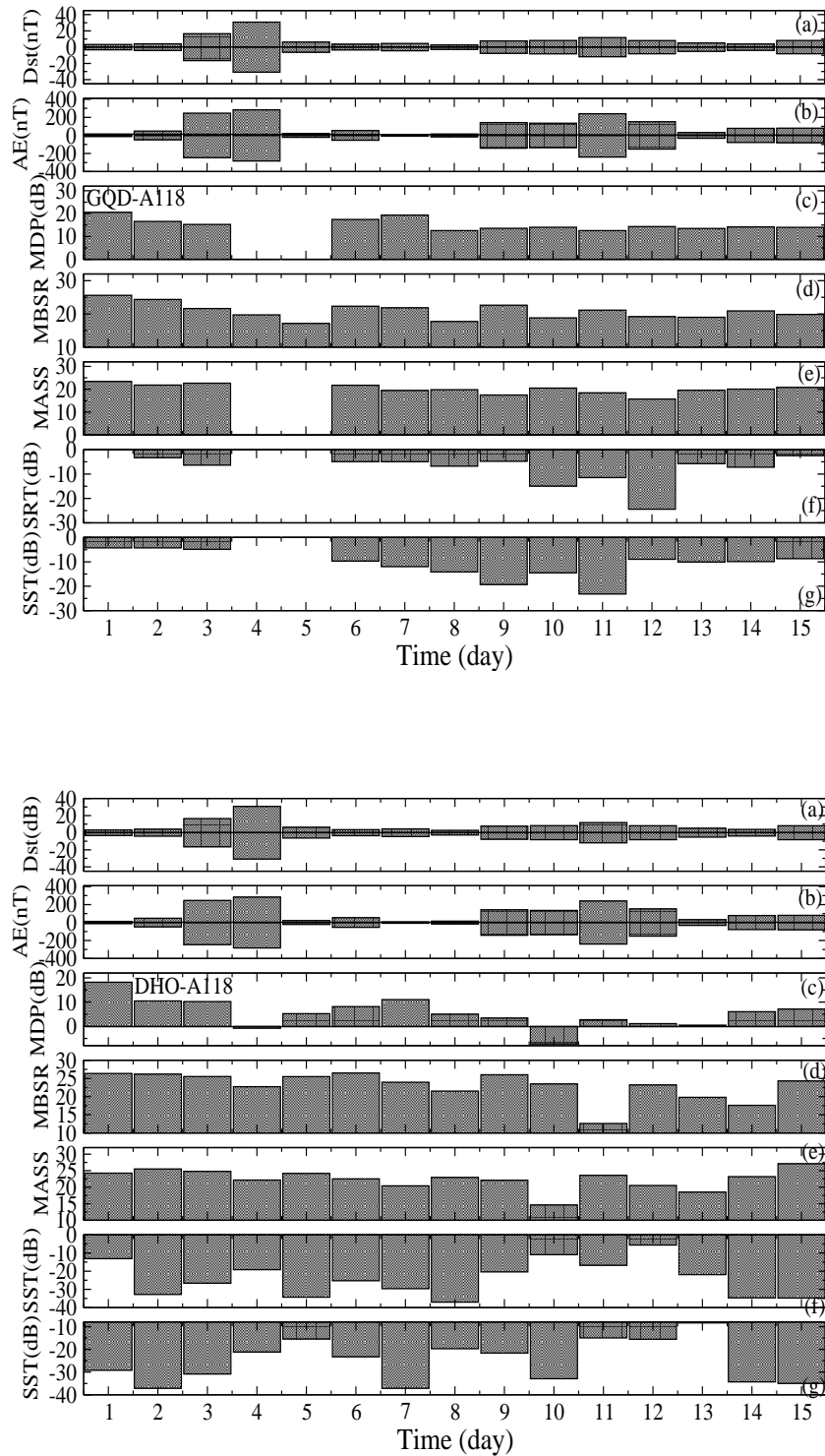


Figure 5.18: Daily deviations of Dst and AE , variations in the peak value of midday signal amplitude (MDP), 4-hour mean signal amplitude before local sunrise (MBSR), 4-hour mean signal amplitude after sunset (MASS), variation in sunrise terminator (SRT) and sunset terminator (SST) for (a) DHO-A118 and (b) GQD-A118 propagation paths during 22 October - 5 November 2011 (from Nwankwo & Chakrabarti. 2016).

of the latter scenario may be elucidating. To further check this scenario, we study and show variations in X-ray flux output and geomagnetic indices on the particular day of the events (3 and 12) to better interpret the prevailing ionospheric conditions at the time.

Table 5.7: Summary of trend in dipping of the signals' metrics during 15 geomagnetic storm case in (a) DHO-A118 and GQD-A118 propagation path (from Nwankwo & Chakrabarti. 2016).

Signal (dB)	GQD-A118 propagation path			DHO-A118 propagation path		
	Available data	No. of dips	% dip	Available data	No. of dips	% dip
MDP	12	8	67	15	12	80
MBSR	13	10	77	15	9	60
MASS	12	7	58	15	10	67
SRT	12	3	25	15	5	33
SST	12	5	42	15	7	47

In Figure 5.20, we show the diurnal VLF amplitude for (a) DHO-A118 and (b) GQD-A118 propagation paths, daily variation in (c) X-ray flux output (d) V_{sw} (e) PD and (f) Dst indices for a day before and after each of the 15 storms condition. A propagation path-matched increase of the MDP signal in both propagation paths for events 3 and 12 have been observed (see, Fig. 5.15a-b). Data showed the occurrence of M-class flare in association with the storm on 22-23 January 2012 (event 3 on 21 January), both events almost having corresponding peaks (see Fig. 5.20 (c and f)). This scenario suggest an enhancement of the instantaneous and background X-ray flux output (as stated earlier), that can cause increase (or, spike) in the signal level, and thus overshadow geomagnetic effects on the signal. This explanation may be argued for events 1 (25-27 Sept. 2011) and 6 (6-8 Mar. 2012). It should, however, be noted that such flare events in the later events started well before the storms, and continued until the storms time (in each case), suggesting an established increase in the overall background X-ray before the storms. Hence, a storm induced dipping of the signal from the already established 'increase' in flux background index is speculated on the storm days. However, further investigation is encouraged, which is beyond the scope of this work. For event 12 (during 15-17 July 2012), we observed that the peak of the storm (that commenced by midnight on 16th) was on 17th (recognised as AE). Therefore, any geomagnetic influence on the signal (e.g., dipping) is expected on 17th (or, after) and not 16th. This is probably why we observed a dipping of the AE signal (on 17th) instead in DHO-A118 propagation path.

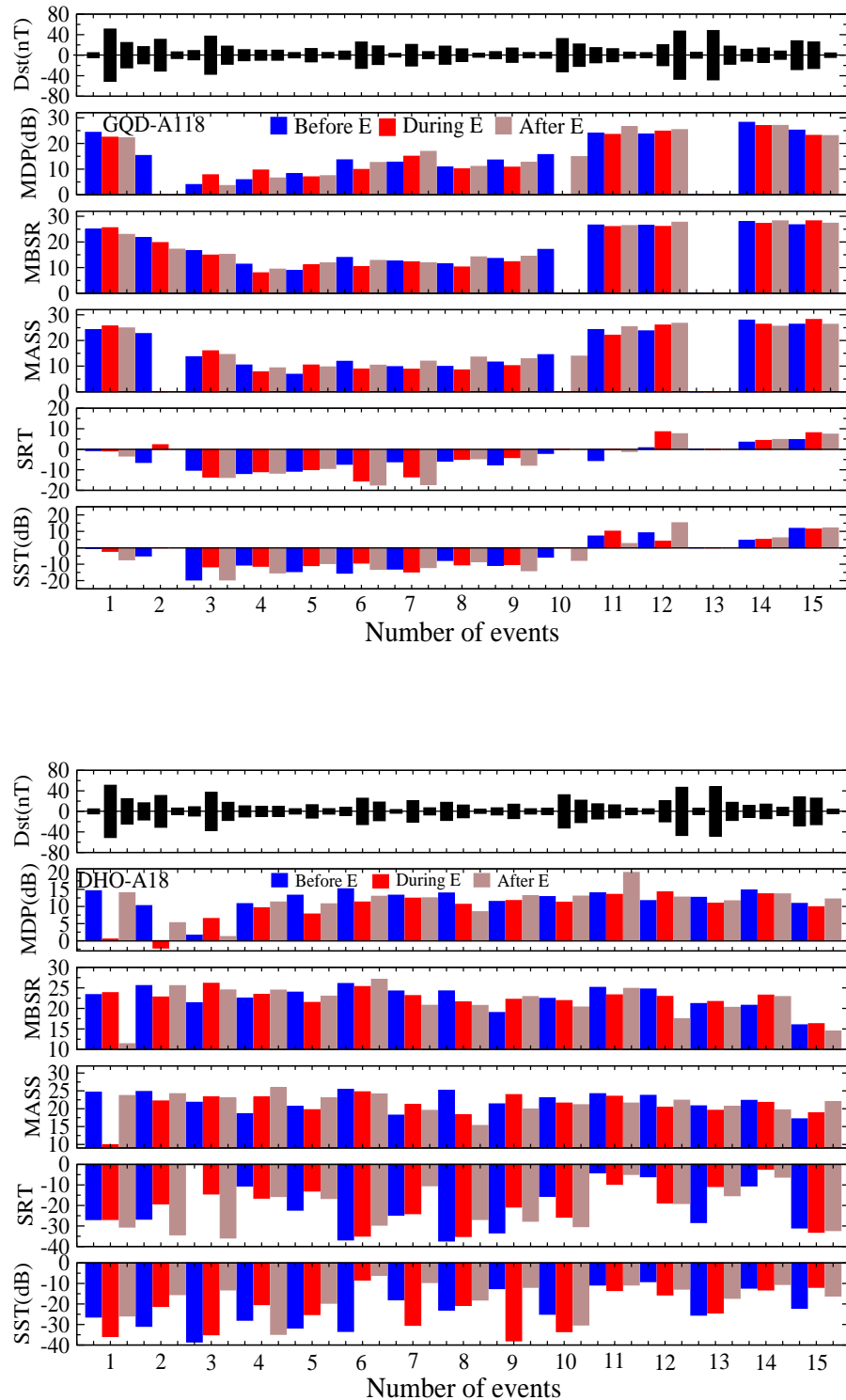


Figure 5.19: Dst deviation (fluctuation), and variations in MDP, MBSR, MASS, SRT and SST signals 1-day before, during and after each of the 15 events for (a) DHO-A118 and (b) GQD-A118 propagation paths (from Nwankwo & Chakrabarti. 2016).

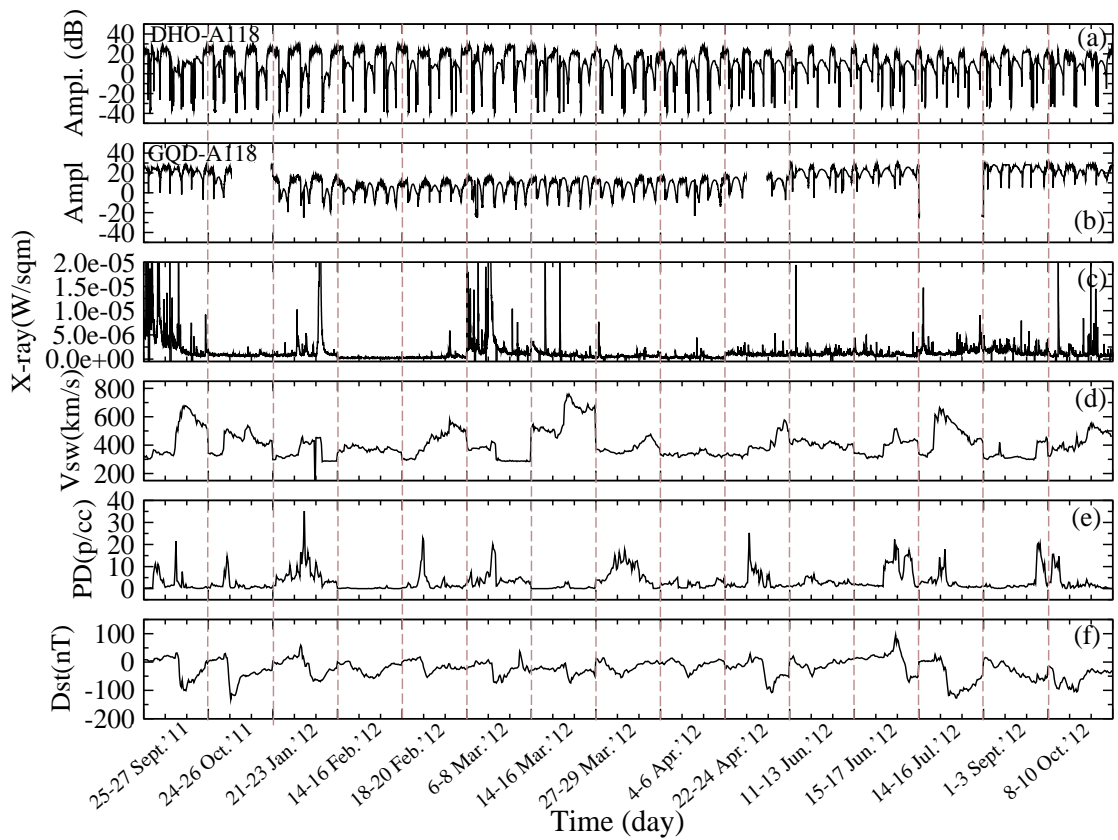


Figure 5.20: Diurnal VLF amplitude for (a) DHO-A118 and (b) GQD-A118 propagation paths, daily variation in (c) X-ray flux output (d) V_{sw} , (e) PD and (f) Dst indices for a day before and after each of the 15 storms (from Nwankwo & Chakrabarti. 2016).

Figure 5.21 shows deviations (fluctuation) in *Dst* index and 2-day mean variations of MDP, MBSR, MASS, SRT and SST signals before, during and after each event for (a) GQD-A118 and (b) DHO-A118 propagation paths. Values of the signal metrics are provided in Appendix 4. This analysis is vital to the corroboration of the result presented in Figure 5.19, because its data selection criterion differ from those of Figure 5.19. Whereas BE, DE and AE represent data for three consecutive days with reference to the event's day (DE) in the former analysis (presented in Fig. 5.19), each acronym (BE, DE or AE) represent a 2-day mean (VLF) with respect to DE (but not necessarily in succession to DE). However, it should be noted that due to the data averaging (2-day), a 'pronounced' increase or dipping in the signals (comparable to those in the former analysis (fig 5.19)) are not expected. Another important data selection criterion for this analysis is a relative geomagnetic quiet day BE and AE with respect to DE.

In GQD-A118 propagation path (left panel), 7 of 12 MDP, 7 of 13 MBSR, 7 of 12 MASS, 6 of 12 SRT and 3 of 12 SST showed dipping of the signals. In the DHO-A118 propagation path (right panel), 10 of 15 MDP, 11 of 15 MBSR, 11 of 15 MASS, 6 of 14 SRT and 6 of 15 SST showed dipping of the signals. These values correspond respectively to 62.5%, 63.5%, 65.5%, 46.5% and 32.5% of the combined cases. The signal levels, along with the percentage dip of the signals are presented in Table 6.3. In general, the trends in variation of the signal metrics considerably reflected the prevailing space weather coupled effects in the lower ionosphere. The MDP signal appears to be more responsive (about 68% for combined analysis shown in figs 6.6 and 6.8) to geomagnetic perturbations than other signal metrics, as was the case in analysis in Chapter 5 (see fig 5.11 and 5.12). However, we anticipate an improvement in analysis with smaller data range for MBSR and MASS because of the high fluctuation of dusk-to-dawn D region ionosphere. This approach will be considered in future analysis. In the last Chapter (also see Nwankwo et al., 2016) we noted a drawback to SRT and SST analysis due to the existence of mode shifts during sunrise and sunsets (which produced the so-called pseudo-SRT and SST) exhibited by diurnal VLF signal (see, Fig. 5.1(e and f)). These are due to higher order destructive interference pattern in signals. It was concluded in the study that the post-storm SRT and SST variations do not appear to have a well-defined trend. Also, the occurrence of solar flares during sunrise/sunset can influence SRT/SST (Chakrabarti et al., 2010). To circumvent this problem, we paid attention to the 'first' SRT and SST values (in case of a pseudo-terminator) during analysis of the signal metrics. In the present analysis, a rise (vertical shift) in SRT and SST amplitude under geomagnetic storm conditions have been favoured in both propagation paths. We found a respective dipping of 46.5% and 32.5% in the combined cases, suggesting a rise in majority of the cases. However, this needs

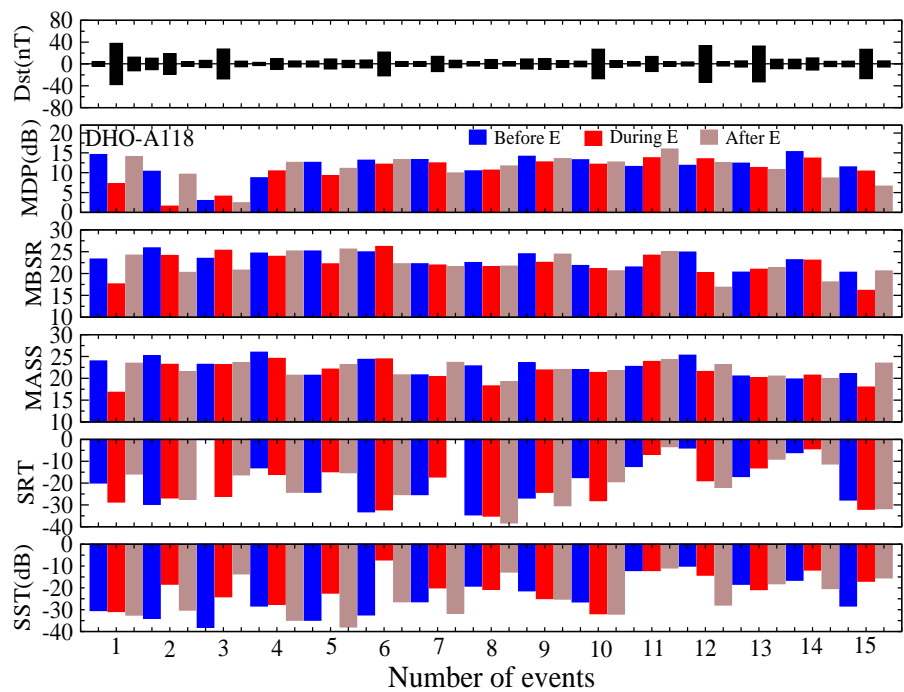
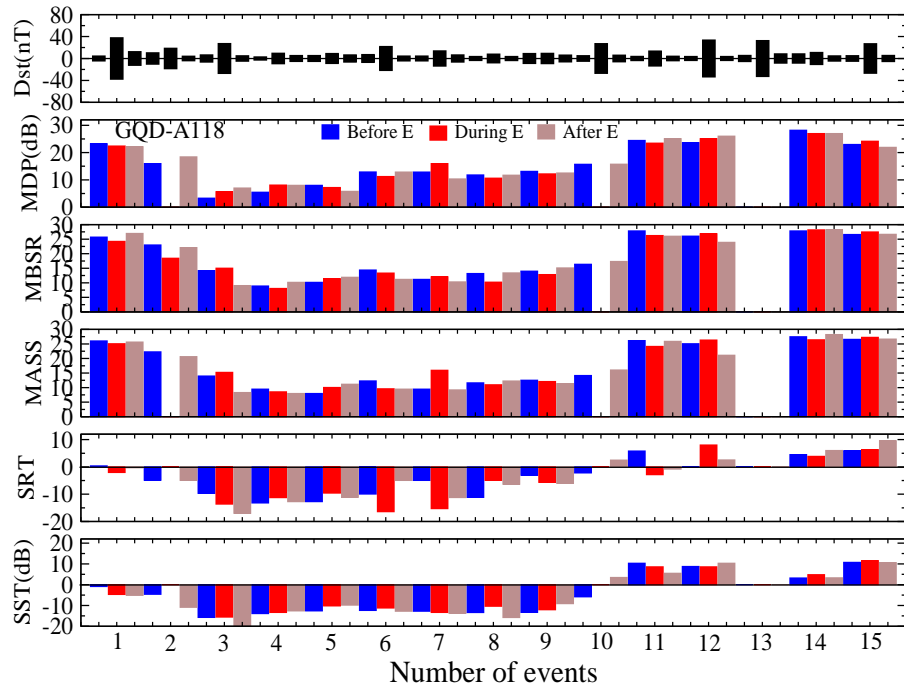


Figure 5.21: Dst deviation and 2-day mean variations of MDP, MBSR, MASS, SRT and SST signals before, during and after each event for (a) GQD-A118 and (b) DHO-A118 propagation paths (from Nwankwo & Chakrabarti. 2016).

to be investigated further. It is important to note that out of the two propagation paths used in this study, the DHO-A118 signal appears to be more sensitive to geomagnetic storm-induced magnetosphere-ionospheric dynamics, as was the case in the analysis in the last section.

Table 5.8: Summary of trend in 2-day mean signals dipping following 15 geomagnetic storm case in (a) DHO-A118 and GQD-A118 propagation path (from Nwankwo & Chakrabarti 2016).

Signal (dB)	GQD-A118 propagation path			DHO-A118 propagation path		
	Available data	No. of dips	% dip	Available data	No. of dips	% dip
MDP	12	7	58	15	10	67
MBSR	13	7	54	15	11	73
MASS	12	7	58	15	11	73
SRT	12	6	50	14	6	43
SST	12	3	25	15	6	40

In this analysis the MDP exhibited characteristic dipping scenario in about 68% of the combined cases in response to the storms. The MDP signals that showed no dipping scenario include some cases of propagation paths-mismatched increase in 3 events, as well as propagation paths-matched increase of the signal in 2 events. While, the mismatched increase of the signal may be related to the distinct characteristics of each propagation path and X-ray flux-induced spike in amplitude, the matched-increase appeared to be influenced by M-class flare concurrent with storm event, and delayed responses of the local ionosphere to storm effects. The MBSR and MASS also showed significant dipping (about 66% and 64%, respectively) following the storms, but appear to be influenced by the event(s) occurrence time and intensity, and the highly variable conditions of dusk-to-dawn D-region ionosphere (as noted in previous analysis). Conversely, the SRT and SST amplitude showed respective dipping of 46.5% and 32.5% of the combined cases, favouring storm-induced rise of the signal instead.

Chapter 6

Summary and Conclusion

6.1 Summary and conclusion

The work presented in this Thesis consists of two main studies. In the first part, we studied space weather-induced variations of thermospheric temperature and density at 400-450 km and the consequential atmospheric drag on LEO satellites leading to accelerated orbit decay. The main goal of the study is to understand both long- and short-term solar forcing-induced variability of the atmosphere and their implications on satellites' normal aerodynamic drag, for the purpose of quantitative estimation of drag-induced orbital decay on LEO satellites. The atmosphere is known to change significantly with respect to temperature, density and composition as a result of variation of solar activity during the entire cycle. Solar energetic particles and electromagnetic radiation from solar energetic events are the main driver of atmospheric variations and consequent drag-induced accelerated orbital decay of LEO satellites. We modeled (or, simulated) atmospheric drag effect on the orbit of two hypothetical LEO satellites (SAT-BCI and SAT-BCII) of different ballistic coefficients initially at 450 km, at different phases of the solar cycle and during intervals of strong geomagnetic perturbations or storm condition. We found strong dependence of the satellites orbital decay rate on the intensity of solar activity and phase, and satellite's ballistic coefficient. We showed that the mean annual decay rate during the peak of 23rd solar maximum was almost twice that 24th maximum phase. SAT-BCI decayed by 48 ± 2 km/year and 25 ± 7 km/year during solar 2000-2002 and 2012-2014 maxima respectively, while SAT-BCII decayed by 62 ± 1 km/year and 31 ± 10 km/year respectively during the maxima. However, a LEO satellite initially at $h=450$ km could experience a decay rate of up to 41 ± 19 km per year (corresponding to ~ 3 km/month) during solar maximum and 11 ± 6 km per year (corresponding to ~ 1 km/month) during the solar minimum. These rates also depend on ballistic coefficient and solar activity. The thermospheric T and ρ range

is about 915-1470 K and 1.15×10^{-12} - 14.70×10^{-12} kg/m³ during the maxima, and about 756-1212 K and 0.31×10^{-12} - 3.59×10^{-12} kg/m³ during the minimum phase. These parameters defines the conditions in near-Earth space environment through which the satellites traversed. The extreme values are mostly associated with intervals of strong geomagnetic disturbances or storms. Also, using a modified density profile model, we found that dominant CIR-induced effects during the declining phase of the solar cycle (or solar minimum) could result to additional decay rate of up to 3 km/year. We also showed that intervals of strong density perturbations due to geomagnetic storms and the resulting additional atmospheric heating can result in additional 60% decay in each event. This impact could vary depending on the severity and duration of the event (also, see Nwankwo et al., 2015).

We then implemented our new drag model on orbits of real satellites, namely, the Challenging Mini-satellite Payload (CHAMP), the Gravity field and steady state Ocean Circulation Explorer (GOCE), the International Space Station (ISS), and on an interplanetary mission spacecraft, the Mangalyaan Mars Orbiter (MMO). The simulated decay profile of CHAMP spacecraft produced a difference of about ~ 1 km between 2003 and 2005 when compared with the actual decay profile. Our model produced a decay of 70.98 km, but the satellite's actual decay profile for the period was 70 km. The GOCE re-entry profile model between 21st October and 11th November 2013 produced about 5-hour difference behind the actual re-entry time (also, see Nwankwo et al., 2015). The simulation of the ISS monthly decay profile produced mean decay rate of about 2.95 km/month during the solar maximum and 1.0 km/month during the solar minimum, corresponding to about 1.975 km/month (Nwankwo and Chakrabarti, 2014). The monthly orbital decay of the ISS have been estimated to be about 2 km. The simulation of drag effect on Mangalyaan Mars orbiter mission produced a cumulative orbit decay of about 720 m for a total perigee height boost of about 250 km during geocentric trajectory, mean altitude variation of about 158 m with respect to the sun during 300-day heliocentric trajectory, and about 701 m during 100-day trajectory in areocentric orbit, based on the presently known Mars-Earth atmosphere density ratio (also, see Nwankwo and Chakrabarti, 2015).

In the second part we performed a diagnostic study of geomagnetic storm-induced ionospheric changes in mid-latitude (40° - 54°) D-region (60-90 km) using VLF radio signal. The aim of the study is to understand VLF signal behaviour that are related to storms driven ionospheric changes, for efficient probing of solar-induced changes in lower ionosphere. The response of diurnal VLF signal to space weather-induced ionospheric disturbances vary from one propagation path to another, and also depend on location of the transmitters and receivers, ionisation and chemistry of the D region over the propagation path, and the intensity of induced pertur-

bations. Other influencing factors include signal frequency and nature of Earth's surface (also see, Mimno, 1937; Mitra, 1974; Poole, 1999; Melia, 2010). Here, we analysed the trends in variation of characterised amplitude metrics of the signal (e.g. MBSR, MDP, MASS, SRT and SST), under varying degrees of 16 geomagnetic storm conditions between February 2011 and June 2012. We found that the trends in variation generally reflected the prevailing space weather conditions at various time scales. In particular, 'dipping' of VLF mid-day signal amplitude (MDP) occurs after geomagnetic perturbed or storm conditions in the time scale of 1-2 days. The mean signal before sunrise (MBSR) and mean signal after sunset (MASS) also exhibit storm-induced dipping, but they appear to be influenced by event's exact occurrence time, and the highly variable conditions of dusk-to-dawn ionosphere. We also observed some cases of the signals rise (e.g., MDP, MBSR or MASS) following a significant geomagnetic event. We speculate that this effect may be related to storms associated phenomena, but also effects arising from sources other than solar origin. The magnitude of induced dipping (or rise) appear to significantly depend on the intensity and duration of event(s), as well as the propagation path of the signal. Also, the post-storm day signal (following a main event, with lesser or significantly reduced geomagnetic activity), exhibited a tendency of recovery to pre-storm day level. In this particular analysis, we do not see a well defined trend in variations of the post-storm sunrise terminator (SRT) and sunset terminator (SST). The SRT and SST signals show more dipping in GQD-A118 propagation path but generally an increase along DHO-A118 propagation path. Thus the result could be propagation path dependent and detailed modeling is required to understand these phenomena (Nwankwo et al., 2016).

In related study we performed a more detailed analysis to further substantiate the previous findings while building on the analysis in previous work (also, see Nwankwo et al., 2016), and also investigated the observed cases of increase of VLF amplitude (against dipping scenario) following geomagnetic storm conditions. The trend in variation of the signal metrics were analysed for up to 20 storm conditions between September 2011 and October 2012. We found to be in agreement with the previous study (Nwankwo et al. 2016). The MDP exhibited characteristic dipping scenario in about 68% of the combined cases in response to the storms. The MDP signals that showed no dipping scenario include some cases of propagation paths-mismatched increase in 3 events, and propagation paths-matched increase of the signal in 2 events. We speculate that the mismatched increase of the signal may be related to distinct characteristics of each propagation path and X-ray flux-induced spike in amplitude. Further analysis showed that the matched-increase appeared to be influenced by M-class flare concurrent with storm event, and delayed responses of the local ionosphere to storm effects. The MBSR and MASS also showed significant

dipping (about 66% and 64%, respectively) due to storms, but also appear to be influenced by the the factors highlighted above (also see Nwankwo et al., 2016). Conversely, the SRT and SST amplitude showed respective dipping of 46.5% and 32.5% of the combined cases, favouring storm-induced rise of the signal instead (also, see Nwankwo and Chakrabarti, 2016).

These studies and subsequent findings (Nwankwo et al., 2016; Nwankwo and Chakrabarti, 2016) demonstrate the applicability and efficiency of VLF radio waves (as a tool) in identification, separation and interpretation of ionospheric dynamics from various forcing origin (e.g., due to geomagnetic storm). However, it is important to note that obtaining a ‘perfect’ consistency in signal trend across all cases in a given analysis remains a challenge, because solar and other forcing mechanisms (whose individual effects are difficult to estimate) also cause significant fluctuation in radio signal, since they are interconnected and possibly non-linearly coupled. It is therefore, recommended that the study or investigation of ionospheric changes due to distinct phenomenon include proper identification and separation of other contributing sources around intervening period of analysis before definite conclusion.

6.2 Future work

1. We plan to extend this work to include application on more LEO satellite under varying space environmental conditions. Also, we anticipate that two solar events E_1 and E_2 may produce different impacts if they occurred in a reversed sequence. Extending this logic to solar cycles, the results of a launch in a solar minimum would be different from that in a solar maximum even if both satellites survives for, say a full cycle. This is due to strong non-linearity in drag effects. This aspect would be included in our future work/model and reported accordingly.
2. The drag model presented in this work is mainly for trajectory of satellites in near-circular orbit. In future work, we plan to extent this idea to model the scenario in other type of orbits (e.g. elliptic), and also implement resulting model to real satellites in elliptical orbit such as the recently launched ASTRONSAT
3. Many researchers have investigated and reported ionospheric and VLF signal anomalies before seismic events (e.g., Hayakawa et al., 1996; Ray and Chakrabarti, 2012; Sasmal and Chakrabarti, 2009). Such anomalies were often attributed to seismicity and therefore viewed as precursors. However, in order to ensure that such VLF anomalies are indeed due to seismic events, it is imperative that other possible and potential drivers of ionospheric anomalies

around intervening period are also investigated, identified and separated. In future, we will investigate possible solar and geomagnetic-induced perturbations of the ionosphere within the time frame in which ionospheric precursors (using VLF signal) were reported. This must be taken into consideration before marking anomalies as precursors. For this two prong approaches are necessary: (i) to reproduce propagation path dependent effects on VLF signals due to number of specific types of solar induced perturbations as in Palit et al. (2013) and (ii) to find statistical correlations among various quantities using data for longer duration.

Appendix

APPENDIX I

GQD-A118										DHO-A118					DST	
DATE	SIG	MBSR	MDP	MASS	SRT	SST	MBSR	MDP	MASS	SRT	SST	DEVIATIONS				
04022011	BE	11.28±1.10	1.71	10.41±1.29	-5.65	-4.14	22.49±1.15	2.80	18.58±1.69	-28.96	-25.53	±20.97				
05022011	DE	10.66±1.77	1.28	11.45±1.13	-6.21	-2.69	21.98±1.76	2.44	22.72±2.70	-36.04	-28.13	±8.99				
06022011	AE	13.54±0.67	5.61	11.16±2.54	-4.34	-2.95	23.64±2.20	3.80	21.41±2.48	-36.40	0.00	±2.23				
28022011	BE	16.04±0.85	8.56	14.49±1.19	-5.31	-2.62	24.74±1.66	4.16	23.07±1.81	-38.62	-9.63	±4.54				
01032011	DE	13.96±1.23	6.00	13.18±1.49	-6.79	-2.20	23.43±1.22	3.58	22.29±2.35	-10.96	-24.76	±36.28				
02032011	AE	13.14±1.79	7.46	10.50±0.65	-1.89	-1.26	22.55±1.60	2.55	16.64±2.54	-29.74	-16.60	±7.26				
04042011	BE	16.81±1.40	14.17	14.23±3.24	0.71	-8.52	21.66±2.05	9.87	21.92±1.87	-37.03	-21.64	±8.28				
06042011	DE	16.17±1.71	13.75	16.14±1.61	-9.21	-14.68	22.31±2.81	9.75	20.48±0.84	-25.25	-9.08	±24.31				
07042011	AE	16.03±1.56	13.44	15.88±1.57	-4.46	-16.83	19.81±2.09	10.10	20.94±2.73	-38.08	-14.93	±12.40				
11042011	BE	17.43±0.74	15.37	20.62±0.50	-3.56	-14.97	19.73±1.20	6.91	20.62±0.50	-37.42	-37.03	±8.92				
12042011	DE	17.78±0.62	14.77	22.27±1.10	-5.31	-15.66	23.49±1.17	8.00	22.27±1.10	-37.81	-25.67	±22.11				
13042011	AE	21.89±1.60	13.79	20.49±1.77	-4.26	-10.05	21.89±1.60	7.61	20.49±1.77	-28.71	-39.04	±10.01				
25092011	BE	24.94±1.16	23.30	24.98±0.96	-0.59	-0.40	23.33±1.29	14.57	24.60±0.99	-26.86	-26.34	±4.56				
26092011	DE	25.52±1.14	22.61	25.62±1.59	-0.75	-2.11	23.81±1.05	0.45	9.90±1.48	-26.79	-35.80	±50.73				
27092011	AE	22.91±1.35	22.15	24.87±1.63	-3.26	-7.25	11.38±1.05	14.00	23.68±1.90	-30.47	-25.82	±24.54				
24102011	BE	21.63±1.02	15.28	22.66±0.93	-6.35	-4.89	25.53±0.92	10.23	24.80±1.33	-26.64	-30.84	±16.55				
25102011	DE	19.70±3.77	0.00	0.00	2.16	0.00	22.75±0.99	-2.12	22.16±1.68	-19.19	-21.17	±30.76				
26102011	AE	17.14±2.59	0.00	0.00	0.00	0.00	25.51±1.22	5.23	24.17±1.18	-34.30	-15.40	±6.25				
21012012	BE	15.11±1.24	3.94	13.62±0.90	-10.18	-19.56	21.36±1.80	1.59	21.78±1.52	0.00	-38.48	±8.80				
22102012	DE	14.86±1.94	7.73	15.92±0.99	-13.47	-11.56	26.10±1.08	6.46	23.28±1.93	-14.35	-34.97	±37.00				
23012012	AE	15.12±1.20	3.55	14.50±1.23	-13.70	-19.51	24.47±1.75	1.17	22.96±1.42	-35.80	-13.12	±17.40				
14022012	BE	11.28±1.10	5.81	10.41±1.29	-11.78	-10.45	22.49±1.15	10.80	18.58±1.69	-10.48	-27.89	±10.63				
15022012	DE	7.92±1.22	9.61	07.75±1.98	-10.86	-11.21	23.38±1.66	9.59	23.23±1.16	-16.42	-20.27	±9.63				
16022012	AE	9.37±0.87	6.49	09.28±1.41	-11.60	-15.23	24.44±1.49	11.27	25.85±1.63	-15.62	-34.75	±9.63				
18022012	BE	8.86±1.54	8.19	06.77±1.84	-10.65	-14.47	23.94±1.32	13.28	20.66±1.22	-22.23	-31.69	±4.97				
19022012	DE	11.00±1.27	6.96	10.39±1.18	-9.89	-10.79	21.44±0.90	7.77	19.77±1.39	-12.93	-25.11	±12.81				
20022012	AE	11.74±0.67	7.39	09.67±2.25	-9.27	-9.56	22.96±1.62	10.76	22.98±2.05	-16.56	-19.62	±5.15				
06032012	BE	13.93±1.19	13.57	11.85±1.16	-7.22	-15.40	26.03±1.07	15.15	25.37±1.30	-36.78	-33.32	±7.91				
07032012	DE	10.34±0.88	9.81	08.82±3.27	-15.40	-9.27	25.29±0.91	11.28	24.72±2.36	-34.86	-8.34	±25.41				
08032012	AE	12.76±1.37	12.56	10.33±2.34	-17.35	-13.08	27.07±0.79	12.95	24.11±1.39	-29.57	-5.97	±17.95				
14032012	BE	12.14±0.64	13.66	09.77±2.18	-6.05	-12.89	24.21±1.41	13.27	18.17±1.42	-24.69	-17.93	±3.31				
15032012	DE	12.21±0.78	14.99	08.78±2.79	-13.39	-14.64	23.10±1.64	12.42	21.16±0.91	-23.95	-30.37	±20.75				
16032012	AE	11.86±0.66	16.87	11.91±1.12	-17.11	-11.99	20.74±0.69	12.50	19.50±1.12	-10.38	-9.53	±6.73				
27032012	BE	11.43±0.93	10.74	09.87±2.18	-5.73	-7.63	24.23±1.98	13.91	25.14±1.92	-37.29	-22.91	±17.50				
28032012	DE	10.20±1.01	10.59	09.47±1.48	-4.87	-10.35	21.53±1.15	10.62	18.24±2.19	-35.09	-20.66	±12.09				
29032012	AE	14.13±0.81	11.02	13.50±1.14	-4.56	-8.43	20.70±1.45	8.45	15.27±2.64	-26.79	-18.03	±3.74				
04042012	BE	13.55±0.78	12.50	11.55±1.15	-7.57	-10.72	18.98±1.90	11.45	21.32±1.42	-33.32	-12.47	±6.73				
05042012	DE	12.24±0.71	11.71	11.23±2.67	-3.99	-10.15	22.19±0.97	11.71	23.92±2.28	-20.71	-37.94	±13.82				
06042012	AE	14.41±0.68	12.61	12.86±1.96	-7.74	-13.90	22.86±2.77	13.16	19.84±2.22	-27.65	-11.85	±4.90				

21042012	BE	17.06±0.82	15.62	14.43±2.75	-1.97	-5.67	22.41±1.71	12.87	22.98±1.95	-15.53	-24.97	±5.64
23042012	DE	0.00	0.00	0.00	0.00	0.00	21.88±3.33	11.24	21.55±1.14	-25.67	-33.43	±32.23
24042012	AE	0.00	14.82	13.84±2.02	0.00	-7.60	20.32±4.92	13.02	21.09±1.41	-30.28	-30.19	±21.65
10062012	BE	28.17±0.10	23.66	26.64±2.21	0.61	4.32	21.36±1.72	11.39	22.73±1.84	-16.28	-11.03	±3.88
11062012	DE	26.05±1.25	23.37	24.22±3.25	-5.44	7.08	25.09±1.61	13.96	24.19±1.40	-4.02	-10.72	±14.58
12062012	AE	25.95±1.00	23.50	24.01±2.30	-0.22	10.05	23.27±1.60	13.52	23.47±1.65	-9.63	-13.39	±12.47
15062012	BE	26.42±1.33	23.60	23.72±2.51	0.67	9.05	24.69±1.23	11.68	23.71±1.44	-5.97	-9.08	±4.80
16062012	DE	26.00±1.97	24.76	25.99±3.05	8.47	3.93	22.90±1.87	14.25	20.34±1.33	-18.78	-15.57	±20.24
17062012	AE	27.66±0.69	25.36	26.64±2.06	7.54	15.18	17.48±2.11	12.73	22.36±0.97	-18.99	-12.74	±46.75

APPENDIX II

DATE/DAY	SIG	GQD-A118					DHO-A118				
		MBSR	MDP	MASS	SRT	SST	MBSR	MDP	MASS	SRT	SST
02-03022011	BE	9.87	5.79	8.15	-3.21	-4.09	19.72	4.61	20.04	-31.6	-12.85
05-06022011	DE	12.10	3.45	11.31	-5.28	-2.82	22.81	3.12	22.07	-36.22	-28.13
08-09022011	AE	10.87	5.17	8.74	-3.94	-8.50	21.90	7.30	21.35	-21.46	-37.49
27-28022011	BE	14.44	7.9	14.11	-3.18	-2.26	23.35	4.16	22.29	-25.85	-10.94
01-02032011	DE	13.55	6.73	11.84	-4.34	-1.73	22.99	3.07	19.47	-20.35	-20.68
04-05032011	AE	12.37	8.8	12.20	-3.55	-2.20	23.10	4.49	19.91	-33.52	-25.43
01-02042011	BE	15.73	15.44	14.78	-4.86	2.66	21.59	11.66	20.78	-33.89	-30.81
06-70042011	DE	15.60	13.70	16.01	-6.84	-15.76	21.06	9.93	20.71	-31.67	-12.01
08-09042011	AE	16.61	14.05	15.11	-1.75	-12.13	22.24	9.17	20.00	-36.54	-31.99
10-11042011	BE	17.88	15.37	17.78	-4.05	-13.14	18.63	8.17	20.63	-35.27	-36.30
12-13042011	DE	19.84	14.28	21.38	-4.79	-12.86	22.69	7.81	21.38	-33.26	-32.36
16-17042011	AE	18.10	13.87	15.29	-10.18	-13.57	21.32	7.78	21.88	-30.58	-36.38
24-25092011	BE	25.68	23.20	25.18	0.36	-0.84	23.30	14.56	23.96	-19.91	-30.38
25-27092011	DE	24.22	22.38	25.25	-2.01	-4.68	17.60	7.23	16.79	-28.63	-30.81
28-29092011	AE	26.94	22.10	25.62	-0.29	-5.09	24.20	14.05	23.43	-15.82	-32.44
23-24102011	BE	22.99	15.94	22.25	-4.83	-4.58	25.86	10.34	25.16	-29.73	-33.97
25-26102011	DE	18.42	0.00	0.00	0.00	0.00	24.13	1.56	23.17	-26.75	-18.29
27-28102011	AE	22.08	18.40	20.61	-4.9	-10.84	20.23	9.59	21.48	-27.44	-30.17
20-21012012	BE	14.15	3.25	13.96	-9.68	-15.72	23.45	2.96	23.17	0.00	-38.08
22-23012012	DE	14.99	5.64	15.21	-13.59	-15.54	25.29	4.08	23.12	-26.08	-24.05
30-31012012	AE	9.02	6.97	8.27	-16.95	-19.87	20.76	2.42	23.56	-16.19	-13.58
10-11022012	BE	8.29	5.44	8.46	-13.18	-13.85	24.65	8.72	25.95	-12.98	-28.28
15-16022012	DE	8.65	8.05	8.52	-11.23	-13.33	23.91	10.43	24.54	-16.02	-27.51
17-18022012	AE	10.13	7.98	7.96	-12.71	-12.56	25.13	12.59	20.67	-24.17	-34.82
17-18022012	BE	10.13	7.98	7.96	-12.71	-12.56	25.13	12.59	20.67	-24.17	-34.82
19-20022012	DE	11.39	7.18	10.03	-9.58	-10.18	22.20	9.27	22.07	-14.75	-22.37
21-22022012	AE	11.88	5.75	11.12	-11.11	-9.78	25.58	11.06	23.06	-15.2	-37.88
05-06032012	BE	14.37	12.85	12.28	-9.92	-12.34	24.93	13.13	24.31	-33.13	-32.36
07-08032012	DE	13.31	11.19	9.58	-16.38	-11.18	26.18	12.12	24.42	-32.22	-7.16
13-14032012	AE	11.16	12.83	9.44	-4.92	-12.75	22.21	13.29	20.76	-25.26	-26.34
13-14032012	BE	11.16	12.83	9.44	-4.92	-12.75	22.21	13.29	20.76	-25.26	-26.34
15-16032012	DE	12.04	15.93	15.93	-15.25	-13.32	21.92	12.46	20.33	-17.17	-19.95
21-22032012	AE	10.30	10.29	9.18	-11.21	-13.78	21.58	9.92	23.61	0.00	-31.63
25-26032012	BE	13.17	11.78	11.11	-11.14	-13.35	22.50	10.46	22.83	-34.53	-19.16
28-29032012	DE	10.20	10.59	10.95	-4.87	-10.35	21.53	10.62	18.24	-35.09	-20.66
30-31032012	AE	13.39	11.67	12.25	-6.29	-15.75	21.67	11.69	19.19	-38.21	-12.74
01-02042012	BE	13.37	13.09	12.50	-3.00	-13.27	24.50	14.13	23.51	-26.78	-21.33
05-06042012	DE	13.00	12.16	12.05	-5.64	-12.03	22.53	12.69	21.88	-24.18	-24.90
07-08042012	AE	15.08	12.47	11.33	-6.00	-9.08	24.42	13.52	22.00	-30.33	-25.14
19-20042012	BE	16.35	15.67	14.12	-2.16	-5.79	21.82	13.24	21.94	-17.44	-26.39
23-24042012	DE	0.00	0.00	0.00	0.00	0.00	21.10	12.13	21.32	-27.98	-31.81
27-28042012	AE	17.32	15.70	16.01	2.46	3.44	20.59	12.67	21.72	-19.30	-32.01
06-07062012	BE	27.82	24.42	26.12	5.8	10.28	21.47	11.56	22.69	-12.35	-12.03
11-12062012	DE	26.21	23.44	24.12	-2.83	8.57	24.18	13.74	23.83	-6.83	-12.06
13-14062012	AE	25.98	25.06	25.85	-0.76	5.45	24.98	15.95	24.21	-3.3	-10.84
14-15062012	BE	26.02	23.60	25.06	0.10	8.71	24.89	11.83	25.29	-3.88	-10.02
16-17062012	DE	26.83	25.06	26.32	8.01	8.56	20.19	13.49	21.54	-18.89	-14.16
21-22-62012	AE	23.87	26.00	21.10	2.52	10.28	16.83	12.53	23.06	-21.94	-27.82

APPENDIX 1

Date	<u>DHO-A118 Signal (in dB)</u>					<u>GQD-A118 Signal (in dB)</u>					Dst(nT) Flare(CMX)	
	MBSR	MDP	MASS	SRT	SST	MBSR	MDP	MASS	SRT	SST		
160911	26.34±1.27	17.84	21.82±2.10	-10.65	-24.48	27.76±0.60	25.00	24.37±1.92	2.93	-3.75	±3.52	14 0 0
170911	22.92±2.68	15.00	21.79±1.03	-15.02	-27.65	28.12±0.20	24.42	23.39±2.03	3.99	-1.60	±32.89	2 0 0
180911	26.39±1.23	14.53	23.71±1.60	-7.57	-29.83	27.94±0.72	24.45	24.63±1.80	5.60	-1.84	±6.85	6 0 0
190911	23.26±1.21	15.00	24.12±1.30	-9.76	-33.97	24.37±0.95	24.33	25.13±1.87	5.26	-0.51	±5.82	4 0 0
200911	24.79±1.11	15.31	25.14±1.32	-21.52	-30.80	25.57±2.00	24.05	23.99±2.05	1.48	-2.40	±2.99	11 0 0
210911	23.61±1.44	14.30	20.86±1.06	-15.53	-28.96	26.76±0.59	25.13	23.74±1.22	2.95	-4.44	±4.62	9 1 0
220911	21.34±1.18	26.11	21.50±1.58	-19.25	-34.63	26.29±0.59	25.85	24.15±1.40	-1.62	-6.38	±5.14	5 1 1
230911	24.07±2.19	14.96	23.01±2.50	-14.97	-32.90	25.94±0.62	23.97	25.32±1.63	-0.34	-6.05	±2.78	9 3 0
240911	23.26±2.04	14.55	23.32±1.00	-12.96	-34.41	26.42±1.02	23.10	25.38±2.10	1.30	-1.28	±4.08	4 8 1
250911	23.33±1.29	14.57	24.60±0.99	-26.86	-26.34	24.94±1.16	23.30	24.98±0.96	-0.59	-0.40	±4.56	4 6 0
260911	23.81±1.05	2.05	9.90±1.48	-26.79	-35.80	25.52±1.14	22.61	25.62±1.59	-0.75	-2.11	±50.73	9 2 0
270911	11.38±1.05	14.00	23.68±1.90	-30.47	-25.82	22.91±1.35	22.15	24.87±1.63	-3.26	-7.25	±24.54	8 0 0
280911	25.90±1.74	12.66	20.98±2.09	-9.85	-28.62	27.31±0.77	22.51	25.13±1.38	3.28	-7.57	±12.37	3 1 0
290911	22.49±2.04	15.43	25.87±3.31	-21.78	-36.25	26.56±1.29	21.69	26.10±2.32	-3.85	-2.61	±6.73	3 0 0
300911	24.57±1.53	12.83	23.05±1.49	-18.63	-34.86	25.33±2.09	23.62	24.55±2.12	2.93	-2.06	±11.49	4 1 0

APPENDIX 2

DATE	DHO-A118 Signal (in dB)					GQD-A118 Signal (in dB)					Dst(nT) Flare(CMX)	
	MBSR	MDP	MASS	SRT	SST	MBSR	MDP	MASS	SRT	SST		
221011	26.38±2.06	18.21	24.27±1.55	-13.12	-29.22	25.59±0.83	20.54	23.41±1.68	-0.06	-4.26	±3.30	3 1 0
231011	26.18±1.05	10.45	25.51±0.82	-32.81	-37.10	24.35±0.88	16.59	21.83±0.87	-3.31	-4.27	±4.08	3 0 0
241011	25.53±0.92	10.23	24.80±1.33	-26.64	-30.84	21.63±1.02	15.28	22.66±0.93	-6.35	-4.89	±16.35	0 0 0
251011	22.75±0.99	-0.75	22.16±1.68	-19.19	-21.17	19.70±3.77	0.00	0.00±0.00	2.16	0.00	±30.76	1 0 0
261011	25.51±1.22	5.23	24.17±1.18	-34.30	-15.40	17.14±2.59	0.00	0.00±0.00	0.00	0.00	±6.25	1 0 0
271011	26.49±1.72	8.16	22.53±4.45	-25.25	-23.23	22.32±1.43	17.45	21.74±1.33	-4.92	-9.69	±3.53	1 0 0
281011	23.96±1.68	11.02	20.42±1.32	-29.63	-37.10	21.83±0.86	19.35	19.47±2.52	-4.97	-11.98	±4.48	3 0 0
291011	21.53±1.66	4.99	22.94±1.78	-37.03	-19.72	17.72±1.51	12.58	19.81±1.84	-6.77	-14.14	±2.73	5 0 0
301011	26.03±1.49	3.39	22.13±1.63	-20.38	-21.64	22.62±1.14	13.59	17.48±0.82	-4.77	-19.30	±7.63	8 0 0
311011	23.48±1.31	-7.23	14.62±1.47	-10.93	-32.90	18.80±1.04	14.05	20.53±2.94	-14.93	-14.51	±8.20	4 2 0
011111	12.63±1.80	2.75	23.60±2.95	-16.74	-14.97	21.14±1.82	12.56	18.46±0.91	-11.45	-23.17	±11.84	6 0 0
021111	23.21±1.47	1.11	20.52±5.62	-5.62	-15.57	19.16±0.89	14.35	15.72±2.01	-24.42	-8.96	±8.15	7 1 0
031111	19.82±1.29	0.07	18.50±2.34	-21.87	-8.37	19.00±0.91	13.51	19.57±0.93	-5.73	-10.08	±5.17	13 2 0
041111	17.60±2.42	6.05	23.19±1.16	-34.63	-34.30	20.89±0.74	14.20	20.06±1.41	-7.19	-9.89	±3.90	6 1 0
051111	24.30±1.98	7.13	27.09±1.39	-34.75	-34.97	19.85±0.70	14.00	20.83±1.18	-2.44	-8.71	±8.16	4 3 0

APPENDIX 3

DHO-A118 Signal (in dB)

GQD-A118 Signal (in dB)

DATE	SIG	MBSR	MDP	MASS	SRT	SST	MBSR	MDP	MASS	SRT	SST	DST(nT)
25092011	BE	24.94±1.16	24.30	24.20±0.96	-0.59	-0.40	23.33±1.29	14.57	24.60±0.99	-26.86	-26.34	±4.56
26092011	DE	25.52±1.14	22.41	25.62±1.59	-0.75	-2.11	23.81±1.05	0.45	9.90±1.48	-26.79	-35.80	±50.73
27092011	AE	22.91±1.35	22.15	24.87±1.63	-3.26	-7.25	11.38±1.05	14.00	23.68±1.90	-30.47	-25.82	±24.54
24102011	BE	21.63±1.02	15.28	22.66±0.93	-6.35	-4.89	25.53±0.92	10.23	24.80±1.33	-26.64	-30.84	±16.55
25102011	DE	19.70±3.77	0.00	0.00±0.00	2.16	0.00	22.75±0.99	-2.12	22.16±1.68	-19.19	-21.17	±30.76
26102011	AE	17.14±2.59	0.00	0.00±0.00	0.00	0.00	25.51±1.22	5.23	24.17±1.18	-34.30	-15.40	±6.25
21012012	BE	16.51±1.24	3.94	13.62±0.90	-10.18	-19.56	21.36±1.80	1.59	21.78±1.52	0.00	-38.48	±8.80
22102012	DE	14.86±1.94	7.73	15.92±0.99	-13.47	-11.56	26.10±1.08	6.46	23.28±1.93	-14.35	-34.97	±37.00
23012012	AE	15.12±1.20	3.55	14.50±1.23	-13.70	-19.51	24.47±1.75	1.17	22.96±1.42	-35.80	-13.12	±17.40
14022012	BE	11.28±1.10	5.81	10.41±1.29	-11.78	-10.45	22.49±1.15	10.80	18.58±1.69	-10.48	-27.89	±10.63
15022012	DE	7.92±1.22	9.61	7.75±1.98	-10.86	-11.21	23.38±1.66	9.59	23.23±1.16	-16.42	-20.27	±9.62
16022012	AE	9.37±0.87	6.49	9.28±1.41	-11.60	-15.23	24.44±1.49	11.27	25.85±1.63	-15.62	-34.75	±9.63
18022012	BE	8.86±1.54	8.19	6.77±1.84	-10.65	-14.47	23.94±1.32	13.28	20.66±1.22	-22.23	-31.69	±4.97
19022012	DE	11.00±1.27	6.96	10.39±1.18	-9.89	-10.79	21.44±0.90	7.77	19.70±1.39	-12.93	-25.11	±12.81
20022012	AE	11.74±0.67	7.39	9.67±2.25	-9.27	-9.56	22.96±1.62	10.76	22.98±2.05	-16.56	-19.62	±5.15
06032012	BE	13.93±1.19	13.57	11.85±1.16	-7.22	-15.40	26.03±1.07	15.15	25.37±1.30	-36.78	-33.32	7.91
07032012	DE	10.34±0.88	9.81	8.82±3.27	-15.40	-9.27	25.29±0.91	11.28	24.72±2.36	-34.86	-8.34	±25.41
08032012	AE	12.76±1.37	12.56	10.33±2.34	-17.35	-13.08	27.07±0.79	12.95	24.11±1.39	-29.57	-5.97	±17.95
14032012	BE	12.54±0.64	12.66	9.77±2.18	-6.05	-12.89	24.21±1.41	13.27	18.17±1.42	-24.69	-17.93	±3.31
15032012	DE	12.21±0.78	14.99	8.78±2.79	-13.39	-14.64	23.10±1.64	12.42	21.16±0.91	-23.95	-30.37	±20.75
16032012	AE	11.86±0.66	16.87	11.91±1.12	-17.11	-11.99	20.74±0.69	12.50	19.50±1.12	-10.38	-9.53	±6.73
27032012	BE	11.43±0.93	10.74	9.87±2.18	-5.73	-7.63	24.23±1.98	13.91	25.14±1.92	-37.29	-22.91	±17.50
28032012	DE	10.20±1.01	10.05	8.47±1.48	-4.87	-10.35	21.53±1.15	10.62	18.24±2.19	-35.09	-20.66	±12.09
29032012	AE	14.13±0.81	11.02	13.50±1.14	-4.56	-8.43	20.70±1.45	8.45	15.27±2.64	-26.79	-18.03	±3.74
04042012	BE	13.55±0.78	13.50	11.55±1.15	-7.57	-10.72	18.98±1.90	11.45	21.32±1.42	-33.32	-12.47	±6.73
05042012	DE	12.24±0.71	10.71	10.13±2.67	-3.99	-10.15	22.19±0.97	11.71	23.92±2.28	-20.71	-37.94	±13.82
06042012	AE	14.41±0.68	12.61	12.86±1.96	-7.74	-13.90	22.86±2.77	13.16	19.84±2.22	-27.65	-11.85	±4.90
21042012	BE	17.06±0.82	15.62	14.43±2.75	-1.97	-5.67	22.41±1.71	12.87	22.98±1.95	-15.53	-24.97	±5.64
23042012	DE	0.00±0.00	0.00	0.00±0.00	0.00	0.00	21.88±3.33	11.24	21.55±1.14	-25.67	-33.43	±32.23
24042012	AE	0.00±0.00	14.82	13.84±2.02	0.00	-7.60	20.32±4.92	13.02	21.09±1.41	-30.28	-30.19	±21.65
11062012	BE	26.55±1.25	24.00	24.22±3.25	-5.44	7.08	25.09±1.61	13.96	24.19±1.40	-4.02	-10.72	±14.58
12062012	DE	25.95±1.00	23.50	22.01±2.30	-0.22	10.05	23.27±1.60	13.52	23.47±1.65	-9.63	-13.39	±12.47
13062012	AE	26.34±0.96	26.51	25.30±3.49	-1.05	2.52	24.86±2.26	19.93	21.55±1.92	-4.82	-10.72	±5.70

15062012	BE	26.42±1.33	23.60	23.72±2.51	0.67	9.05	24.69±1.23	11.68	23.71±1.44	-5.97	-9.08	±4.80
16062012	DE	26.00±1.97	24.76	25.99±3.05	8.47	3.93	22.90±1.87	14.25	20.34±1.33	-18.78	-15.57	±20.24
17062012	AE	27.66±0.69	25.36	26.64±2.06	7.54	15.18	17.48±2.11	12.73	22.36±0.97	-18.99	-12.74	±46.75
14072012	BE	0.00±0.00	0.00	0.00±0.00	0.00	0.00	21.16±0.90	12.64	20.78±1.23	-28.29	-25.39	±5.52
15072012	DE	0.00±0.00	0.00	0.00±0.00	0.00	0.00	21.66±1.27	10.94	19.54±0.94	-10.72	-24.35	±47.88
16072012	AE	0.00±0.00	0.00	0.00±0.00	0.00	0.00	20.24±1.15	11.63	20.64±0.52	-15.19	-17.21	±17.39
01092012	BE	27.86±0.48	28.20	27.89±1.76	3.41	4.53	20.73±0.78	14.81	22.31±1.13	-10.42	-12.25	±11.32
02092012	DE	27.16±0.11	26.90	26.31±1.06	4.25	5.05	23.22±0.70	13.67	21.75±0.64	-2.31	-13.12	±13.86
03092012	AE	28.20±3.57	26.97	25.49±2.13	4.73	6.02	22.85±0.66	13.65	19.66±1.31	-6.18	-10.45	±7.84
08102012	BE	26.67±0.87	25.15	26.30±1.76	4.59	11.76	15.97±1.62	10.88	17.14±3.39	-30.93	-21.99	±27.91
09102012	DE	28.20±6.25	23.10	28.15±0.23	8.00	11.36	16.26±3.49	9.88	18.84±1.32	-33.01	-11.85	±25.64
10102012	AE	27.27±0.68	23.00	26.26±1.29	7.33	12.02	14.43±3.14	12.16	21.97±1.90	-32.19	-16.10	±4.20

APPENDIX 4

DATE	SIG	GQD-A118 Signal (in dB)					DHO-A118 Signal (in dB)				
		MBSR	MDP	MASS	SRT	SST	MBSR	MDP	MASS	SRT	SST
24-25092011	BE	25.68	23.20	25.18	0.36	-0.84	23.30	14.56	23.96	-19.91	-30.38
26-27092011	DE	24.22	22.38	25.25	-2.01	-4.68	17.60	7.23	16.79	-28.63	-30.81
28-29092011	AE	26.94	22.10	25.62	-0.29	-5.09	24.20	14.05	23.43	-15.82	-32.44
23-24102011	BE	22.99	15.94	22.25	-4.83	-4.58	25.86	10.34	25.16	-29.73	-33.97
25-26102011	DE	18.42	0.00	0.00	0.00	0.00	24.13	1.56	23.17	-26.75	-18.29
27-28102011	AE	22.08	18.40	20.61	-4.9	-10.84	20.23	9.59	21.48	-27.44	-30.17
20-21012012	BE	14.15	3.25	13.96	-9.68	-15.72	23.45	2.96	23.17	0.00	-38.08
22-23012012	DE	14.99	5.64	15.21	-13.59	-15.54	25.29	4.08	23.12	-26.08	-24.05
30-31012012	AE	9.02	6.97	8.27	-16.95	-19.87	20.76	2.42	23.56	-16.19	-13.58
10-11022012	BE	8.29	5.44	8.46	-13.18	-13.85	24.65	8.72	25.95	-12.98	-28.28
15-16022012	DE	8.65	8.05	8.52	-11.23	-13.33	23.91	10.43	24.54	-16.02	-27.51
17-18022012	AE	10.13	7.98	7.96	-12.71	-12.56	25.13	12.59	20.67	-24.17	-34.82
17-18022012	BE	10.13	7.98	7.96	-12.71	-12.56	25.13	12.59	20.67	-24.17	-34.82
19-20022012	DE	11.39	7.18	10.03	-9.58	-10.18	22.20	9.27	22.07	-14.75	-22.37
21-22022012	AE	11.88	5.75	11.12	-11.11	-9.78	25.58	11.06	23.06	-15.2	-37.88
05-06032012	BE	14.37	12.85	12.28	-9.92	-12.34	24.93	13.13	24.31	-33.13	-32.36
07-08032012	DE	13.31	11.19	9.58	-16.38	-11.18	26.18	12.12	24.42	-32.22	-7.16
13-14032012	AE	11.16	12.83	9.44	-4.92	-12.75	22.21	13.29	20.76	-25.26	-26.34
13-14032012	BE	11.16	12.83	9.44	-4.92	-12.75	22.21	13.29	20.76	-25.26	-26.34
15-16032012	DE	12.04	15.93	15.93	-15.25	-13.32	21.92	12.46	20.33	-17.17	-19.95
21-22032012	AE	10.30	10.29	9.18	-11.21	-13.78	21.58	9.92	23.61	0.00	-31.63
25-26032012	BE	13.17	11.78	11.11	-11.14	-13.35	22.50	10.80	22.83	-34.53	-19.16
28-29032012	DE	10.20	10.59	10.95	-4.87	-10.35	21.53	10.62	18.24	-35.09	-20.66
30-31032012	AE	13.39	11.67	12.25	-6.29	-15.75	21.67	11.69	19.19	-38.21	-12.74
01-02042012	BE	13.37	13.09	12.50	-3.00	-13.27	24.50	14.13	23.51	-26.78	-21.33
05-06042012	DE	13.00	12.16	12.05	-5.64	-12.03	22.53	12.69	21.88	-24.18	-24.90
07-08042012	AE	15.08	12.47	11.33	-6.00	-9.08	24.42	13.52	22.00	-30.33	-25.14
19-20042012	BE	16.35	15.67	14.12	-2.16	-5.79	21.82	13.24	21.94	-17.44	-26.39
23-24042012	DE	0.00	0.00	0.00	0.00	0.00	21.10	12.13	21.32	-27.98	-31.81
27-28042012	AE	17.32	15.70	16.01	2.46	3.44	20.59	12.67	21.72	-19.30	-32.01
06-07062012	BE	27.82	24.42	26.12	5.8	10.28	21.47	11.56	22.69	-12.35	-12.03
11-12062012	DE	26.21	23.44	24.12	-2.83	8.57	24.18	13.74	23.83	-6.83	-12.06
13-14062012	AE	25.98	25.06	25.85	-0.76	5.45	24.98	15.95	24.21	-3.3	-10.84
14-15062012	BE	26.02	23.60	25.06	0.10	8.71	24.89	11.83	25.29	-3.88	-10.02
16-17062012	DE	26.83	25.06	26.32	8.01	8.56	20.19	13.49	21.54	-18.89	-14.16
21-22062012	AE	23.87	26.00	21.10	2.52	10.28	16.83	12.53	23.06	-21.94	-27.82
13-14072012	BE	0.00	0.00	0.00	0.00	0.00	20.29	12.38	20.51	-16.97	-18.32
15-16072012	DE	0.00	0.00	0.00	0.00	0.00	20.95	11.28	20.09	-13.00	-20.78
20-21072012	AE	0.00	0.00	0.00	0.00	0.00	21.33	10.77	20.48	-9.015	-18.10
3108-01092012	BE	27.81	28.17	27.46	4.47	3.17	23.14	15.30	19.83	-6.00	-16.47
02-03092012	DE	28.18	26.94	26.40	3.83	4.79	23.04	13.66	20.71	-4.25	-11.79
10-11092012	AE	28.20	26.93	28.20	5.99	3.27	18.06	8.65	19.95	-11.20	-20.29
05-06102012	BE	26.58	22.96	26.55	5.88	10.69	20.27	11.44	21.03	-27.74	-28.30
08-09102012	DE	27.44	24.13	27.23	6.30	11.56	16.12	10.38	17.99	-31.97	-16.92
11-12102012	AE	26.64	21.89	26.64	9.54	10.57	20.57	6.59	23.47	-31.68	-15.39

References

- Alfonsi L., Kavanagh A. J., Amata E., Cilliers P., Correia E., Freeman M., Kauristie K., Liu R. Y., Luntama J. P., Mitchell C. N. and Zherebtsov G. A., 2008. Probing the high latitude ionosphere from ground-based observations: The state of current knowledge and capabilities during IPY (2007-2009). *J. Atmos. Solar-Terr. Phys.* 70, 2293-2308.
- Alurkar S. K., 1996. *Solar and interplanetary disturbances*. World Scientific Publishing Co. Pvt. Ltd., Singapore.
- Anselmo L. and Pardini C., 2011. Orbital evolution of the first upper stages used for the new European and Chinese navigation satellite systems. *Acta Astronaut.* 68, 2066-2079.
- Araki T., 1974. Anomalous Phase Changes of Trans-equatorial VLF Radio Waves during Geomagnetic Storms. *J. Geophys. Res.* 79, 4811-4813.
- Baker D. N., 1996. Solar wind-magnetosphere drivers of space weather. *J. Atmos. Solar-Terr. Phys.* 58, 15OW526.
- Baker D. N., 2000. Effects of the Sun on the Earth's environment. *J. Atmos. Solar-Terr. Phys.* 62, 1669-1681.
- Basak T., S. Pal and S. K. Chakrabarti, 2011. VLF study of Ionospheric properties during solar flares of varied intensity for a fixed propagation path. General Assembly and Scientific Symposium, 2011 XXXth URSI, 13-20 Aug. 2011.
- Boeing, 2012. Background: International space station Boeing Defense, Space and Security, St Louis, MO 63166.
- Borovsky J. E. and Denton M. H., 2006. Differences between CME-driven storms and CIR-driven storms, *J. Geophys. Res.* 111.
- Bowman R. B. and Moe K., 2005. Drag coefficient variability at 175-500 km from the orbit decay analysis of spheres. AAS/AIAA, ASS-05-257.

- Bowman B. R., W. Kent Tobiska and Michael J. Kendra, 2008. The thermospheric semiannual density response to solar EUV heating. *J. Atmos. Solar-Terr. Phys.* 70, 1482-1496.
- Braun R. D. and Manning R. M., 2005. Mars Exploration Entry, Descent and Landing Challenges. IEEE-AC paper 0076.
- Brueckner G. E., Howard R. A., Koomen M. J., Korendyke C. M., Michels D. J., Moses J. D., Socker D. G., Dere K. P., Lamy P. L., Llebaria, A., Bout M. V., Schwenn R., Simnett G. M., Bedford D. K. and Eyles C. J., 1995. The Large Angle Spectroscopic Coronagraph (LASCO), *Solar Phys.* 162, 357.
- Bruinsma S., Thuillier G. and Barlier F., 2003. The DTM-2000 empirical thermosphere model with new data assimilation and constraints at lower boundary: accuracy and properties. *J. Atmos. Solar-Terr. Phys.* 65, 1053-1070.
- Budden K. G., 1985. *The propagation of radio waves: the theory of radio waves of low power in the ionosphere and magnetosphere.* Cambridge University Press, Cambridge, ISBN 0521 25461 2.
- Buonsanto M. J., 1999. Ionospheric Storms - A Review, *Space Sci. Rev.* 88, 563-601.
- Burke W. J., 2000. Magnetosphere-ionosphere coupling: selected topics. *J. Atmos. Solar-Terr. Phys.* 62, 817-824.
- Burns A. G., S.C. Solomon, L. Qian, W. Wang, B.A. Emery, M. Wiltberger and D.R. Weimer, 2012. The effects of Corotating interaction region/High speed stream storms on the thermosphere and ionosphere during the last solar minimum. *J. Atmos. Solar-Terr. Phys.* 83, 79-87.
- Carroll B. W. and Ostlie D. A., 1996. *An Introduction to Modern Astrophysics.* First Ed., Addison Wesley Pub. Comp., Michigan.
- Cargill P.J., J. Chen, D. S. Spicer and S. T. Zalesak, 1996. Magnetohydrodynamic simulations of the motion of magnetic flux tubes through a magnetized plasma. *J. Geophys. Res.* 101, 4855-4870.
- Chakrabarti S. K., M. Saha, R. Khan, Mandal S., Acharyya K. and Saha R., 2005. Possible Detection of Ionospheric Disturbances during Sumatra-Andaman Islands. *IJRS Phys.* 34, 314-317.
- Chakrabarti, S. K., Sasmal, S. and Chakrabarti, S., 2010. Ionospheric anomaly due to seismic activities - Part 2: Evidence from D-layer preparation and disappearance times. *Nat. Haz. Earth Syst. Sci.* 10, 1751-1757.

- Chapman S., 1931. The absorption and dissociative or ionizing effect of monochromatic radiation in an atmosphere on a rotating earth. *Proc. Phys. Soc.* 43, 1047-1055.
- Chenette D.L., D. W. Datlowe, R. M. Robinson, T. L. Schumaker, R. R. Vondrak and J. D. Winningham, 1993. Atmospheric energy input and ionization by energetic electrons during the geomagnetic storm of 8-9 November 1991, *Geophys. Res. Lett.* 20, 1323.
- Chen C. H., C. H. Lin, L. C. Chang, J. D. Huba, J. T. Lin, A. Saito and J. Y. Liu, 2013. Thermospheric tidal effects on the ionospheric midlatitude summer nighttime anomaly using SAMI3 and TIEGCM, *J. Geophys. Res.: Space Phys.* 118, 3836-3845.
- Chen G., Jiyao Xu, Wenbin Wang, Jiuhou Lei and Alan G. Burns, 2012. A comparison of the effects of CIR- and CME-induced geomagnetic activity on thermospheric densities and spacecraft orbits: Case studies. *J. Geophys. Res.* 117, A08315.
- Chisham G., Lester M., Milan S. E., Freeman M. P., Bristow W. A., Grocott A., McWilliams K. A., Ruohoniemi J. M., Yeoman T. K., Dyson P. L., Greenwald R. A., Kikuchi T., Pinnock M., Rash J.P.S, Sato N., Sofko G. J., Villain J. P. and A. D. M. Walker, 2007. A decade of the Super Dual Auroral Radar Network (SuperDARN): scientific achievements, new techniques and future directions. *Surv. Geophys.* 28, 33-109.
- Chobotov V. A., 2002. *Orbital Mechanics*, 3rd Ed. AIAA Education series. American Institute of Aeronautics Inc, Virginia. 629.4113, 193-213.
- Clilverd M. A. and Rodger C. J., 1999. Investigating seismoionospheric effects on a long subionospheric path. *J. Geophys. Res.* 104, 28171-28179.
- Clilverd M. A., Rodger C. J., Gamble R. J., Ulich T., Raita T., Seppala A., Green J. C., Thomson N. R., Sauvaud J. A. and Parrot M., 2010. Ground-based estimates of outer radiation belt energetic electron precipitation fluxes into the atmosphere. *J. Geophys. Res.* 115, A12304.
- Cranmer S. R., 2009. Coronal Holes. *Living Rev. Solar Phys.* 6, 3.
- Cook G. E., 1965. Satellite drag coefficients. *Planet. Space Sci.* 13, 929.
- Cook G. E., 1966. Drag coefficients of spherical satellites. *Ann. Geophys.* 22, 53.

- Cowley S. W. H., J. A. Davies, A. Grocott, H. Khan, M. Lester, K. A. McWilliams, S. E. Milan, G. Provan, P. E. Sandholt, J. A. Wild and T. K. Yeoman, 2003. Solar-Wind magnetosphere ionosphere interactions in the Earth's plasma environment. *Phil. Trans. R. Soc. Lond. A* 361, 113-126.
- Danilov A. D. and Lastovicka J., 2001. Effects of Geomagnetic Storms on the Ionosphere and Atmosphere, *International J. Geomag. Aeron.* 2, 209-224.
- Davies K., 1990. *The ionospheric radio*. Peter Peregrinus Ltd, London, ISBN 0-86341-186-X.
- Deng Y., Y. Huang, S. Solomon, L. Qian, D. Knipp, D. R. Weimer and J. S. Wang, 2012. Anomalously low geomagnetic energy inputs during 2008 solar minimum. *J. Geophys. Res.* 117, A09307.
- Doornbos E., 2012. *Thermospheric Density and Wind Determination from Satellite Dynamics*. Springer-Verlag Berlin Heidelberg. Springer Theses.
- Doornbos E. and H. Klinkrad, 2006. Modelling of space weather effects on satellite drag. *Adv. Space Res.* 37, 1229-1239.
- Emmert J. T. and Picone M., 2010. Climatology of globally averaged thermospheric mass density. *J. Geophys. Res.*, 115, A09326.
- ESA1, 2013. *GOCE Completes its Mission*. European Space Agency.
- ESA2, 2013. *GOCE Gives in to Gravity*. European Space Agency.
- ESA3, 2013. *GOCE Satellite*. European Space Agency.
- Ezell E. C. and Ezell L., 2009. *On Mars: Exploration of the Red Planet 1958-1978*. Dover Pub., INC. Mineola, NY.
- Forbes J., Bruinsma S. L., Zhang X. and Oberheide J., 2009. Surface-Exosphere Coupling due to Thermal Tides. *Geophys. Res. Lett.* 36, L15812.
- Fortescue P., John Stark and Graham Swinerd, 2003. *Spacecraft System Engineering*. John Wiley & Sons Ltd. The Atrium, Southern Gate. Chichester. W. S. England.
- Goldstein J., Burch J. L., Sandel B. L., Mende S. B., P. C:son Brandt and Hairston M. R., 2005. Coupled response of the inner magnetosphere and ionosphere on 17 April 2002, *J. Geophys. Res.* 110, A03205.

- Golub L. and Pasachoff J. M., 1997. *The Solar Corona*. 1st Ed. Cambr. Univ. Press, UK.
- Golub L. and Pasachoff J. M., 2010. *The Solar Corona*. 2nd Ed. Cambr. Univ. Press, UK.
- Goncharenko, L. P., A. J. Coster, R. A. Plumb and D. I. V. Domeisen, 2012. The potential role of stratospheric ozone in the stratosphere-ionosphere coupling during stratospheric warmings, *Geophys. Res. Lett.* 39, L08101.
- Gopalswamy N., 2009. Coronal mass ejections and space weather, *Climate and Weather of the Sun-Earth System (CAWSES): Selected Papers from the 2007 Kyoto Symposium*, Edited by T. Tsuda, R. Fujii and M. A. Geller, 77-120. TERRAPUB, Tokyo, 2009.
- Gopalswamy N., 2004. In *The Sun and the Heliosphere as an Integrated System*, Eds., G. Poletto and S.T. Suess, Kluwer, 201.
- Gopalswamy N., 2009. Coronal mass ejections and space weather. *Climate and Weather of the Sun-Earth System (CAWSES): Selected paper from the 2007 Kyoto Symposium*, Edited by T. Tsuda, R. Fuji, K. Shibata and M. A. Geller, 77-120.
- Gosling J. T., 1993. The solar flare myth. *J. Geophys. Res.*, 98, 18937.
- Gosling J. T., S. J. Bame, D. J. McComas, J. L. Phillips, B. E. Goldstein and M. Neugebauer, 1994. The speeds of coronal mass ejections in the solar wind at mid heliographic latitudes: Ulysses, *Geophys. Res. Lett.* 21, 1109.
- Gosling J.T. and Pizzo V.J., 1999. Formation and evolution of corotating interaction regions and their three dimensional structure, *Space Sci. Rev.* 89, 2152.
- Green S. F. and Jones M. H., 2004. *An introduction to the Sun and Stars*. Cambr. Univ. Press, UK.
- Greenwald R. A., K. B. Baker, J. R. Dudeney, M. Pinnock, T. B. Jones, E. C. Thomas, J.-P. Villain, J.-C. Cerisier, C. Senior, C. Hanuise, R. D. Hunsucker, G. Sofko, J. Koehler, E. Nielsen, R. Pellinen, A. D. M. Walker, N. Sato and H. Yamagishi, 1995. Darn/Superdarn: A Global View of the Dynamics of High-Latitude Convection, *Space Sci. Rev.* 71, 761-796.
- Greenwald R. A., J. M. Ruohoniemi, W. A. Bristow, G. J. Sofko, J.-P. Villain, A. Huuskonen, S. Kokubun, and, L. A. Frank, 1996. Mesoscale dayside convection vortices and their relation to substorm phase, *J. Geophys. Res.* 101, 21697-21713.

- Grubor D., Sulic D. and Zigman V., 2005. Influence of solar X-ray flares on the Earth-ionosphere waveguide. *Serb. Astron. J.* 171, 29-35.
- Hamilton D. C., Gloeckler G., Ipavich F. M., Stdemann W., Wilken B. and Kremser G., 1988. Ring current development during the great geomagnetic storm of February 1986. *J. Geophys. Res.: Space Phys.* 93, 14343-14355.
- Hagan M. and Forbes J., 2002. Migrating and Non-migrating Diurnal Tides in the Middle and Upper Atmosphere excited by Tropospheric Latent Heat Release. *J. Geophys. Res.* 107, 4754.
- Han F. and S. A. Cummer, 2010. Midlatitude nighttime D region ionosphere variability on hourly to monthly time scales. *J. Geophys. Res.* 115, A09323.
- Hayakawa M, O. A. Molchanov, Ondoh T. and Kawai E., 1996. The precursory signature effect of Kobe earthquake on VLF subionospheric signals. *Phys. Earth Planet. Inter.* 57, 64-67.
- Hausleitner W., S. Krauss, G. Stangl, J. Weingrill, H. I. M. Lichtenegger, H. Lammer and M. L. Khodachenko, 2007. Response of LEO Satellite Drag Parameters to Anomalies in the Upper Atmosphere during Extreme Solar Events. Kola Science Centre, Russian Academy of Science. 'Physics of Auroral Phenomena', Proc. XXX Annual Seminar, Apatity, 158-162
- Hedin A. E., 1987. MSIS-86 thermospheric model. *J. Geophys. Res.* 92, 4649-4662.
- Heikkila W., 2011. *Earth's Magnetosphere*. Elsevier Kidlington, Oxford, UK.
- Hejda P. and Bochncek J., 2005. Geomagnetically induced pipe-to-soil voltages in the Czech oil pipelines during October - November 2003. *Ann. Geophys.* 23, 3089-3093.
- Honary F, Stocker A. J., Robinson T. R. and Jones T. B., 1995. Ionospheric plasma response to HF radio waves operating at frequencies close to the third harmonic of electron gyrofrequency. *J. Phys. Res.* 100, 21489-21501.
- House L. L., Wagner W. J., Hildner E., Sawyer C. and Schmidt H. U., 1981. Studies of the corona with the Solar Maximum Mission coronagraph/polarimeter, *Astrophys. J.* 244, L117-L121.
- Hundhausen A. J., 1972. *Coronal expansion and solar wind*. Springer-Verlag, NY.
- Hundhausen A. J., 1997. An introduction, in *Coronal Mass Ejections*. Geophys. Monogr. Ser., 99, edited by N. Crooker, J. Joselyn and J. Feynman, 1-7, AGU, Washington, D.C.

- Hunsucker R. D. and Hargreaves J. K., 2003. The high-latitude ionosphere and its effects on radio propagation. Cambr. Univ. Press, UK.
- ISRO, retrieved 2013. Mars Orbiter Mission. Indian Space Research Organisation (ISRO). ISRO Satellite Centre, Bangalore.
- Jibiri N. N., Nwankwo V. U. J. and Kio M., 2011. Determination of the stopping power and failure time of spacecraft components due to proton interaction using GOES 11 acquisition data. *Inter. J. Engr. Sci. Tech.* 3, 6532-6542.
- Johannessen J. A., G. Balmino, C. Le Provost, R. Rummel, R. Sabadini, H. Snkel, C. C. Tscherning, P. Visser, P. Woodworth, C. W. Hughes, P. Legrand, N. Sneeuw, F. Perosanz, M. Aguirre-Martinez, H. Rebhan and M. R. Drinkwater, 2003. The European gravity field and steady-state ocean circulation explorer satellite mission: its impact on geophysics. *Surv. Geophys.* 24, 339-386.
- Jakowski N., 2015. Radio waves for communication and ionospheric probing. *Helio-physics V, Space weather and society.*
- Kahler S. W., 1992. Solar flares and coronal mass ejections. *Annu. Rev. Astron. Astrophys.* 30, 113-141.
- Kallenrode M., 2001. *Space Physics: An introduction to plasma and particles in the heliosphere and magnetosphere.* 2nd Ed., Springer-Verlag Berlin Heidelberg, Germany.
- Kennewell J., 1999. *Satellite Orbital Decay Calculations.* IRS Radio and Space Services, Australian Space Waether Agency, Sydney.
- Kikuchi T. and Evans D.S., 1983. Quantitative study of substorm-associated VLF phase anomalies and precipitating energetic electrons on November 13, 1979. *J. Geophys. Res.: Space Phys.* 88, 871-880.
- Kleimenova N. G., Kozyreva O. V., Rozhnoy A. A. and Soloveva M. S., 2004. Variations in the VLF signal parameters on the Australia-Kamchatka radio path during magnetic storms. *Geomagn. Aeron.* 44, 385-393.
- Kim K. H., Moon Y. J., Cho K. S., Kim H. D. and J.-Y. Park, 2006. Atmospheric drag effects on the KOMPSAT-1 satellite during geomagnetic superstorms. *E-letter, Earth Planets Space*, 58, e25-e28
- KingHele D., 1987. *Satellite Orbits in an Atmosphere: Theory and Applications,* Glasgow, UK.

- Klenzing J., A. G. Burrell, R. A. Heelis, J. D. Huba, R. Pfaff and F. Simes, 2013. Exploring the role of ionospheric drivers during the extreme solar minimum of 2008. *Ann. Geophys.* 31, 2147-2156.
- Klinkrad H., 1996. On the Use of Atmosphere Models in Re-Entry Predictions. *Environment Modelling for Space-based Applications, Symposium Proceedings (ESA SP-392)*. ESTEC Noordwijk, 287-298
- Knipp D., 2014. Space Weather in the Thermosphere: Satellite Drag. NASA Space Weather Training for Mission Operators and Engineers, given by Yihua Zheng or 2014 summer bootcamp.
- Koppenwallner G., 2011. Satellite aerodynamics and determination of thermospheric density and wind. In: *AIP Conf. Proc.* 1333, Pacific Grove, California, 1307.
- Kozyra J. U, G. Crowley, B. A. Emery, X. Fang, G. Maris, M. G. Mlynczak, R. J. Niciejewski, S. E. Palo, L. J. Paxton, C. E. Randall, P.-P. Rong, J. M. Russell III, W. Skinner, S. C. Solomon, E. R. Talaat, Q. Wu and J.-H. Yee, 2006. Response of the Upper/Middle Atmosphere to Coronal Holes and Powerful High-Speed Solar Wind Streams in 2003. *Recurrent Magnetic Storms: Corotating Solar Wind Streams*. Geophysical Monograph 167. Edited by Bruce Tsurutani, Robert McPherron, Walter Gonzalez, Gang Lu, Jos H. A. Sobral and Natchimuthukonar Gopalswamy. ISBN-13: 978-0-87590-432-0. AGU Books Board, AGU, Washington DC USA, 319.
- Kumar A. and Kumar S., 2014. Space weather effects on the low latitude D-region ionosphere during solar minimum. *Earth Planets Space*, 66.
- Kutiev I., I. Tsagouri, L. Perrone, D. Pancheva, P. Mukhtarov, A. Mikhailov, J. Lastovicka, N. Jakowski, D. Buresova, E. Blanch, B. Andonov, D. Altadill, S. Magdaleno, M. Parisi and J. M. Torta, 2013. Solar activity impact on the Earth's upper atmosphere. *J. Space Weather Space Clim.* 3.
- Kwak Y. S., K. H. Kim, Y. Deng and J. M. Forbes, 2011. Response of thermosphere density to changes in interplanetary magnetic field sector polarity. *J. Geophys. Res.: Space Phys.* 116 (A11).
- Lang K. R., 2003. *The Cambridge guide to solar system*. 1st Ed., Cambr. Univ. Press, NY.
- Lang K. R., 2011. *The Cambridge guide to solar system*. 2nd Ed., Cambr. Univ. Press, NY.

- Lastovicka J., 1989. Solar wind and high energy particle effects in the middle atmosphere, *Handb. MAP*, 29, 119.
- Lastovicka J., 1996. Effects of geomagnetic storms in the lower ionosphere, middle atmosphere and troposphere, *J. Atmos. Terr. Phys.* 58, 831-843.
- Leonard J. M., Forbes J. and Born G. H., 2012. Impact of tidal density variability on orbital and reentry predictions, *J. Geophys. Res.: Space Weather*, 10, S12003.
- Lei J., J. P. Thayer, J. M. Forbes, E. K. Sutton, R. S. Nerem, M. Temmer and A. M. Veronig, 2008. Global thermospheric density variations caused by high-speed solar wind streams during the declining phase of solar cycle 23. *J. Geophys. Res.* 113 (A11).
- Lei J., G. Chen, J. Xu and X. Dou, 2013. Impact of Solar Forcing on Thermospheric Densities and Spacecraft Orbits from CHAMP and GRACE. *Intech open science*.
- Lindsay G.M., Russell C.T. and Luhmann J.G., 1994. On the sources of interplanetary shocks at 0.72 AU. *J. Geophys. Res.* 99, 11-17.
- Liu J., L. Liu, B. Zhao, J. Lei, J. P. Thayer and R. L. McPherron, 2012. Superposed Epoch Analyses of Thermospheric Response to CIRs: Solar Cycle and Seasonal Dependencies. *J. Geophys. Res.* 117, A00L10.
- Liu H., Hirano T. and S. Watanabe, 2013. Empirical model of the thermospheric mass density based on CHAMP satellite observation. *J. Geophys. Res.: Space Phys.* 118, 843-848.
- Low B. C., 1994. Magnetohydrodynamic Processes in the Solar Corona-Coronal Mass Ejections and Magnetic Helicity. *Plasma Phys.* 1, 1684-1690.
- MacQueen R.M., J.A. Eddy, J.T. Gosling, E. Hildner, R.H. Munro, G.A. Jr Newkirk, A.I. Poland and C.I. Ross, 1974. The Outer Solar Corona as Observed from Skylab: Preliminary Results. *Astrophys. J.* 187, L85.
- MacQueen R.M., A. Csocke-Poeckh, E. Hildner, L. House, R. Reynolds, A. Stanger, H. Japoel and W. Wagner, 1980. The High Altitude Observatory Coronagraph / Polarimeter on the solar maximum mission. *Solar Phys.* 65, 91-107.
- MacQueen R. M., 1985. Coronal mass ejections: Acceleration and surface associations. *Solar Phys.* 95, 359-361.
- Manckol J. and Veireck R., 2016. GOES X-ray Sensor (XRS) Measurements. NOAA GOES XRS Readme. https://ngdc.noaa.gov/stp/satellite/goes/doc/GOES_XRS_readme.pdf.

- Storz M. F., B. R. Bowman, J. I. Branson, S. J. Casali and W. K. Tobiska, 2005. High accuracy satellite drag model (HASDM). *Adv. Space Res.* 36, 2497-2505.
- McPherron R. L., J. M. Weygand and T.-S. Hsu, 2008. Response of the Earth's magnetosphere to changes in the solar wind. *J. Atmos. Solar-Terr. Phys.* 70, 303-315.
- McRae W. M. and Thomson N. R., 2004. Solar flare induced ionospheric D-region enhancements from VLF phase and amplitude observations. *J. Atm. Solar-Terr. Phys.* 66, 77-87.
- Mehta P. M., McLaughlin C. A. and Sutton E. K., 2013. Drag coefficient modeling for grace using Direct Simulation Monte Carlo. *Adv. Space Res.* 52, 2035-2051.
- Melia A., 2010. Flare Detection using VLF Radio Signal, G3NYK.
- Meyer-Vernet N., 2007. Basics of the solar wind. *Cambr. Univ. Press*, UK.
- Miller N. J. and Brace L. H., 1969. Some winter characteristics of the northern high-latitude ionosphere, *J. Geophys. Res.* 74, 5752-5762.
- Mimmo H. R., 1937. The Physics of the Ionosphere, *Rev. Mod. Phys.* 9, 1-45.
- Mitra W. B., 1974. Ionospheric effects of solar flares. *D. Reidel Pub. Com.*, Dordrecht, Holland.
- Mittal N. and Narain U., 2009. On some properties of coronal mass ejections in solar cycle 23. *New Astron.* 14, 341-346.
- Mildred Moe M., Wallace S. D. and Moe K., 1995. Recommended Drag Coefficients for Aeronomic Satellites. *The Upper Mesosphere and Lower Thermosphere: A Review of Experiment and Theory Geophysical Monograph 87*, AGU.
- Molchanov O. A. and Hayakawa M., 1998. On the generation mechanism of ULF seimogenic electromagnetic emissions, *Phys. Earth Planet. Int.* 105, 201-220.
- Munir M. S., J. Hutton and P. C. Hirschberg, 2012. *Spacecraft Momentum Management using Solar Array*. Palo Alto: Patent Application Pub. Inc.
- Munro R. H., J. T. Gosling, E. Hildner, R. M. MacQueen, A. I. Poland and C. L. Ross, 1979. The association of coronal mass ejection transients with other forms of solar activity, *Solar Phys.* 61, 201.
- NASA, retrieved 2013. International space station: facts and figures. NASA.

- NGS, retrieved 2013. International space station: Cosmic Laboratory. National Geographic Society.
- NOAA1, retrieved 2016. Solar flares (Radio Blackouts). NOAA Space Weather Prediction Centre. [http : //www.swpc.noaa.gov/phenomena/solar-flares-radio-blackouts](http://www.swpc.noaa.gov/phenomena/solar-flares-radio-blackouts).
- NOAA2, retrieved 2014. Satellite Drag. NOAA Space Weather Prediction Centre. [http : //www.swpc.noaa.gov/impacts/satellite-drag](http://www.swpc.noaa.gov/impacts/satellite-drag).
- NOAA3, 2006. Satellites and Space Weather. www.swpc.noaa.gov/info/satellites.html.
- NOAA4, retrieved 2012. Solar particle and geomagnetic indices. www.swpc.noaa.gov/ftpmenu/indices/old_indices.html.
- NOAA5, retrieved 2012. Predicted sunspot number and radio flux values with expected ranges. www.swpc.noaa.gov/ftpdir/weekly/Predict.txt.
- NOAA6, retrieved 2012. Solar proton events affecting the earth environment. NOAA/SWPC. www.swpc.noaa.gov/ftpdir/indices/SPE.txt.
- NOAA7, Retrieved 2016. Geomagnetic Storms. NOAA Space Weather Prediction Center. [http : //www.ngdc.noaa.gov/phenomena/geomagnetic-storms](http://www.ngdc.noaa.gov/phenomena/geomagnetic-storms)
- Nwankwo U. J. N., 2005. Determination of the stopping power and failure time of spacecraft components due to e^+ interaction using GOES 11 Acquisition data. M.Sc. thesis.
- Nwankwo V. U. J, S. Sasmal and Chakrabarti K. S., 2014. A study of magnetosphere-ionosphere coupling as a precursory indicator of Earthquake, IEEE Proc. the General Assembly and Scientific Symposium (URSI GASS), 2014 XXXIth URSI.
- Nwankwo V. U. J and Chakrabarti K. S., 2014. Theoretical modeling of drag force impact on a model international space station (ISS) during variation of solar activity. Trans. JSASS Aerosp. Technol. Jpn. 12, 47-53
- Nwankwo V. U. J., Sandip K. Chakrabarti and Weigel R. S., 2015. Effects of plasma drag on low Earth orbiting Satellites due to solar forcing induced perturbations and heating. Adv. Space Res. 56, 47-56.
- Nwankwo, V. U. J. and Chakrabarti K. S., 2015. Analysis of planetary and solar-induced perturbations on trans-Martian trajectory of Mars missions before and after Mars orbit insertion. Indian J. Phys. 89, 1235-1245.

- Nwankwo V. U. J., Chakrabarti S. K. and Ogunmodimu O., 2016. Probing geomagnetic storm-driven magnetosphere-ionosphere dynamics in D-region via propagation characteristics of very low frequency radio signals, *J. Atmos. Solar-Terr. Phys.* 145, 154-169.
- Nwankwo, V. U. J. and Chakrabarti S. K., 2016. Diagnostic study of geomagnetic storm-induced ionospheric changes in mid-latitude D-region using VLF signal propagation characteristics. *Ann. Geophys. angeo-2016-84* (submitted).
- Oberheide J., Forbes J., Husler K., Wu Q. and Bruinsma S. L., 2009. Tropospheric Tides from 80-400km: Propagation, Interannual Variability and Solar Cycle Effects. *J. Geophys. Res.* 114, D00105.
- Odenwald S., 2015. Space weather: impacts, mitigation, forecasting. *Heliosphysics V. Space weather and society.* 8-44.
- Pancheva D. V., P.J. Mukhtarov, N.J. Mitchell, D.C. Fritts, D.M. Riggin, H. Takahashi, P.P. Batista, B.R. Clemesha, S. Gurubaran and G. Ramkumar, 2008. Planetary wave coupling (5-6-day waves) in the low-latitude atmosphere-ionosphere system. *J. Atm. Solar-Terr. Phy.* 70, 101-122.
- Pardini C., Tobiska K. and Luciano A., 2004. Analysis of the orbital decay of spherical satellites using different solar flux proxies and atmospheric density models. *Adv. Space Res.* 37, 392-400.
- Pardini C., Anselmo L., Moe K. and Moe M. M., 2010. Drag and energy accommodation coefficients during sunspot maximum. *Adv. Space. Res.* 45, 638-650.
- Parker E. N., 1997. *Cosmic winds and the heliosphere.* University of Arizona Press, Tucson, Arizona, 3.
- Pal S., Surya K. M. and S. K. Chakrabarti, 2012. First ever VLF monitoring of the lunar occultation of a solar flare during the 2010 annular solar eclipse and its effects on the D-region electron density profile, *Planet. Space Sci.* 73, 310-317.
- Palit S., Basak T., S. K. Mondal, S. Pal and S. K. Chakrabarti, 2013. Modeling of very low frequency (VLF) radio wave signal profile due to solar flares using the GEANT4 Monte Carlo simulation coupled with ionospheric chemistry, *Atmos. Chem. Phys.* 13, 9159-9168.
- Patton R. J., F. J. Uppal, S. Simani and B. Polle, 2010. Robust FDI applied to thruster faults of a satellite system. *Control Engineering Practice*, 18, 1093-1109, September 2010. *ACA'07 17th IFAC Symposium on Automatic Control in Aerospace Special Issue.* Pub.: Elsevier Science. ISSN: 0967-0661.

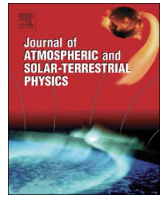
- Peter W. B., Chevalier M. W. and Inan U. S., 2006. Perturbations of mid-latitude sub-ionospheric VLF signals associated with lower ionospheric disturbances during major geomagnetic storms. *J. Geophys. Res.* 111, AO3301.
- Picone J. M., Hedin A. E., Drob D. P. and Aikin A. C., 2002. NRLMSISE-00 empirical model of the atmosphere: Statistical comparisons and scientific issues. *J. Geophys. Res.* 107, 1468.
- Policastri L. A and Joseph M. Simons, 2003. Implementing the MSIS Atmospheric Density Model in OCEAN. AAS 03-166.
- Polyakova A. S., M.A. Chernigovskay and N.P. Perevalov, 2014. Ionospheric effects of sudden stratosphere warmings in Eastern Siberian region. *J. Atmos. Solar-Terr. Phys.* 120, 15-23.
- Poole I., 1999. *Radio Waves and the Ionosphere*. American Radio Relay League, G3YWX.
- Prolss G. W., 2004. *Physics of the Earth's space environment*. Springer Berlin Heidelberg, Germany.
- Raulin J.-P., Pacini A.A., Kaufmann P., Correia E. and Martinez M.A.G., 2006. On the detectability of solar X-ray flares using very low frequency sudden phase anomalies. *J. Atmos. Solar-Terr. Phys.* 68, 1029-1035.
- Raulin J.-P., G. Trottet, M. Kretzschmar, E. L. Macotela, A. Pacini, F. C. P. Bertoni and I. E. Dammasch, 2013. Response of the low ionosphere to X-ray and Lyman- α solar flare emissions. *J. Geophys. Res.* 118, 570-575.
- Rawer K., 1993. *Wave propagation in the ionosphere*. Kluwer, Dordrecht, ISBN 0792307755.
- Ray S. and Chakrabarti S. K., 2012. A study of the behavior of the terminator time shifts using multiple VLF propagation paths during the Pakistan earthquake (M=7.2) of 18 January 2011. *Nat. Hazards Earth Syst. Sci.* 13, 1501-1506.
- Reames D., 1999. Particle acceleration at the Sun and in the heliosphere. *Space Sci. Rev.* 90, 413.
- Rhoden E. A, J. M. Forbes and F. A. Marcos, 2000. The influence of geomagnetic and solar variabilities on lower thermosphere density. *J. Atmos. Solar-Terr. Phys.* 62, 999-1013.

- Reigber Ch, H. Ltihr, and P. Schwintzer, 2002. CHAMP Mission Status. *Adv. Space Res.* 30, 129-134.
- Ruohoniemi J.M. and Greenwald R.A., 2005. Dependencies of high-latitude plasma convection: consideration of interplanetary magnetic field, seasonal, and universal time factors in statistical patterns. *J. Geophys. Res.* 110, A09204.
- Russell A. J. B., A. N. Wright, and A. W. Hood, 2010. Self-consistent ionospheric plasma density modifications by field-aligned currents: Steady state solutions. *J. Geophys. Res.* 115, A04216.
- Russell A. J. B., and A. N. Wright, 2012. Magnetosphere-ionosphere waves. *J. Geophys. Res.* 117, A01202.
- Sasmal S. and S. K. Chakrabarti, 2009. Ionospheric anomaly due to seismic activities Part 1: Calibration of the VLF signal of VTX 18.2 KHz station from Kolkata and deviation during seismic events. *Nat. Hazards Earth Syst. Sci.* 9, 1403-1408.
- Schijver C. J. and Zwaan C., 2000. *Solar and stellar magnetic activity.* Cambr. Univ. Press, UK.
- Shizgal B. D. and Arkos G. G., 1996. Non-thermal escape of the atmospheres of Venus, Earth and Mars. *Rev. Geophys.* 34, 483-505.
- Simoës F., Pfaff R., Berthelier J. and Klenzing, 2012. A Review of Low Frequency Electromagnetic Wave Phenomena Related to Tropospheric-Ionospheric Coupling Mechanisms. *Space Sci. Rev.* 168, 551-593.
- Singer H. J., Matheson L., Grubb R., Newman A. and Bower S. D., 1996. Monitoring space weather with the GOES magnetometers. NOAA Space Environment Center.
- SOHO, retrieved 2012. SOHO LASCO CME CATALOG. cdaw.gsfc.nasa.gov/CME_list
- Solomon S. C., Alan G. Burns, Barbara A. Emery, Martin G. Mlynczak, Liying Qian, Wenbin Wang, Daniel R. Weimer and Michael Wiltberger, 2012. Modeling Studies of the Impact of High-Speed Streams and Co-Rotating Interaction Regions on the Thermosphere-Ionosphere. *J. Geophys. Res.* 117, A00L11.
- Soloviev O.V., Hayakawa M., Ivanov V. I. and Molchanov O. A., 2004. Seismo-electromagnetic phenomenon in the atmosphere in terms of 3D subionospheric radio wave propagation problem. *Phys. Chem. Earth*, 29, 639-647.

- Space.com, retrieved 2014. Failure Common among Mars Missions. *http : //www.space.com/13558 - historic - mars - missions.html*
- Stix M., 2002. The Sun: An introduction, 2nd Ed, Springer-Verlag Berlin Heidelberg.
- Stoker P. H., 1993. Energetic Electron Power Flux Deposition at Sanae (L=4.0) from Riometer Recording. *J. Geophys. Res.* 98, 19111-19116.
- Stockman B., Joe Boyle and John Bacon, 2009. International Space Station Systems Engineering Case Study. Air Force Center for Systems Engineering, USA.
- Sutton E. K., J. M. Forbes and R. S. Nerem, 2005. Global thermospheric neutral density and wind response to the severe 2003 geomagnetic storms from CHAMP accelerometer data. *J. Geophys. Res.* 110 (A9).
- Thomson N. R., Rodger C. J. and Dowden R. L., 2004. Ionosphere gives size of greatest solar flares. *Geophys. Res. Lett.* 31, L06803.
- Tousey R., 1973. The solar corona. *Space Res.* 13, 713.
- TPS, retrieved 2013. Missions to Mars. The Planetary Society (TPS). *www.planetary.org*
- Trinh G. T., 2013. Environmental Testing and Orbital Decay Analysis for a CubeSat. M.Sc. Thesis (Aerospace Engineering). San Jose State University, USA, 18-20.
- Tsurutani B. T. and Meng C. I., 1972. Interplanetary magnetic field variations and substorms. *J. Geophys. Res.* 77, 2964-2970.
- Tsurutani B. T., Gonzalez W. D., Tang F., Akasofu S. I. and Smith E. J., 1988. Origin of interplanetary southward magnetic fields responsible for major magnetic storms near solar maximum (1978-1979). *J. Geophys. Res.* 93, 8519-8531.
- Tsurutani B. T., Gonzalez W. D., Gonzalez A. L. C., Tang F., Arballo J. K., and Okada M., 1995. Interplanetary origin of geomagnetic activity in the declining phase of the solar cycle. *J. Geophys. Res.* 100, 21717-21733.
- Tsurutani B. T. and Gonzalez W. D., 1997. The interplanetary causes of magnetic storms: A review, in: *Magnetic Storms*. Edited by: Tsurutani, B. T., Gonzalez, W. D., Kamide, Y., and Arballo, J. K., Amer. Geophys. Un. Press, Wash. D.C., 98, 77-89.

- Tsurutani B. T., Gonzalez W. D., Gonzalez A. L. C., Guarnieri F. L., Gopalswamy N., Grande M., Kamide Y., Kasahara Y., Lu G., Mann I., McPherron R. L., Soraas F. and Vasyliunas V. M., 2006. Corotating solar wind streams and recurrent geomagnetic activity: A review. *J. Geophys. Res.* 111, A07S01.
- Tsurutani B. T., Echer E., Guarnieri F. L. and Gonzalez W. D., 2011. The properties of two solar wind high speed streams and related geomagnetic activity during the declining phase of solar cycle 23. *J. Atmos. Solar-Terr. Phys.* 73, 164.
- Tsurutani B. T., Echer E. and Gonzalez W. D., 2011. The solar and interplanetary causes of the recent minimum in geomagnetic activity (MGA23): a combination of midlatitude small coronal holes, low IMF BZ variances, low solar wind speeds and low solar magnetic fields. *Ann. Geophys.* 29, 839-849.
- Vallado D. A. and Finkleman D., 2008. A critical assessment of satellite drag and atmospheric density modeling. *AIAA/AAS, AIAA-2008-6442*.
- Verkhoglyadova O. P., Tsurutani B. T., Mannucci A. J., Mlynczak M. G., Hunt L. A. and Runge T., 2013. Variability of ionospheric TEC during solar and geomagnetic minima (2008 and 2009): external high speed stream drivers, *Ann. Geophys.* 31, 263-276.
- Wait J. R., 1959. Diurnal change of ionospheric heights deduced from phase velocity measurements at VLF. *Proc. IRE*, 47, 998.
- Wait J. R. and Spies K. P., 1964. Characteristics of the Earth-ionosphere wave-guide for VLF radio waves. *NBS Tech. Note* 300.
- Wait J. R., 1998. The ancient and modern history of EM ground-wave propagation. *IEEE Antennas and Propagation Magazine*, 40, 5, 7-24.
- Walterscheid R. L., 1989. Solar cycle effects on the upper atmosphere - Implications for satellite drag. *J. Spacecr. Rockets*, 26, 439-444.
- Weigel R. S., 2010. Solar wind density influence on geomagnetic storm intensity. *J. Geophys. Res.* 115, A09201.
- Weigel R. S., Daniel N. Baker, E. Joshua Rigler and Dimitris Vassiliadis, 2004. Predictability of Large Geomagnetic Disturbances Based on Solar Wind Conditions. *IEEE Trans. Plas. Sci.* 32, 1506-1510.
- Wertz J. and W. J. Larson, 1999. *Space Mission Analysis and Design*. Third Edition, Kluwer Academy, El Segundo, Calif, 145.

- Wild J.A., Milan S.E., Cowley S.W.H., Dunlop M.W., Owen C.J., Bosqued J.M., Taylor M.G.G.T., Davies J.A., Lester M., Sato N., Yukimatu A.S., Fazakerley A.N., Balogh A. and Re'eme H., 2003. Coordinated interhemispheric SuperDARN radar observations of the ionospheric response to flux transfer events observed by the Cluster spacecraft at the high-latitude magnetopause. *Ann. Geophys.* 21, 1807-1826.
- Woods T., Loren W. Acton, Scott Bailey, Frank Eparvierl, Howard Garcia, Darrell Judges, Judith Lean, John T. Mariska, Don McMullin, Gerhard Schmidtke, Stanley C. Solomon, W. Kent Tobiska, Harry P. Warrenlo and Rodney Viereck, 2004. Solar Extreme Ultraviolet and X-ray Irradiance Variations. Solar Variability and its Effects on Climate, Geophysical Monograph 141, AGU.
- Xu J., Wang W., Lei J., Sutton E. K. and Chen G., 2011. The effect of periodic variations of thermospheric density on CHAMP and GRACE orbits. *J. Geophys. Res.* 116, 2315.
- Yashiro S., N. Gopalswamy, G. Michalek, O. C. St. Cyr, S. P. Plunkett, N. B. Rich, and R. A. Howard, 2004. A catalog of white light coronal mass ejections observed by the SOHO spacecraft, *J. Geophys. Res.* 109, A07105.
- Zhang S., Fukao S., Oliver W. L. and Otsuka Y., 1999. The height of the maximum ionospheric electron density over the MU radar, *J. Atm. Solar-terr. Phys.* 61, 1367-1383.
- Zhang X., Forbes J. and Hagan, 2010a. Longitudinal Variation of Tides in the MLT Region: 1. Tides Driven by Tropospheric net Radiative Heating. *J. Geophys. Res.* 115, A06316.
- Zurbuchen T. H. and Richardson I. G., 2005. In-situ solar wind and magnetic field signatures of interplanetary coronal mass ejections, *Space Sci. Rev.* 00, 1-15.



Probing geomagnetic storm-driven magnetosphere–ionosphere dynamics in D-region via propagation characteristics of very low frequency radio signals



Victor U.J. Nwankwo^{a,*}, Sandip K. Chakrabarti^{a,b}, Olugbenga Ogunmodimu^c

^a S.N. Bose National Centre for Basic Sciences, Kolkata 700098, India

^b Indian Centre for Space Physics, Kolkata 700084, India

^c Department of Physics, Lancaster University, LA1 4YW, UK

ARTICLE INFO

Article history:

Received 25 August 2015

Received in revised form

10 March 2016

Accepted 27 April 2016

Available online 29 April 2016

Keywords:

D-region ionosphere

Geomagnetic storm

Ionospheric response

Magnetosphere–ionosphere dynamics

VLF radio signals

ABSTRACT

The amplitude and phase of VLF/LF radio signals are sensitive to changes in electrical conductivity of the lower ionosphere which imprints its signature on the Earth–ionosphere waveguide. This characteristic makes it useful in studying sudden ionospheric disturbances, especially those related to prompt X-ray flux output from solar flares and gamma ray bursts (GRBs). However, strong geomagnetic disturbance and storm conditions are known to produce large and global ionospheric disturbances, which can significantly affect VLF radio propagation in the D region of the ionosphere. In this paper, using the data of three propagation paths at mid-latitudes (40–54°), we analyse the trend in variation of aspects of VLF diurnal signal under varying solar and geomagnetic space environmental conditions in order to identify possible geomagnetic footprints on the D region characteristics. We found that the trend of variations generally reflected the prevailing space weather conditions in various time scales. In particular, the ‘dipping’ of mid-day signal amplitude peak (MDP) occurs after significant geomagnetic perturbed or storm conditions in the time scale of 1–2 days. The mean signal amplitude before sunrise (MBSR) and mean signal amplitude after sunset (MASS) also exhibit storm-induced dipping, but they appear to be influenced by event’s exact occurrence time and the highly variable conditions of dusk-to-dawn ionosphere. We also observed few cases of the signals rise (e.g., MDP, MBSR or MASS) following a significant geomagnetic event. This effect may be related to storms associated phenomena or effects arising from sources other than solar origin. The magnitude of induced dipping (or rise) significantly depends on the intensity and duration of event(s), as well as the propagation path of the signal. The post-storm day signal (following a main event, with lesser or significantly reduced geomagnetic activity) exhibited a tendency of recovery to pre-storm day level. In the present analysis, we do not see a well-defined trend in the variation of the post-storm sunrise amplitude terminator (SRT) and sunset terminator (SST). The SRT and SST signals show more dipping in QGD-A118 propagation path but generally an increase along DHO-A118 propagation path. Thus the result could be propagation path dependent and detailed modelling is required to understand these phenomena.

© 2016 Elsevier Ltd. All rights reserved.

1. Introduction

Although separated by thousands of kilometers, the magnetosphere and ionosphere are known to be physically connected (through the Earth’s magnetic field) into one global system. The ionosphere responds to (a) prompt changes in solar energetic events, mainly the solar flare associated bursts in EUV, X-ray and relativistic particles (Mitra, 1974; Buonsanto, 1999; Alfonsi et al.,

2008), (b) delayed changes mainly due to geomagnetic storm conditions with time scale from several hours to 1–3 days (Lestovicka, 1996; Buonsanto, 1999; Kutiev et al., 2013), and (c) periodic changes with time scales of several days to months, and those of several solar cycles (Alfonsi et al., 2008; Kutiev et al., 2013). The ionosphere also exhibits diurnal (day/night) and seasonal (e.g. summer/winter) variations (Miller and Brace, 1969; Zhang et al., 1999). Solar and geomagnetic induced phenomena drive changes in magnetosphere conditions, whose coupling effects modify ionospheric signatures including atmospheric density distribution, total electron content (TEC), ionospheric current

* Corresponding author.

E-mail address: victorujn@bose.res.in (V.U.J. Nwankwo).

system, ionisation rates, and crucial D-region parameters such as conductivity gradient and reference height (Wait, 1959; Wait and Spies, 1964; Mitra, 1974; Buonsanto, 1999; Burke, 2000; Simoes et al., 2012; Nwankwo and Chakrabarti, 2014). The dynamics of ionospheric response to changes in solar and geomagnetic conditions involve the exchange of particles and electromagnetic energy (absorbed, reprocessed and deposited in the ionosphere by the magnetosphere) between magnetically connected regions (Burke, 2000; Streltsov and Lotko, 2004; Goldstein et al., 2005; Russell et al., 2010; Russell and Wright, 2012; Leonard et al., 2012; Kutiev et al., 2013).

1.1. The ionosphere at a glance

The ionosphere is composed of three distinct space regions [D (50–90 km), E (90–120 km), and the F (from 120 km up to 500 km), which often split into two layers, namely, F1 and F2]. Its existence is primarily due to ionisation by solar ultraviolet (UV) radiation and X-ray wavelength (Kelley, 1989; Prolss, 2004; McRae and Thomson, 2004; Raulin et al., 2006; Heikkila, 2011) and isotropic cosmic rays. Recombination also occurs when free electrons are captured by positive ions. Ionisation and recombination efficiency controls the overall electron density at every time instant. The D region ionosphere is highly active during the day (roughly between the local sunrise and sunset) due to high rate of ionisation, but its density falls significantly at night largely due to rapid recombination at the altitude. The E region also maintains the same dynamics (night/day fluctuations) as the D region but ionisation state persists longer due to slower rate of recombination at lower density. Thus, the reflection of signals mainly occurs at the bottom of the nighttime E region (Han and Cummer, 2010 and references therein). The F region is present both day and night; air density and recombination rate is very low in the region. Therefore, ionisation persists in the nighttime (also see Mimno, 1937; Poole, 1999; Prolss, 2004). In general, these layers are severely disturbed by phenomena of solar and geomagnetic origin, as well as planetary and tidal waves, thermospheric tides and stratospheric warming (Pancheva et al., 2008; Leonard et al., 2012; Chen et al., 2013; Goncharenko et al., 2012; Polyakov et al., 2014). However, effects at different heights, locations or latitudes vary in development, depending on time and intensity (of driving force). Ionospheric signature variations reflect different mechanisms and aspects of solar and other induced phenomena.

1.2. VLF propagation in the Earth–ionosphere waveguide

The velocity, direction and amplitude of most electromagnetic waves are distinctly affected when propagating through the ionosphere. This characteristic makes radio waves an ideal tool for ionospheric study (Prolss, 2004). Very low frequency (VLF) radio waves in the 3–30 kHz are effective in the investigation of solar induced variable conditions in the ionosphere (especially the D region) because their amplitude and phase are sensitive to changes in electrical conductivity of the lower ionosphere (Wait and Spies, 1964; Mitra, 1974; Alfonsi et al., 2008). VLF radio signals are reflected alternately by the D region and the Earth's surface due to high conductivity (Mimno, 1937; Poole, 1999). The transmitted wave is thus guided between the Earth and the ionosphere enabling the signal to propagate globally through the Earth–ionosphere waveguide. The signal is then received at various receivers across the world. Variations in daytime VLF signal amplitude and phase appear to be well correlated with solar X-ray output, with almost prompt responses. Hence, it has been used by many researchers to study sudden ionospheric disturbances and changes in the atmosphere (e.g., Araki, 1974; Hayakawa et al., 1996; Molchanov and Hayakawa, 1998; Kleimenova et al., 2004; McRae and

Thomson, 2004; Thomson et al., 2004; Chakrabarti et al., 2005; Grubor et al., 2005; Peter et al., 2006; Sasmal and Chakrabarti, 2009; Chakrabarti et al., 2010; Ciliverd et al., 2010; Raulin et al., 2006, 2010; Basak et al., 2011; Pal et al., 2012; Palit et al., 2013; Ray and Chakrabarti, 2012; Raulin et al., 2013; Nwankwo and Chakrabarti, 2014). Other methods used for ionospheric studies include observational and experimental techniques and tools such as Global Navigation Satellite system (GNSS) receivers, vertical and oblique sounding, Riometers, incoherent scatter radars (e.g., EISCAT), coherent scatter radars (e.g., Goose Bay radar, SuperDARN), magnetometers, etc. (Greenwald et al., 1995, 1996; Honary et al., 1995; Lastovicka, 1996; Wild et al., 2003; Burke, 2000; Danilov and Lastovicka, 2001; Goldstein et al., 2005; Ruohoniemi and Greenwald, 2005; Alfonsi et al., 2008).

1.3. VLF signal detection mechanism of sudden ionospheric disturbances

The D region ionosphere is maintained by Lyman- α radiation at a wavelength of about 121.5 nm, which ionises neutral nitric oxide (NO). With high solar activity, hard X-ray ($\lambda < 1$ nm) may ionise N_2 and O_2 . Galactic cosmic rays are also responsible for the ionisation of the lowest part of the lower ionosphere and the low-lying atmosphere down to the troposphere (also, see Mitra, 1974; Lastovicka, 1996). A huge amount of energy is released during solar flare in the form of highly energetic ultraviolet radiation, mainly X-ray flux enhancement. The radiation penetrates the D region where it increases ionisation rate (of dominant neutral NO molecules), and enhances electron density. These processes enhance the 'thickness' of the D region, thereby decreasing the reflection height (h) in the waveguide. This is normally detected as a sudden change (usually an increase) in the amplitude and phase enhancement of a VLF signal. VLF dusk-to-dawn signal exhibits high variability (or fluctuation) due to a significant fall in density of the D region. The signal is also sensitive to phenomena other than those originating from the Sun. Day time VLF signal is primarily controlled by the Sun.

1.4. Geomagnetic induced variations of the ionosphere and effects

Geomagnetic disturbances and storms are also known to produce significant global disturbances in the ionosphere, including the middle atmosphere and troposphere (Lastovicka, 1996; Danilov and Lastovicka, 2001). Geomagnetic storms are the products of highly variable solar wind speeds and density and associated shock waves (Lastovicka, 1989; Baker, 1996, 2000; Borovsky and Denton, 2006; Tsurutani et al., 2006; Kozyra et al., 2006). The effects of geomagnetic storms on the ionosphere manifest mainly through energetic particles precipitation, which lose their energy by impact and X-ray bremsstrahlung production (Lastovicka, 1996). There is also a consequent and significant enhancement of electron density (Chenette et al., 1993; Stoker, 1993; Lastovicka, 1996), causing significant increase in radio wave absorption and subsequent disappearance of radio signals in MF/HF values (Lastovicka, 1996). Galactic cosmic ray flux (which are modulated by geomagnetic storms) and global electric circuit and atmosphere electricity (affected by local changes of conductivity and ionosphere/magnetosphere electric fields and currents) are assumed to be the processes for ionospheric effects of geomagnetic storms (Danilov and Lastovicka, 2001). VLF signals can be significantly affected by geomagnetic disturbances and storms induced ionosphere perturbations (Kikuchi and Evans, 1983). Nevertheless, a few researchers have used it to study these perturbations with insightful findings (e.g., Araki, 1974; Kleimenova et al., 2004; Peter et al., 2006; Ciliverd et al., 2010; Kumar and Kumar, 2014; Tatsuta et al., 2015).

Apart from X-ray flux induced enhancement of amplitude and phase, anomalies in diurnal VLF signature may convey other important information, especially those related to geomagnetic disturbance or storm-induced ionospheric variations. If substantiated, such information could be instructive and resourceful to the study and understanding of the complex dynamics of Earth's ionosphere. Thus, in addition to well-correlated VLF signal amplitude variation and phase enhancement with X-ray flux induced sudden ionospheric disturbances (SID), this work seeks to understand possible geomagnetic activity footprints in the D region of the ionosphere and their dependence on the propagation path of VLF radio waves. First, the analysis concentrates on four selected periods of significant solar and geomagnetic activities in order of increasing magnitude, followed by a detailed statistical analysis of up to 16 storm conditions.

2. Data and method of analysis

In this work, analysed data mainly include diurnal VLF signal amplitude (of up to three propagation paths) monitored at A118 SID monitoring station in Southern France (<http://sidstation.lou-det.org/data-en.xhtml>), GOES solar X-ray flux, average z-components (B_z) and total magnetic field (H_T) (<http://satdat.ngdc.noaa.gov/sem/goes/data/>), global geomagnetic A_p (NOAA) and disturbance storm time (Dst) index (from World Data Centre for Geomagnetism (WDCG)), solar wind speed (V_{sw}) and particle density (PD) (<ftp://sohofp.nascom.nasa.gov/sdb/goes/ace/>). Analysis was conducted over four different 6-day periods with different geomagnetic conditions of varying disturbance. The space condition during 14–19 February 2011 is recognised as moderately disturbed, the condition during 26–31 May 2011 is recognised as a moderate storm, and condition during 24–29 September and 23–28 October 2011 are recognised as relatively intense storm conditions. The choice of a six days time frame is to give us a reasonable time interval for analysis of data before, during and after the main event(s). The three propagation paths are shown in Fig. 1 and include GQD-A118, ICV-A118, and DHO-A118; GQD (22.1 kHz GQD, lat N54.73° long W002.88°), ICV (20.27 kHz, lat N40.92° long E009.73°), and DHO (23.4 kHz, lat N53.08° long W007.61°).

2.1. Data description

A solar flare is ranked based on its X-ray output, and classified according to the order of magnitude of the peak burst intensity (I), measured at the Earth in 0.1–0.8 nm band, $B = I < 10^{-6} \text{ W/m}^2$, $C = 10^{-6} I < 10^{-5} \text{ W/m}^2$, $M = 10^{-5} I < 10^{-4} \text{ W/m}^2$, $X = 10^{-4} I \text{ W/m}^2$. We investigate solar wind speed conditions because the velocity, density, strength and direction of the solar wind plasma, and strength and direction of its associated magnetic field, influence the structure of the surrounding magnetic field of the Earth and controls the processes by which mass, momentum and energy are transferred from the solar wind to the Earth's magnetosphere-ionosphere system (Lastovicka, 1989; Singer et al., 1996). The B_z component significantly contributes to energy transfer from the solar wind sector to the magnetosphere (Prolss, 2004). H_T data can be used to deduce and check solar wind influence on the magnetosphere. Substorms advance and intensify current systems in the magnetosphere and ionosphere, which can also be detected via H_T component. A_p (or K_p) are planetary indices and are the indicators of geomagnetic activity. The Dst is used to assess or measure the severity of magnetic storms. The strength of the surface magnetic field is inversely proportional to the energy content of the ring current, which increases during geomagnetic storms (Hamilton et al., 1988). The solar wind condition and the mentioned geomagnetic parameters are important for studying and understanding magnetosphere-ionosphere coupling and effects (also see Bucha and Bucha, 1998; Borovsky and Denton, 2006; Tsurutani et al., 2006; Kozyra et al., 2006; Weigel, 2010; Nwankwo and Chakrabarti, 2014; Nwankwo et al., 2015). However, having provided a precise background of the parameters, we will concentrate mainly on how various aspects of diurnal VLF signal vary in response to geomagnetic activity and storm footprints in the D region ionosphere via these parameters, especially the Dst index. Details of geomagnetic indices variation in response to solar wind conditions and sources can be found in some literatures, e.g., Lastovicka (1989), Tsurutani et al. (1972, 1988, 1995, 1997, 2006, 2011), Baker (1996), Kozyra et al. (2006), Weigel (2010) and references therein.

We analyse 2- to 4-h Mean VLF signal amplitude before 'local' sunrise and after sunset (hereafter respectively denoted as MBSR

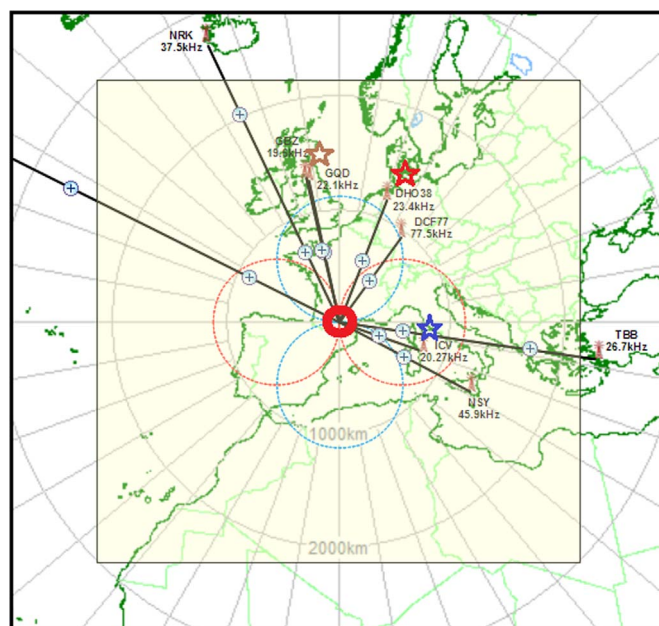


Fig. 1. VLF signal propagation paths (PP) used in the study: A118 receiver (thick red circle), DHO transmitter (red star), GQD (brown star), ICV (blue star) [adopted from A118 SID station web page]. (For interpretation of the references to colour in this figure caption, the reader is referred to the web version of this paper.)

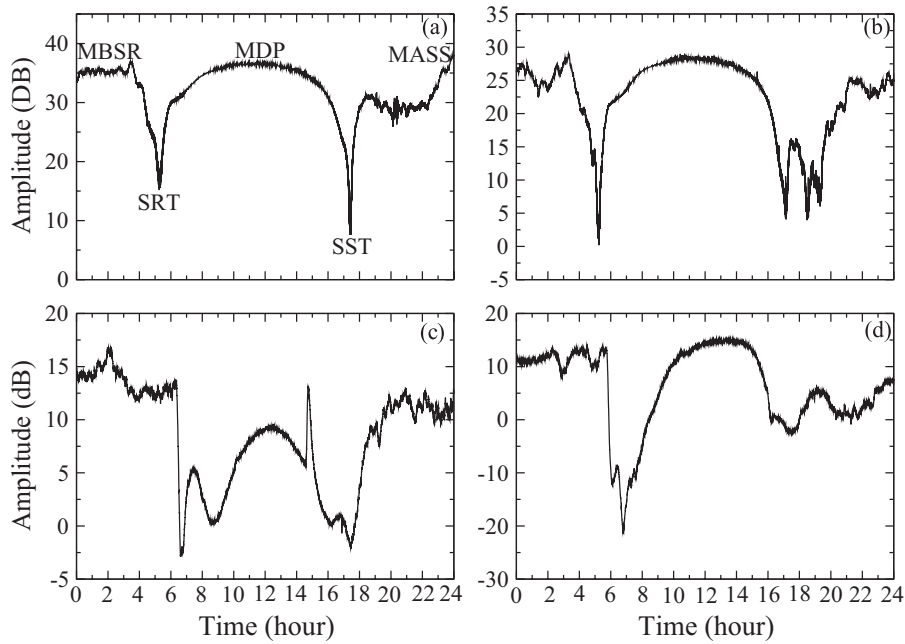


Fig. 2. Diurnal signature of VLF signals from propagation paths showing various aspects as identified in (a).

and MASS), and mid-day signal amplitude peak (MDP). We also identified variations in the so-called sunrise and sunset terminators (hereafter, denoted as SRT and SST). The aspects of a typical VLF signal (MBSR, MDP, MASS, SRT and SST) that were analysed are shown in Fig. 2a–d. In addition, daily solar flare count (for flares $\geq C$) and the standard deviation or fluctuation of daily Dst were calculated. The main goal of the analysis is to investigate the trend in variations of these components under given solar and geomagnetic induced space environmental conditions, for possible identification of geomagnetic footprint in D-region ionosphere in addition to known X-ray flux induced prompt response of VLF amplitude and phase. Data were analysed for two signal propa-

gation paths (PP) in each case. To begin with, we perform a detailed study of four particular cases, and then investigate the statistical significance of our results with more cases (up to 16).

3. Results and discussion

Fig. 3a–h shows diurnal VLF amplitude for GQD-A118 and ICV-A118 propagation paths, X-ray flux output, solar wind speed (V_{sw}), particle density (PD), B_z magnetic field component, H_T magnetic field, daily Dst standard deviation and A_p variation during 14–19 February 2011. The period is associated with high flare activity (up

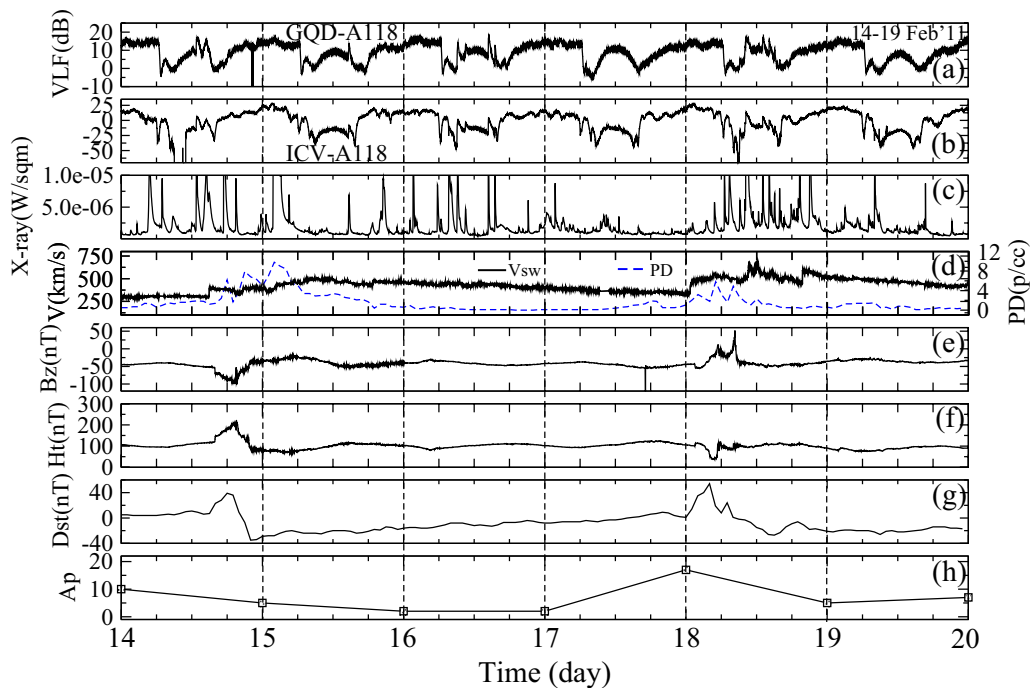


Fig. 3. (a) Diurnal VLF amplitude for GQD-A118 PP; (b) VLF amplitude for ICV-A118 PP; (c) X-ray flux output; (d) solar wind speed (V_{sw}) and particle density (PD); (e) B_z magnetic field component; (f) H_T magnetic field; (g) Dst and (h) A_p variations during 14–19 February 2011.

to 79 flares; $C=69$, $M=9$, $X=1$) and Dst variations of > -50 (also see Table 1). High flare events were observed on 14th, 16th and 18th (Fig. 3c), as well as significant geomagnetic activity on the 14th and 18th February (Fig. 3e–g). Highly variable solar wind speed (V_{sw}) and associated magnetospheric impact (via B_z and H_T) were also observed from 06:00 pm, 14th – 12:00 noon, 15th and during most part of 18th February (Fig. 3d–f). The extent and severity of induced magnetospheric perturbations is highlighted by the Dst during late 14th and the considerable part of 18th (Fig. 3g). The high A_p index of 18 February is therefore not surprising (Fig. 2h). VLF signal amplitude of the two propagation paths responded in a manner consistent with high flare events during the period. However, the flare-induced perturbations are distinct in VLF signals (during local daytime), and appear to overshadow those of geomagnetic activity origin. We therefore analyse and monitor the trend in variation of the signal metrics variation such as MBSR, MDP, MASS, SST and SRT, for possible identification and/or separation of distinct signatures of geomagnetic disturbances.

Fig. 4 shows daily Dst standard deviation, 4-h mean signal amplitude before local sunrise (MBSR), mid-day signal amplitude peak (MDP), 4-h mean signal amplitude after sunset (MASS), variation in sunrise terminator (SRT) and in sunset terminator (SST) for (a) GQD-A118 and (b) ICV-A118 propagation paths during 14–19 February 2011. A summary of relative trend in variations of the parameters over the period is provided in Table 1. The two main geomagnetic disturbed days are 14th (day 1) and the 18th (day 5) presumably due to increase or spikes in solar wind speed (V_{sw}) and particle density (PD) (see Fig. 3d). Proper analysis of a trend on a particular day requires a comparison with the trend of the previous day and the day after the event, because of the varying timescale of ionospheric response to different aspects of solar forcing and mechanisms. Therefore, we consider the trend of pre-event day in order to determine that of the event(s) day, and also consider the post-event(s) day for extended effect. We observed an increase in MBSR and SRT, but ‘dipping’ of MDP, MASS and SST on 15th (day 2) (Fig. 4a). Note the onset of perturbations on 14th (day 1) – during and after sunset. The influence of the induced perturbations is therefore expected to extend into a considerable part of 15th (day 2). There was a quiet geomagnetic condition on the 16th (day 3), and almost all the parameters increased. Of interest is the more (and longer) geomagnetic disturbed condition on the 18th (day 5). Only the SST increased (during which a decrease in the initial induced perturbation was expected), while almost all other parameters (MBSR, MDP, MASS and SRT) ‘dipped’. The observed trend is replicated in ICV-A118 propagation path around 15th (day 2) but quite inconsistent on

18th (day 5) – mainly increase of MBSR, MDP and MASS, but dipping of SRT and SST (Fig. 4b). However, the increase in MDP appeared to be related to flare induced signal amplitude variation on the signal as well as high fluctuation in ICV-A118 propagation path signal level, before and after sunset (see Fig. 3b).

Fig. 5 shows the diurnal VLF signal amplitude variations for GQD-A118 and ICV-A118 propagation paths, X-ray flux, V_{sw} , PD , B_z , H_T , daily Dst standard deviation and A_p variations during 26–31 May 2011. Blue and red lines in the figure indicate the storm commencement and peak time, respectively. The period is associated with moderate flare activity (up to 43; $C=41$, $M=2$, $X=0$), as well as a moderate storm condition (Dst < -50 (up to -91)). The most disturbed days in this case are the 28 and the 29 May, following a geomagnetic storm on the 28th (Fig. 5c–h). The geomagnetic storm of 28 February appears to be related to the sudden (and significant) rise in V_{sw} and PD , possibly of coronal origin. Up to three CMEs with the speed exceeding 1000 km/s occurred between 27th and 29th (http://cdaw.gsfc.nasa.gov/CME_list/UNIVERSAL/2011_05/univ2011_05.html). Solar wind density influences the capability of a given value of the solar wind electric field (SWEF) to create a Dst disturbance or geo-efficiency (Weigel, 2010, Tsurutani et al., 2011a). Also, solar flares and prominence eruptions are known independent and sporadic events, but they do also occur in association with coronal mass ejections (CMEs). However, we do not strictly attribute the solar wind and magnetosphere conditions during this period to CMEs because of limited scope of analysis in this regard. In Fig. 5a–c, we observed that with relatively high flare activity around 28–29 May, the known diurnal (daytime) signal amplitude-spike in response to solar X-ray output in both propagation paths tends to be diminished under geomagnetic storm condition when compared with 14–19 February scenario (Fig. 5a–b). This situation is replicated in the other three storm conditions investigated alongside.

Fig. 6 shows daily Dst standard deviation, 2-h MBSR, MDP, 2-h MASS, SRT and SST variations for (a) GQD-A118 and (b) ICV-A118 propagation paths during 26–31 May 2011. A summary of trend in variation of the parameters over the period is provided in Table 2. Our main focus here is on 28th (day 3), being the most disturbed, as well as the storm day. We observed an increase in MBSR, MDP and MASS, but a dipping of SRT and SST in GQD-A118 propagation path (Fig. 6a). Notwithstanding, dipping of the MBSR and MDP occurred on the day following the storm day (moderate but significantly disturbed 29th (day 2)). In ICV-A118 propagation path, the MASS increased slightly while MBSR, MDP, SRT and SST dipped with high Dst (Fig. 6b). It is important to note that we had to take a two hour mean due to increase in day length. Also note the spike

Table 1

Trend of variation of VLF signal amplitude metrics, Dst and flare count during 15–18 February 2011 for GQD-A118 and ICV-A118 propagation path.

Date	Mean signal peak (dB)			Signal dip (dB)		Dst (nT)	Flare count	
	MBSR	MDP	MASS	SRT	SST		σ_{Dst}	$\geq C$
GQD-A118 propagation path								
14/2/11	14.08 ± 0.78	9.77	12.57 ± 2.18	-4.13	1.96	± 16.19	12	11 1 0
15/2/11	14.20 ± 1.15	8.80	11.22 ± 0.72	-2.85	-2.13	± 3.67	8	7 0 1
16/2/11	14.85 ± 1.07	9.55	12.93 ± 0.95	-2.69	0.47	± 3.71	15	12 3 0
17/2/11	13.89 ± 1.14	10.10	11.40 ± 0.82	-2.83	-2.26	± 5.27	12	12 0 0
18/2/11	13.21 ± 0.90	9.64	11.25 ± 1.09	-3.27	0.28	± 21.29	20	15 5 0
19/2/11	13.99 ± 1.10	8.14	11.81 ± 2.23	-2.10	0.22	± 2.90	12	12 0 0
ICV-A118 propagation path								
14/2/11	12.95 ± 3.82	-12.89	13.46 ± 3.40	-38.82	-33.99	± 16.19	12	11 1 0
15/2/11	21.11 ± 3.11	-16.05	12.05 ± 4.17	-17.30	-40.80	± 3.67	8	7 0 1
16/2/11	13.60 ± 2.38	-14.56	10.56 ± 3.49	-34.52	-32.80	± 3.71	15	12 3 0
17/2/11	9.83 ± 3.81	-14.04	10.24 ± 2.57	-24.08	-40.50	± 5.27	12	12 0 0
18/2/11	20.56 ± 3.24	-13.11	11.39 ± 3.95	-27.65	-41.75	± 21.29	20	15 5 0
19/2/11	19.81 ± 1.25	-16.28	14.26 ± 3.88	-30.42	-35.67	± 2.90	12	12 0 0

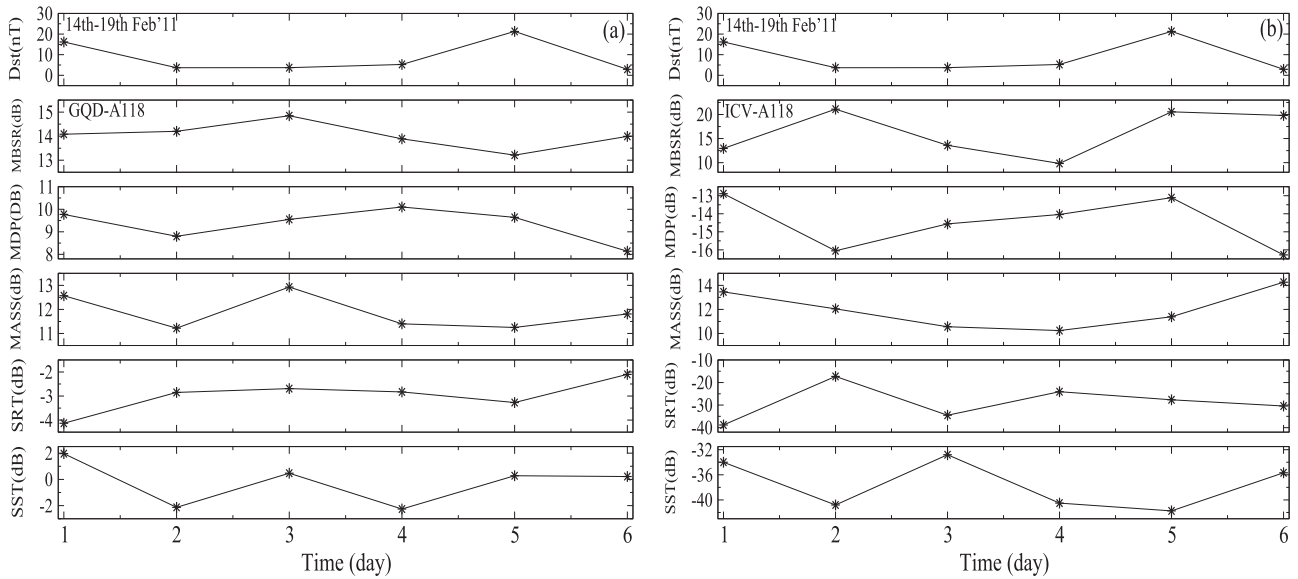


Fig. 4. Daily Dst standard deviation, 4-h mean signal amplitude before sunrise (MBSR), mid-day signal peak (MDP), 4-h mean signal amplitude after sunset (MASS), sunrise terminator (SRT) and sunset terminator (SST) variations for (a) GQD-A118 and (b) ICV-A118 propagation path during 14–19 February 2011.

in MDP due to the possible influence of the flare particularly in GQD-A118 propagation path on 28th (dipping needs to be large or significant to nullify flare-induced influence). Understandably, geomagnetic effects are also not expected on any portion of the signal (e.g., MBSR, MDP, MASS, SRT, and SST) before significant geomagnetic perturbations. The increase (MDP) could also be due to the propagation characteristics of ICV-A118 propagation path, because mode interference significantly depends on ionospheric conditions at the time, propagation paths and energetic electron precipitation level on the ionosphere due to the magnetic storm, which depends on geomagnetic latitude (e.g. Tatsuta et al., 2015).

Fig. 7 shows the diurnal VLF amplitude variations for GQD-A118 and DHO-A118 propagation paths, X-ray flux, V_{sw} , PD , B_z , H_T , daily

Dst standard deviation and A_p variations during 24–29 September 2011. The period is associated with relatively high flare events (up to 51; $C=33$, $M=17$, $X=1$) and intense storm conditions with $Dst \leq -100$. The unique feature of the period is the associated sub-storm of late 26th (red line) following the storm condition that commenced before noon with peak (broken red line), which also marked the sub-storm commencement (Fig. 7e–g). Milder storm conditions also occurred on 28th and 29th. The storm-driving high variable solar wind (and PD spike) is clearly observed in Fig. 6d. Dipping of DHO-A118 propagation path daytime (and MDP) signal on 26th is clearly visible in Fig. 7b, with the post-storm day signal (with lesser geomagnetic index and/or disturbance) on 27th exhibiting a tendency of recovery (or return) to pre-storm level. The

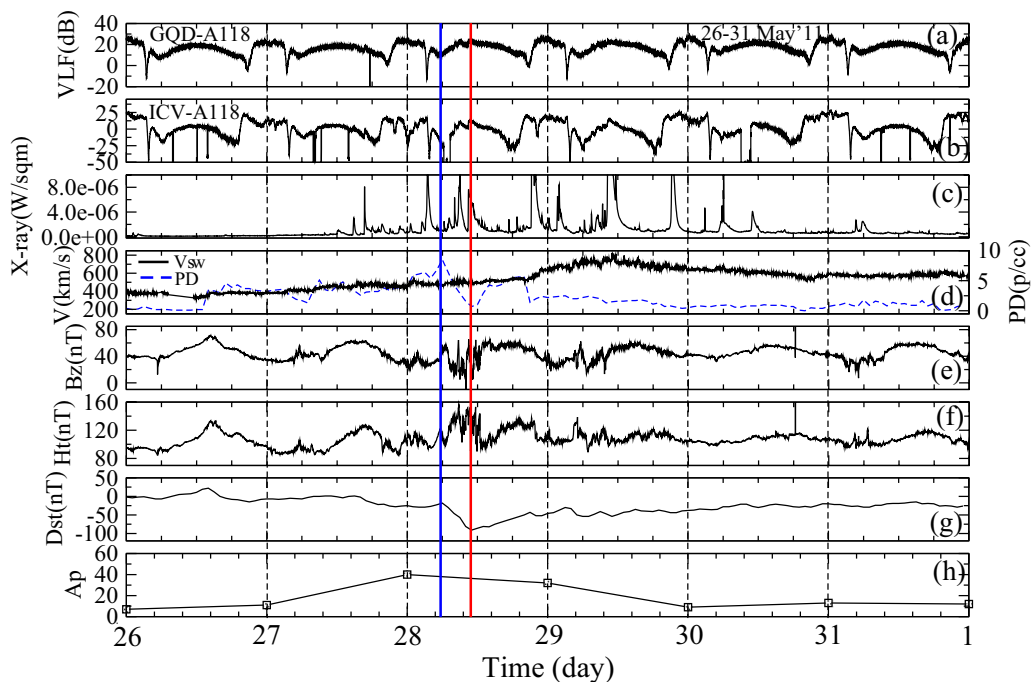


Fig. 5. (a) Diurnal VLF amplitude for GQD-A118 PP; (b) VLF amplitude for ICV-A118 PP; (c) X-ray flux output; (d) solar wind speed (V_{sw}) and particle density (PD); (e) B_z magnetic field component; (f) H_T magnetic field; (g) Dst and (h) A_p variations during 26–31 May 2011 (blue and red lines in the figure indicate storm commencement and peak time respectively). (For interpretation of the references to colour in this figure caption, the reader is referred to the web version of this paper.)

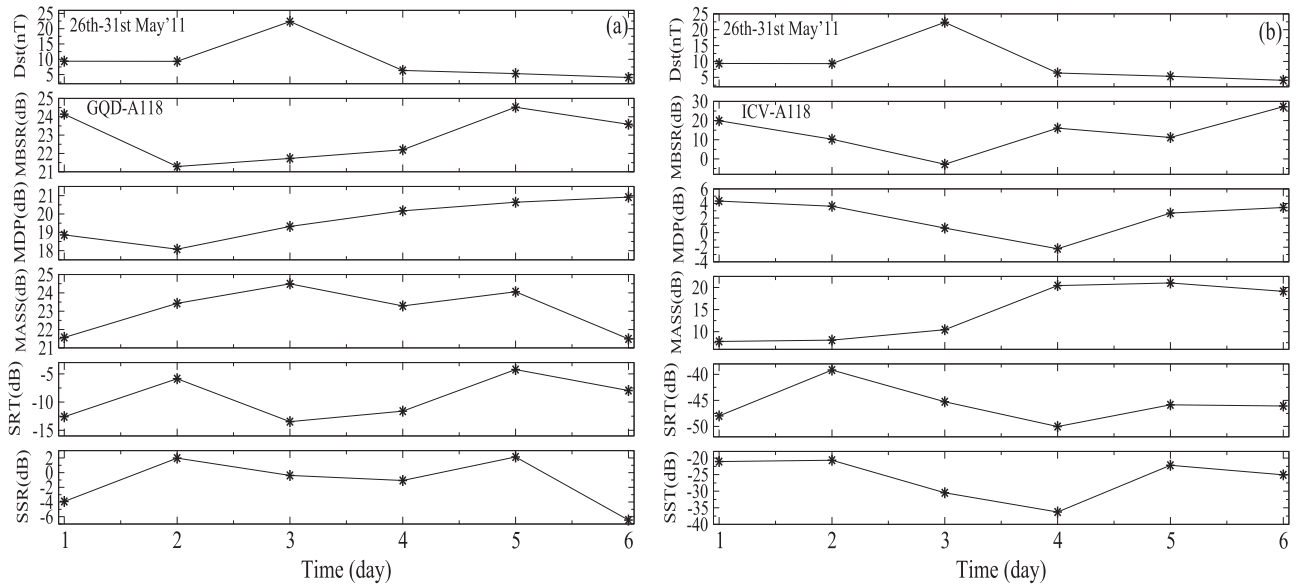


Fig. 6. Daily Dst standard deviation, 2-h mean signal amplitude before sunrise (MBSR), mid-day signal peak (MDP), 2-h mean signal amplitude after sunset (MASS), sunrise terminator (SRT) and sunset terminator (SST) variations for (a) GQD-A118 and (b) ICV-A118 propagation path during 26–31 May 2011.

trend of variations of MBSR, MDP, MASS, SRT and SST has also shown such tendency.

Fig. 8 shows daily Dst standard deviation, 4-h MBSR, MDP, 4-h MASS, SRT and SST variations for (a) GQD-A118 and (b) DHO-A118 propagation paths during 24–29 September 2011. Summary of the trend in variation of the parameters over the period is provided in Table 3. In GQD-A118 propagation path signal, dipping of MDP, SRT and SST was observed on 26th (day 3), while MBSR and MASS increased (Fig. 8a). It is important to note that the peak of the geomagnetic storms-induced perturbations on the ionosphere which commenced during the later part of 26th is expected to greater part of 27th. As could be seen in Fig. 7g, the Dst recovery during 27th is associated with momentary perturbations, followed by the sub-storm commencement around 06:00 pm on that day. Further dippings of MBSR, MDP, MASS and SST were also observed on 27th (day 4; see Fig. 8a). Thereafter, the MBSR, MDP and MASS increased with reduced Dst on the 28th. Notwithstanding, storm conditions were also recorded on the 28th and 29th, but the associated perturbations are not comparable to those of 26th–27th. In DHO-A118 propagation path, dipping of the MDP, MASS and SST was observed on the 26th (day 3) and 28th (day 5; see Fig. 8b). On the other hand, there is a relative increase in MBSR and SRT on the

days (3 and 5). While the trends in the two propagation paths appear to significantly reflect the space weather conditions, the dipping or increase of the signal varied.

Fig. 9 shows the diurnal VLF amplitude variations for GQD-A118 and DHO-A118 propagation paths, X-ray flux, V_{sw} , PD , B_z , H_r , daily Dst standard deviation and A_p variations during 23–28 October 2011. This period is associated with relatively low flare activity (only 11 C class flares), but with an intense storm condition ($Dst < -100$ (reaching -132)). The storm occurred during the early hours of 25th, which commenced late 24th (around 06:00 pm), presumably due to high speed solar wind (HSS) and PD condition of 24th October (Fig. 9d–h). VLF signal data for GQD-A118 propagation path during 12:00 noon, 25th – 06:00 pm, 26th October (Fig. 9a) are not available. It is worth mentioning that only DHO-A118 propagation path (at A118 SID receiving station) recorded data during this time interval. Data of about 6 other propagation paths (e.g., GBZ-A118, ICV-A118, NAA-A118, TBB-A118) in the series are also not available (see Fig. 1 for PP identification). As this period probably corresponds to the peak of induced ionosphere perturbations, it will be interesting to further investigate possible cause of the scenario (this is beyond the scope of this work), with respect to the prevailing geomagnetic condition. Again, dipping of DHO-A118 propagation

Table 2
Trend of variation of VLF signal amplitude metrics, Dst standard deviation and flare count during 26–31 May 2011 for GQD-A118 and ICV-A118 propagation path.

Date	Mean signal peak (dB)			Signal dip (dB)		Dst (nT)	Flare count		
	MBSR	Mid-day	MASS	SRT	SST		σ_{Dst}	$\geq C$	C M X
GQD-A118 propagation path									
26/5/11	24.14 ± 1.24	18.86	21.57 ± 1.01	-12.59	-3.93	± 9.37	0	0 0 0	
27/5/11	21.29 ± 1.05	18.08	23.43 ± 0.65	-5.86	1.98	± 9.31	5	5 0 0	
28/5/11	21.73 ± 1.00	19.32	24.49 ± 1.22	-13.47	-0.38	± 22.33	19	18 1 0	
29/5/11	22.20 ± 1.42	20.17	23.29 ± 1.63	-11.60	-1.07	± 6.35	13	12 1 0	
30/5/11	24.52 ± 1.74	20.64	24.06 ± 1.07	-4.24	2.14	± 5.31	4	4 0 0	
31/5/11	23.59 ± 2.14	20.92	19.11 ± 4.10	-7.75	-6.46	± 4.04	2	2 0 0	
ICV-A118 propagation path									
26/5/11	19.92 ± 4.32	4.33	7.79 ± 2.62	-47.18	-21.05	± 9.37	0	0 0 0	
27/5/11	10.26 ± 4.32	3.62	8.08 ± 8.74	-39.18	-20.66	± 9.31	5	5 0 0	
28/5/11	-2.74 ± 8.39	0.63	10.44 ± 9.05	-45.27	-30.47	± 22.33	19	18 1 0	
29/5/11	16.07 ± 2.28	-2.21	20.42 ± 3.17	-50.02	-36.28	± 6.35	13	12 1 0	
30/5/11	11.19 ± 2.94	2.68	21.02 ± 3.28	-45.85	-22.17	± 5.31	4	4 0 0	
31/5/11	22.21 ± 3.83	3.45	19.11 ± 4.10	-46.08	-25.07	± 4.04	2	2 0 0	

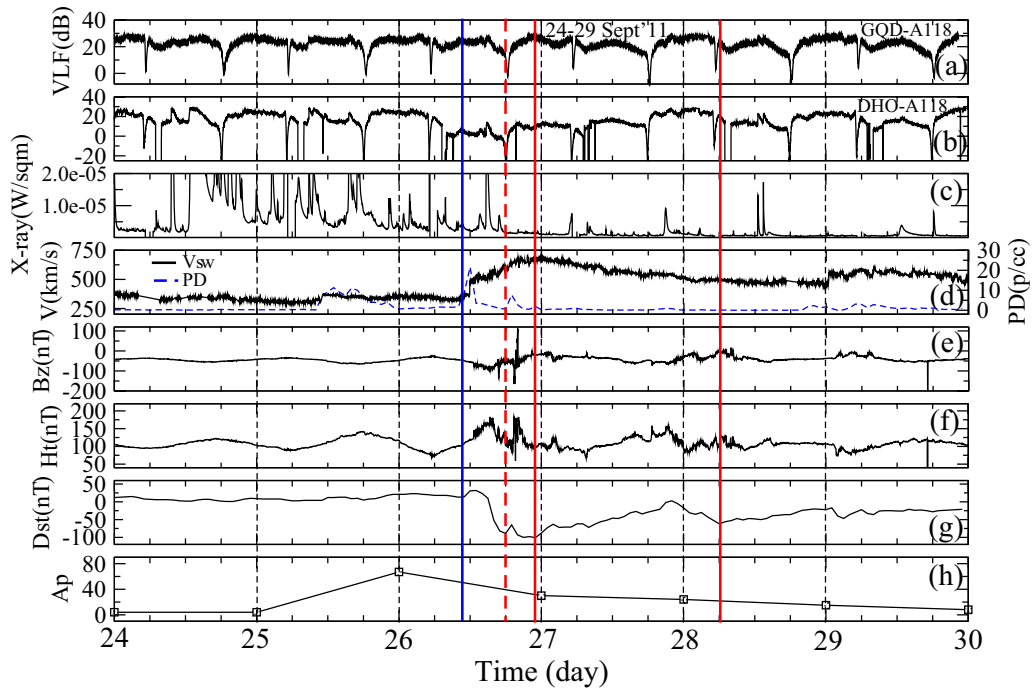


Fig. 7. (a) Diurnal VLF amplitude for GQD-A118 PP, (b) diurnal VLF amplitude for DHO-A118 PP, (c) X-ray flux output, (d) solar wind speed (V_{sw}) and particle density (PD), (e) B_z magnetic field component, (e) H_t magnetic field, (f) Dst , and (g) A_p variations during 24–29 September 2011 (blue and red lines in the figure indicate storm commencement and peak time respectively). (For interpretation of the references to colour in this figure caption, the reader is referred to the web version of this paper.)

path daytime and MDP signal on 25th (most disturbed day) is clearly visible (Fig. 9b), with the post-storm day signal exhibiting a drop or recovery to pre-storm level.

Fig. 10 shows daily Dst standard deviation, 4-h MBSR, MDP, 4-h MASS, SRT and SST variations for (a) GQD-A118 and (b) DHO-A118 propagation paths during 23–28 October 2011. Summary of the trend in variation of the parameters over the period is provided in Table 4. GQD-A118 propagation path data during 25th and 26th is inadequate for the present analysis (Fig. 10a). The DHO-A118 propagation path signal showed dipping of the MBSR, MDP and MASS on 25th (day 3), corresponding to the storm’s peak day, but an increase in SRT and SST (Fig. 10a). The space weather condition (with peak) of 25th (day 3) commenced at around 06:00 pm on 24th (day 2). Interestingly, dipping of the MDP and MASS also

commenced on 24th (day 2). There is a post-storm day increase of MBSR, MDP and MASS with significant Dst low on 26th, a scenario that is characteristic of most post-storm day signals. We therefore viewed such scenario as post-storm day signal recovery tendency.

We now identify the most disturbed day(s) in each of the four 6-day periods, and analyse the trend in the signal metrics variation on the day, namely, event 1 (E_1) on 18 February 2011; event 2 (E_2) on 28 May 2011; event 3 (E_3) on 26–27 September 2011; and event 4 (E_4) on 25 October 2011. Due to the peculiarity of the events during 26–27 September 2011 (recurrent substorm), two days have been allowed for the analysis. In general, two of three events (E_{1-3}) showed dipping of MDP in GQD-A118 propagation path (VLF data during E_4 is not available). Three of the four events (E_{1-4}) showed dipping of MDP in ICV/DHO-A118 propagation

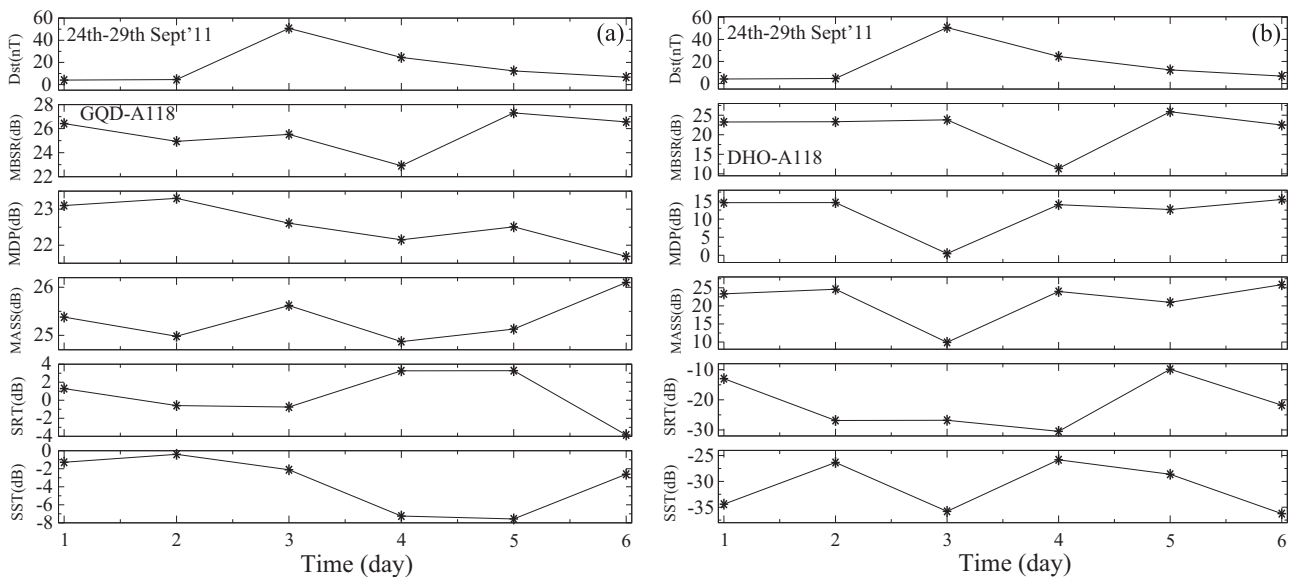


Fig. 8. Daily Dst standard deviation, 4-h mean signal amplitude before sunrise (MBSR), mid-day signal peak (MDP), 4-h mean signal amplitude after sunset (MASS), sunrise terminator (SRT) and sunset terminator (SST) variations for (a) GQD-A118 and (b) DHO-A118 propagation path during 24–29 September 2011.

Table 3
Trend of variation of VLF signal amplitude metrics, Dst and flare count during 25–28 September 2011 for GQD-A118 and HO-A118 propagation path.

Date	Mean signal peak (dB)			Signal dip (dB)		Dst (nT)	Flare count		
	MBSR	Mid-day	MASS	SRT	SST		σ_{Dst}	$\geq C$	C M X
GQD-A118 propagation path									
24/9/11	26.42 ± 1.02	23.10	25.38 ± 2.10	1.30	−1.28	± 4.08	13	4 8 1	
25/9/11	24.94 ± 1.16	23.30	24.98 ± 0.96	−0.59	−0.40	± 4.56	10	4 6 0	
26/9/11	25.52 ± 1.14	22.61	25.62 ± 1.59	−0.75	−2.11	± 50.73	11	9 2 0	
27/9/11	22.91 ± 1.35	22.15	24.87 ± 1.63	−3.26	−7.25	± 24.54	8	8 0 0	
28/9/11	27.31 ± 0.77	22.51	25.13 ± 1.38	3.28	−7.57	± 12.37	4	3 1 0	
29/9/11	26.56 ± 1.29	21.69	26.10 ± 2.32	−3.85	−2.61	± 6.73	3	3 0 0	
DHO-A118 propagation path									
24/9/11	23.26 ± 2.04	14.55	23.32 ± 1.00	−12.96	−34.41	± 4.08	13	4 8 1	
25/9/11	23.33 ± 1.29	14.57	24.60 ± 0.99	−26.86	−26.34	± 4.56	10	4 6 0	
26/9/11	23.81 ± 1.05	0.45	9.90 ± 1.48	−26.79	−35.80	± 50.73	11	9 2 0	
27/9/11	11.38 ± 1.05	14.00	23.68 ± 1.90	−30.47	−25.82	± 24.54	8	8 0 0	
28/9/11	25.90 ± 1.74	12.66	20.98 ± 2.09	−9.85	−28.62	± 12.37	4	3 1 0	
29/9/11	22.49 ± 2.04	15.43	25.87 ± 3.31	−21.78	−36.25	± 6.73	3	3 0 0	

paths. We note that solar flare occurred around mid-day in the days when MDP showed no dipping. This suggests possible flare induced increase of signal amplitude on the MDP or resulting from other atmospheric phenomena. Two of four events (E_{1-4}) showed dipping of MBSR in GQD-A118 propagation path, and dipping in all the four events in ICV/DHO-A118 propagation paths. Two of three events (E_{1-3}) showed dipping of MASS in GQD-A118 propagation path (VLF data during E_4 is not available), and two of the four events in ICV/DHO-A118 propagation path. Three of the four events showed dipping of SRT in GQD-A118 propagation path, and two of the four in ICV/DHO-A118 propagation paths. Two of the four events showed dipping of SST in GQD-A118 propagation path, and three of the four in ICV/DHO-A118 propagation paths. We have also observed that within the local day time interval (24 h), the events occurred well before or after four of five MBSR and MASS, and five of six SRT and SST that showed no dipping (or maintained amplitude) in accordance with the events. Among other possible inferences, this trend suggests that geomagnetic effects are not

expected on any aspect of the signal (e.g., MBSR, MDP, MASS, SRT, and SST) before significant geomagnetic perturbations, and if the event occurs well before the component, the induced ionospheric perturbations is expected to have significantly reduced at the time interval. Of the three propagation paths, the signal of DHO-A118 appears to be the most sensitive to geomagnetic induced magnetospheric-ionospheric dynamics. However, given the few number of the cases analysed so far, drawing a firm conclusion may be difficult at this stage. Therefore, we include more cases in the next analysis (see Table 5), and combine different signal aspects on a single graph for a better view of the trends.

We analyse and study the trend in variations of combined signal aspects for 16 storm cases ($Dst = -50$ to -132) between February 2011 and June 2012 for two propagation paths (GQD-A118 and DHO-A118). Details of the storm events are provided in Table 5. Analysis include taking values of the (a) signal metrics (MBSR, MDP, MASS, SRT and SST) 1-day before an event (BE), during an event (DE) and after an event (AE) and (b) a 2-day mean

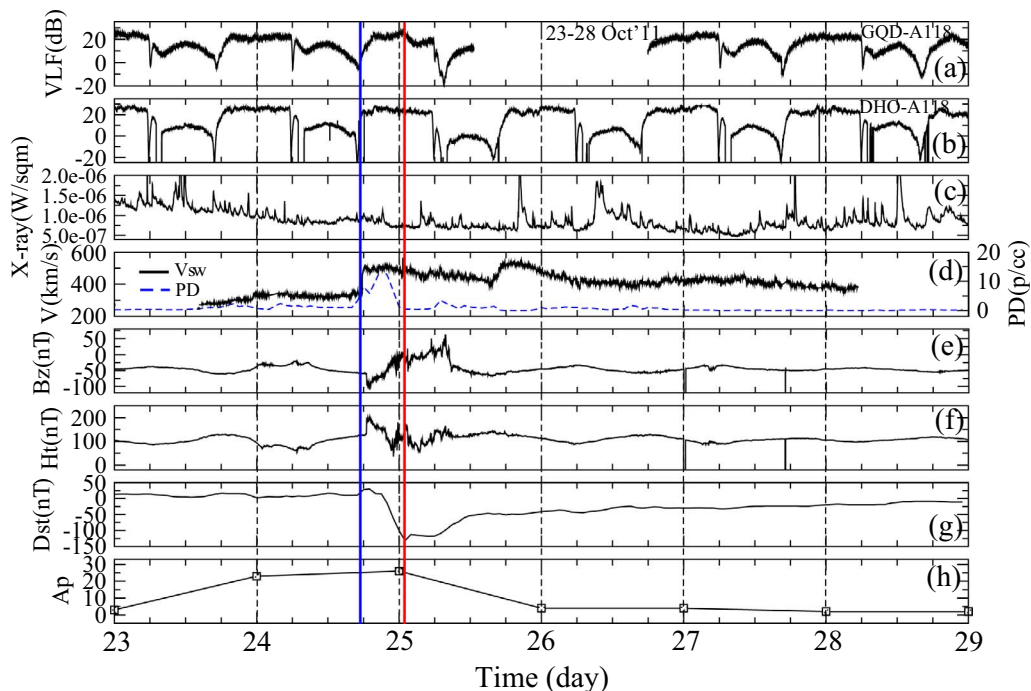


Fig. 9. (a) Diurnal VLF amplitude for GQD-A118 PP, (b) diurnal VLF amplitude for DHO-A118 PP, (c) X-ray flux output, (d) solar wind speed, (d) B_z magnetic field component, (e) H_t magnetic field, (f) Dst, and (g) A_p variations during 23–28 October 2011.

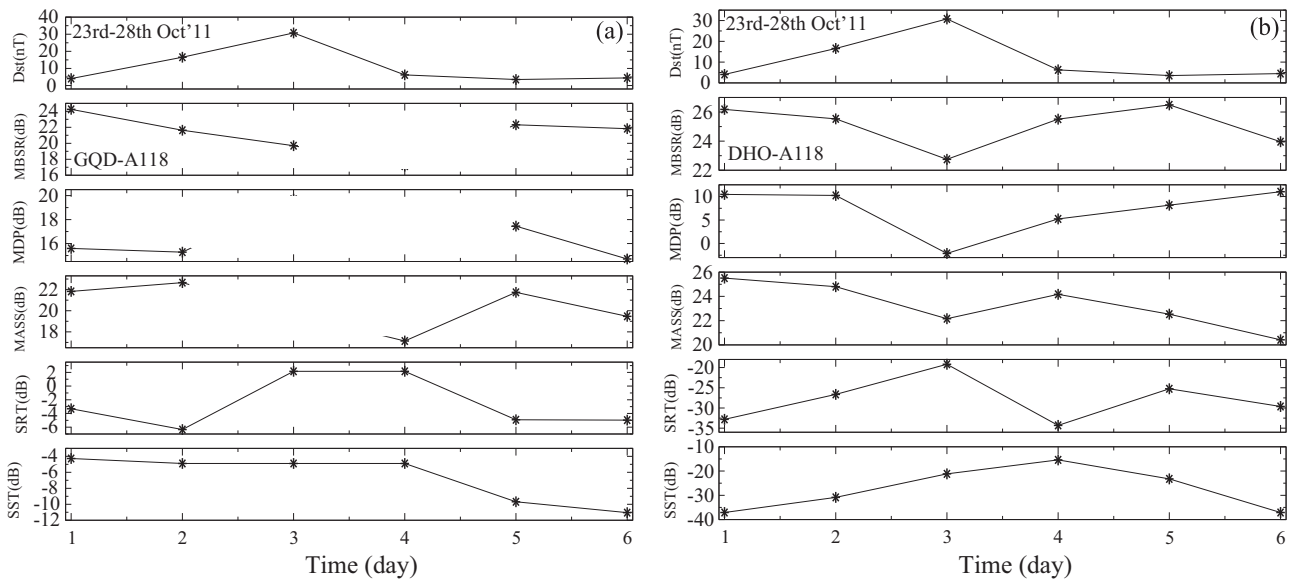


Fig. 10. Daily Dst standard deviation, 4-h mean signal amplitude before sunrise (MBSR), mid-day signal peak (MDP), 4-h mean signal amplitude after sunset (MASS), sunrise terminator (SRT) and sunset terminator (SST) variations for (a) GQD-A118 and (b) DHO-A118 propagation path during 23–28 October 2011.

signal metric BE, DE and AE. An event is selected based on factors such as availability and quality of VLF signal data on the day, and relatively quiet BE and AE, particularly for the 2-day mean analysis. Although BE and AE data were carefully chosen to be consistent with relative geomagnetic quiet condition, a few choices on significantly perturbed days were unavoidable due to intervals of extended geomagnetic active condition and recurrent storms. This scenario can cause high variability of VLF radio signal. Other than solar induced fluctuations, the ionosphere and VLF radio signal also response to effects originating from a number of other sources (see Section 1.1). Some of the effects are interconnected (with possible interference), leading to a high variability of signal strength. Therefore, a 'perfect' consistency in trend across all the cases is not expected. Fig. 11 shows Dst deviation (fluctuation) and trend in variation of signals MDP, MBSR, MASS, SRT and SST one day before and after (successive) each of the 16 selected storm conditions for (a) GQD-A118 and (b) DHO-A118 propagation paths. Detail of the data is provided in Table A1 (Appendix A).

For GQD-A118 propagation path, 10 of 14 MDP, 10 of 15 MBSR, 7 of 14 MASS, 9 of 14 SRT and 7 of 14 SST have shown a dipping of the signals. These correspond respectively to 71.4%, 66.7%, 50%,

Table 5
Summary of analysed geomagnetic storm conditions.

No.	Date	Max Dst (nT)	σ_{Dst}	Flare count ($\geq C$) C M X
1	05/02/2011	-51	± 8.99	0 0 0
2	01/03/2011	-81	± 36.28	7 0 0
3	06/04/2011	-65	± 24.31	3 0 0
4	12/04/2011	-51	± 22.11	3 0 0
5	26/09/2011	-101	± 50.73	9 2 0
6	25/10/2011	-132	± 30.76	1 0 0
7	22/01/2012	-67	± 37.00	4 0 0
8	15/02/2012	-58	± 9.63	0 0 0
9	19/02/2012	-54	± 12.8	1 0 0
10	07/03/2012	-74	± 25.41	1 0 0
11	15/03/2012	-74	± 20.75	1 0 0
12	28/03/2012	-55	± 12.09	1 0 0
13	05/04/2012	-54	± 13.82	3 0 0
14	23/04/2012	-95	± 32.23	3 0 0
15	12/06/2012	-51	± 12.47	13 0 0
16	16/06/2012	95	± 20.24	4 0 0
17*	17/06/2012	80	± 46.75	7 0 0

Table 4
Trend of variation of VLF signal amplitude metrics, Dst and flare count during 23–28 October 2011 for GQD-A118 and DHO-A118 propagation path.

Date	Mean signal peak (dB)			Signal dip (dB)		Dst (nT)	Flare count	
	MBSR	Mid-day	MASS	SRT	SST		$\geq C$	C M X
GQD-A118 propagation path								
23/10/11	24.35 \pm 0.88	16.59	21.83 \pm 0.87	-3.31	-4.27	± 4.08	3	3 0 0
24/10/11	21.63 \pm 1.02	15.28	22.66 \pm 0.93	-6.35	-4.89	± 16.35	0	0 0 0
25/10/11	19.70 \pm 3.77	-	-	2.16	-	± 30.76	1	0 0 0
26/10/11	17.14 \pm 2.59	-	-	-	-	± 6.25	1	1 0 0
27/10/11	22.32 \pm 1.43	17.45	21.74 \pm 1.33	-4.92	-9.69	± 3.53	1	1 0 0
28/10/11	21.83 \pm 0.86	19.35	19.47 \pm 2.52	-4.97	-11.98	± 4.48	5	5 0 0
DHO-A118 propagation path								
23/10/11	26.18 \pm 1.05	10.45	25.51 \pm 0.82	-32.81	-37.10	± 4.08	3	3 0 0
24/10/11	25.53 \pm 0.92	10.23	24.80 \pm 1.33	-26.64	-30.84	± 16.35	0	0 0 0
25/10/11	22.75 \pm 0.99	-2.12	22.16 \pm 1.68	-19.19	-21.17	± 30.76	1	1 0 0
26/10/11	25.51 \pm 1.22	5.23	24.17 \pm 1.18	-34.30	-15.40	± 6.25	1	1 0 0
27/10/11	26.49 \pm 1.72	8.16	22.53 \pm 4.45	-25.25	-23.23	± 3.53	1	1 0 0
28/10/11	23.96 \pm 1.68	11.02	20.42 \pm 1.32	-29.63	-37.10	± 4.48	5	5 0 0

64.3% and 50.0% of the combined cases. In DHO-A118 propagation path 13 of 16 MDP, 9 of 16 MBSR, 8 of 16 MASS, 5 of 14 SRT and 7 of 16 SST showed dipping of the signals. These correspond to respective 81.3%, 56.3%, 50%, 35.7% and 43.8% of the combined cases. Note that dipping of any of DE and AE signal metric in cases 15 and 16 is taken as a response to the event because storm condition or the event commenced during late DE and peaked in AE. Also, recurrent storms occurred on the day after case 16. Whereas majority of MDP in both propagation paths have shown a notable evidence of dipping, few number of PP-mismatched incidences of MDP signal rise (or increase) on some events day have been observed (e.g., events 8, 11 and 16 in GQD and 4 and 13 in DHO). The increase may be related to flare induced signal amplitude spike on the signal or

phenomena arising from sources other than storm events. We also observed a notable matched-increase of the diurnal signal level (including MDP, MBSR and MASS) on DE 7 (22 January 2012) in both propagation paths. While further investigation is vital for accurate interpretation, a closer look at available data showed occurrence of storm associated M-class flare with corresponding peaks, suggesting an enhancement of not only the instantaneous but also background X-ray flux output. Fig. 12 shows Dst deviation (fluctuation) and trend in variation of 2-day mean MDP, MBSR, MASS, SRT and SST signals before, during and after each event for (a) GQD-A118 and (b) DHO-A118 propagation paths. Details of the data is provided in Table B1 (Appendix B). Using a different criterion for data selection, the analysis presented in Fig. 12 is a follow up on the one

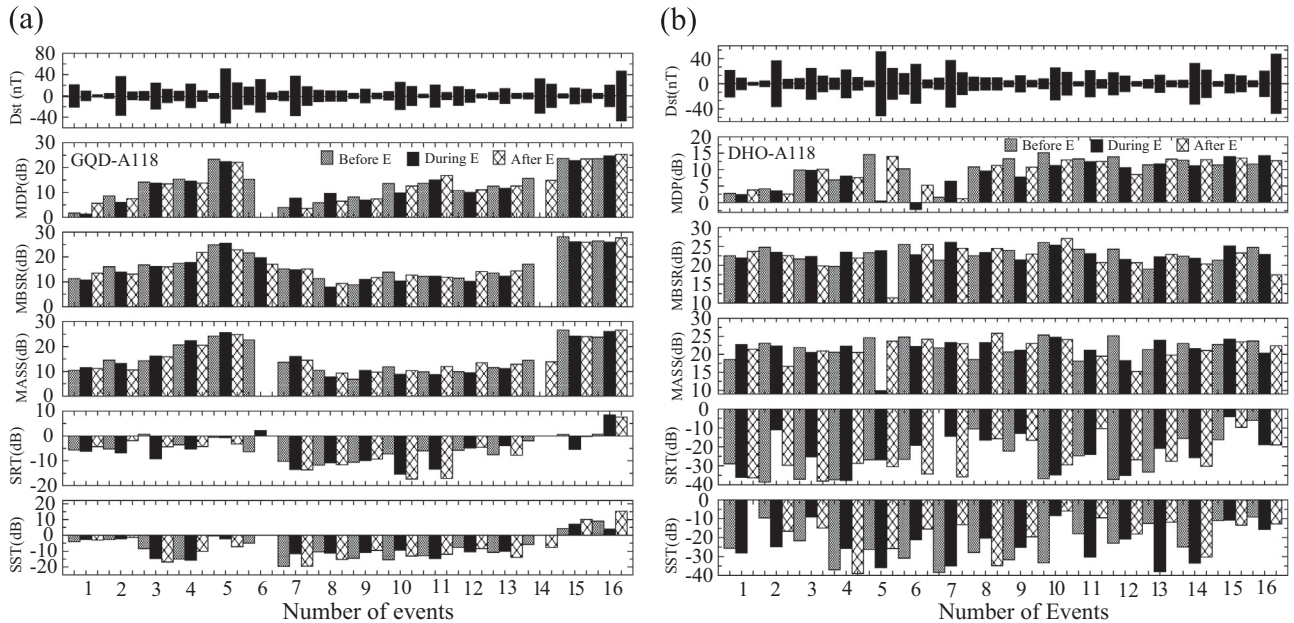


Fig. 11. Daily Dst deviation, and trend in variation of MDP, MBSR, MASS, SRT and SST signals one day before and after each of the 16 considered storm conditions for (a) GQD-A118 and (b) DHO-A118 propagation paths. A '0' indicates absence of data.

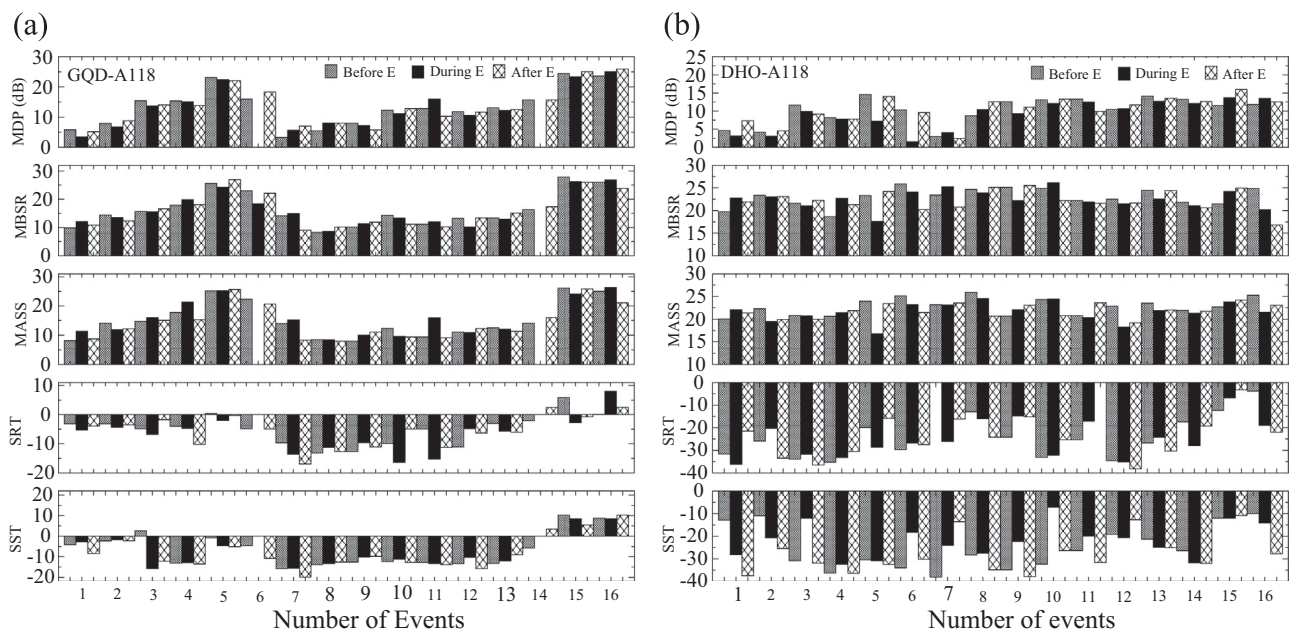


Fig. 12. Daily Dst deviation (fluctuation) and trend in variation of 2-day mean MDP, MBSR, MASS, SRT and SST before, during and after an event for (a) GQD-A118 and (b) DHO-A118 propagation paths. A '0' indicates absence of data.

presented in Fig. 11, and expected to provide resourceful clue towards a better conclusion of the results. Whereas BE, DE and AE represent data of three consecutive days with reference to the event's day (DE) in the former analysis (Fig. 11), each acronym (BE, DE or AE) represent a 2-day mean (VLF) with respect to DE (but not necessarily in succession to DE). Besides data availability and quality, an important data selection criterion is a relative geomagnetic quiet BE- and AE-day with respect to DE – hence, one or more days gap before or after DE (in some cases).

For GQD-A118 propagation path, 10 of 14 MDP, 9 of 15 MBSR, 7 of 14 MASS, 11 of 16 SRT and 5 of 14 SST showed dipping of the signals. These corresponds to respective 71.4%, 60.0%, 50.0%, 68.8% and 35.7% of the combined cases. For DHO-A118 propagation path, 11 of 16 MDP, 11 of 16 MBSR, 10 of 16 MASS, 6 of 14 SRT and 7 of 16 SST showed dipping of the signals, corresponding to respective 68.8%, 68.8%, 62%, 42.9% and 43.8% of the combined cases. In general, MDP signal has shown a high probability of a dipping scenario following significant geomagnetic disturbance or storm condition. The MBSR and MASS signals have also shown good probability of exhibiting such storm-induced dipping, but appear to be influenced by event's occurrence time and the highly variable conditions of dusk-to-dawn ionosphere (as stated earlier). However, a few cases have shown a rise or increase of the components instead (e.g., MDP, MBSR, and MASS) following a significant geomagnetic event. We speculate that such a scenario (signal rise) may be related to storm associated phenomena or of sources other than solar origin, rather than being a case against the 'favoured' dipping – this need be studied further. In contrast, the SRT and SST signals have shown significant post-storm dipping in GQD-A118 propagation path but mostly increase in DHO-A118 propagation path. Does the trend in post-storm SRT and SST variation depend on signal propagation path? This important question may not be conclusively answered based on this present analysis. Thus, a clear dependence of SRT and SST on geomagnetic disturbance or storm conditions seems inconclusive.

We consider it important to highlight the constraints associated with this analysis that may have also influenced our results and/or findings. Besides flare and X-ray flux induced amplitude variation (see Fig. 2c), the daytime diurnal signal between SRT and SST of VLF radio waves are generally quite stable. No doubt, their stability has contributed to the consistency of MDP trend in the overall pattern of the results – the combined analysis showed about 73% dipping of the MDP. On the other hand, high variability or fluctuation of dusk-to-dawn signal (see Fig. 2a–d) remains a major drawback to analysis relating to MBSR and MASS – the combined analysis showed 63% and 53% dipping of the MBSR and MASS respectively. Similarly, the pseudo-SRT and SST (occurrence of double or multiple-tipped sunrise and/or sunset terminator) exhibited by diurnal VLF signal also hampers proper analysis of the signals – the combined analysis showed 52% and 43% dipping of the SRT and SST respectively. Deciding which of the tips to measure (in case of a pseudo-SRT/SST) is important but challenging. Nevertheless, a proper study that probes the cause of such fluctuations and occurrence of pseudo-terminators in VLF signature will be highly valuable. Such a study in addition to further investigating the observed, as well as an interesting propagation paths (matched and mismatched) signal-rise during some cases of geomagnetic storm conditions have been initiated. This is beyond the scope of the present work and will be published elsewhere in due course.

4. Summary and conclusion

The characteristic response of diurnal VLF signal to space weather induced ionospheric disturbances varies from one propagation path to another, and also depends on location of the transmitters and receivers, ionisation and chemistry of the D region over the propagation path, and the intensity of induced perturbations. Other influencing

factors include signal frequency and nature of Earth's surface (also see Mimno, 1937; Poole, 1999; Melia, 2010). In principle, known strong perturbations from solar flares and gamma-ray bursts on VLF signals can be reproduced from ab initio calculations (Palit et al., 2013). In this paper, we used condensed metrics of diurnal VLF signal (such as MBSR, MDP, MASS, SRT and SST) to investigate the footprint of geomagnetic activity in D layer ionosphere at mid-latitude (40–54°) region, under varying degree of 16 storm conditions (and consequent disturbances). Although the strength of diurnal signals significantly varied from one propagation path to another, the trend of variations of the characteristic signal appears to reflect the prevailing space weather conditions of varying time scale. We found a significant dipping of the mid-day amplitude peak (MDP) of the signal within 1–2 days of significant geomagnetic disturbance or storm conditions. The MBSR and MASS signals have also generally shown such storm-induced dipping. However, they appear to be influenced by events' occurrence time and the highly variable condition of dusk-to-dawn ionosphere. We observed a few cases of rise of the signals (e.g., MDP, MBSR or MASS) following a significant geomagnetic event. However, this may be related to storm-associated events or due to effects arising from sources other than solar origin. The extent of the induced dipping (or rise) significantly depends on the intensity and duration of event(s), as well as the propagation path of the signal. The post-storm day signal (following a main event, with lesser or significantly reduced geomagnetic activity) exhibited a tendency of recovery to pre-storm day level. In the present analysis, the post-storm SRT and SST variations do not appear to have a well-defined trend – the signals have shown more post-storm dipping in GQD-A118 propagation path but mostly increase in DHO-A118 propagation path.

Many researchers have investigated and reported ionospheric and VLF signal anomalies before seismic events (e.g., Hayakawa et al., 1998; Ray and Chakrabarti, 2012; Sasmal and Chakrabarti, 2009). Such anomalies were often attributed to seismicity and therefore viewed as pre-cursors. However, in order to ensure that such VLF anomalies are indeed due to seismic events, it is imperative that other possible and potential drivers of ionospheric anomalies around intervening period are investigated, identified and separated. In future, we will investigate possible solar and geomagnetic-induced perturbations of the ionosphere within the time frame in which ionospheric precursor (using VLF signal) was reported. This must be taken into consideration before marking anomalies as pre-cursors. For this two prong approaches are necessary: (i) to reproduce propagation path dependent effects on VLF signals due to number of specific types of solar induced perturbations as in Palit et al. (2013) and (ii) to find statistical correlations among various quantities using data for longer duration. The work is in progress and would be published elsewhere.

Acknowledgement

Victor U.J.N. acknowledge TWAS/ICTP, Trieste, Italy and the S.N. Bose National Centre for Basic Sciences for the research fellowship during which this work was done. Authors thank Dr. William Denig (NOAA), Margaret Tilton (NOAA affiliate at Cooperative Institute for Research in Environmental Sciences (CIRES), University of Colorado at Boulder) and Daniel Wilkinson (NOAA) for their help with relevant data link and tips. Authors also acknowledge NOAA, WDCG, SWEPAM and A118 SID database.

Appendix A

See Table A1.

Table A1

Variations in MDP, MBSR, MASS, SRT and SST signals 1-day before, during and after each of the 16 events for (a) DHO-A118 and (b) GQD-A118 propagation path.

Date	SIG	GQD-A118					DHO-A118					DST DEVIATIONS
		MBSR	MDP	MASS	SRT	SST	MBSR	MDP	MASS	SRT	SST	
04/02/2011	BE	11.28 ± 1.10	1.71	10.41 ± 1.29	-5.65	-4.14	22.49 ± 1.15	2.80	18.58 ± 1.69	-28.96	-25.53	± 20.97
05/02/2011	DE	10.66 ± 1.77	1.28	11.45 ± 1.13	-6.21	-2.69	21.98 ± 1.76	2.44	22.72 ± 2.70	-36.04	-28.13	± 8.99
06/02/2011	AE	13.54 ± 0.67	5.61	11.16 ± 2.54	-4.34	-2.95	23.64 ± 2.20	3.80	21.41 ± 2.48	-36.40	-	± 2.23
28/02/2011	BE	16.04 ± 0.85	8.56	14.49 ± 1.19	-5.31	-2.62	24.74 ± 1.66	4.16	23.07 ± 1.81	-38.62	-9.63	± 4.54
01/03/2011	DE	13.96 ± 1.23	6.00	13.18 ± 1.49	-6.79	-2.20	23.43 ± 1.22	3.58	22.29 ± 2.35	-10.96	-24.76	± 36.28
02/03/2011	AE	13.14 ± 1.79	7.46	10.50 ± 0.65	-1.89	-1.26	22.55 ± 1.60	2.55	16.64 ± 2.54	-29.74	-16.60	± 7.26
04/04/2011	BE	16.81 ± 1.40	14.17	14.23 ± 3.24	0.71	-8.52	21.66 ± 2.05	9.87	21.92 ± 1.87	-37.03	-21.64	± 8.28
06/04/2011	DE	16.17 ± 1.71	13.75	16.14 ± 1.61	-9.21	-14.68	22.31 ± 2.81	9.75	20.48 ± 0.84	-25.25	-9.08	± 24.31
07/04/2011	AE	16.03 ± 1.56	13.44	15.88 ± 1.57	-4.46	-16.83	19.81 ± 2.09	10.10	20.94 ± 2.73	-38.08	-14.93	± 12.40
11/04/2011	BE	17.43 ± 0.74	15.37	20.62 ± 0.50	-3.56	-14.97	19.73 ± 1.20	6.91	20.62 ± 0.50	-37.42	-37.03	± 8.92
12/04/2011	DE	17.78 ± 0.62	14.77	22.27 ± 1.10	-5.31	-15.66	23.49 ± 1.17	8.00	22.27 ± 1.10	-37.81	-25.67	± 22.11
13/04/2011	AE	21.89 ± 1.60	13.79	20.49 ± 1.77	-4.26	-10.05	21.89 ± 1.60	7.61	20.49 ± 1.77	-28.71	-39.04	± 10.01
25/09/2011	BE	24.94 ± 1.16	23.30	24.98 ± 0.96	-0.59	-0.40	23.33 ± 1.29	14.57	24.60 ± 0.99	-26.86	-26.34	± 4.56
26/09/2011	DE	25.52 ± 1.14	22.61	25.62 ± 1.59	-0.75	-2.11	23.81 ± 1.05	0.45	9.90 ± 1.48	-26.79	-35.80	± 50.73
27/09/2011	AE	22.91 ± 1.35	22.15	24.87 ± 1.63	-3.26	-7.25	11.38 ± 1.05	14.00	23.68 ± 1.90	-30.47	-25.82	± 24.54
24/10/2011	BE	21.63 ± 1.02	15.28	22.66 ± 0.93	-6.35	-4.89	25.53 ± 0.92	10.23	24.80 ± 1.33	-26.64	-30.84	± 16.55
25/10/2011	DE	19.70 ± 3.77	0	0	2.16	0	22.75 ± 0.99	-2.12	22.16 ± 1.68	-19.19	-21.17	± 30.76
26/10/2011	AE	17.14 ± 2.59	0	0	0	0	25.51 ± 1.22	5.23	24.17 ± 1.18	-34.30	-15.40	± 6.25
21/01/2012	BE	15.11 ± 1.24	3.94	13.62 ± 0.90	-10.18	-19.56	21.36 ± 1.80	1.59	21.78 ± 1.52	0	-38.48	± 8.80
22/10/2012	DE	14.86 ± 1.94	7.73	15.92 ± 0.99	-13.47	-11.56	26.10 ± 1.08	6.46	23.28 ± 1.93	-14.35	-34.97	± 37.00
23/01/2012	AE	15.12 ± 1.20	3.55	14.50 ± 1.23	-13.70	-19.51	24.47 ± 1.75	1.17	22.96 ± 1.42	-35.80	-13.12	± 17.40
14/02/2012	BE	11.28 ± 1.10	5.81	10.41 ± 1.29	-11.78	-10.45	22.49 ± 1.15	10.80	18.58 ± 1.69	-10.48	-27.89	± 10.63
15/02/2012	DE	7.92 ± 1.22	9.61	07.75 ± 1.98	-10.86	-11.21	23.38 ± 1.66	9.59	23.23 ± 1.16	-16.42	-20.27	± 9.63
16/02/2012	AE	9.37 ± 0.87	6.49	09.28 ± 1.41	-11.60	-15.23	24.44 ± 1.49	11.27	25.85 ± 1.63	-15.62	-34.75	± 9.63
18/02/2012	BE	8.86 ± 1.54	8.19	06.77 ± 1.84	-10.65	-14.47	23.94 ± 1.32	13.28	20.66 ± 1.22	-22.23	-31.69	± 4.97
19/02/2012	DE	11.00 ± 1.27	6.96	10.39 ± 1.18	-9.89	-10.79	21.44 ± 0.90	7.77	19.77 ± 1.39	-12.93	-25.11	± 12.81
20/02/2012	AE	11.74 ± 0.67	7.39	09.67 ± 2.25	-9.27	-9.56	22.96 ± 1.62	10.76	22.98 ± 2.05	-16.56	-19.62	± 5.15
06/03/2012	BE	13.93 ± 1.19	13.57	11.85 ± 1.16	-7.22	-15.40	26.03 ± 1.07	15.15	25.37 ± 1.30	-36.78	-33.32	± 7.91
07/03/2012	DE	10.34 ± 0.88	9.81	08.82 ± 3.27	-15.40	-9.27	25.29 ± 0.91	11.28	24.72 ± 2.36	-34.86	-8.34	± 25.41
08/03/2012	AE	12.76 ± 1.37	12.56	10.33 ± 2.34	-17.35	-13.08	27.07 ± 0.79	12.95	24.11 ± 1.39	-29.57	-5.97	± 17.95
14/03/2012	BE	12.14 ± 0.64	13.66	09.77 ± 2.18	-6.05	-12.89	24.21 ± 1.41	13.27	18.17 ± 1.42	-24.69	-17.93	± 3.31
15/03/2012	DE	12.21 ± 0.78	14.99	08.78 ± 2.79	-13.39	-14.64	23.10 ± 1.64	12.42	21.16 ± 0.91	-23.95	-30.37	± 20.75
16/03/2012	AE	11.86 ± 0.66	16.87	11.91 ± 1.12	-17.11	-11.99	20.74 ± 0.69	12.50	19.50 ± 1.12	-10.38	-9.53	± 6.73
27/03/2012	BE	11.43 ± 0.93	10.74	09.87 ± 2.18	-5.73	-7.63	24.23 ± 1.98	13.91	25.14 ± 1.92	-37.29	-22.91	± 17.50
28/03/2012	DE	10.20 ± 1.01	10.59	09.47 ± 1.48	-4.87	-10.35	21.53 ± 1.15	10.62	18.24 ± 2.19	-35.09	-20.66	± 12.09
29/03/2012	AE	14.13 ± 0.81	11.02	13.50 ± 1.14	-4.56	-8.43	20.70 ± 1.45	8.45	15.27 ± 2.64	-26.79	-18.03	± 3.74
04/04/2012	BE	13.55 ± 0.78	12.50	11.55 ± 1.15	-7.57	-10.72	18.98 ± 1.90	11.45	21.32 ± 1.42	-33.32	-12.47	± 6.73
05/04/2012	DE	12.24 ± 0.71	11.71	11.23 ± 2.67	-3.99	-10.15	22.19 ± 0.97	11.71	23.92 ± 2.28	-20.71	-37.94	± 13.82
06/04/2012	AE	14.41 ± 0.68	12.61	12.86 ± 1.96	-7.74	-13.90	22.86 ± 2.77	13.16	19.84 ± 2.22	-27.65	-11.85	± 4.90
21/04/2012	BE	17.06 ± 0.82	15.62	14.43 ± 2.75	-1.97	-5.67	22.41 ± 1.71	12.87	22.98 ± 1.95	-15.53	-24.97	± 5.64
23/04/2012	DE	0	0	0	0	0	21.88 ± 3.33	11.24	21.55 ± 1.14	-25.67	-33.43	± 32.23
24/04/2012	AE	0	14.82	13.84 ± 2.02	0	-7.60	20.32 ± 4.92	13.02	21.09 ± 1.41	-30.28	-30.19	± 21.65
10/06/2012	BE	28.17 ± 0.10	23.66	26.64 ± 2.21	0.61	4.32	21.36 ± 1.72	11.39	22.73 ± 1.84	-16.28	-11.03	± 3.88
11/06/2012	DE	26.05 ± 1.25	23.37	24.22 ± 3.25	-5.44	7.08	25.09 ± 1.61	13.96	24.19 ± 1.40	-4.02	-10.72	± 14.58
12/06/2012	AE	25.95 ± 1.00	23.50	24.01 ± 2.30	-0.22	10.05	23.27 ± 1.60	13.52	23.47 ± 1.65	-9.63	-13.39	± 12.47
15/06/2012	BE	26.42 ± 1.33	23.60	23.72 ± 2.51	0.67	9.05	24.69 ± 1.23	11.68	23.71 ± 1.44	-5.97	-9.08	± 4.80
16/06/2012	DE	26.00 ± 1.97	24.76	25.99 ± 3.05	8.47	3.93	22.90 ± 1.87	14.25	20.34 ± 1.33	-18.78	-15.57	± 20.24
17/06/2012	AE	27.66 ± 0.69	25.36	26.64 ± 2.06	7.54	15.18	17.48 ± 2.11	12.73	22.36 ± 0.97	-18.99	-12.74	± 46.75

Appendix B

See Table B1.

Table B1

2-day mean variations of MDP, MBSR, MASS, SRT and SST signals before, during and after each event for (a) GQD-A118 and (b) DHO-A118 propagation path.

Date/Day	SIG	GQD-A118					DHO-A118				
		MBSR	MDP	MASS	SRT	SST	MBSR	MDP	MASS	SRT	SST
02-03/02/2011	BE	9.87	5.79	8.15	-3.21	-4.09	19.72	4.61	20.04	-31.6	-12.85
05-06/02/2011	DE	12.10	3.45	11.31	-5.28	-2.82	22.81	3.12	22.07	-36.22	-28.13
08-09/02/2011	AE	10.87	5.17	8.74	-3.94	-8.50	21.90	7.30	21.35	-21.46	-37.49
27-28/02/2011	BE	14.44	7.9	14.11	-3.18	-2.26	23.35	4.16	22.29	-25.85	-10.94
01-02/03/2011	DE	13.55	6.73	11.84	-4.34	-1.73	22.99	3.07	19.47	-20.35	-20.68
04-05/03/2011	AE	12.37	8.8	12.20	-3.55	-2.20	23.10	4.49	19.91	-33.52	-25.43
01-02/04/2011	BE	15.73	15.44	14.78	-4.86	2.66	21.59	11.66	20.78	-33.89	-30.81
06-07/04/2011	DE	15.60	13.70	16.01	-6.84	-15.76	21.06	9.93	20.71	-31.67	-12.01
08-09/04/2011	AE	16.61	14.05	15.11	-1.75	-12.13	22.24	9.17	20.00	-36.54	-31.99
10-11/04/2011	BE	17.88	15.37	17.78	-4.05	-13.14	18.63	8.17	20.63	-35.27	-36.30
12-13/04/2011	DE	19.84	14.28	21.38	-4.79	-12.86	22.69	7.81	21.38	-33.26	-32.36
16-17/04/2011	AE	18.10	13.87	15.29	-10.18	-13.57	21.32	7.78	21.88	-30.58	-36.38
24-25/09/2011	BE	25.68	23.20	25.18	0.36	-0.84	23.30	14.56	23.96	-19.91	-30.38
25-27/09/2011	DE	24.22	22.38	25.25	-2.01	-4.68	17.60	7.23	16.79	-28.63	-30.81
28-29/09/2011	AE	26.94	22.10	25.62	-0.29	-5.09	24.20	14.05	23.43	-15.82	-32.44
23-24/10/2011	BE	22.99	15.94	22.25	-4.83	-4.58	25.86	10.34	25.16	-29.73	-33.97
25-26/10/2011	DE	18.42	0	0	0	0	24.13	1.56	23.17	-26.75	-18.29
27-28/10/2011	AE	22.08	18.40	20.61	-4.9	-10.84	20.23	9.59	21.48	-27.44	-30.17
20-21/01/2012	BE	14.15	3.25	13.96	-9.68	-15.72	23.45	2.96	23.17	0	-38.08
22-23/01/2012	DE	14.99	5.64	15.21	-13.59	-15.54	25.29	4.08	23.12	-26.08	-24.05
30-31/01/2012	AE	9.02	6.97	8.27	-16.95	-19.87	20.76	2.42	23.56	-16.19	-13.58
10-11/02/2012	BE	8.29	5.44	8.46	-13.18	-13.85	24.65	8.72	25.95	-12.98	-28.28
15-16/02/2012	DE	8.65	8.05	8.52	-11.23	-13.33	23.91	10.43	24.54	-16.02	-27.51
17-18/02/2012	AE	10.13	7.98	7.96	-12.71	-12.56	25.13	12.59	20.67	-24.17	-34.82
17-18/02/2012	BE	10.13	7.98	7.96	-12.71	-12.56	25.13	12.59	20.67	-24.17	-34.82
19-20/02/2012	DE	11.39	7.18	10.03	-9.58	-10.18	22.20	9.27	22.07	-14.75	-22.37
21-22/02/2012	AE	11.88	5.75	11.12	-11.11	-9.78	25.58	11.06	23.06	-15.2	-37.88
05-06/03/2012	BE	14.37	12.85	12.28	-9.92	-12.34	24.93	13.13	24.31	-33.13	-32.36
07-08/03/2012	DE	13.31	11.19	9.58	-16.38	-11.18	26.18	12.12	24.42	-32.22	-7.16
13-14/03/2012	AE	11.16	12.83	9.44	-4.92	-12.75	22.21	13.29	20.76	-25.26	-26.34
13-14/03/2012	BE	11.16	12.83	9.44	-4.92	-12.75	22.21	13.29	20.76	-25.26	-26.34
15-16/03/2012	DE	12.04	15.93	15.93	-15.25	-13.32	21.92	12.46	20.33	-17.17	-19.95
21-22/03/2012	AE	10.30	10.29	9.18	-11.21	-13.78	21.58	9.92	23.61	0	-31.63
25-26/03/2012	BE	13.17	11.78	11.11	-11.14	-13.35	22.50	10.46	22.83	-34.53	-19.16
28-29/03/2012	DE	10.20	10.59	10.95	-4.87	-10.35	21.53	10.62	18.24	-35.09	-20.66
30-31/03/2012	AE	13.39	11.67	12.25	-6.29	-15.75	21.67	11.69	19.19	-38.21	-12.74
01-02/04/2012	BE	13.37	13.09	12.50	-3.00	-13.27	24.50	14.13	23.51	-26.78	-21.33
05-06/04/2012	DE	13.00	12.16	12.05	-5.64	-12.03	22.53	12.69	21.88	-24.18	-24.90
07-08/04/2012	AE	15.08	12.47	11.33	-6.00	-9.08	24.42	13.52	22.00	-30.33	-25.14
19-20/04/2012	BE	16.35	15.67	14.12	-2.16	-5.79	21.82	13.24	21.94	-17.44	-26.39
23-24/04/2012	DE	0	0	0	0	0	21.10	12.13	21.32	-27.98	-31.81
27-28/04/2012	AE	17.32	15.70	16.01	2.46	3.44	20.59	12.67	21.72	-19.30	-32.01
06-07/06/2012	BE	27.82	24.42	26.12	5.8	10.28	21.47	11.56	22.69	-12.35	-12.03
11-12/06/2012	DE	26.21	23.44	24.12	-2.83	8.57	24.18	13.74	23.83	-6.83	-12.06
13-14/06/2012	AE	25.98	25.06	25.85	-0.76	5.45	24.98	15.95	24.21	-3.30	-10.84
14-15/06/2012	BE	26.02	23.60	25.06	0.10	8.71	24.89	11.83	25.29	-3.88	-10.02
16-17/06/2012	DE	26.83	25.06	26.32	8.01	8.56	20.19	13.49	21.54	-18.89	-14.16
21-22/06/2012	AE	23.87	26.00	21.10	2.52	10.28	16.83	12.53	23.06	-21.94	-27.82

References

- Alfonsi, L., Kavanagh, A.J., Amata, E., Cilliers, P., Correia, E., Freeman, M., Kauristie, K., Liu, R.Y., Luntama, J.P., Mitchell, C.N., Zherebtsov, G.A., 2008. Probing the high latitude ionosphere from ground-based observations: the state of current knowledge and capabilities during IPY (2007–2009). *J. Atmos. Sol.-Terr. Phys.* 70 (18), 2293–2308.
- Araki, T., 1974. Anomalous phase changes of trans equatorial VLF radio waves during geomagnetic storms. *J. Geophys. Res.* 79, 4811–4813.
- Baker, D.N., 1996. Solar wind-magnetosphere drivers of space weather. *J. Atmos. Sol.-Terres. Phys.* 58, 150W526.
- Baker, D.N., 2000. Effects of the sun on the earth's environment. *J. Atmos. Sol.-Terres. Phys.* 62, 1669–1681.
- Basak, T., Pal, S., Chakrabarti, S.K., 2011. VLF study of ionospheric properties during solar flares of varied intensity for a fixed propagation path. In: 2011 XXXth URSI General Assembly and Scientific Symposium, 13–20 August 2011. <http://dx.doi.org/10.1109/URSIGASS.2011.6051004>.
- Borovsky, J.E., Denton, M.H., 2006. Differences between CME-driven storms and CIR-driven storms'. *J. Geophys. Res.*, 111.
- Burke, W.J., 2000. Magnetosphere-ionosphere coupling: selected topics. *J. Atmos. Sol.-Terr. Phys.* 62, 817–824.
- Bucha, V., Bucha Jr., V., 1998. Geomagnetic forcing of changes in climate and in the atmospheric circulation. *J. Atmos. Sol.-Terr. Phys.* 60 (2), 145–169.
- Buonsanto, M.J., 1999. Ionospheric storms – a review. *Space Sci. Rev.* 88, 563–601.
- Chakrabarti, S.K., Saha, M., Khan, R., Mandal, S., Acharyya, K., Saha, R., 2005. Possible detection of ionospheric disturbances during Sumatra-Andaman islands. *IJRS Phys.* 34, 314–317.
- Chakrabarti, S.K., Sasmal, S., Chakrabarti, S., 2010. Ionospheric anomaly due to seismic activities – part 2: evidence from D-layer preparation and disappearance times. *Nat. Hazards Earth Syst. Sci.* 10, 1751–1757.
- Chen, C.H., Lin, C.H., Chang, L.C., Huba, J.D., Lin, J.T., Saito, A., Liu, J.Y., 2013. Thermospheric tidal effects on the ionospheric midlatitude summer nighttime anomaly using SAMI3 and TIEGCM. *J. Geophys. Res. Space Phys.* 118, 3836–3845. <http://dx.doi.org/10.1002/jgra.50340>.
- Chenette, D.L., Datlowe, D.W., Robinson, R.M., Schumaker, T.L., Vondrak, R.R., Winningham, J.D., 1993. Atmospheric energy input and ionization by energetic electrons during the geomagnetic storm of 8–9 November 1991. *Geophys. Res. Lett.* 20, 1323.
- Cliilverd, M.A., Rodger, C.J., Gamble, R.J., Ulich, T., Raita, T., Seppala, A., Green, J.C., Thomson, N.R., Sauvaud, J.A., Parrot, M., 2010. Ground-based estimates of outer radiation belt energetic electron precipitation fluxes into the atmosphere. *J. Geophys. Res.* 115, A12304.
- Danilov, A.D., Lastovicka, J., 2001. Effects of geomagnetic storms on the ionosphere and atmosphere. *Int. J. Geomagn. Aeron.* 2, 209–224.
- Goldstein, J., Burch, J.L., Sandel, B.L., Mende, S.B.P., Brandt, C., son, Hairston, M.R., 2005. Coupled response of the inner magnetosphere and ionosphere on 17 April 2002. *J. Geophys. Res.* 110, A03205. <http://dx.doi.org/10.1029/2004JA010712>.
- Goncharenko, L.P., Coster, A.J., Plumb, R.A., Domeisen, D.I.V., 2012. The potential role of stratospheric ozone in the stratosphere-ionosphere coupling during stratospheric warmings. *Geophys. Res. Lett.* 39, L08101. <http://dx.doi.org/10.1029/2012GL051261>.
- Greenwald, R.A., Baker, K.B., Dudeney, J.R., Pinnock, M., Jones, T.B., Thomas, E.C., Villain, J.-P., Cerisier, J.-C., Senior, C., Hanuise, C., Hunsucker, R.D., Sofko, G., Koehler, J., Nielsen, E., Pellinen, R., Walker, A.D.M., Sato, N., Yamagishi, H., 1995. Darn/superdarn: a global view of the dynamics of high-latitude convection. *Space Sci. Rev.* 71, 761–796. <http://dx.doi.org/10.1007/BF00751350>.
- Greenwald, R.A., Ruohoniemi, J.M., Bristow, W.A., Sofko, G.J., Villain, J.-P., Huuskonen, A., Kokubun, S., Frank, L.A., 1996. Mesoscale dayside convection vortices and their relation to substorm phase. *J. Geophys. Res.* 101, 21697–21713.
- Grubor, D., Sulic, D., Zizman, V., 2005. Influence of solar X-ray flares on the earth-ionosphere waveguide. *Serbian Astron. J.* 171, 29–35.
- Hamilton, D.C., Gloeckler, G., Ipavich, F.M., Stüdemann, W., Wilken, B., Kremser, G., 1988. Ring current development during the great geomagnetic storm of February 1986'. *J. Geophys. Res.: Space Phys.* 93, 14343–14355.
- Han, F., Cummer, S.A., 2010. Midlatitude nighttime D region ionosphere variability on hourly to monthly time scales. *J. Geophys. Res.* 115, A09323. <http://dx.doi.org/10.1029/2010JA015437>.
- Hayakawa, M., Molchanov, O.A., Ondoh, T., Kawai, E., 1998. The precursory signature effect of Kobe earthquake on VLF subionospheric signals. *Phys. Earth Planet. Inter.* 105, 239–248.
- Heikkila, W., 2011. Earth's Magnetosphere. Elsevier, Kidlington, Oxford, UK.
- Honary, F., Stocker, A.J., Robinson, T.R., Jones, T.B., 1995. Ionospheric plasma response to HF radio waves operating at frequencies close to the third harmonic of electron gyrofrequency. *J. Phys. Res.* 100, 21489–21501.
- Kelley, M.C., 1989. The Earth's Ionosphere. Academic Press Inc., San Diego, California.
- Kikuchi, T., Evans, D.S., 1983. Quantitative study of substorm-associated VLF phase anomalies and precipitating energetic electrons on November 13, 1979. *J. Geophys. Res. Space Phys.* 88, 871–880.
- Kleimenova, N.G., Kozyreva, O.V., Rozhnoy, A.A., Soloveva, M.S., 2004. Variations in the VLF signal parameters on the Australia-Kamchatka radio path during magnetic storms. *Geomagn. Aeron.* 44, 385–393.
- Kozyra J.U., Crowley, G., Emery, B.A., Fang, X., Maris, G., Mlynczak, M.G., Niciejewski, R.J., Palo, S.E., Paxton, L.J., Randall, C.E., Rong, P.-P., Russell III, J.M., Skinner, W., Solomon, S.C., Talaat, E.R., Wu, Q., Yee, J.-H., 2006. Response of the upper/middle atmosphere to coronal holes and powerful high-speed solar wind streams in 2003. In: Tsurutani, Bruce, McPherron, Robert, Gonzalez, Walter, Lu, Gang, Sobral, Jos H.A., Gopalswamy, Natchimuthukonar (Eds.), Recurrent Magnetic Storms: Corotating Solar Wind Streams. Geophysical Monograph, vol. 167. AGU Books Board, AGU, Washington, DC USA, p. 319 (ISBN-13: 978-0-87590-432-0).
- Kumar, A., Kumar, S., 2014. Space weather effects on the low latitude D-region ionosphere during solar minimum. *Earth Planet. Space*, 66.
- Kutiev, I., Tsagouri, Ioanna, Perrone, Loredana, Pancheva, Dora, Mukhtarov, Plamen, Mikhailov, Andrei, Lastovicka, Jan, Jakowski, Norbert, Buresova, Dalia, Blanch, Estefania, Andonov, Borislav, Altadill, David, Magdaleno, Sergio, Parisi, Mario, Torta, Joan Miquel, 2013. Solar activity impact on the Earth's upper atmosphere. *J. Space Weather Space Clim.*, 3.
- Lastovicka, J., 1989. Solar wind and high energy particle effects in the middle atmosphere. In: Handbook for MAP, vol. 29, p. 119.
- Lastovicka, J., 1996. Effects of geomagnetic storms in the lower ionosphere, middle atmosphere and troposphere. *J. Atmos. Terr. Phys.* 58, 831–843.
- Leonard, J.M., Forbes, J., Born, G.H., 2012. Impact of tidal density variability on orbital and reentry predictions. *J. Geophys. Res. Space Weather* 10, S12003. <http://dx.doi.org/10.1029/2012SW000842>.
- McRae, W.M., Thomson, N.R., 2004. Solar flare induced ionospheric D-region enhancements from VLF phase and amplitude observations. *J. Atmos. Sol.-Terr. Phys.* 66, 77–87. <http://dx.doi.org/10.1016/j.jastp.2003.09.009>.
- Melia, A., 2010. Flare Detection Using VLF Radio Signal. G3NYK.
- Miller, N.J., Brace, L.H., 1969. Some winter characteristics of the northern high-latitude ionosphere. *J. Geophys. Res.* 74, 5752–5762.
- Mimmo, H.R., 1937. The physics of the ionosphere. *Rev. Mod. Phys.* 9, 1–45.
- Mitra, W.B., 1974. Ionospheric Effects of Solar Flares. D. Reidel Publishing Company, Dordrecht, Holland.
- Molchanov, O.A., Hayakawa, M., 1998. On the generation mechanism of ULF seismogenic electromagnetic emissions. *Phys. Earth Planet. Inter.* 105, 201–220.
- Nwankwo, V.U.J., Chakrabarti, S.K., 2014. A probe of magnetosphere-ionosphere coupling using very low frequency (VLF) radio signal from North-West Cape (Australia) to Kolkata (India). In: 40th COSPAR Scientific Assembly. Held 2–10 August 2014, Moscow, Russia, CO.4-21-14.
- Nwankwo, V.U.J., Chakrabarti, Sandip K., Weigel, R.S., 2015. Effects of plasma drag on low earth orbiting satellites due to solar forcing induced perturbations and heating. *Adv. Space Res.* 56, 47–56.
- Pal, S., Maji, Surya K., Chakrabarti, Sandip K., 2012. First ever VLF monitoring of the lunar occultation of a solar flare during the 2010 annular solar eclipse and its effects on the D-region electron density profile. *Planet Space Sci.* 73, 310–317.
- Palit, S., Basak, T., Mondal, S.K., Pal, S., Chakrabarti, S.K., 2013. Modeling of very low frequency (VLF) radio wave signal profile due to solar flares using the GEANT4 Monte Carlo simulation coupled with ionospheric chemistry. *Atmos. Chem. Phys.* 13, 9159–9168.
- Pancheva, D.V., Mukhtarov, P.J., Mitchell, N.J., Fritts, D.C., Riggan, D.M., Takahashi, H., Batista, P.P., Clemesha, B.R., Gurubaran, S., Ramkumar, G., 2008. Planetary wave coupling (5–6-day waves) in the low-latitude atmosphere-ionosphere system. *J. Atmos. Sol.-Terr. Phys.* 70, 101–122.
- Peter, W.B., Chevalier, M.W., Inan, U.S., 2006. Perturbations of mid-latitude sub-ionospheric VLF signals associated with lower ionospheric disturbances during major geomagnetic storms. *J. Geophys. Res.* 111, A03301.
- Polyakov, A.S., Chernigovskay, M.A., Perevalov, N.P., 2014. Ionospheric effects of sudden stratosphere warmings in Eastern Siberian region. *J. Atmos. Sol.-Terr. Phys.* 120, 15–23.
- Poole, I., 1999. Radio Waves and the Ionosphere. American Radio Relay League, G3YWX.
- Pross, G.W., 2004. Physics of the Earth's Space Environment. Springer, Berlin, Heidelberg, Germany.
- Raulin, J.-P., Pacini, A.A., Kaufmann, P., Correia, E., Martinez, M.A.G., 2006. On the detectability of solar X-ray flares using very low frequency sudden phase anomalies. *J. Atmos. Sol.-Terr. Phys.* 68, 1029–1035.
- Raulin, J.-P., Bertoni, Fernando C.P., Gaviln, Herman R., Guevara-Day, Walter, Rodriguez, Rodolfo, Fernandez, Germn, Correia, Emilia, Kaufmann, Pierre, Pacini, Alessandra, Stekel, Tardelli R.C., Lima, Washington L.C., Schuch, Nelson J., Fagundes, Paulo R., Hadano, Rubens, 2010. Solar flare detection sensitivity using the South America VLF Network (SAVNET). *J. Geophys. Res.* 115, A07301. <http://dx.doi.org/10.1029/2009JA015154>.
- Raulin, J.-P., Trotter, Gard, Kretzschmar, Matthieu, Macotela, Edith L., Pacini, Alessandra, Bertoni, Fernando C.P., Dammasch, Ingolf E., 2013. Response of the low ionosphere to X-ray and Lyman- α solar flare emissions. *J. Geophys. Res.* 118, 570–575. <http://dx.doi.org/10.1029/2012JA017916>.
- Ray, S., Chakrabarti, S.K., 2012. A study of the behavior of the terminator time shifts using multiple VLF propagation paths during the Pakistan earthquake ($M=7.2$) of 18 January 2011. *Nat. Hazards Earth Syst. Sci.* 13, 1501–1506.
- Ruohoniemi, J.M., Greenwald, R.A., 2005. Dependencies of high-latitude plasma convection: consideration of interplanetary magnetic field, seasonal, and universal time factors in statistical patterns. *J. Geophys. Res.* 110, A09204. <http://dx.doi.org/10.1029/2004JA010815>.
- Russell, A.J.B., Wright, A.N., Hood, A.W., 2010. Self-consistent ionospheric plasma density modifications by field-aligned currents: steady state solutions. *J. Geophys. Res.* 115, A04216. <http://dx.doi.org/10.1029/2009JA014836>.
- Russell, A.J.B., Wright, A.N., 2012. Magnetosphere-ionosphere waves. *J. Geophys. Res.* 117 (A01202), 2012. <http://dx.doi.org/10.1029/2011JA016950>.
- Sasmal, S., Chakrabarti, S.K., 2009. Ionospheric anomaly due to seismic activities –

- Part 1: calibration of the VLF signal of VTX 18.2 KHz station from Kolkata and deviation during seismic events. *Nat. Hazards Earth Syst. Sci.* 9, 1403–1408.
- Simoës, F., Pfaff, R., Berthelier, J., Klenzing, 2012. A review of low frequency electromagnetic wave phenomena related to tropospheric–ionospheric coupling mechanisms. *Space Sci. Rev.* 168, 551–593.
- Singer, H.J., Matheson, L., Grubb R., Newman, A., Bouwer, S.D., Monitoring space weather with the GOES magnetometers, In: Proceedings of the SPIE, GOES-8 and Beyond, 299, vol. 2812, 1996. <http://dx.doi.org/10.1117/12.254077>.
- Stoker, P.H., 1993. Energetic electron power flux deposition at $L=4.0$ from riometer recording. *J. Geophys. Res.* 98, 19111–19116.
- Streltsov, A.V., Lotko, W., 2004. Multiscale electrodynamics of the ionosphere–magnetosphere system. *J. Geophys. Res.* 109, A09214. <http://dx.doi.org/10.1029/2004JA010457>.
- Tatsuta, K., Hobará, Y., Pal, S., Balikhin, M., 2015. Sub-ionospheric VLF signal anomaly due to geomagnetic storms: a statistical study. *Ann. Geophys.* 33, 1457–1467.
- Thomson, N.R., Rodger, C.J., Dowden, R.L., 2004. Ionosphere gives size of greatest solar flares. *Geophys. Res. Lett.* 31, L06803.
- Tsurutani, B.T., Meng, C.I., 1972. Interplanetary magnetic field variations and substorms. *J. Geophys. Res.* 77, 2964–2970.
- Tsurutani, B.T., Gonzalez, W.D., Tang, F., Akasofu, S.I., Smith, E.J., 1988. Origin of interplanetary southward magnetic fields responsible for major magnetic storms near solar maximum (1978–1979). *J. Geophys. Res.* 93, 8519–8531.
- Tsurutani, B.T., Gonzalez, W.D., Gonzalez, A.L.C., Tang, F., Arballo, J.K., Okada, M., 1995. Interplanetary origin of geomagnetic activity in the declining phase of the solar cycle. *J. Geophys. Res.* 100, 21717–21733.
- Tsurutani, B.T., Gonzalez, W.D., 1997. The interplanetary causes of magnetic storms: a review. In: Tsurutani, B.T., Gonzalez, W.D., Kamide, Y., Arballo, J.K. (Eds.), *Magnetic Storms*, vol. 98. American Geophysical Union Press, Washington, DC, pp. 77–89.
- Tsurutani, B.T., Gonzalez, W.D., Gonzalez, A.L.C., Guarnieri, F.L., Gopalswamy, N., Grande, M., Kamide, Y., Kasahara, Y., Lu, G., Mann, I., McPherron, R.L., Soraas, F., Vasyliunas, V.M., 2006. Corotating solar wind streams and recurrent geomagnetic activity: a review. *J. Geophys. Res.* 111, A07S01. <http://dx.doi.org/10.1029/2005JA011273>.
- Tsurutani, B.T., Echer, E., Guarnieri, F.L., Gonzalez, W.D., 2011a. The properties of two solar wind high speed streams and related geomagnetic activity during the declining phase of solar cycle 23. *J. Atmos. Sol.-Terr. Phys.* 73, 164. <http://dx.doi.org/10.1016/j.jastp.2010.04.003Z>.
- Tsurutani, B.T., Echer, E., Gonzalez, W.D., 2011b. The solar and interplanetary causes of the recent minimum in geomagnetic activity (MGA23): a combination of midlatitude small coronal holes, low IMF BZ variances, low solar wind speeds and low solar magnetic fields. *Ann. Geophys.* 29, 839–849.
- Wait, J.R., 1959. Diurnal change of ionospheric heights deduced from phase velocity measurements at VLF. *Proc. IRE* 47, 998.
- Wait J.R., Spies K.P., 1964. Characteristics of the Earth–Ionosphere Wave-Guide for VLF Radio Waves. NBS Technical Note 300.
- Weigel, R.S., 2010. Solar wind density influence on geomagnetic storm intensity. *J. Geophys. Res.* 115, A09201. <http://dx.doi.org/10.1029/2009JA015062>.
- Wild, J.A., Milan, S.E., Cowley, S.W.H., Dunlop, M.W., Owen, C.J., Bosqued, J.M., Taylor, M.G.G.T., Davies, J.A., Lester, M., Sato, N., Yukimatu, A.S., Fazakerley, A.N., Balogh, A., Re'eme, H., 2003. Coordinated interhemispheric SuperDARN radar observations of the ionospheric response to flux transfer events observed by the cluster spacecraft at the high-latitude magnetopause. *Ann. Geophys.* 21, 1807–1826.
- Zhang, S., Fukao, S., Oliver, W.L., Otsuka, Y., 1999. The height of the maximum ionospheric electron density over the MU radar. *J. Atmos. Sol.-Terr. Phys.* 61, 1367–1383. [http://dx.doi.org/10.1016/S1364-6826\(99\)00088-7](http://dx.doi.org/10.1016/S1364-6826(99)00088-7).

Diagnostic study of geomagnetic storm-induced ionospheric changes in mid-latitude D-region using VLF signal propagation characteristics

Victor U. J. Nwankwo¹ and Sandip K. Chakrabarti^{1,2}

¹S N Bose National Centre for Basic Sciences, JD Block, Salt lake, Kolkata-700098, India

²Indian Centre for Space Physics, 43-Chalantika, Garia Station Road, Kolkata-700084, India

Correspondence to: Victor U. J. Nwankwo (victorujn@bose.res.in)

Abstract. We perform a diagnostic study of geomagnetic disturbances or storm induced ionospheric changes in mid-latitude D region using propagation characteristics of VLF radio signal (3-30 kHz). We analysed the trend in variations of condensed amplitude metrics of VLF diurnal signal during 20 storm conditions (including pre-storm and post-storm day conditions) to understand signal propagation characteristics that are attributable to geomagnetic storms induced variations in the D-region.

5 We found that the midday signal amplitude peak (MDP) exhibited characteristic dipping in about 68% of the combined cases in response to the storms. We also observed few cases of propagation path-mismatched increase of MDP, as well as propagation path-matched increase of the signal during some events. Whereas the mismatched increase of the signal could be related to the characteristics of each propagation path and X-ray flux induced spikes in signal amplitude, the matched increase appears to be influenced by M-class flares concurrent with the storm events, and delayed response of the local ionosphere. The mean
10 signal amplitude before sunrise (MBSR) and mean signal amplitude after sunset (MASS) also showed significant dipping due to geomagnetic storms (66% and 64%, respectively), but appear to be influenced by the event occurrence time and intensity, and the highly variable conditions of dusk-to-dawn D-region ionosphere. Conversely, the sunrise terminator (SRT) and sunset terminator (SST) amplitude showed respective dipping of 46.5% and 32.5% of the combined cases, favouring storm-induced rise of the signals instead (from statistical view point).

15 1 Introduction

Geomagnetic storms are the leading driver of large-scale coupled magnetosphere-ionosphere dynamics in the geospace environment. The magnetosphere is formed by the interaction of solar wind streams with the Earth's magnetic field. The size, shape and behaviour of the magnetosphere are controlled by the varying properties of the solar wind plasma and the attached magnetic fields (McPherron et al., 2008). The ionosphere is the ionised component of the Earth's atmosphere, consisting of
20 distinct regions - D (50 km to 90 km), E (90 km to 120 km), and the F (from 120 km up to 500 km), which often split into F1 and F2 layers. It is principally created via ionisation by solar ultraviolet (UV) radiation and X-ray wavelength (Mitra, 1974) and isotropic cosmic rays. Although separated by thousands of kilometers, solar and geomagnetic footprints in the magnetosphere are conveyed to the ionosphere via the linkage of the Earth's magnetic field, thereby making the regions physically

connected into a single global system (Nwankwo et al., 2016). Geomagnetic storms are mainly products of strong variations in solar wind conditions via energy transfer, especially during coronal mass ejections (CMEs) and intervals of sustained high speed solar wind streams. Conditions of sustained periods of high speed solar wind, and a southward directed solar wind magnetic field at the dayside of the magnetosphere largely favours the initiation of geomagnetic storms (Lastovicka, 1989; Baker, 2000; Borovsky and Denton, 2006; Kozyra et al., 2006; McPherron et al., 2008; Tsurutani et al., 1995, 2006, 2011). The impact of Earth-directed CME with its embedded magnetic field (reaching Earth within several hours to 1-3 days) on the magnetosphere has direct consequence of producing geomagnetic storms and associated phenomena. Similarly, the emergence of high-speed solar wind streams (HSS) from the sun's corona, interacts with preceding low-speed solar winds, creating a corotating interactive region (CIR); an interface that can interact with the Earth's magnetosphere, potentially initiating geomagnetic disturbances and/or storm condition (Gosling and Pizzo, 1999; Borovsky and Denton, 2006; Tsurutani et al., 2006, 2011; Burns et al., 2012; Kutiev et al., 2013; Verkhoglyadova et al., 2013; Nwankwo et al., 2015). CME-induced geomagnetic storms are often large, more geo-effective and frequent during solar maxima, while HSS/CIR-induced storms are usually less intense and dominates the solar minima. However, more energy is transferred (or, deposited) into the magnetosphere during HSS/CIR induced storms over a characteristic longer duration (a week or more) in comparison to CME-induced storm scenario (lasting about 1 day) (Tsurutani et al., 2011; Verkhoglyadova et al., 2013).

In the ionosphere, effects of geomagnetic storms manifest mainly through joule heating, and precipitation of energetic particles (especially below the dynamo region, 95-100 km), which lose their energy by impact and X-ray production by bremsstrahlung (Lastovika, 1996) causing significant enhancement of electron density (Chenette et al., 1993; Stoker 1993; Lastovika, 1996). It can also be through modulation of galactic cosmic ray flux, global electric circuit, atmospheric electricity (Danilov and Lastovika, 2001), whose coupling effects modify atmospheric density distribution, ionisation rates, and conductivity gradient and reference height of the D-region (Wait, 1959; Wait and Spies, 1964; Mitra, 1974; Buonsanto, 1999; Burke, 2000; Simoes et al., 2012; Nwankwo et al., 2016). The ionosphere also responds to prompt changes from other solar energetic events such as solar flares associated bursts in EUV, X-ray and relativistic particles (Mitra, 1974; Bounsanto, 1999; Alfonsi et al., 2008). Solar flare/X-ray flux-induced ionospheric disturbances in the D-region are normally detected as a sudden change (usually an increase) in the amplitude and enhancement in phase of very low frequency (VLF) radio signal. We presented a description of VLF signal detection mechanism of sudden ionospheric disturbances in D region in Nwankwo et al. (2016), which also serve as a background to this work.

VLF signals can be significantly affected by geomagnetic disturbances and/or storms induced ionosphere perturbations (Kikuchi and Evans, 1983). While the daytime VLF signal amplitude and phase are well correlated with X-ray flux induced sudden ionospheric disturbances (e.g., during solar flares and gamma ray bursts, see, Figs. 2c-d) and well studied, geomagnetic storm-induced disturbances are usually not immediately detectable on the signal's signature. The response of VLF signal to geomagnetically induced ionospheric disturbances, however, depends on the propagation characteristics of signal propagation path, and the signal mode interference significantly depends on ionospheric conditions at the time, propagation paths and ener-

getic electron precipitation level on the ionosphere due to the magnetic storm, which also depends on geomagnetic latitude (e.g. Tatsuta et al., 2015). Kikuchi and Evans (1983) reported the occurrence of VLF phase anomaly associated with sub-storm of 13 November 1979 in trans-auroral propagation path. Peter et al. (2006) reported the depression of VLF signal amplitude of up to 5 dB in magnitude in mid-latitude during storms of 7 April 2000 and 31 October 2003, and later observed in lower latitudes.

5 Kumar and Kumar (2014) later reported a depression in VLF signal strength in low latitude during severe storm condition of 15 December 2006. Nwankwo et al. (2016) also reported dipping of VLF mid-day signal amplitude (MDP), mean signal amplitude before sunrise (MBSR) and mean signal amplitude before sunset (MASS) in majority of 16 storm cases studied in mid-latitude during February 2011 to June 2012.

10 Whereas there are similarities in the work of the above mentioned authors, Nwankwo et al. (2016) have, in addition, included several cases of storms with the goal of bringing in and investigating the statistical significance of the observations, especially in mid-latitude ionosphere. This goal-oriented analysis led to an insightful finding that opened a new front for further investigation. While majority of the MDP signal (in all the propagation paths (PP) used) showed a noteworthy evidence of dipping following a storm condition, a few PP-mismatched incidences of MDP signal rise (or, increase) on some events day were also

15 observed. A notable PP-matched increase of the diurnal signal level (instead of a dip) in the propagation paths was observed as well. In principle, the signal level or strength of VLF radio wave can also increase following a geomagnetic storm, depending on a storm's characteristics, associated phenomena or signal's propagation path. We made an attempt to further investigate such scenario in the present work. Building on the analysis in Nwankwo et al. (2016), we perform a more detailed analysis to substantiate the findings of the previous work (e.g., duration of mean signal amplitude calculation for intervals of 2 to 4

20 hours before sunrise and after sunset (MBSR and MASS) was increased by 30 minutes, and the mid-day signal amplitude peak values (MDP) were restricted to period around 12.00 noon to 12.30 pm). We also investigate observed cases of increase of VLF amplitude (against dipping scenario) following geomagnetic storm conditions. The study of trends in variation of VLF diurnal signal is proving to be useful to understand space weather effects in the lower ionosphere (e.g. Araki, 1974; Kikuchi and Evans, 1983; Kleimenov et al., 2004; Peter et al., 2006; Clilverd et al., 2010; Kumar and Kumar, 2014; Tatsuta et al., 2015,

25 Nwankwo et al., 2016), as well as ionospheric changes from other atmospheric and lithospheric sources.

2 Data and Method

Diurnal VLF amplitude data for two propagation paths (DHO-A118 and GQD-A118) received at A118 SID monitoring station in Southern France, were analysed. The transmitters (GQD (22.1 kHz GQD, lat N54.73° long W002.88°) and DHO (23.4 kHz, lat N53.08° long W007.61°)) and the receiver (A118) are shown in Figure 1. Other data include GOES solar X-ray flux, solar

30 wind speed (V_{sw}) and particle density (PD) (<ftp://sohoftp.nascom.nasa.gov/sdb/goes/ace/>), global geomagnetic A_p (NOAA) and disturbance storm time (Dst) index (from World Data Centre for Geomagnetism (WDCG)). These data have been described in detail in Nwankwo et al. (2016) and references therein.



Figure 1. VLF signal propagation paths (DHO-A118 and GQD-A118) used in the study

Analysis was first conducted over two 15-day periods that include geomagnetic storms of varying disturbance index viz 16th-31st September and 22 October-5 November 2011. We analysed 2- to 4-hour mean VLF signal amplitude before ‘local’ sunrise and after sunset (hereafter respectively denoted as MBSR and MASS), and mid-day signal amplitude peak (MDP). We also identified typical values of the signal at sunrise and sunset, also recognised as sunrise and sunset terminators (hereafter, 5 denoted as SRT and SST). The diurnal VLF radio signal for different propagation paths (indicating portion of the condensed metrics - MBSR, MDP, MASS, SRT and SST) are shown in Fig. 2 (a-f) - fig 2(a and c) for DHO-A118 propagation path, fig 2(b and d) for GQD-A118 propagation path and fig 2(e and f) are shown for purpose of illustration and/or description that is to follow hereafter. The signals were analysed in conjunction with geomagnetic indices, to describe storm-induced magnetosphere-ionosphere coupling dynamics in mid-latitude D region ionosphere. We thus study the trend in variations of 10 these key metrics under varying geomagnetic storm conditions via the the signals’ (VLF) propagation characteristics to understand behaviour or propagation characteristic attributable to geomagnetic storms induced variations in the D-region ionosphere (besides detectable response of the signal’s amplitude and phase to solar flare/X-ray flux).

2.1 Results and Discussion

15 Figure 3 shows diurnal VLF amplitude for (a) DHO-A118 and (b) GQD-A118 propagation paths, daily variation in (c) X-ray flux output (d) solar wind speed (V_{sw}) (e) solar particle density (PD) (f) Disturbance storm time (Dst) (g) planetary geomagnetic A_p and (h) Auroral Electrojet (AE) indices during 16-30 September 2011. Four storm conditions were recorded during the period - moderate storm on 17th ($Dst=-60$) and consecutive storms on 26th ($Dst=-101$), 27th ($Dst=-88$) and 28th ($Dst=-62$), presumably driven by the significant increase in V_{sw} and PD on 17th and 26th (Fig. 3a-f). However, the main reference 20 storms are those of 17th and 26th. The variation of the AE (especially between 26th and 29th) appear to be consistent with

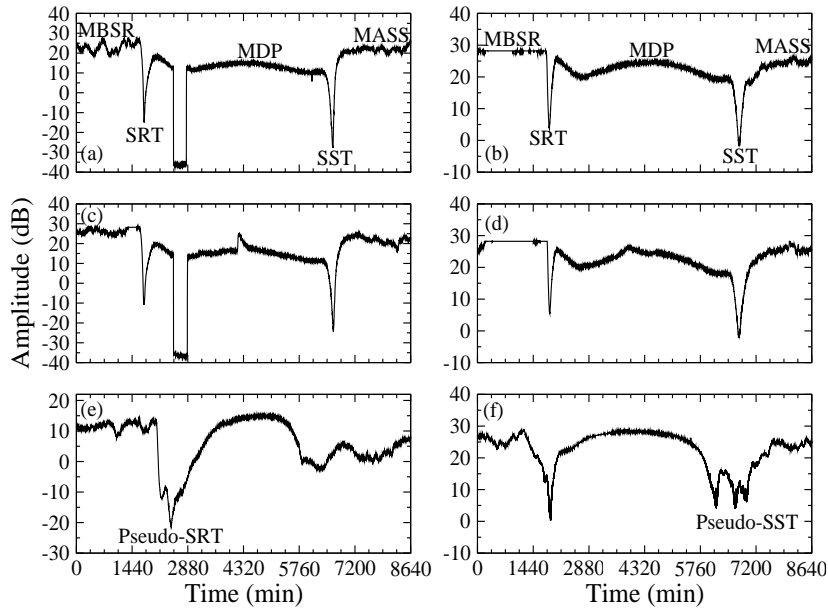


Figure 2. Diurnal VLF signal amplitude signatures showing analysed signal metrics. Fig (a) and (c) for DHO-A118 propagation path, fig (b) and (d) for GQD-A118 propagation path and fig (e) and (f) for illustration of pseudo-terminator.

high-intensity, long-duration continuous AE activity events (HILDCAAs). Hence, ‘fresh energy was being injected’ in the magnetosphere in the process (Tsurutani et al., 2011). We observed a notable drop in DHO-A118 VLF signal level on 26th around midday following the relatively intense storm condition with Dst up to -101 (Fig. 3a). This scenario (signal strength decrease) have been associated with storm-induced variations in energetic electron precipitation flux (e.g., Kikuchi and Evans, 5 1983; Peter et al., 2006). During a geomagnetic storm, the current system in the ionosphere, and the energetic particles that precipitate into the ionosphere deposit energy in the form of heat that can influence the density and distribution of density in the atmosphere (NOAA4). Some reasonable metrics (e.g., MBSR, MDP, MASS, SST and SRT) of the VLF signal amplitude makes it easier to quantify the influence of the storms on the D-region by observing their trends of variation. We therefore investigate variations in the signals trend for possible distinction of storm induced signatures in the ionosphere.

10

Figure 4 shows daily fluctuation of Dst and AE , and variations in the VLF midday signal amplitude peak (MDP), 4-hour mean signal amplitude before local sunrise (MBSR), 4-hour mean signal amplitude after sunset (MASS), sunrise terminator (SRT) and sunset terminator (SST) for (a) DHO-A118 and (b) GQD-A118 propagation paths during 16-30 September 2011. Values of the parameters over the period is presented in Appendix 1. In GQD-A118 propagation path (Fig. 4a), we observed a 15 dipping of the MDP on 17th (extending to 20th), as well as dipping of the MASS on 17th, but an increase of the MBSR, SRT and SST. Following the recurrent storms of 26th-28th, we observed dipping of the MDP on 26th (extending to 29th). The slight increase of the signal (MDP) on 28th appear to be due to the significant flare activity (3 C-class and 1 M-class), suggesting the

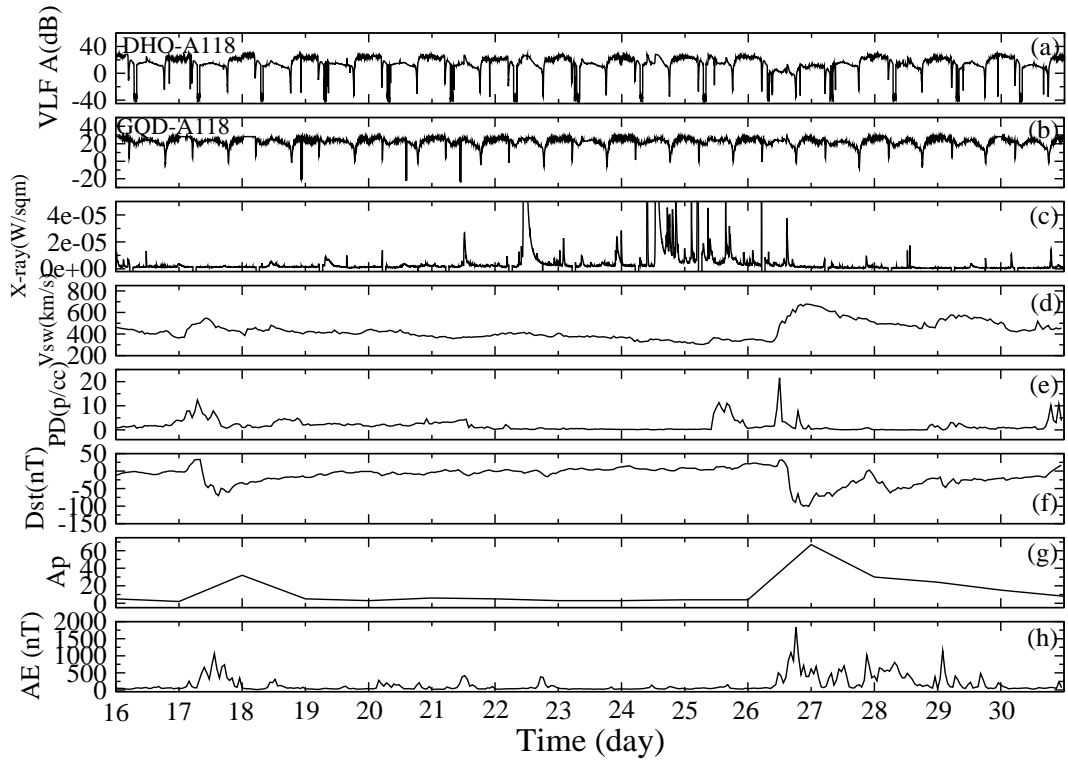


Figure 3. (a) Diurnal VLF amplitude for DHO-A118 and (b) GQD-A118 propagation paths (c) daily variation in X-ray flux output (d) solar wind speed (V_{sw}) (e) solar particle density (PD) (f) Disturbance storm time (Dst) (g) planetary A_p and (h) Auroral Electrojet (AE) indices during 16-30 September 2011

increase of both instantaneous and background X-ray flux output that usually results to spike in signal amplitude. High flare activity often overshadows the signal's response to geomagnetic storms when significant flare and storm events are concurrent (Nwankwo et al., 2016). There is also a significant dipping of all signal metrics (MDP, MBSR, MASS, SRT and SST) on 27th. We note dipping of the MBSR on the days following the main (reference) storms on 18th and 27th. Since the events occurred after dawn (around midday), the post-storm ionospheric effects are expected well into the day following the storm. The trend (post-storm day signal dip), therefore, suggest that the signals dipped in response to post-storm ionospheric effects on the days following the events. However, such response also depend on the characteristics of the signals propagation path. In DHO-A118 propagation path, dipping of the MDP, MBSR, SRT and SST have been observed on the 17th, and those of MDP, MASS and SST on 26th. The MASS and SRT maintained the pre-storm day values of 16th and 25th, respectively. Whereas the MBSR increased slightly on 26th (main storm day), there is a significant dipping of the signal following recurrent storm of 27th.

Figure 5 shows diurnal VLF amplitude for (a) DHO-A118 and (b) GQD-A118 propagation paths, daily variation in (c) X-ray flux output (d) V_{sw} (e) PD (f) Dst (g) A_p and (h) AE indices during 22 October - 5 November 2011. This period is associated

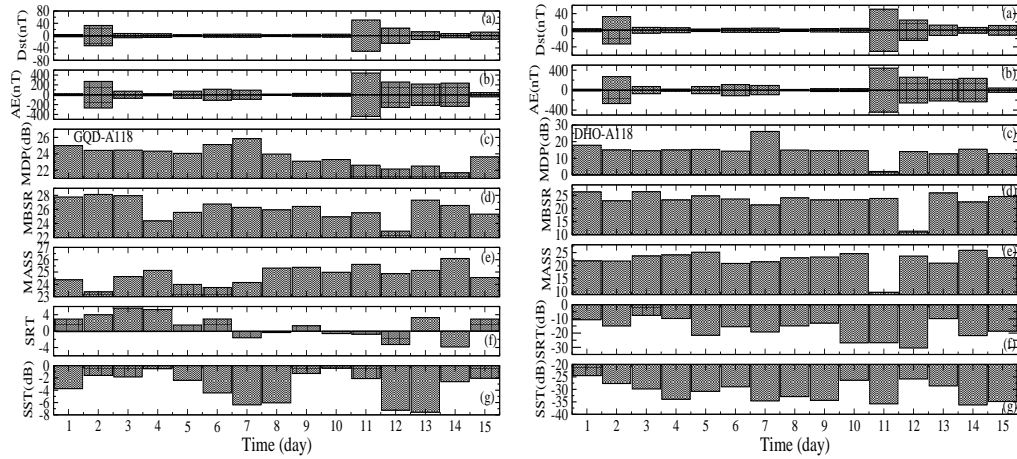


Figure 4. Daily deviations of Dst and AE , variations in the peak value of midday signal amplitude (MDP), 4-hour mean signal amplitude before local sunrise (MBSR), 4-hour mean signal amplitude after sunset (MASS), variation in sunrise terminator (SRT) and sunset terminator (SST) for (a) DHO-A118 and (b) GQD-A118 propagation paths during 16-30 September 2011.

with three storms - a severe storm with main phase on 25th October ($Dst=-132$) and consecutive storms on 1st ($Dst=-71$) and 2nd November ($Dst=-57$), presumably induced by the highly variable V_{sw} and PD (Fig. 5d-e). It has been shown that the capability of a given value of the solar wind electric field (SWEF) to create a Dst disturbance or geo-efficiency is enhanced by high solar wind density (Weigel, 2010; Tsurutani et al., 2011). Variation of the AE between 30th Oct. and 3rd Nov. also appear
5 to be consistent with HILDCAAs (Fig. 5h). The DHO-A118 VLF signal level on 25th around midday also showed a visible reduction following the intense storm condition with Dst up to -132 (Fig. 5a). VLF signal data for GQD-A118 propagation path are not available during 12:00 noon, 25th - 06:00 pm, 26th October (Fig. 5b).

Figure 6 shows daily deviations of Dst and AE , and variations in the MDP, MBSR, MASS, SRT and SST for (a) DHO-
10 A118 and (b) GQD-A118 propagation paths during 22 October - 5 November 2011. Values of the parameters over the period are presented in Appendix 2. Although data for GQD-A118 propagation path during 25th and 26th is inadequate for the present analysis, we did observe a dipping of the MBSR on the main storm day, 25th Oct. Dipping of the MDP, MASS and SST have been observed on 1st Nov., and those of MBSR, MASS, and SRT on 2nd Nov., following the consecutive storms. In DHO-
15 A118 propagation path, we observed dipping of the MDP, MBSR, MASS, and SRT on 25th Oct., dipping of the MDP, MBSR, MASS, and SST on 1st Nov., and dipping of the MBSR and SRT on 2nd Nov. Similar to the first case (Figs. 4 and 5), we note the high flare events on 2nd Nov (up to 7 C-class and 1 M-class), that may have caused a spike in the MDP on the day in both GQD-A118 and DHO-A118 propagation paths. Although dipping of the MDP signal (following storm events) has shown a considerable consistency across the cases presented so far, the MBSR and MASS (in particular) appear to be influenced by storms occurrence time; pre-sunrise event appears to have more influence on the MBSR (dawn signal), while pre-sunset event

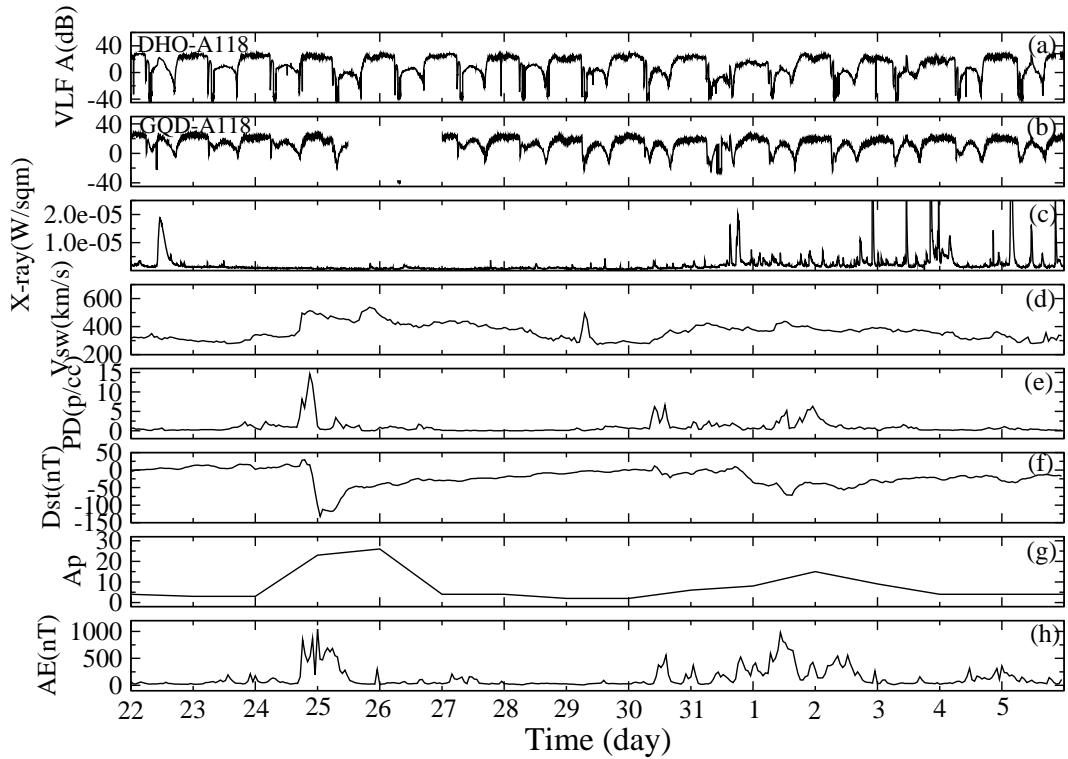


Figure 5. (a) Diurnal VLF amplitude for DHO-A118 and (b) GQD-A118 propagation paths (c) daily variation in X-ray flux output (d) solar wind speed (V_{sw}) (e) solar particle density (PD) (f) Disturbance storm time (Dst) (g) planetary A_p and (h) Auroral Electrojet (AE) indices during 22 October to 5 November 2011

appears to have more influence on the MASS (dusk signal). Also, the high variability or fluctuation of dusk-to-dawn ionosphere (and signal) does influence variations in MBSR and MASS, and hence their analysis (Nwankwo et al., 2016). However, presenting a consistency across a substantial number of cases is vital to better conclusion of this work. Against this backdrop, we statistically analyse up to 15 more storm cases between September 2011 and October 2012 in order to check the statistical significance of the observations. The 15 storm cases are presented in Table 1, which excluded some cases that were previously analysed in Nwankwo et al. (2016), but also included new cases.

In Figure 7, we show Dst deviation or fluctuation and trend in variation of the MDP, MBSR, MASS, SRT and SST signals during successive one-day before and after each of the 15 selected storm cases for (a) GQD-A118 and (b) DHO-A118 propagation paths. Values of the signal metrics are provided in Appendix 3. We recognised 3 consecutive days as day before an event (BE), during event (DE) and after event (AE). A '0' indicate absence of data. In GQD-A118 propagation path, about 8 of 12 MDP, 10 of 13 MBSR, 7 of 12 MASS, 3 of 12 SRT and 5 of 12 SST showed dipping of the signals, and 12 of 15 MDP, 9 of 15 MBSR, 10 of 15 MASS, 5 of 15 SRT and 7 of 15 SST showed dipping of the signals in DHO-A118 propagation path. These

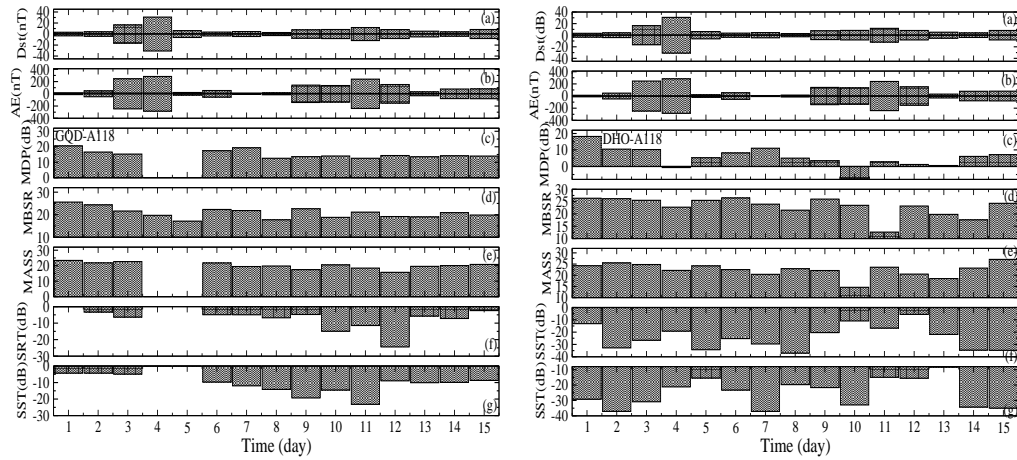


Figure 6. Daily deviations of Dst and AE , variations in the peak value of midday signal amplitude (MDP), 4-hour mean signal amplitude before local sunrise (MBSR), 4-hour mean signal amplitude after sunset (MASS), variation in sunrise terminator (SRT) and sunset terminator (SST) for (a) DHO-A118 and (b) GQD-A118 propagation paths during 22 October - 5 November 2011.

Table 1. Summary of analysed 15 geomagnetic storm events

No.	Date	Max Dst (nT)	σ_{Dst}	Flare count(C M X)
1	26092011	-101	± 50.73	9 2 0
2	25102011	-132	± 30.76	1 0 0
3	22012012	-67	± 37.00	4 0 0
4	15022012	-58	± 9.63	0 0 0
5	19022012	-54	± 12.8	1 0 0
6	07032012	-74	± 25.41	1 0 0
7	15032012	-74	± 20.75	1 0 0
8	28032012	-55	± 12.09	1 0 0
9	05042012	-54	± 13.82	3 0 0
10	23042012	-95	± 32.23	3 0 0
11	12062012	-51	± 12.47	13 0 0
12	16062012	95	± 20.24	4 0 0
13	15072012	-126	± 47.88	8 0 0
14	02092012	-54	± 13.86	5 0 0
15	09102012	-105	± 25.64	10 1 0

values respectively corresponds to 73.5%, 68.5%, 62.5%, 29.0% and 44.5% of the combined cases. The signal levels, along with the percentage dip of the signals are presented in Table 2. The MDP signals (in both the propagation paths) have generally shown remarkable evidence of dipping following geomagnetic storm conditions. However, we did also observe few scenarios

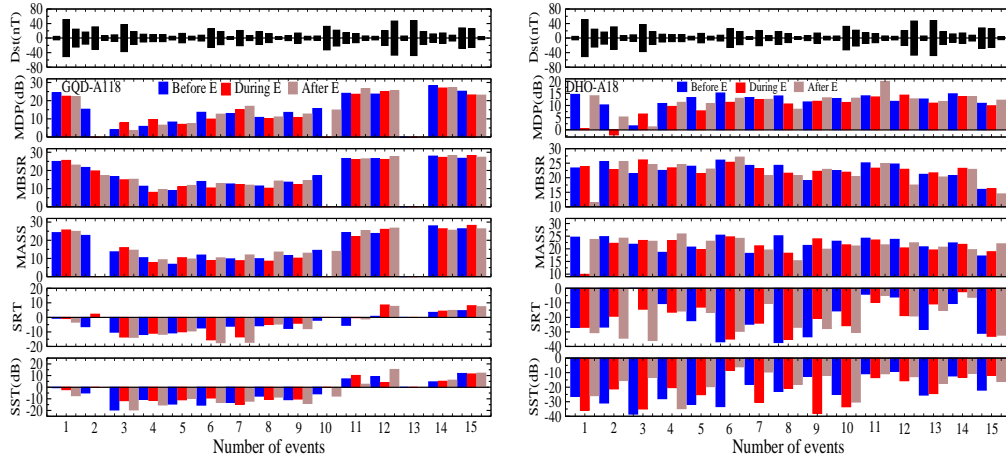


Figure 7. Dst deviation (fluctuation), and variations in MDP, MBSR, MASS, SRT and SST signals 1-day before, during and after each of the 15 events for (a) DHO-A118 and (b) GQD-A118 propagation paths.

of propagation path-mismatched increase (of MDP) on some events day (e.g., events 4 and 7 in GQD-A118 and 9 in DHO-A118), as well as propagation path-matched increase of the signal in both propagation paths (e.g., events 3 and 12). Whereas the probable reason for the former scenario is suggestive of the distinct propagation characteristics of each propagation path and X-ray flux induced spike in amplitude, further investigation of the latter scenario may be elucidating. To further check this scenario, we study and show variations in X-ray flux output and geomagnetic indices on the particular day of the events (3 and 12) to better interpret the prevailing ionospheric conditions at the time.

Table 2. Summary of trend in dipping of the signals' metrics during 15 geomagnetic storm case in (a) DHO-A118 and GQD-A118 propagation path

Signal (dB)	GQD-A118 propagation path			DHO-A118 propagation path		
	Available data	No. of dips	% dip	Available data	No. of dips	% dip
MDP	12	8	67	15	12	80
MBSR	13	10	77	15	9	60
MASS	12	7	58	15	10	67
SRT	12	3	25	15	5	33
SST	12	5	42	15	7	47

In Figure 8, we show the diurnal VLF amplitude for (a) DHO-A118 and (b) GQD-A118 propagation paths, daily variation in (c) X-ray flux output (d) V_{sw} (e) PD and (f) Dst indices for a day before and after each of the 15 storms condition. A propagation path-matched increase of the MDP signal in both propagation paths for events 3 and 12 have been observed (see, Fig.

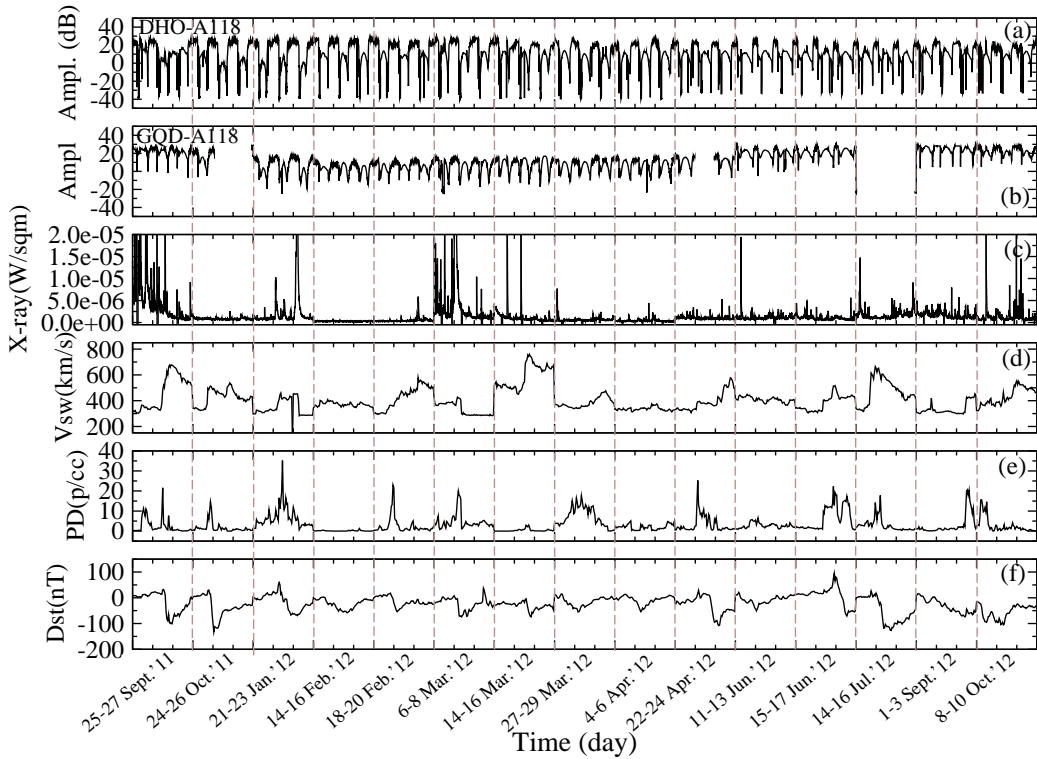


Figure 8. Diurnal VLF amplitude for (a) DHO-A118 and (b) GQD-A118 propagation paths, daily variation in (c) X-ray flux output (d) V_{sw} , (e) PD and (f) Dst indices for a day before and after each of the 15 storms

7a-b). Data showed (Fig. 8c, Fig. 8f) the occurrence of M-class flare in association with the storm on 22-23 January 2012 (event 3 on 21 January), both events almost having corresponding peaks. This scenario suggest an enhancement of the instantaneous and background X-ray flux output (as stated earlier), that can cause increase (or, spike) in the signal level, and thus overshadow geomagnetic effects on the signal. Whereas this explanation may be argued for events 1 (25-27 Sept. 2011) and 6 (6-8 Mar. 2012), it should be noted that such flare events started well before the storms, and continued until the storms time (in each case), suggesting an established increase in the overall background X-ray before the storms. Hence, a storm induced dipping of the signal from the already established flux background is speculated on the storm days. However, further investigation is encouraged, which is beyond the scope of this work. For event 12 (during 15-17 July 2012), we observed that the peak of the storm (that commenced by midnight on 16th) was on 17th (recognised as AE). Therefore, any geomagnetic influence on the signal (e.g., dipping) is expected on 17th (or, after) and not 16th, hence we observed a dipping of the AE signal (on 17th) instead in DHO-A118 propagation path.

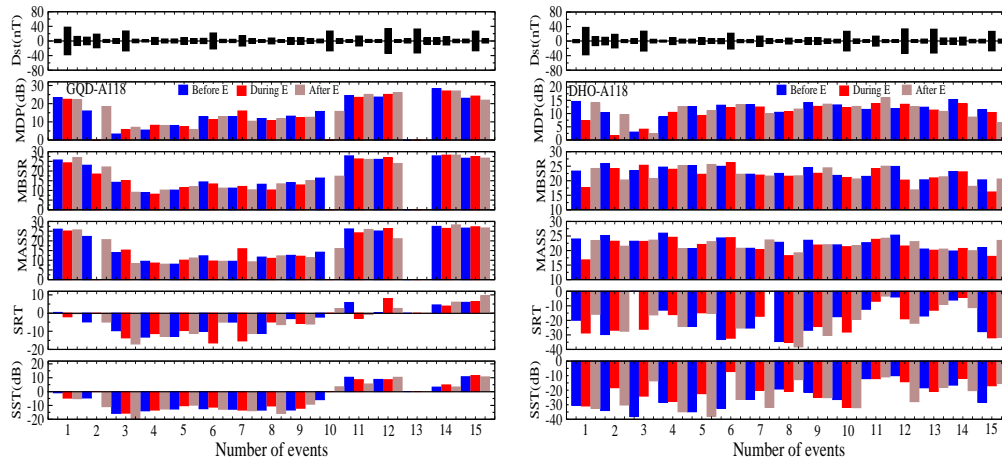


Figure 9. Dst deviation and 2-day mean variations of MDP, MBSR, MASS, SRT and SST signals before, during and after each event for (a) GQD-A118 and (b) DHO-A118 propagation paths.

Figure 9 shows Dst deviation (fluctuation) and 2-day mean variations of MDP, MBSR, MASS, SRT and SST signals before, during and after each event for (a) GQD-A118 and (b) DHO-A118 propagation paths. Values of the signal metrics are provided in Appendix 4. This analysis is vital to the corroboration of the result presented in Figure 7, because its data selection criterion differ from those of Figure 7. Whereas BE, DE and AE represent data for three consecutive days with reference to the event's day (DE) in the former analysis (presented in Fig. 7), each acronym (BE, DE or AE) represent a 2-day mean (VLF) with respect to DE (but not necessarily in succession to DE). However, it should be noted that due to the data averaging (2-day), a 'pronounced' increase or dipping in the signals (comparable to those in the former analysis (fig 7)) are not expected. Another important data selection criterion for this analysis is a relative geomagnetic quiet day BE and AE with respect to DE.

In GQD-A118 propagation path, 7 of 12 MDP, 7 of 13 MBSR, 7 of 12 MASS, 6 of 12 SRT and 3 of 12 SST showed dipping of the signals. In DHO-A118 propagation path, 10 of 15 MDP, 11 of 15 MBSR, 11 of 15 MASS, 6 of 14 SRT and 6 of 15 SST showed dipping of the signals. These values correspond to respective 62.5%, 63.5%, 65.5%, 46.5% and 32.5% of the combined cases. The signal levels, along with the percentage dip of the signals are presented in Table 3. In general, the trend of variation of the signal metrics considerably reflected the prevailing space weather coupled effects in the lower ionosphere. The MDP signal appears to be more responsive (about 68% for combined analysis shown in figs 7 and 9) to geomagnetic perturbations than other signal metrics. However, we anticipate an improvement with analysis of smaller range calculation of mean values of MBSR and MASS due to high fluctuation of dusk-to-dawn D region ionosphere - this will be considered in future analysis. Nwankwo et al. (2016) noted a drawback in SRT and SST analysis viz the existence of pseudo-SRT and SST exhibited by diurnal VLF signal (see, Fig. 2e and Fig. 2f), due to secondary destructive interference pattern in signals. Authors concluded in their study that the post-storm SRT and SST variations do not appear to have a well-defined trend (Nwankwo et al., 2016).

Also, the occurrence of solar flares during sunrise/sunset can influence the SRT/SST. To improve on such a demerit, we paid attention to the 'first' SRT and SST values (in case of a pseudo-terminator) during analysis of the signal metrics. In the present analysis, a rise (vertical shift) in SRT and SST amplitude under geomagnetic storm conditions have been favoured in both propagation paths. We found a respective dipping of 46.5% and 32.5% in the combined cases, suggesting a rise in majority of the cases. However, this needs to be investigated further. It is important to note that out of the two propagation paths used in this study, the DHO-A118 signal appears to be more sensitive to geomagnetic storm-induced magnetosphere-ionospheric dynamics. This study was not conducted with expectation (or, anticipation) of a 'perfect' consistency in signal trend and variations across all cases, because solar and other forcing mechanisms (of lithospheric and atmospheric sources), whose individual effects are difficult to estimate, also cause significant fluctuations in radio signals and thus there could be non-linear effects due to coupling of various processes (Nwankwo et al., 2016).

Table 3. Summary of trend in 2-day mean signals dipping following 15 geomagnetic storm cases in (a) DHO-A118 and GQD-A118 propagation path

Signal (dB)	GQD-A118 propagation path			DHO-A118 propagation path		
	Available data	No. of dips	% dip	Available data	No. of dips	% dip
MDP	12	7	58	15	10	67
MBSR	13	7	54	15	11	73
MASS	12	7	58	15	11	73
SRT	12	6	50	14	6	43
SST	12	3	25	15	6	40

3 Conclusions

We performed a diagnostic study of geomagnetic disturbance and/or storm-induced magnetosphere-ionosphere dynamics in mid-latitude D-region using propagation characteristics of VLF radio signals (21.1 and 23.4 kHz). The trends in variation of diurnal VLF signal metrics were analysed for up to 20 storm conditions between September 2011 and October 2012 in conjunction with geomagnetic indices, in order to understand deviations in the signal propagation characteristics, which could be attributed to geomagnetic storms-induced variations in the D-region ionosphere. 5 storm characteristics and their effects on the signals were studied in detail, followed by statistical analysis of 15 other cases, which included pre-storm and post-storm day conditions. We found that the midday signal amplitude peak (MDP) exhibited characteristic dipping scenario in about 68% of the combined cases in response to the storms. The MDP signals that showed no dipping scenario include some cases of propagation paths-mismatched increase (of MDP) in 3 events, as well as propagation paths-matched increase of the signal in 2 events. Whereas the mismatched increase of the signal could be related to distinct characteristics of each propagation path and X-ray flux-induced spike in amplitude, the matched increase appeared to be influenced by M-class flare concurrent with storm

event, and delayed responses of the local ionosphere to storm effects. The mean signal amplitude before sunrise (MBSR) and mean signal amplitude after sunset (MASS) also showed significant dipping (about 66% and 64%, respectively) due to storms, but appear to be influenced by the event(s) occurrence time and intensity, and the highly variable conditions of dusk-to-dawn D-region ionosphere. Conversely, the sunrise terminator (SRT) and sunset terminator (SST) amplitude showed respective dipping of 46.5% and 32.5% of the combined cases, favouring storm-induced rise of the signal instead.

Our study demonstrates the applicability and efficiency of VLF radio waves (as a tool) in identification, separation and interpretation of ionospheric dynamics from various forcing origin (e.g. due to geomagnetic storm). However, it is important to note that obtaining a ‘perfect’ consistency in signal trend across all cases in a given analysis remains a challenge, because solar and other forcing mechanisms (whose individual effects are difficult to estimate) also cause significant fluctuation in radio signal, since they are interconnected and possibly non-linearly coupled. It is therefore, recommended that the study or investigation of ionospheric changes due to distinct phenomenon include identification and isolation of other contributing sources around intervening period of analysis before definite conclusion.

Acknowledgements. V.U.J. Nwankwo acknowledges TWAS/ICTP, Trieste, Italy and the S.N. Bose National Centre for Basics Sciences for the research fellowship during which this work was done. Authors thank Dr. Bruce Tsurutani (Jet Propulsion Laboratory, California Institute of Technology) and Dr. Jan Lastovicka for clarification of some aspects of geomagnetic data and processes.

References

- Alfonsi L., Andrew J. Kavanagh, Ermanno Amata et al. (2008), Probing the high latitude ionosphere from ground-based observations: The state of current knowledge and capabilities during IPY (2007 ? 2009), *J Atm. Solar-Terres. Phys.*, 70, 2293 - 2308.
- Araki T. (1974), Anomalous Phase Changes of Trans equatorial VLF Radio Waves during Geomagnetic Storms, *J Geophys. Res.*, 79, 4811-4813
- 5 Baker D. N. (2000), Effects of the Sun on the Earth's environment, *J. Atm. Solar-Terres. Phys.*, 62, 1669-1681.
- Borovsky J. E. and Denton M. H. (2006), Differences between CME-driven storms and CIR-driven storms, *J Geophys. Res.*, 111
- Bucha V. and Bucha Jr. V., Geomagnetic forcing of changes in climate and in the atmospheric circulation, *J. Atmos. Sol-Terr. Phys.*, 60, 145 - 169.
- 10 Buonsanto M.J. (1999), Ionospheric storms ? a review, *Space Sci. Rev.*, 88, 563 - 601.
- Burke W. J. (2000), Magnetosphere-ionosphere coupling: selected topics, *J Atmo. Solar-Terres. Phys.* 62, 817-824.
- Burns A. G., S.C. Solomon, L. Qian, W. Wang, B.A. Emery, M. Wiltberger, and D.R. Weimer (2012), The effects of Corotating interaction region/High speed stream storms on the thermosphere and ionosphere during the last solar minimum, *J Atm. Solar-Terres Phys.*, 83, 79-87
- Chenette D.L., Datlowe D. W., Robinson R. M., Schumaker T. L., Vondrak R. R., and Winningham J. D. (1993), Atmospheric energy input and ionization by energetic electrons during the geomagnetic storm of 8-9 November 1991, *Geophys. Res. Lett.*, 20, 1323.
- 15 Clilverd M. A., Rodger C. J., Gamble R. J., Ulich T., Raita T., Seppala A., Green J. C., Thomson N. R., Sauvaud J. A., and Parrot M. (2010), Ground-based estimates of outer radiation belt energetic electron precipitation fluxes into the atmosphere, *J Geophys. Res.*, 115, A12304.
- Cowley S. W. H., Davies J. A., Grocott A., Khan H., Lester M., McWilliams K. A., Milan S. E., Provan B., Sandholt P. E., Wild J. A. and Yeoman T. K. (2003), Solar-wind-magnetosphere-ionosphere interactions in the Earth's plasma environment, *Phil. Trans. R. Soc. Lond. A*, 361, 113-126.
- 20 Danilov A. D. and Lastovicka J. (2001), Effects of Geomagnetic Storms on the Ionosphere and Atmosphere, *Inter. J. Geomagn. Aeron.*, 2, 209-224.
- Gosling J.T. and Pizzo V.J. (1999), Formation and evolution of corotating interaction regions and their three dimensional structure, *Space Sci. Rev.* 89, 2152.
- 25 Heikkila W. (2011), Earth's Magnetosphere, *Elsevier Kidlington*, Oxford, UK.
- Kelley M. C. (1989), The Earth's Ionosphere, *Academic Press Inc. San Diego*, California.
- Kikuchi T. and Evans D.S. (1983), Quantitative study of substorm-associated VLF phase anomalies and precipitating energetic electrons on November 13, 1979, *J. Geophys. Res.*, 88, 871-880.
- Kleimenova N. G., Kozyreva O. V., Rozhnoy A. A. and Soloveva M. S. (2004), Variations in the VLF signal parameters on the Australia-Kamchatka radio path during magnetic storms, *Geomagn. Aeron.* 44, 385-393.
- 30 Koga D., Sobral J. H. A., Gonzalez W. D., Arruda D. C. S., Abdu M. A., deCastilho V. M., Mascarenhas M., Gonzalez A. C., Tsurutani B. T., Denardini C. M., and Zamlutti C. J. (2011), Electro-dynamic coupling processes between the magnetosphere and the equatorial ionosphere during a 5-day HILDCAA event, *J. Atmos. Solar Terr. Phys.*, 73, 148-155.
- Kozyra J. U, G. Crowley, B. A. Emery, X. Fang, G. Maris, M. G. Mlynchak, R. J. Niciejewski, S. E. Palo, L. J. Paxton, C. E. Randall, P.P. Rong, J. M. Russell III, W. Skinner, S. C. Solomon, E. R. Talaat, Q. Wu and J.H. Yee (2006), Response of the Upper/Middle Atmosphere to Coronal Holes and Powerful High-Speed Solar Wind Streams in 2003. Recurrent Magnetic Storms: Corotating Solar Wind
- 35

- Streams. *Geophysical Monograph 167*. Edited by Bruce Tsurutani, Robert McPherron, Walter Gonzalez, Gang Lu, Jose H. A. Sobral and Natchimuthukonar Gopalswamy. ISBN-13: 978-0-87590-432-0. AGU Books Board, AGU, Washington, DC USA, 319.
- Kumar A. and Kumar S. (2014), Space weather effects on the low latitude D-region ionosphere during solar minimum. *Earth, Planets and Space*, 66.
- 5 Kutiev I., Ioanna Tsagouri, Loredana Perrone, Dora Pancheva, Plamen Mukhtarov, Andrei Mikhailov, Jan Lastovicka, Norbert Jakowski, Dalia Buresova, Estefania Blanch, Borislav Andonov, David Altadill, Sergio Magdaleno, Mario Parisi and Joan Miquel Torta (2013), Solar activity impact on the Earth's upper atmosphere, *Journal of Space Weather and Space Climate*, 3.
- Lastovicka J. (1989), Solar wind and high energy particle effects in the middle atmosphere, *Handb. MAP*, 29, 119.
- Lastovicka J. (1996), Effects of geomagnetic storms in the lower ionosphere, middle atmosphere and troposphere, *J. Atm. Sol. Terr. Phys.*, 10 58, 831-843.
- Lu G., Cowley S. W. H., Milan S. E., Sibeck D. G., Greenwald R. A., Moretto T. (2002), Solar wind effects on ionospheric convection: a review, *J. Atm. Solar-Terr. Phys.*, 64, 145-157.
- McRae W. M. and Thomson N. R. (2004), Solar flare induced ionospheric D-region enhancements from VLF phase and amplitude observations, *J Atm. Solar-Terr. Phys.*, 66, 77-87. DOI:10.1016/j.jastp.2003.09.009
- 15 Mitra W. B. (1974), Ionospheric effects of solar flares, *D. Reidel Publishing Company, Dordrecht, Holland*.
- NOAA SWPC (Retrieved 2012), Solar Particle and Geomagnetic Indices. swpc.noaa.gov/ftpmenu/indices/old_indices.html
- NOAA SWPC (Retrieved 2015), Solar wind speed, proton/particle density and magnetic field components. <ftp://sohoftp.nascom.nasa.gov/sdb/goes/ace/>
- NOAA SWPC (Retrieved 2015), Auroral Electrojet (AE) Index. ftp://ftp.ngdc.noaa.gov/STP/GEOMAGNETIC_DATA/INDICES/AURORAL_ELECTROJET/
- 20 NOAA (Retrieved 2016), Geomagnetic Storms, *NOAA Space Weather Prediction Center* <http://www.ngdc.noaa.gov/phenomena/geomagnetic-storms>
- Nwankwo V. U. J., Chakrabarti S. K. and R. S. Weigel (2015), Effects of plasma drag on low Earth orbiting satellites due to solar forcing induced perturbations and heating, *Adv. Space Res.*, 56, 47-56.
- Nwankwo V. U. J., Chakrabarti S. K. and Ogunmodimu O. (2016), Probing geomagnetic storm-driven magnetosphere-ionosphere dynamics 25 in D-region via propagation characteristics of very low frequency radio signals, *J. Atmos. Sol-Terres. Phys.*, 145, 154-169.
- Peter W. B., Chevalier M. W., and Inan U. S. (2006), Perturbations of mid-latitude sub-ionospheric VLF signals associated with lower ionospheric disturbances during major geomagnetic storms, *J Geophys. Res.*, 111, AO3301.
- Prolss G. W. (2004), Physics of the Earth's space environment, *Springer Berlin Heidelberg*, Germany.
- Raulin, J.-P., Pacini, A.A., Kaufmann, P., Correia, E., Martinez, M.A.G. (2010). On the detectability of solar X-ray flares using very low 30 frequency sudden phase anomalies, *J Atmo. Solar-Terres. Phys.*, 68, 1029-1035.
- Simoes F., Pfaff R., Berthelier J. and Klenzing (2012), A Review of Low Frequency Electromagnetic Wave Phenomena Related to Tropospheric-Ionospheric Coupling Mechanisms, *Space Sci. Rev.*, 168, 551-593.
- Stoke P. H. (1993), Energetic Electron Power Flux Deposition at Sanae (L=4.0) from Riometer Recording, *J Geophys. Res.*, 98, 19111-19116.
- Tatsuta K., Hobara Y., Pal S. and Balikhin M. (2015), Sub-ionospheric VLF signal anomaly due to geomagnetic storms: a statistical study, 35 *Ann. Geophys.*, 33, 1457-1467.
- Tsurutani B. T., Gonzalez W. D., Gonzalez A. L. C., Tang F., Arballo J. K., and Okada M. (1995), Interplanetary origin of geomagnetic activity in the declining phase of the solar cycle, *J. Geophys. Res.*, 100, 21717-21733.

- Tsurutani B. T., Gonzalez W. D., Gonzalez A. L. C., Guarnieri F. L., Gopalswamy N., Grande M., Kamide Y., Kasahara Y., Lu G., Mann I., McPherron R. L., Soraas F., and Vasyliunas V. M. (2006), Corotating solar wind streams and recurrent geomagnetic activity: A review. *J. Geophys. Res.*, *111*, A07S01, doi:10.1029/2005JA011273
- 5 Tsurutani B. T., Echer E., Guarnieri F. L. and Gonzalez W. D. (2011), The properties of two solar wind high speed streams and related geomagnetic activity during the declining phase of solar cycle 23, *J. Atmos. Solar-Terr. Phys.*, *73*, 164, doi:10.1016/j.jastp.2010.04.003
- Verkhoglyadova O. P., Tsurutani B. T., Mannucci A. J., Mlynczak M. G., Hunt L. A., and Runge T. (2013), Variability of ionospheric TEC during solar and geomagnetic minima (2008 and 2009): external high speed stream drivers, *Ann. Geophys.*, *31*, 263-276, doi:10.5194/angeo-31-263-2013.
- Wait J. R. (1959), Diurnal change of ionospheric heights deduced from phase velocity measurements at VLF, *Proc. IRE*, *47*, 998.
- 10 Wait J. R. and Spies K. P. (1964), Characteristics of the Earth-ionosphere wave-guide for VLF radio waves, *NBS Tech. Note 300*
- WDCG (Retrieved 2014), Geomagnetic Equatorial Dst index, *World Data Centre for Geomagnetism*, <http://wdc.kugi.kyoto-u.ac.jp/dstdir/index.html>
- Wei Y., Hong M., Wan W., Du A., Lei J., Zhao B., Wang W., Ren Z., and Yue X. (2008), Unusually long lasting multiple penetration of interplanetary electric field to equatorial ionosphere under oscillating IMF Bz, *Geophys. Res. Lett.*, *35*, L02102, doi:10.1029/2007GL032305.
- 15 Weigel R. S. (2010), Solar wind density influence on geomagnetic storm intensity, *J. Geophys. Res.*, *115*, A09201, doi:10.1029/2009JA015062.
- Weigel R. S., Baker D. N., Rigler E. J., and Vassiliadis D. (2004), Predictability of large geomagnetic disturbances based on solar wind conditions, *IEEE Trans. Plas. Sci.*, *32*, 1506-1510.

Figure Captions

Figure 1: VLF signal propagation paths (DHO-A118 and GQD-A118) used in the study

Figure 2: Diurnal VLF signal amplitude signatures showing analysed signal metrics. Fig (a) and (c) for GQD-A118 propagation path, fig (b) and (e) for DHO-A118 propagation path and fig (d) and (f) for NWC-ICSP propagation path.

Figure 3: (a) Diurnal VLF amplitude for DHO-A118 and (b) GQD-A118 propagation paths (c) daily variation in X-ray flux output (d) solar wind speed (V_{sw}) (e) solar particle density (PD) (f) Disturbance storm time (Dst) (g) planetary A_p and (h) Auroral Electrojet (AE) indices during 16-30 September 2011

10

Figure 4: Daily deviations of Dst and AE , variations in the peak value of midday signal amplitude (MDP), 4-hour mean signal amplitude before local sunrise (MBSR), 4-hour mean signal amplitude after sunset (MASS), variation in sunrise terminator (SRT) and sunset terminator (SST) for (a) DHO-A118 and (b) GQD-A118 propagation paths during 16-30 September 2011.

15 Figure 5: (a) Diurnal VLF amplitude for DHO-A118 and (b) GQD-A118 propagation paths (c) daily variation in X-ray flux output (d) solar wind speed (V_{sw}) (e) solar particle density (PD) (f) Disturbance storm time (Dst) (g) planetary A_p and (h) Auroral Electrojet (AE) indices during 22 October to 5 November 2011

Figure 6: Daily deviations of Dst and AE , variations in the peak value of midday signal amplitude (MDP), 4-hour mean signal amplitude before local sunrise (MBSR), 4-hour mean signal amplitude after sunset (MASS), variation in sunrise terminator (SRT) and sunset terminator (SST) for (a) DHO-A118 and (b) GQD-A118 propagation paths during 22 October - 5 November 2011.

Figure 7: Dst deviation (fluctuation), and variations in MDP, MBSR, MASS, SRT and SST signals 1-day before, during and after each of the 15 events for (a) DHO-A118 and (b) GQD-A118 propagation paths.

Figure 8: Diurnal VLF amplitude for (a) DHO-A118 and (b) GQD-A118 propagation paths, daily variation in (c) X-ray flux output (d) V_{sw} , (e) PD and (f) Dst indices for a day before and after each of the 15 storms

30 Figure 9: Dst deviation and 2-day mean variations of MDP, MBSR, MASS, SRT and SST signals before, during and after each event for (a) GQD-A118 and (b) DHO-A118 propagation paths.

Effects of plasma drag on low Earth orbiting satellites due to solar forcing induced perturbations and heating [☆]

Victor U.J. Nwankwo ^{a,*}, Sandip K. Chakrabarti ^{a,b}, Robert S. Weigel ^c

^a S. N. Bose National Centre For Basic Sciences, Kolkata 700098, India

^b Indian Centre for Space Physics, Kolkata 700084, India

^c George Mason University, 4400 University Drive, Fairfax, VA 22030, USA

Received 16 September 2014; received in revised form 14 January 2015; accepted 30 March 2015

Available online 9 April 2015

Abstract

The upper atmosphere changes significantly in temperature, density and composition as a result of solar cycle variations, which causes severe storms and flares, and increases in the amount of absorbed solar radiation from solar energetic events. Satellite orbits are consequently affected by this process, especially those in low Earth orbit (LEO). In this paper, we present a model of atmospheric drag effects on the trajectory of two hypothetical LEO satellites of different ballistic coefficients, initially injected at $h = 450$ km. We investigate long-term trends of atmospheric drag on LEO satellites due to solar forcing induced atmospheric perturbations and heating at different phases of the solar cycle, and during short intervals of strong geomagnetic disturbances or magnetic storms. We show dependence of orbital decay on the severity of both solar cycle and phase and the extent of geomagnetic perturbations. The result of the model compares well with observed decay profile of some existing LEO satellites and provide a justification of the theoretical considerations used here. © 2015 COSPAR. Published by Elsevier Ltd. All rights reserved.

Keywords: Ballistic coefficient; LEO satellite trajectory; Plasma drag; Solar cycle variations; Solar energetic events

1. Introduction

Once launched, the optimum performance and survival of a satellite depend on its ability to weather both gravitational and non-gravitational perturbing forces including atmospheric drag, especially for satellites at low Earth orbit. Atmospheric drag on LEO satellites (corresponding to altitudes of < 800 km) can cause untimely re-entry of satellites, difficulty in identifying and tracking of satellites and other space objects, maneuvering and prediction of lifetime and actual re-entry (Klinkrad, 1996; Mark et al., 2005;

Doornbos and Klinkrad, 2006; Xu et al., 2011; Walterscheid, 1989; Nwankwo and Chakrabarti, 2014, 2015). Accelerated orbit decay due to atmospheric drag on low Earth orbiting satellites is mainly due to solar forcing induced variations in thermospheric density profile. There have been studies that investigated the response of thermospheric density and/or satellites orbit to variations in solar forcing due to solar activity using one or combination of several methods such as simulations, satellite drag data, on-orbit mass spectrometers, accelerometers, sounding rockets and ground-based incoherent scatter radars (Klinkrad, 1996; Xu et al., 2011; Burns et al., 2012; Leonard et al., 2012; Kutiev et al., 2013; Lei et al., 2013; Chen et al., 2012; Kwak et al., 2011; Solomon et al., 2012; Liu et al., 2012; Lei et al., 2008; Sutton et al., 2005; Deng et al., 2012; Walterscheid, 1989; Weigel et al., 2004; Weigel, 2010; Nwankwo and Chakrabarti, 2014, 2015). It is known that density of the thermosphere and the vertical

[☆] Presented in COSPAR 2014, Moscow, Russia.

* Corresponding author at: S. N. Bose National Centre For Basic Sciences, Kolkata, JD Block, Salt Lake, Kolkata 700098, India. Tel.: +91 33 2335 5706; fax: +91 33 2335 9176.

E-mail addresses: victorujn@bose.res.in (V.U.J. Nwankwo), chakraba@bose.res.in (S.K. Chakrabarti), rweigel@gmu.edu (R.S. Weigel).

extent of the upper atmosphere varies on time scales of solar flare event (few hours), geomagnetic storms (1–3 days) and the solar cycle (~ 11 years) (Alfonsi et al., 2008; Bounsanto, 1999; Kutiev et al., 2013). There is a significant heating and consequent expansion of the upper atmosphere during solar and geomagnetic activities. Studies have shown that solar EUV and thermospheric temperature could increase by a factor of two (or more), and thermospheric density by a factor of up to ten from solar minimum to solar maximum (Emmert and Picone, 2010; Walterscheid, 1989). The contribution to upper atmospheric heating by solar EUV radiation is larger than that associated with geomagnetic current enhancement during time interval of enhanced geomagnetic activity. However, geomagnetic field induced Joule heating becomes important during short-term strong geomagnetic perturbations and can increase by up to 134% when the Kp index increases from 1 to 6 or Ap index from 4 to 80 (Rhoden et al., 2000; Kim et al., 2006; Chen et al., 2012; Kutiev et al., 2013).

Solar energetic events that cause atmospheric heating include solar wind streams, coronal mass ejections (CMEs), solar flares and corotating interaction regions (CIRs). When a solar wind high-speed stream (HSS) emanates from the sun, it interacts with preceding low-speed solar winds and form a corotating interactive region (CIR). The interface between low and high speed solar plasma (CIR) interacts with the Earth's magnetosphere and produces geomagnetic disturbances and storms (Borovsky and Denton, 2006; Burns et al., 2012; Gosling and Pizzo, 1999; Kutiev et al., 2013; Tsurutani et al., 2006). There are many studies which investigated the effects of CIRs or solar wind conditions on the thermosphere and satellite orbits (Burns et al., 2012; Solomon et al., 2012; Liu et al., 2012; Lei et al., 2008; Borovsky and Denton, 2006). CIRs and HSSs are known to be the dominant drivers of storm induced atmospheric perturbations during the declining phase of the solar cycle and are, therefore important to thermospheric density and satellite orbital variations during this phase of the cycle (Burns et al., 2012; Chen et al., 2012; Nwankwo and Chakrabarti, 2014). CMEs and solar flares are sporadic events and are known to vary with phase of a solar 11-year cycle. They are more frequent and intense during a solar maximum (Richardson et al., 2001; Gopalswamy, 2009). Thermal tides propagating upwards from the lower atmosphere can also influence atmospheric density and satellite orbits (Forbes et al., 2009; Hagan and Forbes, 2002; Zhang et al., 2010; Oberheide et al., 2009; Leonard et al., 2012; Nwankwo and Chakrabarti, 2014). Thermospheric density also exhibits annual, semiannual and diurnal oscillations (Emmert and Picone, 2010; Doornbos, 2012).

Some insightful investigations on space weather effects on thermosphere density and satellite orbit includes that of Walterscheid (1989), Chen et al. (2012), Leonard et al. (2012), Lei et al. (2013) and others. Walterscheid (1989) studied effects of the solar cycle on upper atmosphere

and their implications on satellite drag and pointed out that a typical satellite initially at a height of 500 km could have a lifetime of about 30 years under typical solar cycle minimum conditions and only about 3 years under the solar maximum conditions (Nwankwo and Chakrabarti, 2014). Chen et al. (2012) investigated and compared effects of CIR- and CME-induced geomagnetic activity on thermospheric densities and spacecraft orbits, and found that CME-induced storms (although of shorter duration) causes larger thermosphere density disturbances and a resultant larger orbital decay rates during its main phase than CIR storms, but the mean thermospheric density and satellite orbit decay during CIR storms could be much larger than those during the CME-induced storms in each case because of longer duration of CIR phase. Lei et al. (2013) also studied the impact of solar forcing on thermospheric densities and spacecraft orbits from CHAMP and GRACE satellite's data during the events (CMEs and CIR) of September 14–28 and November 19–22, 2003, and showed that variations of the satellite's semi-major axis was 243 m for CIR-induced perturbations during September 15–27, 2003 and about 130 m for CME-induced storm event during November 19–22, 2003. These studies only used the data (on-orbit mass spectrometers and accelerometers) on existing satellites (e.g. CHAMP and GRACE). In this study, we incorporate the NRLMSISE-00 empirical atmospheric model into our drag model to investigate short- and long-term trends of atmospheric drag effects on LEO satellite orbits due to atmospheric density perturbations and heating by solar energetic events at different phases of the solar cycle. This study is important for understanding how satellite orbits are affected during short- and long-term variations in solar and geomagnetic activity using a realistic atmospheric density and drag model. We are aware of the difficulties associated with exact determination of atmospheric density and orbital predictions at very low Earth orbits. Therefore, we ignore impacts of tidal effects at this stage.

2. Upper atmospheric density profile

An accurate prediction of a satellite's lifetime, re-entry or drag depends on good knowledge of atmospheric density profile, which is an important space environmental parameter for satellite operation in the near-Earth space (Kwak et al., 2011; Chen et al., 2012). Although this quantity is not precisely known at any given instant, many atmospheric models have been developed (and more are being developed) over the years with good approximation. However, despite the unprecedented improvements in modeling atmospheric density, concerns about the accuracy of the models remain, because the individual effects of various solar forcing mechanism, which causes fluctuations in neutral and ionized density are very difficult to estimate and/or model (also, see Kutiev et al. (2013), Storz et al. (2005)). Particularly important are the hysteresis effects where the effects of the same event may depend on the history of events which took place before it. Some

atmospheric models in use include that of Picone et al. (2002), Bruinsma et al. (2003), Bowman et al. (2008), Emmert and Picone, 2010, Liu et al. (2013) and others. In our work, atmospheric density profiles are obtained from the NRLMSISE-00 empirical atmospheric model. Details of the model can be found in Picone et al. (2002). In addition to other outputs, NRLMSISE-00 gives total atmospheric mass density as a function of time, location, solar and geomagnetic activity. The model has also been used in some other works, such as, Policastri and Simons (2003), Doornbos (2012) and Klenzing et al. (2013).

3. Procedure

In this work, we consider two hypothetical satellites (SAT-BCI and SAT-BCII) with different ballistic coefficients [BCI ($m_s = 250$ kg, $A_s = 0.25$ m², $C_d = 2.2$) and BCII ($m_s = 522$ kg, $A_s = 0.72$ m², $C_d = 2.2$)], initially injected at an altitude of 450 km. The ballistic and/or drag coefficient used in this study were explained in Nwankwo and Chakrabarti (2014). We compute atmospheric drag force on the satellites due to long-term solar and geomagnetic activity at different phases of the solar cycle, viz. 2000–2002 (to represent a typical solar peak activity during the last solar maximum), 2004–2006 (to represent a typical solar ‘quiet’ period during last solar minimum), and 2012–2014 (to represent the period around current solar maximum). We thus obtain an estimate of the mean annual decay rate of the satellites at different phases of the solar cycle (minimum and maximum). We also compute and investigate the drag effect for short-term strong geomagnetic disturbances and/or storms in three regimes, with and without control on the solar parameters, aimed at providing insight into how the model works. Solar radio flux (F10.7), geomagnetic Ap index and the moving average of F10.7 over three solar rotations (81 days) were used in the model (NRLMSISE-00) as inputs to obtain thermosphere density profile (NOAA-1). Solar radio flux (F10.7) indirectly estimates upper atmospheric heating from solar energetic particles and solar extreme ultra-violet (EUV). Planetary Ap (or Kp) index estimates additional Joule heating associated with geomagnetic activity (Pardini et al., 2004; IRS Radio, 1999; NOAA, 2006). The moving average of F10.7 flux over three or four solar rotations, denoted by $\bar{F}_{10.7}$ represents a slowly varying component of solar radiation (Doornbos, 2012; Nwankwo and Chakrabarti, 2014).

4. Computation of orbital decay due to plasma drag

The orbital decay due to atmospheric drag on SAT-BCI and SAT-BCII are computed from two sets of equations to study both short- and long-term effects of space environmental perturbations on the trajectory of the model satellites. A spherical polar co-ordinate system (r, θ, ϕ) was used, with origin at the center of the Earth. We assume

that the satellite always remain in the same plane (i.e., $\theta =$ constant). The first set of the equations used consists of four coupled differential equations (Nwankwo and Chakrabarti, 2014, 2015):

$$\dot{v}_r = -\frac{GM_e}{r^2} + r\dot{\phi}^2 \quad (1)$$

$$\dot{r} = v_r \quad (2)$$

$$\ddot{\phi} = -\frac{1}{2}r\rho\dot{\phi}^2\frac{A_sC_d}{m_s} \quad (3)$$

$$\dot{\phi} = v_\phi/r \quad (4)$$

where, v_r and v_ϕ are the radial and tangential velocity components, G is the gravitational constant, M_e is the mass of the Earth, r is the instantaneous radius of the orbit, ρ could be the atmospheric density, A_s is the omni-directional projected area of the satellite, m_s is the mass of the satellite, and C_d is the drag coefficient at an altitude of r .

The equations were solved to obtain instantaneous position and velocity of the satellite. Orbital decay due to atmospheric drag on the model satellites were computed under varying space weather conditions, while tracking their position and time by the azimuthal parameters ($\phi, \dot{\phi}$). Other integration (such as, $-\dot{\phi}r^2(A_sC_d/m_s)$) gave similar results (Chobotov, 2002). The second equation is a differential equation ($dr/dt = -\rho(A_sC_d/m_s)\sqrt{GM}r$), that describes changes in the mean radius of the satellite orbit per revolution (MRPR) (Xu et al., 2011; Chen et al., 2012; Wertz and Larson, 1999). Model results of orbital decay profile in the two set of equations (or methods) generally agree.

4.1. Modeling CIR-induced periodic changes in atmospheric density profile

The empirical atmospheric model used in this work is assumed to have a good representation of the background thermospheric density including storm induced fluctuations and a varying component due to solar rotation (introduced through the solar radio flux, geomagnetic Ap index and the $\bar{F}_{10.7}$). CIR-induced effects on thermospheric density is known to be dominant during the solar minimum and, therefore produces significant decay of satellite orbits at this phase of the solar cycle. Although the model to some extent includes CIR effects through the geomagnetic activity index input, its associated effects may be underestimated due to its high frequency (dominance) at this phase. Lindsay et al. (1994) detected occurrences of up to two CIRs per solar rotation prior to solar maximum. To incorporate this effect, we introduce a term ρ_y that would account for the enhanced (short-term) thermospheric density due to periodic CIRs during solar minimum. A comparison between sunspot number, yearly CME, stream CIR interaction, and interplanetary shock rate is shown in Fig. 1. A modified density ρ that includes ρ_y was used to model the CIR effect,

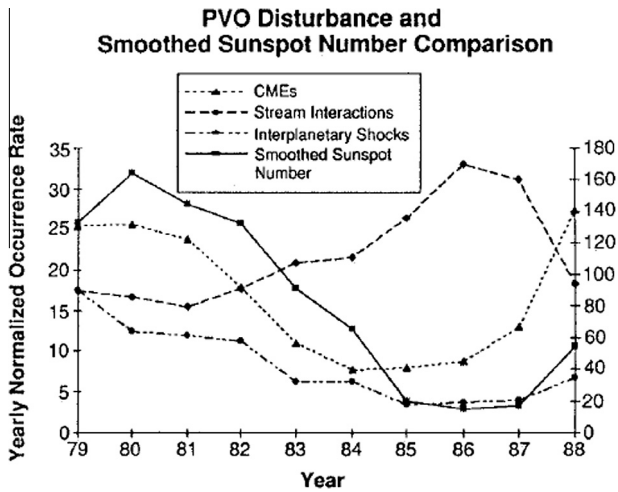


Fig. 1. Comparison between sunspot number (smoothed), CME, CIR, and interplanetary shock rates (Lindsay et al., 1994).

$$\rho = \rho_{bcir} + \rho_{\gamma} \tag{5}$$

where, ρ_{bcir} is the thermospheric density before the CIR and ρ_{γ} is the thermospheric density increase due to CIR-induced effect, modeled as

$$\rho_{\gamma} = (\rho - \rho_{bcir})\alpha \exp[-(\gamma t - 1)^2/2]$$

where, α is the amplitude of density oscillation (ρ increases by a factor of up to 2), γ is the frequency of oscillation ($2\pi/T$), T is the period of oscillation (13.5 days in this study).

5. Results and discussion

5.1. Trends of orbital decay at difference phases of the solar cycle

The model (calculations) of solar cycle (long-term) trends of atmospheric drag due to solar and geomagnetic activity at different phases of a cycle are presented for two maxima (2000–2002 and 2012–2014) and a minimum (2004–2006). Typical range of values of mean altitude, decay rate, thermosphere temperature and density for each satellite in a given regime are provided. The mean annual decay rates of the satellites at different phases were thus estimated.

5.1.1. Solar maximum decay trend

Fig. 2 shows time variations of model satellite’s mean altitude, orbit decay rate, thermosphere temperature and density for (a) SAT-BCI and (b) SAT-BCII initially at 450 km in 2000–2002. SAT-BCI (Fig. 2a) experienced a respective decay of 46.13, 49.10 and 47.38 km in 2000, 2001 and 2002, corresponding to a mean decay of 48 ± 2 km per year. The mean orbit decay rate is 47 – 327 m/day. SAT-BCII (Fig. 2b) respectively decayed by 61.14, 62.23 and 61.19 km (during the same period), corresponding to a mean decay of about 62 ± 1 km per year. The orbit decay

rate varied between 55 and 391 m/day. Thermosphere temperature variations during the respective years are 1075 – 1416, 1021 – 1469 and 1004 – 1470 K. Density variations are 2.27×10^{-12} – 7.96×10^{-12} , 2.06×10^{-12} – 14.70×10^{-12} and 1.15×10^{-12} – 8.23×10^{-12} kg/m³ respectively. Extreme values of the computed parameters occurred between July 2001 and early 2002 with up to 30 km decay in 175 days.

5.1.2. Solar minimum decay trend

Fig. 3 shows time variations of model satellite’s mean altitude, orbit decay rate, thermosphere temperature and density for (a) SAT-BCI and (b) SAT-BCII initially at 450 km in 2004 – 2006. SAT-BCI (Fig. 3a) decayed by 13.55, 9.03 and 6.15 km in 2004, 2005 and 2005 respectively, corresponding to an average decay of 10 ± 4 km per year. The mean orbital decay rate is 9 – 92 m/day. SAT-BCII (Fig. 3b) respectively decayed by 18.77, 12.51 and 8.17 km, corresponding to decay of about 13 ± 6 km per year. The mean variation in orbital decay rate is 10 – 133 m/day. The respective variations in thermosphere temperature are 834 – 1212, 790 – 1129 and 756 – 975 K. Ranges of density variations are 0.73×10^{-12} – 3.59×10^{-12} , 0.50×10^{-12} – 1.83×10^{-12} and 0.31×10^{-12} – 1.18×10^{-12} kg/m³ respectively. The mean values of computed parameters dropped consecutively in 2004–2006 as solar minimum approached (in 2006). Computation using the CIR effect model produced respective decay of 16.5, 11 and 7.5 km for SAT-BCI and 24.3, 15.8 and 10.7 km for SAT-BCII. The annual mean decay rate is about 12 ± 5 km and 17 ± 8 km per year for SAT-BCI and SAT-BCII respectively. There is an additional 2–4 km (per year) from the contribution of assumed periodic occurrence of two CIRs per solar rotation during solar minimum phase.

5.1.3. Emerging solar maximum decay trend

Fig. 4 shows time variations of model satellite’s mean altitude, orbit decay rate, thermosphere temperature and density for (a) SAT-BCI and (b) SAT-BCII in 2012–2014. This computation was based on two and a half years archival data (January 2000–June 2014) and 6 months predicted solar radio flux (July–December 2014) and assumed geomagnetic Ap data (NOAA-2). SAT-BCI (Fig. 4a) experienced respective decay of 19.88, 21.17 and 32.44 km in 2012, 2013 and 2014, corresponding to a mean decay of 25 ± 7 km per year. The mean orbit decay rate was 30 – 125 m/day. SAT-BCII (Fig. 4b) respectively decayed by 24.77, 25.90 and 41.65 km, corresponding to decay of about 31 ± 10 km per year. Mean orbital decay rate varied between 27 and 219 m/day. Thermosphere temperature variations during the respective year are 889 – 1180, 879 – 1203 and 959 – 1254 K. The density variations are 1.48×10^{-12} – 3.03×10^{-12} , 1.38×10^{-12} – 3.77×10^{-12} and 1.62×10^{-12} – 5.51×10^{-12} kg/m³ respectively. The observed trend in the mean values of computed parameters is a

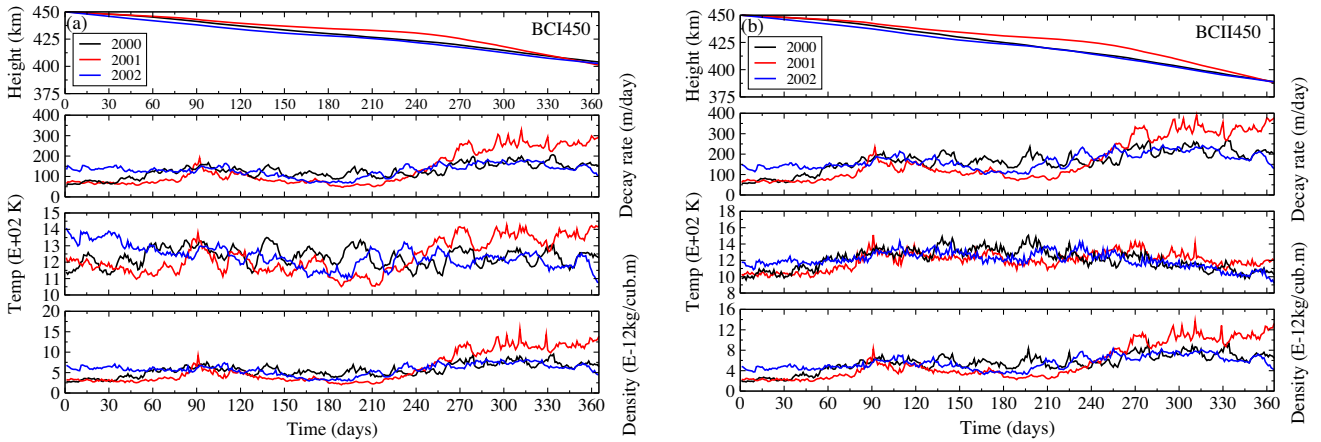


Fig. 2. Time variations of model satellite's mean altitude, orbit decay rate, thermospheric temperature and density in 2000–2002 for (a) SAT-BCI and (b) SAT-BCII.

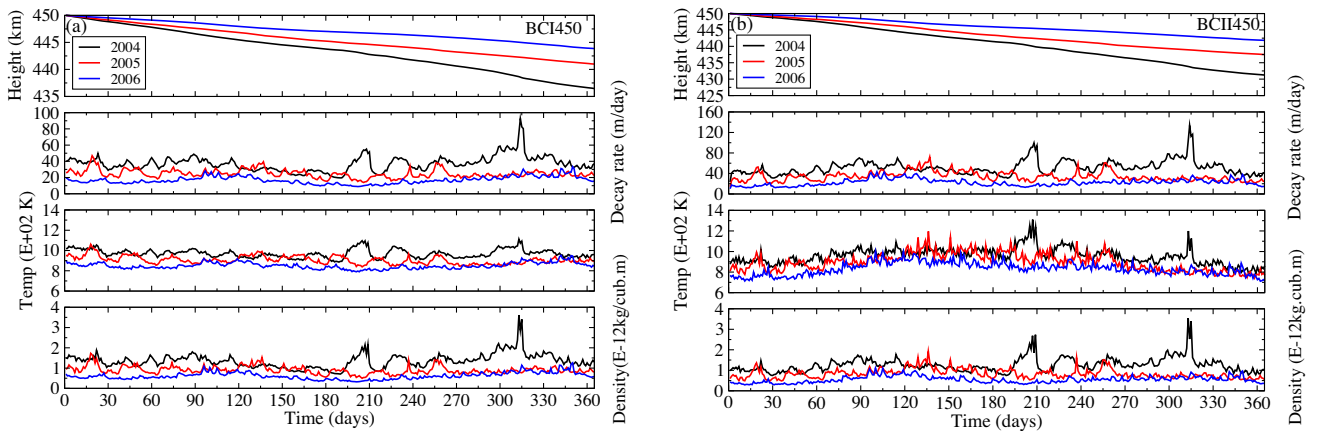


Fig. 3. Time variations of model satellite's mean altitude, orbit decay rate, thermospheric temperature and density in 2004–2006 for (a) SAT-BCI and (b) SAT-BCII.

consecutive increase from 2012 to 2014. The general consensus is that the current solar peak would occur in 2013/2014. Clearly, the annual mean decay rate of both satellites in the current solar peak is half less than the last (2000–2002) peak.

The difference between the area-to-mass ratio of SAT-BCI (0.001) and SAT-BCII (0.00138) is 3.8×10^{-4} . This difference produced decay rate increase of about 13.98, 3.57 and 6.24 km per year in the respective 3 regimes (for SAT-BCII). Summary of the trends of computed parameters for SAT-BCI and SAT-BCII is presented in Table 1.

5.2. Trend of Orbital decay during short-term strong geomagnetic disturbances

Solar data showed significant (high) solar and geomagnetic activity in July 2000. The mean F10.7 and Ap index values during 1st–31st July, 2000 was approximately 200 and 22 respectively; with up to F10.7 = 253 (20th July) and Ap = 152 (15th July). On 14th July, 2000, data showed

a record of occurrence of a halo CME (with speed up to 1674 km/s) and associated X class solar flares (X5), followed by solar energetic particle event on 15th July (SOHO; NOAA-3). In Fig. 5, we show plot of values of geomagnetic Ap and disturbance storm time (Dst) index for July 2000. Dst is a measure of geomagnetic activity used to estimate the extent of geomagnetic storms, based on the measure of value of the horizontal component of the Earth's magnetic fields. The strength of the surface magnetic field at low latitudes varies inversely with the energy content of the ring current, which significantly increases during geomagnetic storms (Hamilton et al., 1988). Clearly, there were consequent strong geomagnetic perturbations and storms, associated with preceding solar energetic events - a sudden increase in the number of high speed solar wind particles, fueled by coronal mass ejections and solar flares (Doornbos, 2012), and the increase in solar flux (F10.7) connected with 27-day solar rotation of the active region (Woods et al., 2004; Doornbos, 2012).

In this Section, we investigate the effects of this scenario of periodic (4 weeks) EUV enhancement and the short-

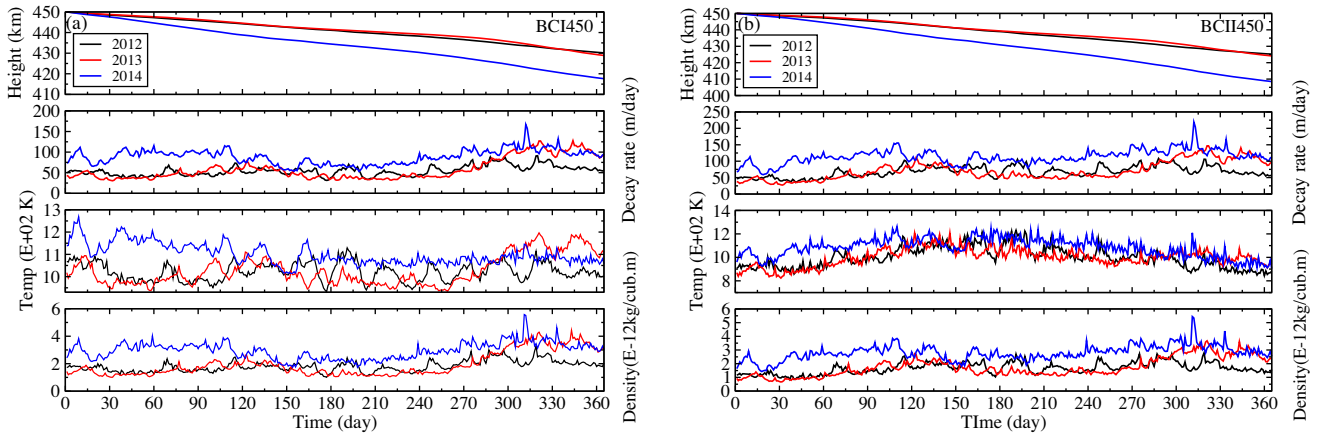


Fig. 4. Time variations of model satellite's altitude, orbit decay rate, thermospheric temperature and density in 2012–2014 for (a) SAT-BCI and (b) SAT-BCII.

Table 1

Trends of time variation of mean altitude, orbit decay rate, thermosphere temperature and density for SAT-BCI and SAT-BCII at different phases of the solar cycle.

Year	Decay (km)		Decay rate (m/day)				Temperature (K)		Density (10^{-12} kg/m ³)	
	BCI	BCII	Low BCI	Low BCII	High BCI	High BCII	Mean Low BCI/BCII	Mean High BCI/BCII	Mean Low BCI/BCII	Mean High BCI/BCII
2000	46.13	61.14	55.00	57.51	205.86	265.28	1075.12	1416.03	2.27	7.96
2001	49.10	62.23	47.25	57.89	327.10	391.31	1021.24	1469.05	2.06	14.70
2002	47.38	61.19	67.68	102.65	182.21	245.62	1004.13	1417.17	3.15	8.23
Mean	47.54	61.52								
2004	13.55	18.77	19.57	23.19	92.85	133.69	834.44	1212.36	0.73	3.59
2005	9.03	12.51	13.91	14.20	46.9	72.33	790.33	1129.29	0.50	1.83
2006	6.15	8.17	9.03	10.33	33.36	43.06	756.22	975.34	0.31	1.18
Mean	9.58	13.15								
2012	19.88	24.77	31.42	35.06	91.15	105.68	889.24	1180.41	1.48	3.03
2013	21.17	25.90	30.51	27.22	127.69	146.87	879.34	1203.29	1.38	3.77
2014	32.44	41.56	53.69	58.94	157.68	219.50	959.18	1254.10	1.62	5.51
Mean	24.50	30.74								

term strong geomagnetic disturbances on the upper atmospheric temperature, density and satellite orbit. Computations were done in three regimes, viz. (1) with

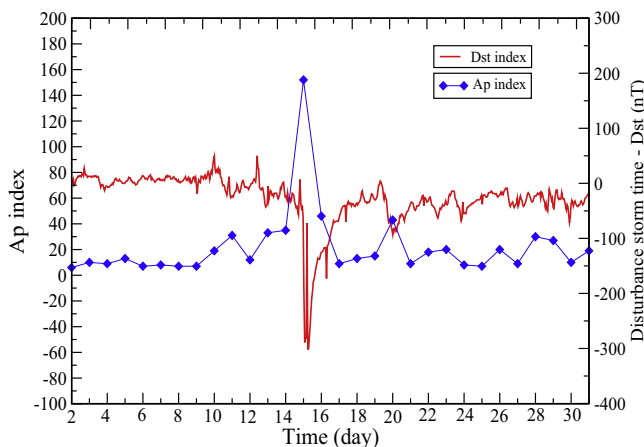


Fig. 5. Ap and Dst index variations during 1st–31st July 2000.

actual daily F10.7 and Ap index (raw data) associated with the event ($F_{10.7}, A_p$); (2) mean F10.7 and Ap index during the observed period ($\overline{F_{10.7}}, \overline{A_p}$), and (3) keeping F10.7 constant (mean value) while Ap (raw) varied accordingly ($\overline{F_{10.7}}, A_p$), in a manner consistent with the disturbances. Fig. 6a and b shows time variations of model satellite's mean altitude, orbit decay rate, thermosphere temperature and density for SAT-BCI and SAT-BCII during 1st–31st July 2000.

The total decay is about 2.57 km for SAT-BCI and 3.67 km for SAT-BCII. The range of thermospheric temperature and density variations are 1183 – 1407 K and $2.87 \times 10^{-12} - 5.61 \times 10^{-12}$ kg/m³ respectively. Orbit decay rate for SAT-BCI increased from 63 m/day (1st July) to a peak of 113 m/day on the day of the geomagnetic event (15th July). For SAT-BCII, decay value increased from 91 to 170 m/day. In the third regime (F10.7 constant (red plot)), the decay rate for SAT-BCI increased from a mean value (dotted black line) of 82 m/day to about 111 m/day, and 118 m/day to 166 m/day for SAT-BCII.

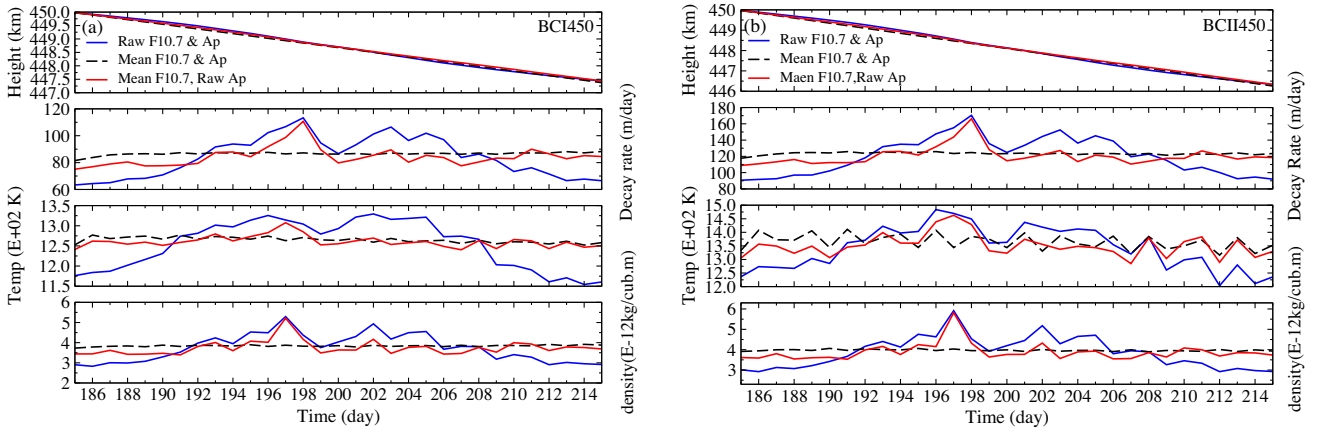


Fig. 6. Time variations of model satellite’s mean altitude, orbit decay rate, thermosphere temperature and density for SAT-BCI and SAT-BCII during 1st–31st July 2000.

This corresponds to an additional respective decay of 29 and 48 m/day from short-term geomagnetic disturbances and/or storm-induced thermospheric density perturbations and heating. The summary of variation rates of mean altitude, orbit decay rate, thermospheric temperature and density for SAT-BCI and SAT-BCII during July 2000 is shown in Table 2.

5.3. Model implementation on real satellites’ orbit

Xu et al., 2011 investigated effects of periodic variations of thermospheric density on CHAMP (~ 450 km) and GRACE (~ 500 km) satellites orbits. They showed and stated that the orbit of the satellites decayed by 70 and 20 km respectively between 2003 and 2005 due to thermospheric density drag. The Gravity field and steady-state Ocean Circulation Explorer (GOCE) satellite was launched into near-circular orbit with mean altitude 300–250 km in March 2009. GOCE mission ended in October 2013 and re-entered the atmosphere from an approximate height of 224 km on 11 November 2013 (ESA1, 2013; ESA2, 2013). We now implement and/or apply our drag model on CHAMP and GOCE decay scenarios. SAT-BCII has similar ballistic coefficient and orbit as that of CHAMP satellite; $h = 450$ km, $m_s = 522$ kg, $A_s = 0.72$ m², $C_d = 2.2$ (Hausleitner et al., 2007; Koppenwallner, 2011). The orbit and ballistic parameters used in this model for GOCE are ~ 268 km (mean height), $m_s = 1100$ kg, $A_s = 1.1$ m²,

$C_d = 3.65$ (Fehringer et al., 2008; Bruinsma and Pilinski, 2011; Koppenwallner, 2011; ESA3, 2013). In Fig. 7, we present the model decay profile of (a) CHAMP for the period 2003–2005 and (b) GOCE during 17th March 2009–21 October 2013 (before re-entry), as a function of actual solar and geomagnetic indices.

CHAMP model result show a decay of about 70.98 km (Fig. 7(a)). There is, however, an approximate 1 km increase in orbital decay when compared with CHAMP’s actual decay profile for the period. The peculiarity of GOCE trajectory is its aerodynamic design. The craft was designed to minimize air drag and torque and excludes mechanical disturbances due to the need for low flight and stability. An electric ion thruster at the back of the satellite constantly generate small forces that compensates for any drag in flight. Against this backdrop, we modeled GOCE trajectory with minimal drag force, allowing (conditioned) only 5% of the total drag force experienced by a satellite with similar ballistic coefficient at the injected height. The normal drag force on the satellite was restored (in the simulation) when the spacecraft ran out of fuel (21st October, 2013). The model mean height of GOCE in October 2013 (just before re-entry) is about 224.0487 km (Fig. 7b). The time variations of the satellites’ orbit decay rate, thermosphere temperature and density are also consistent with reported values (Koppenwallner, 2011). In Fig. 8, we present the model result of GOCE re-entry evolution between 21st October and 11th November 2013.

Table 2

Trends of time variation of mean altitude, orbit decay rate, thermosphere temperature and density for SAT-BCI and SAT-BCII (initially at $h = 450$ km) during interval of strong geomagnetic perturbations and/or storms in July 2000

	Decay (km)		Decay rate (m/day)				Temperature (K)		Density (10^{-12} kg/m ³)	
	BCI	BCII	Low BCI	Low BCII	High BCI	High BCII	Mean BCI/BCII	Mean High BCI/BCII	Mean Low BCI/BCII	Mean High BCI/BCII
$F_{10.7}, A_p$	2.57	3.67	63.36	90.68	113.30	170.39	1183.32	1407.20	2.87	5.61
$\overline{F}_{10.7}, A_p$	2.63	3.74	81.53	117.64	88.25	124.77	1284.41	1344.14	3.82	3.99
$\overline{\overline{F}}_{10.7}, A_p$	2.56	3.66	75.11	108.84	110.65	166.15	1265.09	1386.40	3.50	5.52

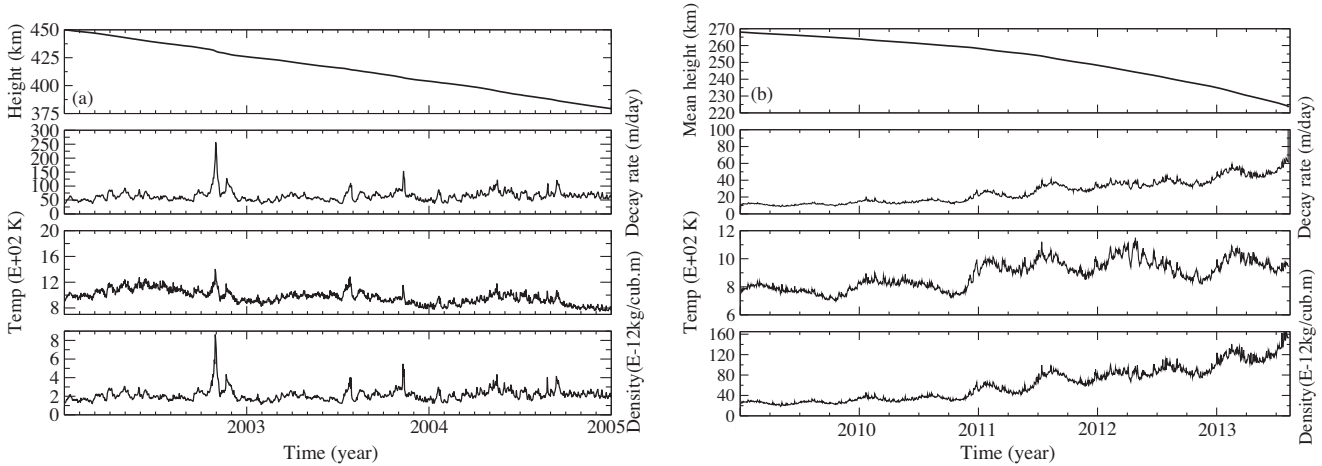


Fig. 7. Model decay profile of (a) CHAMP satellite during 2003–2005 (b) GOCE satellite during 2009–2013.

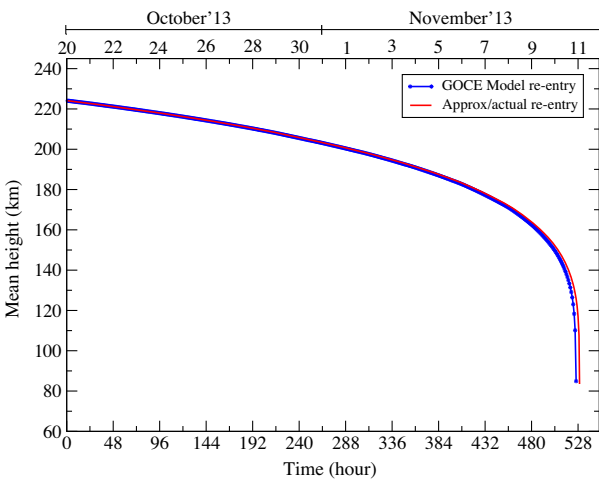


Fig. 8. Model re-entry evolution of GOCE satellite during 21st October–11 November 2013.

The model GOCE re-entry (blue curve) is compared with the approximate/actual re-entry (red curve) evolution. Model re-entry occurred about 5 h (10/11/2013, 20:00 CET) before the actual/reported re-entry (11/11/2013, 01:00 CET). The deviations in our model results are ~ 1 km for CHAMP decay profile and ~ 5 h for GOCE re-entry evolution. However, our computed/modeled values compare well with the real-time decay and/or re-entry evolution of these real satellites. In view of the computational inadequacies, this work/model is being improved for better accuracy and expanded to include application on more LEO satellite under varying space environmental conditions.

6. Conclusion

The model of atmospheric drag on the orbit of two hypothetical LEO satellites is presented in this paper. We model and compared how satellites of different ballistic coefficients respond to the effect. We investigated consequences of solar cycle variations on the orbit of the

satellites and during interval of strong geomagnetic activity, mainly results of solar forcing induced perturbations and heating of thermospheric density; driven by solar energetic events. We show dependence of orbital decay rate on the severity of both solar cycle and phase. The mean yearly decay rate during the last solar max (2000–2002) was almost twice that of current phase (2012–2014): $[48 \pm 2, 62 \pm 1 \text{ km/year}]$ and $[25 \pm 7, 31 \pm 10 \text{ km/year}]$ respectively for the model Satellites (SAT-BCI and SAT-BCII). However, depending on ballistic coefficient and nature of a solar cycle phase, a typical LEO satellite initially at $h = 450$ km could experience a decay rate of up to 41 ± 19 km per year (~ 3 km/month) during solar maximum and 11 ± 6 km per year (~ 1 km/month) during the solar minimum. Dominant CIR-induced effects during solar minimum phase could result to additional decay rate of up to 3 km/year. We showed that intervals of strong density perturbations and additional heating due to geomagnetic activity and/or storms can result in an additional 60% decay in each event. This impact could vary depending on the severity and duration of the event. In the literature similar drag effects are computed often taking average behavior. We show in our simulations the importance of taking the sequence of events into account. Two events E_1 and E_2 may produce different impacts if they occurred in a reversed sequence. Extending this logic to solar cycles, the results of a launch in a solar minimum would be different from that in a solar maximum even if both satellites survives for, say a full cycle. This is due to strong non-linearity in drag effects. This aspect and an extended application of this model to more LEO satellites and solar cycles would be reported in another paper.

Acknowledgment

VUJN acknowledges TWAS/ICTP, Trieste, Italy and S.N. Bose National Centre for TWAS-Bose research fellowship. Authors thank reviewers for their resourceful comments and suggestions.

References

- Alfonsi, L., Kavanagh, Andrew J., Amata, Ermanno, Cilliers, Pierre, Correia, Emilia, Freeman, Mervyn, Kauristie, Kirsti, Liu, Ruiyuan, Mitchell, Cathryn N., Luntama, Juha-Pekka, Zherebtsov, G.A., 2008. Probing the high latitude ionosphere from ground-based observations: the state of current knowledge and capabilities during IPY (2007–2009). *J. Atmos. Solar-Terr. Phys.* 70, 2293–2308.
- Borovsky, J.E., Denton, M.H., 2006. Differences between CME-driven storms and CIR-driven storms. *J. Geophys. Res.* 111, A07S08. <http://dx.doi.org/10.1029/2005JA011447>.
- Bounsanto, M.J., 1999. Ionospheric storms a review. *Space Sci. Rev.* 88, 563601.
- Bowman, B.R., Kent Tobiska, W., Kendra, Michael J., 2008. The thermospheric semiannual density response to solar EUV heating. *J. Atmos. Solar-Terr. Phys.* 70 (11–12), 14821496. <http://dx.doi.org/10.1016/j.jastp.2008.04.020>.
- Bruinsma, S., Pilinski, M., 2011. Drag coefficients. NADIR workshop – October 25–26.
- Bruinsma, S., Thuillier, G., Barlier, F., 2003. The DTM-2000 empirical thermosphere model with new data assimilation and constraints at lower boundary: accuracy and properties. *J. Atmos. Solar-Terr. Phys.* 65 (9), 1053–1070.
- Burns, A.G., Solomon, S.C., Qian, L., Wang, W., Emery, B.A., Wiltberger, M., Weimer, D.R., 2012. The effects of Corotating interaction region/High speed stream storms on the thermosphere and ionosphere during the last solar minimum. *J. Atmos. Solar-Terr. Phys.* 83, 79–87.
- Chen, G., Jiyao, Xu., Wang, Wenbin, Lei, Jiuhou, Burns, Alan G., 2012. A comparison of the effects of CIR- and CME-induced geomagnetic activity on thermospheric densities and spacecraft orbits: case studies. *J. Geophys. Res.* 117, A08315. <http://dx.doi.org/10.1029/2012JA017782>.
- Chobotov, V.A., 2002. *Orbital Mechanics*, third ed., AIAA Education Series. American Institute of Aeronautics Inc, Virginia, 629.4113, pp. 193–213.
- Deng, Y., Huang, Y., Solomon, S., Qian, L., Knipp, D., Weimer, D.R., Wang, J.S., 2012. Anomalously low geomagnetic energy inputs during 2008 solar minimum. *J. Geophys. Res.* 117, A09307. <http://dx.doi.org/10.1029/2012JA018039>.
- Doornbos, E., 2012. *Density and Wind Determination from Satellite Dynamics*. Thermospheric. Springer-Verlag, Berlin Heidelberg. <http://dx.doi.org/10.1007/978-3-642-25129-02>, Springer Theses.
- Doornbos, E., Klinkrad, H., 2006. Modelling of space weather effects on satellite drag. *Adv. Space Res.* 37, 12291239.
- Emmert, J.T., Picone, M., 2010. Climatology of globally averaged thermospheric mass density. *J. Geophys. Res.* 115, A09326.
- ESA1, 2013. GOCE Completes its Mission. European Space Agency.
- ESA2, 2013. GOCE Gives in to Gravity. European Space Agency.
- ESA3, 2013. GOCE Satellite. European Space Agency.
- Fehringer, M., Andre, Gerard, Lamarre, Daniel, Maeusli, Damien, 2008. GOCE: a jewel in ESA's crown. *ESA Bull.* 133, 14–23.
- Forbes, J., Bruinsma, S.L., Zhang, X., Oberheide, J., 2009. Surface-exosphere coupling due to thermal tides. *Geophys. Res. Lett.* 36 (15), L15812.
- Gopalswamy, N., 2009. Coronal mass ejections and space weather. In: *Climate and Weather of the Sun System (CAWSES)*. TERRAPUB, Tokyo, pp. p 77–118.
- Gosling, J.T., Pizzo, V.J., 1999. Formation and evolution of corotating interaction regions and their three dimensional structure. *Space Sci. Rev.* 89, 2152.
- Hagan, M., Forbes, J., 2002. Migrating and non-migrating diurnal tides in the middle and upper atmosphere excited by tropospheric latent heat release. *J. Geophys. Res.* 107 (D24), 4754.
- Hausleitner, W., Krauss, S., Stangl, G., Weingrill, J., Lichtenegger, H.I.M., Lammer, H., Khodachenko, M.L., 2007. Response of LEO satellite drag parameters to anomalies in the upper atmosphere during extreme solar events. In: *Physics of Auroral Phenomena*, Proc. XXX Annual Seminar, Kola Science Centre, Russian Academy of Science, Apatity, pp. 158–162.
- IRS Radio, 1999. & Space Services, Satellite Orbital Decay Calculations. Australian Space Weather Agency, Sydney.
- Kim, K.H., Moon, Y.J., Cho, K.S., Kim, H.D., Park, J.-Y., 2006. Atmospheric drag effects on the KOMPSAT-1 satellite during geomagnetic superstorms. *E-letter Earth Planets Space* 58, e25–e28.
- Klenzing, J., Burrell, A.G., Heelis, R.A., Huba, J.D., Pfaff, R., Simes, F., 2013. Exploring the role of ionospheric drivers during the extreme solar minimum of 2008. *Ann. Geophys.* 31, 21472156. <http://dx.doi.org/10.5194/angeo-31-2147-2013>.
- Klinkrad, H., 1996. On the use of atmosphere models in re-entry predictions. In: *Environment Modelling for Space-based Applications*, Symposium Proceedings (ESA SP-392). ESTEC Noordwijk, pp. 287–298.
- Koppenwallner, G., 2011. Satellite aerodynamics and determination of thermospheric density and wind. In: *AIP Conf. Proc.* 1333, Pacific Grove, California, p. 1307.
- Kutiev, I., Tsagouri, Ioanna, Perrone, Loredana, Pancheva, Dora, Mukhtarov, Plamen, Mikhailov, Andrei, Lastovicka, Jan, Jakowski, Norbert, Buresova, Dalia, Blanch, Estefania, Andonov, Borislav, Altadill, David, Magdaleno, Sergio, Parisi, Mario, Torta, Joan Miquel, 2013. Solar activity impact on the Earths upper atmosphere. *J. Space Weather Space Clim.* 3, A06. <http://dx.doi.org/10.1051/swsc/2013028>.
- Kwak, Y.-S., Kim, K.-H., Deng, Y., Forbes, J.M., 2011. Response of thermosphere density to changes in interplanetary magnetic field sector polarity. *J. Geophys. Res.* 116, A11316.
- Lei, J., Thayer, J.P., Forbes, J.M., Sutton, E.K., Nerem, R.S., Temmer, M., Veronig, A.M., 2008. Global thermospheric density variations caused by high-speed solar wind streams during the declining phase of solar cycle 23. *J. Geophys. Res.* 113 (A11). <http://dx.doi.org/10.1029/2008JA013433>.
- Lei, J., Guangming Chen, Jiyao Xu, Xiankang Dou, 2013. Impact of Solar Forcing on Thermospheric Densities and Spacecraft Orbits from CHAMP and GRACE, Intech open science, doi: 10.5772/56599.
- Leonard, J.M., Forbes, J., Born, G.H., 2012. Impact of tidal density variability on orbital and reentry predictions. *Space Weather* 10, S12003. <http://dx.doi.org/10.1029/2012SW000842>.
- Lindsay, G.M., Russell, C.T., Luhmann, J.G., 1994. On the sources of interplanetary shocks at 0.72 AU. *J. Geophys. Res.* 99, 11–17.
- Liu, J., Liu, Libo, Zhao, Biqiang, Thayer, Jeffrey P., Lei, Jiuhou, McPherron, Robert L., 2012. Superposed epoch analyses of thermospheric response to CIRs: solar cycle and seasonal dependencies. *J. Geophys. Res.* 117, A00L10. <http://dx.doi.org/10.1029/2011JA017315>.
- Liu, H., Hirano, T., Watanabe, S., 2013. Empirical model of the thermospheric mass density based on CHAMP satellite observation. *J. Geophys. Res. Space Phys.* 118, 843848. <http://dx.doi.org/10.1002/jgra.50144>.
- NOAA-1, Solar Particle and Geomagnetic Indices. <www.swpc.noaa.gov/ftpmenu/indices/oldindices.html> (Retrieved March 2011).
- NOAA-2, Predicted Sunspot Number And Radio Flux Values With Expected Ranges. <www.swpc.noaa.gov/ftppdir/weekly/Predict.txt> (Retrieved March 2011).
- NOAA, 2006. Satellites and space weather. <www.swpc.noaa.gov/info/satellites.html>.
- NOAA-3, Solar Proton Events Affecting the Earth Environment. NOAA Space Weather Prediction Center. <www.swpc.noaa.gov/ftppdir/indices/SPE.txt> (Retrieved March 2011).
- Nwankwo, V.U.J., Chakrabarti, K.S., 2014. Theoretical modeling of drag force impact on a model international space station (ISS) during variation of solar activity. *Trans. JSASS Aerosp. Technol. Jpn.* 12, 47–53.
- Nwankwo, V.U.J., Chakrabarti, S.K., 2015. Analysis of planetary and solar induced perturbations on trans-Martian trajectory of Mars missions before and after Mars orbit insertion. *Indian J. Phys.*

- Oberheide, J., Forbes, J., Husler, K., Wu, Q., Bruinsma, S.L., 2009. Tropospheric tides from 80–400 km: propagation, interannual variability and solar cycle effects. *J. Geophys. Res.* 114, D00105.
- Pardini, C., Tobiska, K., Luciano, A., 2004. Analysis of the orbital decay of spherical satellites using different solar flux proxies and atmospheric density models. *Adv. Space Res.* 37 (2), 392–400.
- Picone, J.M., Hedin, A.E., Drob, D.P., Aikin, A.C., 2002. NRLMSISE-00 empirical model of the atmosphere: Statistical comparisons and scientific issues. *J. Geophys. Res.* 107 (A12), 1468.
- Polcastri, L.A., Joseph, M., Simons, 2003. Implementing the MSIS atmospheric density model in OCEAN, AAS 03-166.
- Rhoden, E.A., Forbes, J.M., Marcos, F.A., 2000. The influence of geomagnetic and solar variabilities on lower thermosphere density. *J. Atmos. Solar-Terr. Phys.* 62, 999–1013.
- Richardson, I.G., Cliver, E.W., Cane, H.V., 2001. Sources of geomagnetic storms for solar minimum and maximum conditions during 1972–2000. *Geophys. Res. Lett.* 28 (13), 2569–2572.
- SOHO/LASCO, SOHO LASCO CME CATALOG. cdaw.gsfc.nasa.gov/CMElist (Retrieved March 2011).
- Solomon, S.C., Burns, Alan G., Emery, Barbara A., Mlynczak, Martin G., Qian, Liying, Wang, Wenbin, Weimer, Daniel R., Wiltberger, Michael, 2012. Modeling studies of the impact of high-speed streams and co-rotating interaction regions on the thermosphere-ionosphere. *J. Geophys. Res.* 117, A00L11.
- Storz, Mark F., Bowman, Bruce R., Branson, Major James I., Casali, Stephen J., Kent Tobiska, W., 2005. High accuracy satellite drag model (HASDM). *Adv. Space Res.* 36, 24972505.
- Storz, M.F., Bruce, R., Bowman, Major James, Branson, I., Casali, Stephen J., Kent Tobiska, W., 2005. High accuracy satellite drag model (HASDM). *Adv. Space Res.* 36, 24972505.
- Sutton, E.K., Forbes, J.M., Nerem, R.S., 2005. Global thermospheric neutral density and wind response to the severe 2003 geomagnetic storms from CHAMP accelerometer data. *J. Geophys. Res.* 110 (A9).
- Tsurutani, B.T., Gonzalez, Alicia L.C., Gonzalez, Walter D., Guarnieri, Fernando L., Gopalswamy, Nat, Grande, Manuel, Kamide, Yohsuke, Kasahara, Yoshiya, Lu, Gang, Mann, Ian, McPherron, Robert, Soraas, Finn, Vasylunas, Vytenis, 2006. Corotating solar wind streams and recurrent geomagnetic activity: a review. *J. Geophys. Res.: Space Phys.* 111, A07S01. <http://dx.doi.org/10.1029/2005JA011273>.
- Walterscheid, R.L., 1989. Solar cycle effects on the upper atmosphere – implications for satellite drag. *J. Spacecraft Rockets* 26 (6), 439–444. <http://dx.doi.org/10.2514/3.26089>.
- Weigel, R.S., 2010. Solar wind density influence on geomagnetic storm intensity. *J. Geophys. Res.* 115, A09201. <http://dx.doi.org/10.1029/2009JA015062>.
- Weigel, R.S., Baker, Daniel N., Joshua Rigler, E., Vassiliadis, Dimitris, 2004. Predictability of large geomagnetic disturbances based on solar wind conditions. *IEEE Trans. Plasma Sci.* 32 (4), 1506–1510.
- Wertz, J., Larson, W.J., 1999. *Space Mission Analysis and Design*, third ed. Kluwer Academy, El Segundo, Calif, pp 145.
- Woods, T., Loren W. Acton, Scott Bailey, Frank Eparvierl, Howard Garcia, Darrell Judges, Judith Lean, John T. Mariska, Don McMullin, Gerhard Schmidtke, Stanley C. Solomon, Kent Tobiska, W., Harry P. Warrenlo, Rodney Viereck, 2004. Solar extreme ultraviolet and x-ray irradiance variations. Solar variability and its effects on climate, Geophysical Monograph 141, American Geophysical Union, doi:10.1029/141GM11.
- Xu, J., Wang, W., Lei, J., Sutton, E.K., Chen, G., 2011. The effect of periodic variations of thermospheric density on CHAMP and GRACE orbits. *J. Geophys. Res. (Space Phys.)* 116 (A15), 2315. <http://dx.doi.org/10.1029/2010JA015995>.
- Zhang, X., Forbes, J., Hagan, 2010. Longitudinal variation of tides in the MLT region: 1. Tides driven by tropospheric net radiative heating. *J. Geophys. Res.* 115, A06316.

Further reading

- Bowman, B., Pilinski, M., 2011. Drag coefficients. NADIR workshop – October 25–26.

Analysis of planetary and solar-induced perturbations on trans-Martian trajectory of Mars missions before and after Mars orbit insertion

V U J Nwankwo¹ and S K Chakrabarti^{1,2*}

¹S N Bose National Centre for Basic Sciences, Kolkata 700 098, West Bengal, India

²Indian Center for Space Physics, Kolkata 700 084, West Bengal, India

Received: 19 February 2015 / Accepted: 16 April 2015 / Published online: 28 May 2015

Abstract: Interplanetary missions are susceptible to gravitational and nongravitational perturbing forces at every trajectory phase, assuming, of course, that the man made rockets and thrusters work as expected. These forces are mainly due to planetary and solar-forcing-induced perturbations during geocentric, heliocentric and Martian trajectories, and before orbit insertion. In this study, we review and/or analyze Mars orbiters mission associated perturbing forces and their possible impacts before Mars Orbit Insertion viz Earth's oblateness, Third body (solar and lunar), solar radiation pressure, solar energetic radiation environment and atmospheric drag forces. We also model the significance of atmospheric drag force on Mangalyaan Mars orbiter mission, as a function of appropriate space environmental parameters during its 28 days in Earth's orbit (around and during perigee passage), 300 days of heliocentric and 100 days of Martian trajectory. We have found that for a total perigee height boost of about 250 km, the cumulative orbit decay can be approximately 720 m. The approximate altitude variation could be up to 158 m with respect to the sun during 300 days of interplanetary journey toward Mars. After Mars orbit insertion, the total decay experienced by the spacecraft could be up to 701 m with decay rate of up to 9 m/day during 100 days of Martian trajectory, based on Mars–Earth atmosphere density ratio. In principle, resulting deviations due to perturbing forces are usually corrected before Earth departure (and/or Mars orbit insertion) and are beyond the scope of this work. However, the knowledge is important for mission planning, design, implementation and situational awareness. We find that the deviations are small enough and should be correctable.

Keywords: Dynamics of atmosphere; Interplanetary physics; Satellites; Space weather

PACS Nos.: 92.60.–e; 96.50.–e; 95.40.+s; 94.05.Sd

1. Introduction

Driven by the quest for the possibility of life in Mars, clues to the evolution of our solar system, fascination with the chemistry, geology and meteorology of another planets, the National Aeronautics and Space Administration (NASA) has launched the first (successful) Mars mission (Mars orbiter and lander—Viking 1) in August 1975, which has arrived near Mars on the June 19 and has landed on July 20, 1976 [1]. While Viking 1 mission has operated between June 1975 and 1980, more than four other orbiter and/or lander missions have also made it to the 'red planet' within

about three decades. Current active Mars missions include Mars Odyssey (NASA/USA, launched in April 2001 with arrival in October 2001 [2]), Mars Express and Beagle 2 (ESA/Europe, launched in June 2003 with arrival in December 2003 [3]), Mars Exploration Rover Opportunity (NASA/USA, launched in July 2003 with arrival in January 2004 [4]), Mars Reconnaissance Orbiter (NASA/USA, launched in August 2005 with arrival in March 2006 [5]) and Curiosity Mars Science Laboratory (NASA/USA, launched in November 2011 with arrival in August 2012). Russia, the Soviet Union, had also recorded a 'short-lived' success in their past attempts with MARS 2, 3, 5 and 6 missions (among others). The Indian Space Research Organisation (ISRO) in her first ever attempt has launched an interplanetary (Mars) mission on November 5, 2013. The country's Mars orbiter mission (also known as

*Corresponding author, E-mail: chakraba@bose.res.in

Mangalyaan) orbited the Earth between November 5, 2013 and December 1, 2013, basically building up the required velocity ($+\Delta V$), which is needed to escape the Earth's sphere of influence (ESOI). It has begun a 300-day journey to Mars on December 1, 2013 with successful Mars orbital insertion on September 24, 2014.

Quite a large number of attempts have been made in the past, toward interplanetary missions (IPMs), but only a few successes have been recorded so far. It has been estimated that more than half of the attempted missions to explore the 'red planet' (Mars) failed [6]. However, instructive and resourceful lessons have been learned from each failure, which has made subsequent attempts more successful [1, 7]. Although IPM attempts date back to the 1960s, more than half of successful ones have been launched within the last two decades. The high failure rate in IPM may be associated with planetary and solar-induced perturbations (after launch) among other causality, especially during transit and arrival to their destined planet. High precision and accuracy in calculations are important to successful design and implementation of interplanetary missions. Very small and apparently insignificant parametric fluctuations (in some cases) due to perturbing forces may introduce sporadic errors that can hamper the success of such IPMs. Other potential causes of IPMs failure include under- and/or over-performance of thrusters, miscalculations in firing directions and Liquid Apogee Motor (LAM) alignments, failure of launch vehicles, communication/radio failures and nature/mode of entry [6–9]. Mangalyaan is not an exception to these IPM-associated challenges.

This work is a pointer to some sources of fluctuations that may arise due to planetary and solar-forcing-induced perturbations. We review some IPM-associated perturbing forces with reference to Mangalyaan spacecraft, based on established theory. In detail, we also analyze (by model) and investigate the significance of atmospheric drag force on Mangalyaan spacecraft, as a function of space environmental parameters during geocentric (28 days in Earth's orbit), heliocentric (300 days in the sun's orbit) and Martian trajectory (assumed to be up to 100 days in Mars orbit (after MOI), in this paper for concreteness). Atmospheric drag causes change in orbital parameters making it difficult to identify and track satellites and other space objects, maneuvering and predicting lifetime and reentry [10–13]. In principle, deviations due to associated perturbations under consideration (e.g., Decay, Solar Radiation Pressure, Third body) are corrected before Earth departure and/or MOI. Such adjustments are beyond the scope of this work. However, the knowledge of their relative significance is

important to mission planning, design, implementation and situational awareness.

2. Interplanetary trajectories and Mars mission system engineering challenges

Interplanetary mission requires a succession of transfer of a satellite from one orbit to another by means of a change of velocity (ΔV) as the system moves through successive phase mission plan to a destined planet. For a Mars-bound spacecraft (from Earth), three-phase trajectory is required—geocentric, heliocentric and Martian. In this paper, our emphasis will be on Mars interplanetary missions. One common type of orbit transfers employed in interplanetary missions is the Hohmann transfer or trajectory. The Hohmann transfer is considered to be the minimum two-impulse transfer between coplanar circular orbits [14, 15]. This type of transfer requires elliptical paths that are tangent to the launch and arrival orbits. Three main groups of trajectories can evolve from the Hohmann transfer—staying tangential to the larger orbit but intersecting the smaller one, intersecting the larger orbit and staying tangential to the smaller one and intersecting both orbits [15]. The equation of Earth departure, heliocentric and Mars arrival trajectory velocities of a Mars interplanetary mission is given by the following:

(i) Earth departure velocity

$$v_{bo} = \sqrt{2 \left[\frac{\mu_e}{R_e + h} + E_e \right]} \quad (1)$$

where v_{bo} is the burnout velocity, R_e is the equatorial radius of Earth, h is the altitude at injection, μ_e is the gravitational parameter of the Earth and E_e is the energy of escape hyperbola.

(ii) Heliocentric trajectory velocity at perihelion is

$$v_p = \sqrt{\mu_s \left(\frac{2}{r_e} - \frac{1}{a} \right)} \quad (2)$$

The transfer orbit at apoapsis is

$$v_a = \sqrt{\mu_s \left(\frac{2}{r_m} - \frac{1}{a} \right)} \quad (3)$$

The velocity at exit from the Earth's sphere of influence is

$$v_\infty = v_p - v_e \quad (4)$$

where r_m is the radius of Mars, r_e is the radius of the Earth at 1 A.U., a is the apoapsis ($r_e + r_m/2$) = 1.262 A.U., μ_s is

the gravitational parameter of the sun, v_e is the mean velocity in Earth's orbit.

(iii) Mars arrival phase: The retro velocity at Mars surface is

$$v_{\text{retro}} = \sqrt{2 \left(\frac{\mu_m}{R_m} + E_m \right)} \quad (5)$$

where μ_m is the gravitational parameter of Mars, R_m is the equatorial radius of Mars and E_m is the energy of the hyperbolic orbit at Mars [15]. E_m is given by Eq. (6):

$$E_m = \frac{v_\infty^2}{2} = \frac{(v_m - v_a)}{2} \quad (6)$$

Depending on the type of mission (orbiter or lander), Mars orbiter spacecrafts begin their missions after successful orbit insertion, mainly exploration of Mars surface and/or atmosphere. Mars lander missions (e.g., Curiosity Rover) require entry, descent and subsequent landing in the red planet. This is yet another challenging phase. Braun and Manning [16] in their study has pointed out some system challenges associated with Mars exploration entry, descent, and landing emanating from three sources: (i) an atmosphere which is thick enough to create substantial heating, but not low enough to reduce terminal descent velocity, (ii) a surface environment of complex rocks, craters, dusts and terrain patterns and (iii) the cost of replicating a Mars-relevant environment for space flight qualification of new entry, descent and landing technologies [16]. In our present situation, we would be interested in shrinking of the orbits due to repeated passage of Mangalyaan at the perigee, interplanetary phase and periapsis once in the Martian orbit.

3. Mangalyaan Mars orbiter mission at a glance

The Mangalyaan MOM is launched aboard Polar Satellite Launcher Vehicle PSLV-XL. At delivery, the observed initial perigee height is about 248.4 km, apogee 23,500 km and inclination = 19.2°, where it has used its own propulsion system to insert itself into its trans-Martian interplanetary trajectory within a period of about 4 weeks. The space probe has a mass of about 1337 kg (with a dry mass of about 475 kg, including five payloads of about 15 kg) and carries a fuel of about 852 kg. It has similar core structure and spacecraft system and mission largely based on the Chandrayaan-1 Moon Orbiter. Mangalyaan is equipped with a single deployable solar array that consists of three panels (each being 1.4 × 1.8 m in size) with yoke and drive mechanism, capable of providing up to 840 Watts of electrical power at Mars. It is fed to a power distribution unit that provides power to the various systems and payloads and also controls the state of charge of a 36-amp-h battery for night passes. Other compositions of the MOM include

bi-propellant main propulsion system and an altitude control system, four reaction wheels, a 2.2-m-diameter High Gain Antenna and a number of other High Technological equipment that meets critical mission operations and stringent requirements. The 15-kg payload consists of a suite of five science instruments that equip MOM for its distinct mission objectives—Lyman Alpha Photometer (LAP), Martian Exospheric Neutral Composition Analyzer (MENCA), Mars Colour Camera (MCC), Methane Sensor for Mars (MSM) and Thermal Infrared Imaging System (TIS) (also see [17, 18]). Mangalyaan is saddled with the mission to explore Mars surface feature, morphology, topography, mineralogy and Martian atmosphere. On a specific mission, it will carry out the search for methane on the 'red planet.' The pictorial representation of the deployed and dissembled view of Mangalyaan is shown in Fig. 1(a) and 1(b).

4. Mangalyaan mission plan and the trans-Martian flight profile

After delivery to an initial elliptical orbit of 248.4 km (perigee, r_p) by 23,500 km (apogee, r_a) and inclination of about 19.2°, the Mars probe has to enter three phases of mission plan to reach Mars—(i) the geocentric phase, (ii) the heliocentric phase and (iii) the Mars-centric (areocentric) phase. The three phases required that MOM fires its liquid apogee motor (LAM) six times at a given interval when passing perigee, to gradually increase the apogee of the orbit and consequently moves through the phases up until departure to Mars. The trajectory design is shown in Fig. 2(a). At the geocentric phase, the spacecraft with six engine burns gradually maneuver into a 'depart' hyperbolic trajectory with which it escapes from the Earth's sphere of influence and with orbital velocity boost. Beyond the Earth's sphere of influence, the perturbing force on the orbiter is due to the sun. Between November 5, 2013 and November 16, 2013, the apogee has been raised to approximately 192,874 km from the initial 23,500 km after five consecutive raising maneuvers. In the computation which follows, we have assumed a corresponding perigee rises to approximately 500 km from an initial of about 248.4 km (a total incremental height of 250 km) during velocity boost (+ ΔV). The maneuvered apogee heights after each velocity boost are shown in Fig. 2(b).

This work has been started shortly after the launch of the spacecraft with continuous update until MOI. It has departed Earth's orbit and tangentially (to its orbit) encountered Mars orbit, as shown in Fig. 2(a). At the areocentric orbital phase, the spacecraft has reached the Mars sphere of influence in a hyperbolic trajectory on September 24, 2014. At closest approach to Mars, it is captured into the planned orbit around Mars by imparting ΔV retro (also Mars orbit

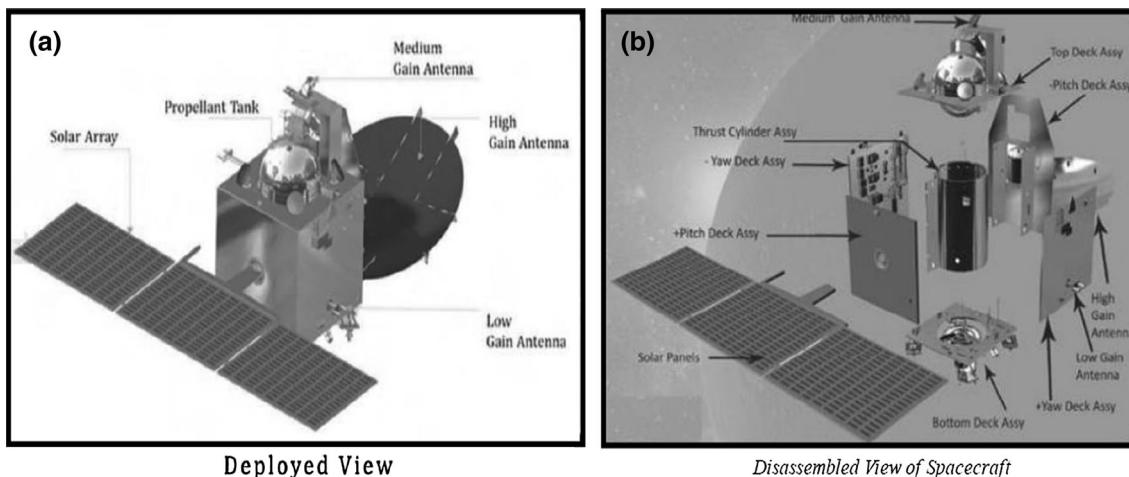


Fig. 1 (a) Deployed view of Mangalyaan spacecraft, (b) the disassembled view [17]

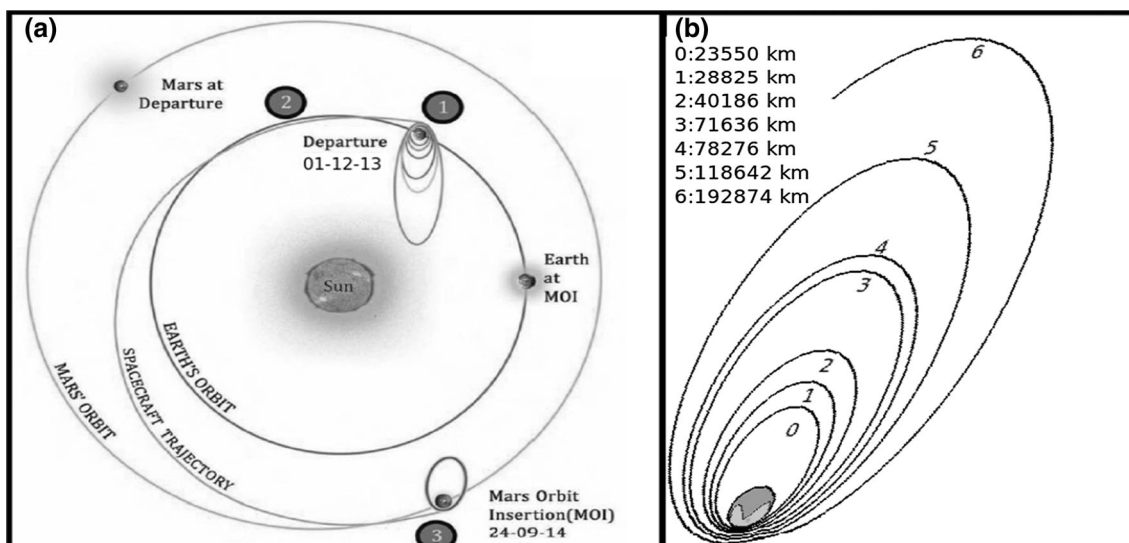


Fig. 2 (a) Planned trans-Martian trajectory of Mangalyaan spacecraft, (b) maneuvered orbits (heights) after consecutive velocity boost (adapted from [17])

Insertion) maneuver [17]. Figure 3 shows planned ‘Mangalyaan’ trajectory in Martian orbit.

5. Procedure

In this work, we have analyzed IPM-associated perturbing forces and their possible impact on trans-Martian trajectory and/or mission (before MOI), based on established theory. In Sect. 6.4, we have computed orbital decay of ‘Mangalyaan’ due to atmospheric drag during geocentric, heliocentric and Martian phase trajectories. We have assumed that drag effect around and during apogee passage is negligible during geocentric trajectory because of the large distance between the spacecraft and the Earth. We have computed drag force impact on the spacecraft as a function

of thermospheric density and space environmental parameters around and during the perigee passage for 28 days in Earth’s orbit, 300 days heliocentric trajectory and 100 days of Martian orbit trajectory. The elliptic orbit geometric analysis of the spacecraft in Earth and Martian orbit at perigee distances for atmospheric density and drag analysis is given in Sect. 6.4.3.

5.1. Mangalyaan orbital parameters required for our study

The effective exposed area of the spacecraft (in the direction of motion) is critical to atmospheric drag force. We have estimated this parameter from the satellite’s main-frame elements and/or specifications. Hence, we have considered three parts of relative importance—the solar

MOI Epoch	: 24-09-2014, 02:34
Periapsis	: 365.3 km
Apo-apsis	: 80000 km
Inclination	: 150.0°
AOP	: 203.5°
RAAN	: 61.4°
Period	: 76.72 hr
Sun Elevation	: 6.8°

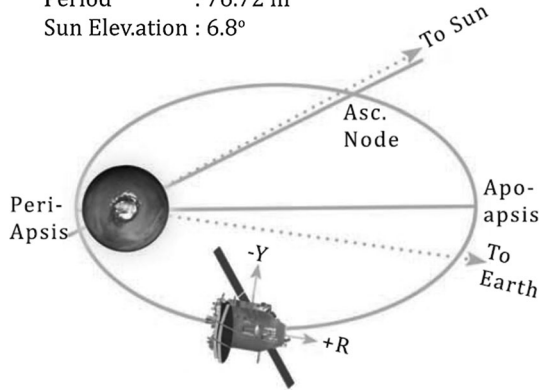


Fig. 3 Planned orbital parameters and trajectory of Mangalyaan spacecraft

panels, the Yaw and Pitch deck assembly and the top and bottom deck assembly. The dissembled view of the spacecraft is shown in Fig. 1b, indicating the mainframe view. For simplicity, each of the deck assembly is assumed to be square-shaped of approximately 3.34 m². It is generally the case that the solar panel wings of most satellites are usually designed to constantly adjust to maintain an optimum amount of battery charging and minimize frontal area projected to the ram direction, thereby minimizing the drag (which also saves propellant) [19]. We, therefore, have assumed the projected surface area (during its trajectory) to be about 5.04 m². This value may change due to solar panel directional changes, which are usually offset with respect to the sun direction [20].

6. Analysis of perturbations associated with mangalyaan MOM trajectory

Space probes must be weather-strong perturbing forces during their mission in space to survive. The trans-Martian trajectory and flight profile of IPM has been explained in Sects. 2 and 4. In general, IPMs experience gravitational perturbing force, mainly solar/lunar gravitational attractions and Earth's oblateness (J_2) and its triaxiality and nongravitational force such as atmospheric drag, solar radiation pressure and/or environment, outgassing and tidal effects [15]. The forces that influence the trajectory of the mission vary from one phase of the trajectory to another, and the probability and/or extent of these perturbation forces driven impacts may also be affected by factors such as phase of the 11-year solar cycle, nature of the spacecraft

orbit, local time and position of the satellite relative to Earth–Sun direction [21]. The induced variations (by perturbing forces) on the orbital elements of the system may be secular, short-period or long-period, or a combination of such variations. Secular variations constitute a linear variation in the element. Short-period variations represent periodic variations with a period less than or equal to the orbital period and long-period variations with a period greater than the orbital period [9]. We have analyzed some of the associated orbit perturbing forces on the orbit of MOM during geocentric, heliocentric and Martian trajectories. The general form of motion and perturbations associated with satellite trajectory is given by Eq. (7):

$$\frac{d^2 r}{dt^2} = -\frac{\mu}{r^3} \bar{r} + a_p \quad (7)$$

where a_p is the sum of acceleration caused by perturbation forces. The perturbing acceleration and/or force may be gravitational or nongravitational (as mentioned earlier).

In general, the perturbing acceleration a_p of a satellite due to a perturbing body having a mass M_p and gravitational parameter is given by the equation:

$$a_p = \mu_p \sqrt{(R.R)} \quad (8)$$

where

$$R = \frac{r_{sp}}{r_{sp}^3} - \frac{r_p}{r_p^3}$$

where r_{sp} is the distance between the satellite and the ‘perturber’ and r_p is the distance of the perturber from the planet. Expressions that provide approximate average rates of change of orbital elements for a single disturbing body can be found in [22, 23]. The relative magnitudes of some of the sources of perturbations acting upon an Earth-orbiting spacecraft are illustrated in Fig. 4. For each effect, the logarithm of the disturbing acceleration, normalized to 1 g, is shown as a function of altitude. Clearly, the effect of the drag force of the earth becomes very weak near the apogee of the earth orbit, but important near the perigee.

6.1. Earth's oblateness (J_2) effects

Mangalyaan, like any other interplanetary mission, may experience effects of Earth's oblateness (J_2) during the first 28 days, especially at the altitude (height) around the perigee [9, 15, 22, 23]. This is mainly an off-center gravitational pull due to Earth's equatorial bulge. The principal effects of the J_2 zonal harmonic or Earth oblateness are secular motions of the node (Ω) and perigee (ω) of an orbit. This introduces a force component toward the equator. The resultant acceleration causes the satellite to reach the equator (node) short of the crossing point for a spherical Earth [15]. This effect becomes less important

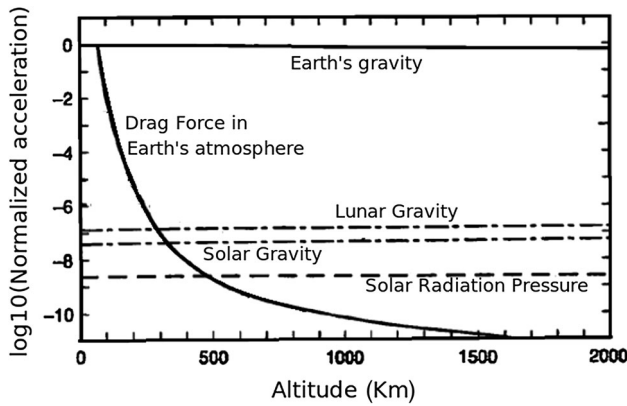


Fig. 4 Relative magnitudes of main sources of perturbation acting upon an Earth-orbiting spacecraft (Adapted from [9])

with increasing perigee distance from the Earth, at which solar and lunar gravitational perturbations become significant, especially at or around the apogee height. The only effect to compete with these gravity-induced effects is aerodynamic drag [9]. The effects of oblateness on the right ascension of the ascending node, argument of pericentron and mean anomaly were calculated from the prescriptions given in [23, 24].

6.2. Third-body perturbations

There is a significant gravitational pull from the sun and moon (solar and lunar) especially around and during the apogee passage, which increases as it builds up both velocity and altitude. The gravitational forces of the sun and moon (and other bodies in the solar system) cause periodic variations of most of the orbital elements. The right ascension of the ascending node, argument of perigee and mean anomaly experiences secular variations [9, 22, 23, 25]. These secular variations arise from a ‘spinning’ (gyroscopic) precession of the orbit about the ecliptic pole. The relative magnitude of solar and lunar perturbations acting upon an Earth-orbiting spacecraft is shown in Fig. 4.

6.3. Solar radiation pressure (SRP)

SRP on satellites is due to the impingement and absorption, and reflection of photons from the sun on the surface of a satellite including on the solar panels. The main effect of this phenomenon is a change in the eccentricity and longitude of perigee. The extent of variation of these elements depends on the effective area, surface reflection and inverse of satellite’s mass [15, 26]. The effects caused by solar radiation pressure exceed that of atmospheric drag at altitudes above 900 km, as shown in Fig. 4. The changes in perigee height induced by SRP can have significant effects on satellite lifetime [15]. The perturbing acceleration of a

satellite due to SRP-induced effects can be computed from Eq. (9) [26]:

$$\vec{a}_{\text{srp}} = -\rho_{\text{sr}} \frac{C_r A_{\text{sun}}}{m} \frac{\vec{r}_{\text{sat-sun}}}{r_{\text{sat-sun}}} \quad (9)$$

where ρ_{sr} is the incoming pressure which depends on the time of the year and the intensity of the solar output. It is derived from the incoming solar flux and values of about 1358–1373 W/m². C_r is the coefficient of reflectivity. It depends on the absorptive properties of the material and thus the susceptibility to incoming solar radiation. A_{sun} is the cross-sectional area, which changes constantly (without altitude control). It can vary by up to a factor of 10 or more depending on satellite configuration. m is the mass of the satellite. Although m is usually constant but can be influenced by factors such as thrusting and ablation. $r_{\text{sat-sun}}$ is the orientation of the satellite-sun vector. Detail equations and derivation of variations in Keplerian parameters can be found in [27–29]. We have, therefore, not repeated the derivations here.

6.4. Atmospheric drag force effect

The Mangalyaan is susceptible to significant atmospheric drag force around and during the apogee passage in Earth orbit (geocentric orbit). This effect is insignificant in heliocentric orbit due to the large distance of the spacecraft from the sun and its transit origin (the Earth). In Martian orbit (and atmosphere), drag effect is important but much less compared to that in Earth orbit (which, of course, depends on the type of orbit), especially on a long-term trajectory profile. Mangalyaan would experience significant drag around the periapsis (365.3 km) over time in its areocentric orbit. We, therefore, investigate the significance of these effects at each trajectory phase.

Atmospheric drag on low Earth-orbiting satellites (>1000 km) is primarily caused by solar-forcing-induced variations in thermospheric density profile. Energetic particles (and EM radiations) emitted from the sun during solar energetic events (e.g., solar wind streams, coronal mass ejections, solar flares) are subsequently deposited in the upper atmosphere [30, 31]. The upper atmospheres heat up and expand as a consequence and alter (change) thermosphere density profile, leading to accelerated drag on satellites [31–33]. Atmospheric drag, therefore, varies in direct proportion with atmospheric density. The prediction of the lifetime, reentry and/or computation of drag on low Earth orbit satellites (LEOSs) largely depend on a good knowledge of the variations of thermospheric densities, which is an important space environmental parameter for satellite operations in near-Earth space [34, 35]. Although this quantity is not precisely known at any given instant, but many empirical atmospheric models have been

developed and more are being developed, with increasing sophistication and good approximation [36–40]. We use one such model, the *NRLMSISE-00* empirical atmospheric model, in our drag model for a good representation of the space weather condition under which this space system traverses. Atmospheric drag experienced by a satellite at perigee can significantly lower the apogee, causing the orbit to become more and more circular, until the entire orbit is at the perigee altitude. This situation can result to satellite reentry [15, 41]. Detailed analysis and/or computation of drag force impact on Earth-orbiting satellites can be found in our earlier works [32, 33]. In the present circumstance, the earth orbit is not the reference, but the Martian orbit is expected to slowly circularize and MOM may crash onto Mars after a few tens of years.

6.4.1. Computation of satellite orbital decay due to atmospheric drag

To compute the actual earth orbital decay during the first month, the *NRLMSISE-00* empirical atmospheric model into our drag model has been incorporated. We have analyzed the drag effects due to space environmental perturbations on the trajectory of Mangalyaan satellite. We have assumed the satellite having a projected surface area of 5.04 m², a mass of 1337 kg and orbiting the Earth at an initial injected elliptical orbit of radius 250 km perigee by 23,500 km. We have chosen a spherical polar coordinate system (r, ϕ) having origin $r = 0$ at the center of the Earth and assume that the satellite always remains in the same plane (i.e., $\theta = \text{constant}$). The effects of the drag force have been computed from two sets of equations. The first set consists of four coupled differential equations represented by Eq. (10) [32, 33]:

$$\begin{aligned} \dot{v}_r &= -\frac{GM_e}{r^2} + r\dot{\phi}^2, & \dot{r} &= v_r, \\ \ddot{\phi} &= -\frac{1}{2}r\dot{\phi}^2\frac{A_s C_d}{m_s}, & \dot{\phi} &= v_\phi/r \end{aligned} \quad (10)$$

where v_r and v_ϕ are the radial and tangential velocity components. G is the gravitational constant, M_e is the mass of the Earth, r is the instantaneous radius of the orbit, ρ is the atmospheric density, A_s is the omni-directional projected area of the satellite, m_s is the mass of the satellite and C_d the drag coefficient at an altitude of r . The four differential equations have been solved to obtain instantaneous positions and velocity components of the satellite in an orbit. To measure the decay of the orbital radius per orbit, we assume that the energy is constant per orbit. Incorporating the solution of orbit semimajor axis decay rate for near-circular orbit [15], we compute drag impact on the model Mangalyaan satellite under varying space weather condition while tracking its position and

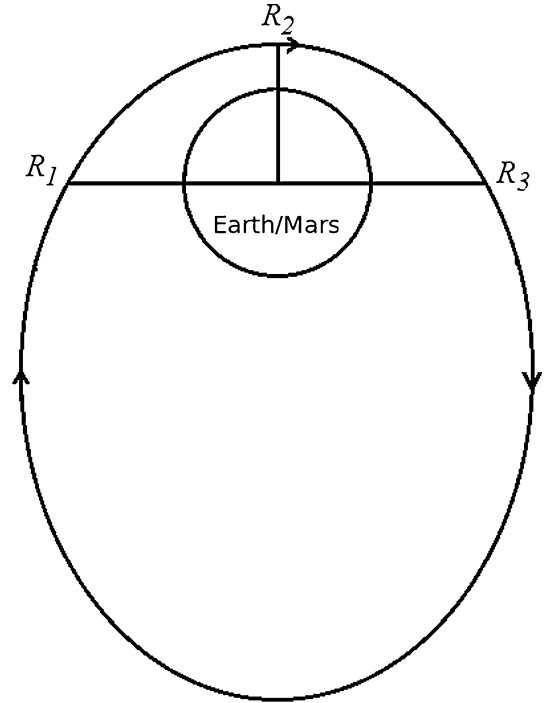


Fig. 5 Region of the orbit R_1 to R_3 where the drag effects have been considered, while the spacecraft is in Earth and Martian orbits

time by the tangential component parameters. Computations have been done using differential equation of changes in the mean radius of the satellite orbit per revolution (MRPR) [12, 22, 31, 34].

$$\frac{dr}{dt} = -\rho \frac{A_s C_d}{m_s} \sqrt{GM_e r} \quad (11)$$

6.4.2. Heliocentric phase trajectory

We have assumed a Hohmann-transfer heliocentric trajectory from Earth to Mars [15]. In heliocentric motion, the formulation of the above equations including the perigee and apogee velocity is with respect to the sun. The required perihelion velocity v_p and apoapsis velocity v_a at transfer orbit are given by the Eqs. (2) and (3).

6.4.3. Earth and Martian atmospheric density profile

The biggest challenge associated with computation of atmospheric drag force is the density profile of the atmosphere because it is not precisely known at any given instant. However, there are empirical atmospheric models with good approximation, such as the one used in this study. The *NRLMSISE-00* model gives outputs of altitude profiles of temperature, number densities of Helium, Oxygen (and its molecule), Nitrogen (and its molecule), Argon and Hydrogen, in equilibrium at the temperature, total mass (atmosphere) density and the number density of

a high-altitude ‘anomalous’ oxygen component of total mass density that is not in thermal equilibrium at the temperature $T(z)$. This model is mainly developed for the Earth’s atmosphere. Although Mars is similar to Earth in many ways, but their atmospheric constituents and/or conditions are not the same. For instance, the percentage composition of carbon dioxide and nitrogen in Martian atmosphere is about 93 and 2.7 %, while that of Earth is less than 1 and 78 %, respectively. In this analysis, without strict consideration for individual constituent of Martian atmosphere, we assume that the total mass density of Mars atmosphere is only one percent (1 %) that of Earth’s

atmosphere. Again, we assume the geometry of the ellipse orbit as shown in Fig. 5 for analysis and computation of drag around and during satellite perigee passage in Earth and Martian orbits. We neglect drag effect around and during apogee passage and compute density (and drag) at an average distance (R_m) of

$$R_m = (R_1^2 + R_2^2 + R_3^2)^{1/2}.$$

Thus, the effect of drag is assumed to be significant only during the period when the satellite moves from R_1 to R_3 .

7. Results and discussion

Mangalyaan altitude at maneuvered orbits and the corresponding computed decay rate are shown in Fig. 6. We find that the spacecraft experienced orbital decay rate of about 47.34, 47.14, 51.01, 34.12, 22.67, 18.62, 12.42 and 6.87 m/day at respective maneuvered orbits of 248.4, 252.0, 257.0, 304, 348, 380, 420 and 500 km. The triangles at specified heights indicate the number of days the spacecraft stayed in corresponding orbit before velocity boost or orbit-rising. Wherever perigee height for each orbit boost/rise (maneuvered) is not explicitly provided, reasonable values were assumed.

The rate at which the spacecraft decayed decreased with increased altitude (subsequent to orbit-rising). This is expected since the density and drag force are reduced with increase in height from the earth depending on value of solar and geomagnetic index. Although orbit-rising reduces

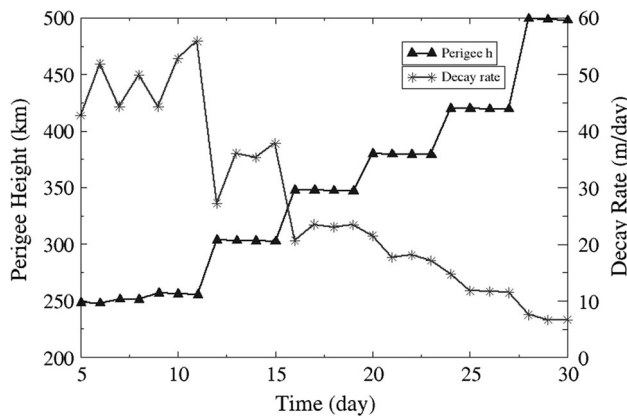
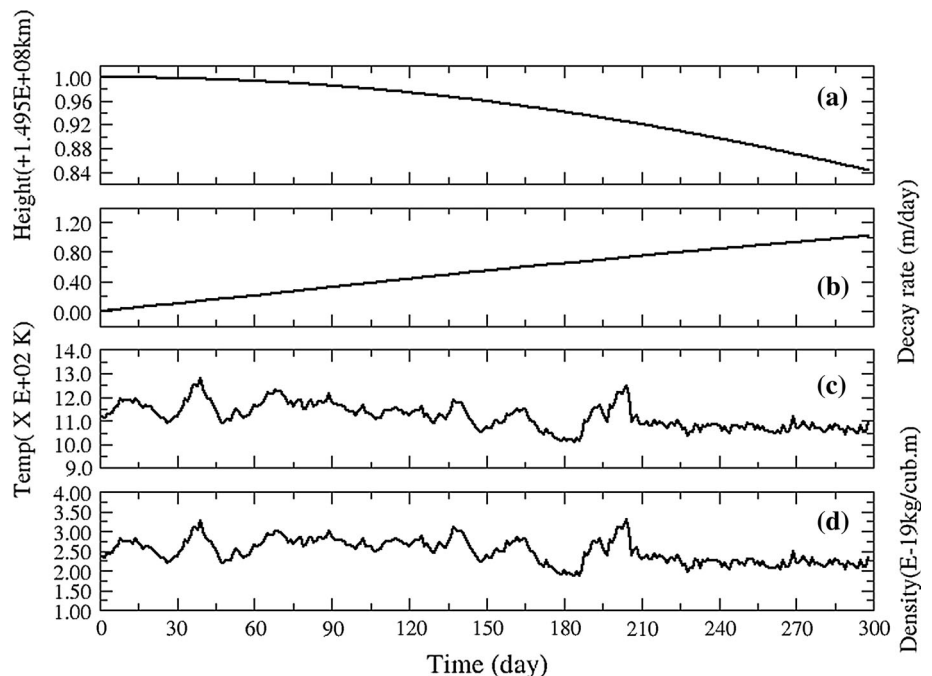


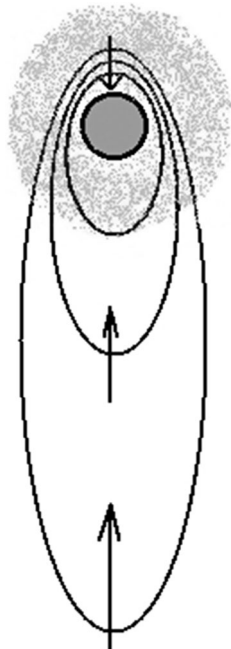
Fig. 6 Maneuvered orbits of Mangalyaan Mars orbiter (Black curve with triangles) with corresponding decay rate (gray curve with stars). Triangles correspond to number of days the MOM stayed before the orbit boost

Fig. 7 Mangalyaan (a) mean altitude, (b) orbit decay rate, (c) thermospheric temperature and (d) density during heliocentric trajectory



drag force on the spacecraft, we have observed that severe space weather condition, especially during high geomagnetic activity, increased the drag force sporadically on the system. Orbit decay rate increases significantly on the ninth and eleventh days (after launch date), due to high solar and/or geomagnetic activity. Upper atmospheric heating and associated density fluctuations are largely due to solar EUV. However, geomagnetic field-induced heating is

Fig. 8 Schematic diagram of Orbital decay effect (circularization) on Mangalyaan in Martian orbit



important during short interval of geomagnetic disturbances and/or storms [32–34]. We find that when perigee height increased by a total sum of about 250 km, it decayed by a total of about 720 m due to atmospheric drag force within about 28 days in the Earth’s orbit during geocentric trajectory.

Figure 7(a)–7(d) show computed (a) mean altitude of Mangalyaan, (b) rate of its orbit decay, (c) thermospheric density and (d) thermospheric temperature during the heliocentric trajectory for 10 months. We have assumed an elliptical orbit with mean radius (altitude) of 149,502,370 km during Earth–Mars (heliocentric) transfer. Typically, thermospheric temperature varies between 1050 K and approximately 1350 K and density varies between 2.0×10^{-19} and 3.5×10^{-19} kg/m³. The total orbital decay is about 157.6 m. These calculations and/or values are based on the indices of solar and geomagnetic activity in the intervening period as inputs. Atmospheric drag and subsequent decay that may be experienced by Mangalyaan during heliocentric trajectory (300 days) is small compared to geocentric (28 days) trajectory scenario (up to a factor of four). Although quite nominal, but the implication of the seemingly small amount of decay is that the planned orbital parameters (such as the Periapsis and Apoapsis) at Mars orbit insertion may be influenced. This unforeseen change must be corrected before Mars arrival Phase. On the other hand, if the expected orbital parameters and hence the retro velocity requirement are not critical (stringent requirement), fluctuation of this magnitude (157.6 m) may not influence the craft’s safe Mars orbit insertion.

Fig. 9 Mangalyaan (a) mean periapsis height and (b) decay rate during first 100 days of Martian trajectory

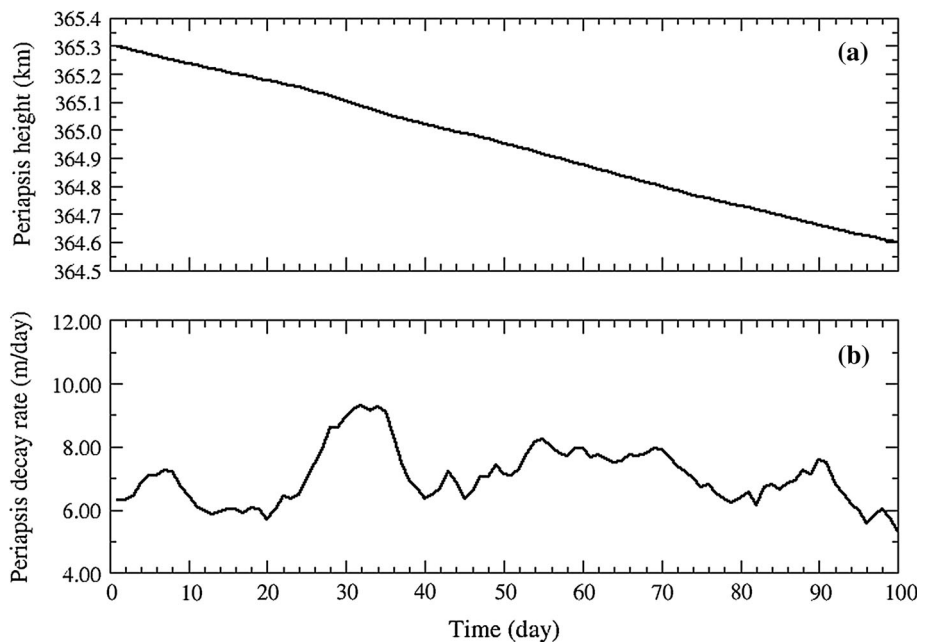


Figure 8 shows the computed decay profile of the spacecraft after its insertion into Martian orbit. The Martian atmosphere causes a drag only on a small part of the planned $365 \text{ km} \times 80,000 \text{ km}$ elliptical orbit. Since the density in Mars atmosphere is only about 1 % of that of the Earth, drag effect is expected to be very minimal. However, this becomes important over a long term. For a very small decay of apoapsis, the periapsis would decay by a large amount and thus, eventually the orbit would be circularized. Under such scenario, the orbit decays faster and would theoretically crash into Martian atmosphere. Figure 9(a) and 9(b) show (a) the mean periapsis height and (b) decay rate of Mangalyaan during 100 days trajectory after Mars orbit insertion. Our result shows a total decay of about 700.8 m and a decay rate of up to 9 m/day in areocentric orbit. Our computation is based on the actual observed indices of solar and geomagnetic activity as inputs between September 24, 2014 and December 31, 2014 (after MOI), and assumed atmospheric density profile of Mars. Calculation (and/or model) of Mars atmosphere is based on Mars–Earth atmosphere (about 1 %) and temperature ratio using the *NRLMSISE-00* empirical model. We are now working on developing approximate Martian atmosphere density model for more accurate calculation and/or prediction. This will be submitted elsewhere.

8. Conclusions

In this study, natural perturbing forces associated with Mars (and/or interplanetary) mission during geocentric, heliocentric and Martian trajectories have been identified and their possible effects analyzed. These forces are mainly planetary and/or solar-forcing-induced. Earth's oblateness (J_2), Third body (solar and lunar), solar radiation pressure, solar energetic radiation environment and atmospheric drag forces can influence the trajectory of the mission. We also have modeled the impact of atmospheric drag force on Mangalyaan Mars orbiter mission as a function of appropriate space environmental parameters during about 28 days of geocentric trajectory, 300 days of heliocentric, and 100 days of areocentric trajectory. We have found that for a total perigee height boost of about 250 km (in Earth orbit), the cumulative orbit decay can be approximately 720 m. Our computation suggests that approximate altitude variation was up to 158 m with respect to the sun during 300 days of interplanetary journey toward Mars. After MOI, the total decay experienced by the spacecraft would be about 701 m with decay rate of up to 9 m/day during 100 days of Martian trajectory based on Mars–Earth atmosphere density ratio. In our analysis, we find that in all the three phases, only minor corrections are required. With actual density model of the Martian atmosphere, we are

now in a position to compute drag over the whole solar cycle and the results will be published in another paper.

Acknowledgments VUJN acknowledges TWAS/ICTP, Trieste, Italy and the S.N. Bose National Centre for Basics Sciences for the research fellowship for this work.

References

- [1] E C Ezell and L Ezell *On Mars: Exploration of the Red Planet* (New York: Dover Inc.) (2009)
- [2] NASA *Mars Odyssey Arrival* (Washington, DC: NASA Jet Propulsion Laboratory) (2001)
- [3] I P Wright, M R Sims and C T Pilinger *Acta Astronaut.* **52** 219 (2003)
- [4] NASA *Mars Exploration Rover* (Washington, DC: NASA Jet Propulsion Laboratory) (2004)
- [5] NASA *Mars Reconnaissance Orbiter* (Washington DC: NASA Jet Propulsion Laboratory) (2006)
- [6] Space.com, *Failure Common among Mars Missions* (<http://www.space.com/13558-historic-mars-missions.html>) (Retrieved 2014)
- [7] TPS *Missions to Mars* (The Planetary Society: www.planetary.org) (Retrieved 2013)
- [8] R J Patton, F J Uppal, S Simani and B Polle *Contr. Eng. Practice* **18** 1093 (2010)
- [9] P Fortescue, J Stark and G Swinerd *Spacecraft System Engineering* (England: Wiley) (2003)
- [10] M F Storz, B R Bowman, M J I Branson, S J Casali and W K Tobiska *Adv. Space Res.* **36** 2497 (2005)
- [11] E Doornbos and H Klinkrad *Adv. Space Res.* **37** 1229 (2006)
- [12] J Xu, W Wang, J Lei, E K Sutton and G Chen *J. Geophys Res.* **116** 2315 (2011)
- [13] R L Walterscheid *J. Spacecraft Rockets* **26** 439 (1989)
- [14] W Hohmann *Die Erreichbarkeit der Himmelskorper—The Attainability of Heavenly Bodies* (Washington: NASA Technical Translations) (1960)
- [15] V A Chobotov *Orbital Mechanics* (Virginia: American Institute of Aeronautics Inc.) (2002)
- [16] R D Braun and R M Manning *Mars Entry, Descent and Landing Challenges* IEEE Aerospace Conference (Montana: Big sky) (2006)
- [17] ISRO *Mars Orbiter Mission* (Bangalore: Indian Space Research Organisation) (2013)
- [18] Spaceflight *Mars Orbiter Mission: Spacecraft and Mission Overview* (www.spaceflight101.com/mars-orbiter-mission.html) (Retrieved 2013)
- [19] B Stockman, J Boyle and J Bacon *International Space Station Systems Engineering Case Study* (USA: Air Force Center for Systems Engineering) (2009)
- [20] M S Munir, J Hutton and P C Hirschberg *Spacecraft Momentum Management using Solar Array* (Palo Alto: Patent Application Publication Inc.) (2012)
- [21] NOAA *Satellites and Space Weather* (NOAA: www.swpc.noaa.gov/info/satellites.html) (Retrieved 2006)
- [22] J Wertz and W J Larson *Space Mission Analysis and Design* (California: Kluwer Academy) (1999)
- [23] G Xu, T Xu, T Yeh and W Chen *Mon. Not. R. Astron. Soc.* **410** 645 (2011)
- [24] M J Sidi *Spacecraft Dynamics and Control* (Cambridge: Cambridge University Press) (1997)
- [25] K Daneshjou, A Alasty and S Rezaei *J. Aerospace Sci. Tech.* **1** 23 (2004)

- [26] P Gurfil *Modern Astrodynamics* (Amsterdam: Elsevier Ltd) (2006)
- [27] Y Kozai *Smithson. Contrib. Astrophys.* **6** 109 (1963)
- [28] J P Murphy *On the Long-Period Motion in the Semi-Major Axis of the Orbit of the TELSTAR 2 Satellite* (Washington DC: NASA) (1966)
- [29] W L Boulton *Planet Space Sci.* **32** 287 (1984)
- [30] N N Jibiri, V U J Nwankwo and M Kio *IJEST* **3** 6532 (2011)
- [31] J Lei, G Chen, J Xu and X Dou *Geodetic Sciences - Observations, Modeling and Applications* (Croatia: InTech Publishers) (2013). doi:[10.5772/56599](https://doi.org/10.5772/56599)
- [32] V U J Nwankwo and S K Chakrabarti *TJSAS/Aerosp. Tech. Jap.* **12** 47 (2014)
- [33] V U J Nwankwo and S K Chakrabarti Moscow: 40th COSPAR Scientific Assembly (2014)
- [34] G Chen, J Xu, W Wang, J Lei and A G Burns *J. Geophys. Res.* **117** A08315 (2012)
- [35] Y S Kwak, K H Kim, Y Deng and J M Forbes *J. Geophys. Res.* **116**, A11316 (2011). doi:[10.1029/2011JA016938](https://doi.org/10.1029/2011JA016938)
- [36] J M Picone, A E Hedin, D P Drob and A C Aikin *J. Geophys. Res.* **107** 1468 (2002)
- [37] S Bruinsma, G Thuillier and F Barlier *JASTP* **65** 1053 (2003)
- [38] B R Bowman, W K Tobiska and J M Kendra *JASTP* **70** 1482 (2008)
- [39] J T Emmert and M Picone *J. Geophys. Res.* **115** A09326 (2010)
- [40] H Liu, T Hirano and S Watanabe *J. Geophys. Res.* **118** 843 (2013)
- [41] J Ellison *Atmospheric Drag and the Day of Satellite Orbit* (Application Essay Part 3) (2007)

Theoretical Model of Drag Force Impact on a Model International Space Station Satellite due to Solar Activity

By Victor U. J. NWANKWO¹⁾ and Sandip K. CHAKRABARTI^{1),2)}

¹⁾ S. N. Bose National Centre For Basic Sciences, Kolkata, India

²⁾ Indian Centre for Space Physics, Kolkata, India

(Received September 22nd, 2013)

The International Space Station (ISS) is the single largest and most complex scientific and engineering space structure in human history. Its orbital parameters make it extremely vulnerable to atmospheric drag force. The complex interactions between the atmosphere's molecular structure, solar energetic particles, extreme ultraviolet (EUV) radiation and the geomagnetic field cause heating and subsequent expansion of the upper atmosphere. This condition increases drag on low Earth orbit satellites and varies with current space weather conditions. In this work we applied empirical atmospheric density model as a function of space environmental parameters, to model drag force impact on a model LEO Satellite during variation of solar activity. Applying the resulting drag model on a model ISS satellite we found that depending on the severity of solar events, stage of the solar cycle and orbital parameters, a massive artificial satellite could experience orbit decay rate of up to 2.95km/month during solar maximum and up to 1km/month during solar minimum.

Key Words: Drag Force, LEO Satellite, Model ISS, Orbit Decay, Solar Activity

1. Introduction

It was long envisaged that a time would come when humanity would leave the provenance of the Earth and occupy the outer space even before the successful launch of the first artificial satellite (Sputnik-1) in October 1957. In April 1971, the Soviet Union launched Salyut 1, the first space station. The station was de-orbited about six months later (11th October 1971), due to mechanical related faults and associated risks. In the late 1980s, NASA in partnership with other space agencies across the world thought of launching the International Space Station (ISS). The first module of the ISS was later launched in 1998 – a structure now known as 'the largest, most complex international scientific and engineering space project in history, and the largest endeavour into space to date' [also see Ref. ¹⁻³⁾]. After launch, the performance and survival of this space system largely depended on a number of factors, including its ability to weather 'perturbing tides' associated with the vast 'ocean' of the space through which it traverses. Gravitational and non-gravitational forces have been identified as the two types of forces perturbing the trajectory of these space objects ⁴⁾. However, atmospheric drag, a non-gravitational force, is the strongest force perturbing satellite orbits at low Earth orbit (LEO) or thermospheric altitude.

Quite a number of satellites have been affected and/or experienced re-entry due to atmospheric drag effects.

These include Skylab (11th July 1979), Russian RORSATs, Kosmos-954 (24 January 1979) and Kosmos-1402 (7th February 1983), Space Station compound Salyut-7/Kosmos-1686 (7th February 1991), and the Chinese FSW-1-5 capsule (12th March 1996) ⁵⁾. Atmospheric drag can also make identification and tracking of satellites and other space objects difficult as well as satellite manoeuvre, lifetime and re-entry predictions ⁶⁻⁹⁾.

The drag force experienced by low Earth orbit satellites (LEOs) is largely due to solar-forcing induced variations on thermospheric density. Effects of solar activity on atmospheric density and/or satellite orbit have been studied by several authors ^{5,8-17)}. However, the impact of long-term drag force at different phases/stages of a solar cycle due to solar-induced space environmental perturbation has not been fully explored, especially for large and/or massive artificial satellite such as the ISS. The density of the thermosphere changes in response to heating and subsequent expansion of the upper atmosphere by energetic extreme ultraviolet (EUV) and particle radiation emitted from the sun during solar and geomagnetic activity, which also varies with current space weather conditions. There is a significant upper atmospheric variation in temperature, density, composition, and winds as a consequence of variations in solar radiation absorbed in the thermosphere at various phases of a solar cycle ¹⁸⁾. Known processes which produce perturbations in the sun-Earth space environment, and causes atmospheric

heating are primarily driven by solar events such as solar wind streams, coronal mass ejections (CMEs), and solar flares. They are sporadic and are known to vary with the phase of the 11-year solar cycle, especially CMEs and solar flares. Co-rotating interaction region (CIR) and/or solar wind high-speed streams (HSS) and their effects on the upper atmosphere and orbit have also been identified and studied^{9,12,15,19-22}. This solar wind driven phenomenon influences atmospheric density profile and induces geomagnetic storms especially during solar minimum and consequently affect satellite orbits. Thermal tides propagating from the lower atmosphere can also influence atmospheric density and significantly contribute to drag on LEO Satellites²³⁻²⁷.

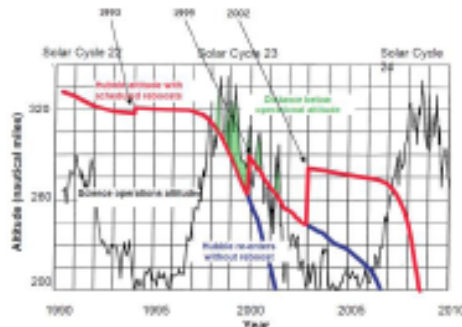


Fig. 1. The three HST servicing missions in 1993, 1999 and 2002 (courtesy: G. Williams, NASA)²⁸

The trajectory of a satellite can be significantly perturbed during intervals of extreme space weather conditions due to consequent atmospheric density increase or variation. Walterscheid (1989) studied solar cycle induced effects on the upper atmosphere and its implications for satellite drag and pointed out that a typical satellite initially at 500km could have a lifetime of about 30 years under typical solar cycle minimum conditions and only about 3 years under solar maximum conditions¹⁸. Atmospheric drag experienced by a satellite at perigee can also significantly lower the apogee, causing the orbit to become more and more circular, until the entire orbit is at the perigee altitude. This situation can result to satellite re-entry. It was reported that increasing activity during past solar peak heated and subsequently expanded Earth's upper atmosphere in the late 1970s. The expanded atmosphere increased drag on Skylab, which was originally at 435 km, and brought it down two years earlier than expected^{5,29}. Hubble Space Telescope (HST) also experienced a severe atmospheric drag during its mission and suffered severe orbital decay²⁹. But for NASA's adoption of a three-year on-orbit maintenance (and its subsequent implementation), to keep it in orbit, it would have

re-entered the atmosphere before the end of its mission. Figure 1 show three of the four HST on-orbit servicing missions in 1993, 1997, 1999 and 2002.

2. The International Space Station at a glance

The first ISS module (Zarya) was launched in November 1998. Construction and assembly of other modules in space continued until its completion in 2011/2012. The ISS is pictured as an orbiting laboratory and construction site that synthesizes the scientific expertise of about 16 nations (that maintains this habitable structure in the outer space)³⁰ [Also see Ref³¹]. The satellite (ISS) is maintained and operated by five space agencies: Canadian Space Agency (CSA), European Space Agency (ESA), Japan Space Exploration Agency (JAXA), National Aeronautics and Space Administration (NASA) and the Russian Federal Space Agency (ROSCOSMOS). These space agencies are drawn from 16 countries - Belgium, Brazil, Canada, Denmark, France, Germany, Italy, Japan, Netherlands, Norway, Spain, Sweden, Switzerland, Russia, United Kingdom and United States³². The model International Space Station containing parameters and/or specifications used in this study is shown in Figure 2.

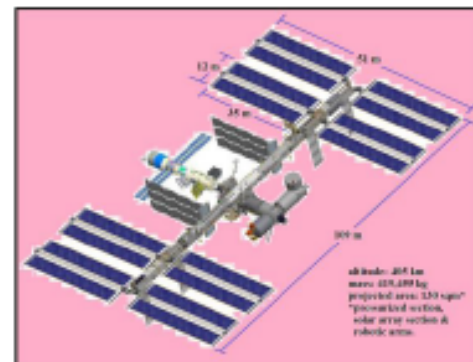


Fig. 2. Model International Space Station (courtesy: www.nasa.gov)

2.1 General characteristics of ISS at completion

Length (pressurized section): 167 feet (51.0 m)
Total Length: 192 feet (58.5 m)
Total Height: 100 feet (30.5 m)
Solar Array Wingspan (tip to tip): 239 feet (72.8 m)
Integrated Truss Length: 357 feet (109m)
***Mass (weight):** 919,964 lbs (419,455kg)
Operating Altitude: 220 nmi average (407 km)
Inclination: 51.6 degrees to the equator
Atmosphere Inside: 14.7 psi (101.36 kilopascals)
***Pressurized Volume:** 34,700 cubic feet (habitable volume of 14,400 cubic feet.)
Computers to control ISS: 52
Robotic Arms: 55-foot robot arm assembly that can lift 220,000 pounds and is used for assembly of main ISS

elements. European Robotic arm: 30-foot robotic arm based on the Russian laboratory and used to move external experiments; Japanese robotic arm: 30-foot robotic arm based on Kibo and used to move and deploy experiments on the Japanese External Facility. *Power Generation*: 84 to 120 kilowatts (usable power) *Maximum Crew Size*: Six
**assumes two Soyuz vehicles are docked to station*²⁹.

3. Study Objective and Orbital Parametric Determination of Model ISS

In this work, we study (by model) the long-term trend of the impact of atmospheric drag on the orbit of a large (massive) LEO satellite (the ISS) at different phases of the solar cycle. We also predict how the trajectory of the spacecraft may be affected in the future. The idea is not to replicate the exact orbital evolutionary scenario of the existing ISS, as that requires precise knowledge of several parameters, but to obtain an estimate for a real case application and drag impact mitigation. Thus we make use of realistic (available) facts and figures for determination and/or approximation of the orbital parameters of the model ISS. One of the parameters critical to computation of orbital decay due to atmospheric drag is the area-to-mass ratio of the system, which is embedded in the ballistic coefficient of the satellite.

3.1 Ballistic (B) and drag coefficients (C_d)

The ballistic coefficient (BC) of a satellite is the parameter that is used to quantify the ability of the body to overcome air resistance (or atmospheric drag) in flight. Satellites that have a high value of $m/A, C_d$ will stay longer in orbit while those with low value will experience accelerated decay. The BC of a satellite can be affected by its orientation and can vary up to a factor of 10^5 ³⁰. The ballistic coefficient B is given by the equation:

$$B = \frac{A_s C_d}{m_s} \quad (1)$$

where A_s is the omni-directional projected area of the satellite, m_s is the mass of the satellite and C_d the drag coefficient at an altitude of r . C_d is the ratio of the drag on a body moving through air to the product of the velocity and the surface area of the body. In determining the exposed area A_s (in the direction of travel) of model ISS, we considered three sections of the ISS – the pressurized section, the solar array section and other connecting sections. ISS uses eight solar array wings. When fully extended, they are about 35 m by 12 m each^{3,31}. The wings are adjusted to maintain an optimum depth of battery discharge, and minimized frontal area projected to the ram direction, thereby reducing drag, and also saving propellant³⁰. Against this backdrop, we assume a minimal

effective projected area for the model ISS. The drag coefficient C_d assumed in this computation is 2.2. It is related to shape, and important to accurate determination of atmospheric density. The value of C_d used in this study is the typical value for most spacecraft, but studies have shown that this assumption introduces a bias into thermospheric density model, because C_d is affected by the complex interaction of reflection, molecular content, altitude etc., such that it varies with altitude³⁰. However, the variation is typically small because the satellite materials usually remain constant³⁴. Another important factor in atmospheric drag computation is the thermospheric density profile. Although this quantity is not precisely known at any given instant, empirical atmospheric models are being continuously improved, with increasing sophistication and good approximation³⁷. In this work we use one such model, namely, the NRLMSISE-00 empirical atmospheric model to compute our drag, for a good representation of the space weather condition through which ISS traverses.

4. Procedure

In this work, we first compute orbital decay of a model satellite ($m_s=250$ kg, $A_s=0.25$ m², $h=480$ km) in low earth orbit during variations of solar activity, as a function of solar parameters using past solar parameter data as tracers or indicators of solar activity. Detailed procedure of this computation can be found in our preceding paper³⁵. Using archival data of solar parameters and solar cycle forecast, we computed and estimated how the hypothetical LEO satellite orbit could be affected at different stages of the solar cycle and around the peak of emerging solar maximum. We then apply the resulting drag model on a model ISS in the LEO (described in section 5). The model ISS orbital decay was computed for the periods during (i) 2000-2002, last solar maximum (ii) 2005-2007, last solar minimum, and (iii) 2012-2014, assumed to be current emerging solar maximum stage. Our goal is to study and demonstrate how the ISS orbit could be affected during these phases/stages of the solar cycle.

The space environmental parameters used (as input data) in the thermospheric density model include solar flux (F10.7), geomagnetic Ap index, and the moving average of F10.7 over three rotations (about 81 days). Detail of the representation of these solar parameters in the model is given in³⁵ [See also Ref. ³⁶⁻³⁸]. The upper atmosphere expands as a direct consequence of the heating as measured by these solar parameters. This causes atmospheric density to increase resulting to an increase in drag on satellites especially those at LEO. The affected satellite orbit decays and causes its re-entry into the Earth if appropriate corrective measures are not taken to stabilize its orbital

parameters^{35,39,40}.

5. Computation of Orbital Decay Due to Atmospheric Drag Force

To compute orbital decay of a satellite orbit, we incorporated the empirical atmospheric model (NRLMSISE-00) into our drag force model. We assumed that the model ISS has an effective (projected towards the direction of motion) surface area of 130 m² (pressurized section=20 m²; solar array section=100 m² and other connecting sections, including the robotic arms=15 m²), mass of 419,455 kg and orbiting the Earth at an initial injected circular orbit of radius 405 km. In reality, mass, size and/or shape of the 'ideal' ISS could have varied during the time (years) for which computations were done due to continuous assembly, upgrade and/or on-orbit maintenance. However, we ignore such variations at this stage. We compute drag force effects from two basic sets of equations. The first set consists of four coupled differential equations³⁵.

$$\begin{aligned} \dot{v}_r &= -\frac{GM_E}{r^2} + r\dot{\phi}^2, \quad \dot{r} = v_r, \\ \dot{\phi} &= -\frac{1}{2}r\dot{\rho}\dot{\phi}^2/B, \quad \dot{\phi} = v_\theta/r \end{aligned} \quad (2)$$

where, v_r and v_θ are the radial and tangential velocity components respectively. G is the gravitational constant, M_E mass of the Earth, r is the instantaneous radius of the orbit, ρ is the atmospheric density, and B is the ballistic coefficient. We ignore the possible Coriolis force term as the radial motion is very slow. The four differential equations were solved by fourth order Runge-Kutta method to obtain instantaneous positions and velocity components of the satellite in an orbit. Incorporating the solution of orbit semi-major axis decay rate ($-\dot{\phi}r^2/B$) for near-circular orbit⁴¹, we compute drag force impact on the model satellite and subsequently on the model ISS, under varying space environmental conditions. Computations were also done by the differential equation of changes in the mean radius of the satellites orbit per revolution (MRPR)^{35,41}, and both methods generally agree. The atmospheric model used in this work is the NRLMSISE-00 empirical atmospheric density model⁴².

6. Results and Discussions

6.1 Impact of Drag force on model ISS satellite

The orbital decay of a model LEO satellite due to atmospheric drag impact was computed. Considering a five-year analysis, result showed that the model LEO satellite experienced a decay rate of about 38±14 km/year

during solar maximum (1999-2003), 7±4 km/year during solar minimum (2004-2008) and up to 27±5 km/year during current emerging solar maximum, with about 5 km contribution from major solar event³⁵.

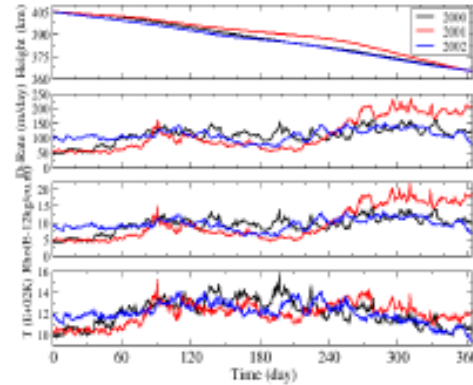


Fig. 3. The time variation (yearly) of model ISS altitude, orbit decay rate, thermospheric density and temperature during 2000-2002

The time variation of model ISS altitude, orbital decay rate, thermospheric density and temperature during the peak of the last solar maximum (2000-2002) is presented in Fig. 3. Applied to the model ISS scenario, results showed a decay of about 39.93 km, 40.56 km and 40.06 km in year 2000, 2001 and 2002 respectively. The mean decay per year is about 40 km per year. Typically, time variation of orbit decay rate, atmospheric density and temperature were 50-230 m/day, 4×10^{-12} - 25×10^{-12} kg/m³ and 1000-1500 K respectively, with the extreme values occurring in 2001.

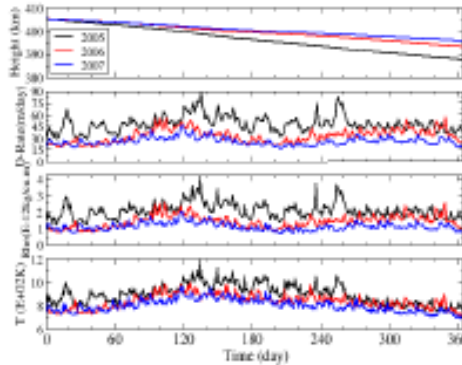


Fig. 4. The time variation of model ISS altitude, orbit decay rate, thermospheric density and temperature during 2005-2007

Figure 4 shows trajectory of model ISS and space environmental condition (indicated by thermospheric temperature and density) through which it traverses during

last solar minimum, 2005-2007. The satellite experienced mean orbital decay of about 17.31km, 11.72 km and 9.23 km per year in 2005, 2006 and 2007 respectively. Mean decay per year during this period is about 13 ± 5 km per year. The time variation of orbit decay rate, atmospheric density and temperature were 15-90 m/day, 0.8×10^{-12} - 4.0×10^{-12} kg/m³ and 700-1150 K respectively.

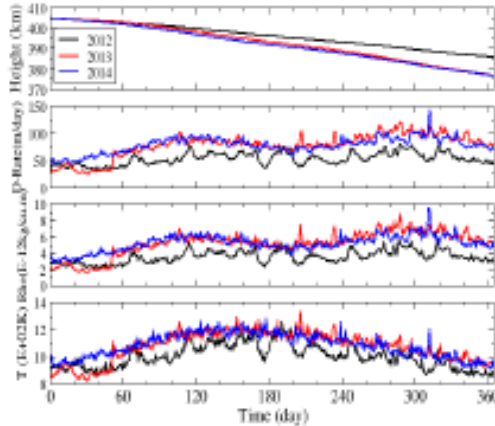


Fig. 5. The time variation of prototype ISS altitude, orbit decay rate, thermospheric density and temperature during 2012-2014

Figure 5 shows time variation of model ISS altitude, decay rate, thermospheric density and temperature during the current emerging peak (2012-2014). Model results show yearly decay of about 19.16 km, 28.12 km and 28.28 km in 2012, 2013 and 2014 respectively. The mean decay per year is about 25 ± 5 km. We assumed that this value excludes contribution from any possible major solar event during March 2013 to December 2014, since the data is the predicted value. We therefore estimated that the occurrence of all major events during the time (predicted data) will cause the satellite additional 5.5 km per year, bringing the mean decay per year to about 31 ± 5 km. This computation was based on more than 18 months of predicted space parameter values (March 2013-December 2014), and an assumed geomagnetic conditions of the year preceding last solar maximum. The time variation of orbit decay rate, atmospheric density and temperature were 25-150 m/day, 10×10^{-12} - 4.0×10^{-12} kg/m³ and 700-1150 K respectively.

There are quite a number of engineering models in use, which applied neutral atmospheric models to compute satellite drag. Chen et al. (2012) studied CIR- and CME-induced effects on CHAMP satellite orbit ($h=450$ km, $m_s=522$ kg, $A_s=0.72$ m², $C_d=2.2$) during day 324-340 in 2006, and showed that the rate of its orbit decay due to CIR- and CME-induced effect was about 50 and 80 m/day respectively⁹⁾. Our modeled result showed

a respective decay of about 42 and 50 m/day³⁵⁾.

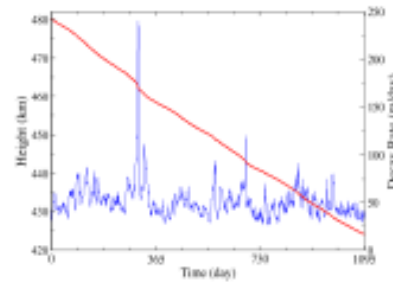


Fig. 6. Time variation of model satellite's altitude (red) and orbit decay rate (blue) during 2003-2005

Xu et al. (2011) stated in their work that CHAMP orbit decayed by 70 km between 2003 and 2005 due to thermospheric density drag⁴⁾. Our model satellite decayed by about 55.84 km (see Fig. 6) during the same period. Although the orbital parameters of the two satellites (CHAMP and model LEOS) are not the same but their area-to-mass ratio are quite close. This factor is important to the drag effect under consideration in this work.

7. Conclusions

We modeled the effects of atmospheric drag force on a hypothetical low Earth orbit satellite during variation of solar activity at different phases of the solar cycle, and applied the model on a model ISS satellite. We show that the severity of impact strongly depends on the phase of the solar cycle. When applied to a model ISS, we found that, depending on the severity of solar events, stage of the solar cycle and the orbital parameters, a large (massive) artificial satellite could experience orbital decay of up to 35 ± 6 km per year during solar maximum and 13 ± 5 km per year during solar minimum. These values correspond to respective mean decay rate of about 2.95 km/month and 1.0 km/month.

Acknowledgments

V. U. J. Nwankwo acknowledges TWAS/ICTP, Trieste, Italy and the S.N. Bose National Centre for Basics Sciences for the TWAS-Bose Research fellowship during which this work was done. We also thank the reviewers for their useful comments and suggestions.

References

- 1) Peter Bond (2002), 'The continuing story of the international space station'. Springer, and Praxis Publishing, Chichester, UK. ISBN 1-85233-567-X

- 2) Boeing (2012), 'Background: International Space Station'. Boeing Defense, Space and Security. St Louis, MO 63166
- 3) Stockman B., Joe Boyle and John Bacon (2009), 'International Space Station Systems Engineering Case Study'. Air Force Center for Systems Engineering.
- 4) Chobotov, V. A. (2002), 'Orbital Mechanics', Third Edition. AIAA Education series. American Institute of Aeronautics Inc, Virginia. 629.4113, p 193-213
- 5) Klinkrad, H (1996), 'On the Use of Atmosphere Models in Re-Entry Predictions'. Environment Modelling for Space-based Applications, Symposium Proceedings (ESA SP-392). ESTEC Noordwijk, pp 287-298
- 6) Storz M. F., Bruce R. Bowman, Major James I. Branson, Stephen J. Casali and W. Kent Tobiska (2005), 'High accuracy satellite drag model (HASDM)'. *Advances in Space Research* **36**, pp 2497-2505
- 7) Doornbos E. and H. Klinkrad (2006), 'Modelling of space weather effects on satellite drag'. *Advances in Space Research* **37**, pp 1229-1239.
- 8) Xu, J., Wang, W., Lei, J., Sutton, E. K., and Chen, G. (2011), 'The effect of periodic variations of thermospheric density on CHAMP and GRACE orbits'. *Journal of Geophysical Research (Space Physics)*, **116**(A15):2315. doi:10.1029/2010JA015995.
- 9) Chen G., Jiyao Xu, Wenbin Wang, Jiahou Lei, and Alan G. Burns (2012), 'A comparison of the effects of CIR- and CME-induced geomagnetic activity on thermospheric densities and spacecraft orbits: Case studies'. *Journal of Geophysical Research*, **117**, A08315. Doi:10.1029/2012JA017782
- 10) Emmert, J. T., and Picone M. (2010), Climatology of globally averaged thermospheric mass density, *Journal of Geophysical Research*, **115**, A09326
- 11) Lei J., Guangming Chen, Jiyao Xu and Xiankang Dou (2013), 'Impact of Solar Forcing on Thermospheric Densities and Spacecraft Orbits from CHAMP and GRACE'. *Intech open science*, DOI: 10.5772/56599
- 12) Burns A. G., S.C. Solomon, L. Qian, W. Wang, B.A. Emery, M. Wiltberger, and D.R. Weimer (2012), 'The effects of Corotating interaction region/High speed stream storms on the thermosphere and ionosphere during the last solar minimum'. *Journal of Atmospheric and Solar-Terrestrial Physics*, **83**, pp 79-87
- 13) Kwak Y. S., K. H. Kim, Y. Deng, J. M. Forbes (2011), 'Response of thermosphere density to changes in interplanetary magnetic field sector polarity'. *Journal of Geophysical Research: Space Physics*, **116** (A11). doi:10.1029/2011JA016938
- 14) Solomon S. C., Alan G. Burns, Barbara A. Emery, Martin G. Mlynecak, Liying Qian, Wenbin Wang, Daniel R. Weimer and Michael Wiltberger (2012), 'Modeling Studies of the Impact of High-Speed Streams and Co-Rotating Interaction Regions on the Thermosphere-Ionosphere'. *Journal of Geophysical Research*, **117**, A00L11. doi:10.1029/2011JA017417
- 15) Liu J., Libo Liu, Biqiang Zhao, Jiahou Lei, Jeffrey P. Thayer, and Robert L. McPherron (2012), 'Superposed Epoch Analyses of Thermospheric Response to CIRs: Solar Cycle and Seasonal Dependencies'. *Journal of Geophysical Research*, **117**, A00L10. doi:10.1029/2011JA017315
- 16) Lei, J., J. P. Thayer, J. M. Forbes, E. K. Sutton, R. S. Nerem, M. Temmer, and A. M. Veronig (2008), 'Global thermospheric density variations caused by high-speed solar wind streams during the declining phase of solar cycle 23'. *Journal of Geophysical Research*, **113** (A11). doi:10.1029/2008JA013433
- 17) Sutton E. K., J. M. Forbes and R. S. Nerem (2005), 'Global thermospheric neutral density and wind response to the severe 2003 geomagnetic storms from CHAMP accelerometer data'. *Journal of Geophysical Research*, **110** (A9)
- 18) Walterscheid R. L. (1989), 'Solar cycle effects on the upper atmosphere - Implications for satellite drag'. *Journal of Spacecraft and Rockets*, **26**(6), pp. 439-444. doi: 10.2514/3.26089
- 19) Borovsky J. E. and Denton M. H. (2006), 'Differences between CME-driven storms and CIR-driven storms'. *Journal of Geophysical Research*, **111**, A07S08. Doi:10.1029/2005JA011447
- 20) Tsurutani B. T., Walter D. Gonzalez, Alicia L. C. Gonzalez, Fernando L. Guarnieri, Nat Gopalswamy, Manuel Grande, Yohsuke Kamide, Yoshiya Kasahara, Gang Lu, Ian Mann, Robert McPherron, Finn Soraas, and Vytienis Vasyliunas (2006), 'Corotating solar wind streams and recurrent geomagnetic activity: A review'. *Journal of Geophysical Research: Space Physics*, **111**, A07S01. Doi:10.1029/2005JA011273
- 21) Kutiev I., Ioanna Tsaouri, Loredana Ferrone, Dora Pancheva, Plamen Mukhtarov, Andrei Mikhailov, Jan Lastovicka, Norbert Jakowski, Dalia Buresova, Estefania Blanch, Borislav Andonov, David Altadill, Sergio Magdaleno, Mario Parisi and Joan Miquel Torta (2013), 'Solar activity impact on the Earth's upper atmosphere'. *Journal of Space Weather and Space Climate*, **3**, A06. Doi:10.1051/swsc/2013028
- 22) Lei J., Guangming Chen, Jiyao Xu and Xiankang Dou (2013), 'Impact of Solar Forcing on Thermospheric Densities and Spacecraft Orbits from CHAMP and GRACE'. *Intech open science*, DOI: 10.5772/56599
- 23) Hagan, M. and Forbes J. (2002), 'Migrating and Non-migrating Diurnal Tides in the Middle and Upper Atmosphere excited by Tropospheric Latent Heat Release'. *Journal of Geophysical Research*, **107**(D24), 4754.
- 24) Forbes, J., Bruinsma, S. L., Zhang, X. and Oberheide, J. (2009), 'Surface-Exosphere Coupling due to Thermal Tides'. *Geophysical Research Letters*, **36**(15), L15812
- 25) Zhang, X., Forbes J. and Hagan (2010a), 'Longitudinal Variation of Tides in the MLT Region: 1. Tides Driven by Tropospheric net Radiative Heating'. *Journal of Geophysical Research*, **115**, A06316
- 26) Oberheide, J., Forbes, J., Zhang X., and Bruinsma, S. L. (2011a), 'Climatology of Upward Propagating Diurnal and Semi-diurnal Tides in the Thermosphere'. *Journal of Geophysical Research*, **116**, A11306.

- 27) Leonard, J. M., Forbes J., and Born G. H. (2012), 'Impact of tidal density variability on orbital and reentry predictions'. *Space Weather*, **10**, S12003.
- 28) John Ellison (2007), 'Atmospheric drag and the day of Satellite orbit'. Application Essay part 3. 1419/zill.10/563, pp 564-655
- 29) US Air force Academy (2012), 'How to Keep a Satellite in Orbit'. US Air force Academy Laboratory Exercise. cosmos.phy.tufts.edu/sim_zirbel/laboratories/Satellite.pdf
- 30) National Geographic Society (2013). 'International Space Station: Cosmic Laboratory'. <http://science.nationalgeographic.co.in/science/space/space-exploration/international-space-station-article>
- 31) NASA (2013a), 'International Space Station: Facts and Figures'. http://www.nasa.gov/mission_pages/station/main/onthestation/facts_and_figures.html
- 32) Greenfield T. Trinh (2013), 'Environmental Testing and Orbital Decay Analysis for a CubeSat'. M.Sc. Thesis (Aerospace Engineering). San Jose State University, USA, pp 18-20
- 33) Bowman R. B. and Moe K. (2005), 'Drag coefficient Variability at 175-500 km from the Orbit Decay Analysis of Spheres'. AAS/AIAA, ASS-05-257
- 34) Vallado D. A. and Finkleman D. (2008), 'A Critical Assessment of Satellite Drag and Atmospheric Density Modeling'. AIAA/AAS, AIAA-2008-6442
- 35) Nwankwo V. U. J., and Chakrabarti S. K. (2014), 'Analysis of Drag Effects on a Model LEO Orbiting Satellite due to the Influence of Upper Atmosphere by Solar events'. (Communicated)
- 36) Poole L. (2002), 'Understanding Solar Indices'. NASA, G3YWX, pp 38-40, 2002.
- 37) NOAA, (2006a), 'Satellites and Space Weather'. www.swpc.noaa.gov/info/satellites.html.
- 38) IRS Radio & Space Services (1999), 'Satellite Orbital Decay Calculations'. Australian Space Weather Agency, Sydney.
- 39) Victor U. J. Nwankwo and S. K. Chakrabarti (2013), 'Theoretical Modeling of Orbital decay of International Space Station (ISS) during variation of solar activity'. International Symposium on Space Technology and Science (ISTS), Nagoya, Japan, 2013-r-32.
- 40) Victor U. J. Nwankwo and S. K. Chakrabarti (2013); 'Computation and Prediction of Drag on LEO satellite due to Upper Atmosphere Influenced by CMEs and other Solar Events'. International Symposium on Space Technology and Science (ISTS), Nagoya, Japan, 2013-r-31.
- 41) Wertz J. and Larson W. J. (1999), 'Space Mission Analysis and Design'. Third Edition, Kluwer academy, El Segundo, Calif, pp145
- 42) Picone, J. M., Hedin A. E., Deob, D. P. and Aikin A. C. (2002), NRLMSISE-00 empirical model of the atmosphere: Statistical comparisons and scientific issues, *Journal of Geophysical Research*, **107**(A12), 1468.